



UNIVERSITÀ DEGLI STUDI DI UDINE

TESI DI DOTTORATO DI RICERCA

Per ottenere il titolo di

**Dottore di Ricerca dell'Università di Udine**

**Dipartimento di Ingegneria Elettrica, Gestionale e Meccanica**  
Corso di Dottorato in Ingegneria Industriale e dell'Informazione, XXV ciclo

Alan PAUSSA

Udine, 23 aprile 2013

**Numerical Simulation of Advanced CMOS and Beyond  
CMOS Nanoscale Transistors**

Tutor:  
**David ESSENI**

**Commissione esaminatrice**

Prof. Stefano Tonchia

Prof. Eugenio Brusa

Prof. Giovanni Franceschini

Prof. Antonio Gnudi



# Contents

<b>Contents</b>	<b>I</b>
<b>Abbreviations and Acronyms</b>	<b>V</b>
<b>Abstract</b>	<b>VII</b>
<b>1 Novel Device Architectures and New Materials for CMOS and Beyond CMOS Transistors</b>	<b>1</b>
1.1 The Moore's law and the MOSFETs scaling . . . . .	2
1.2 Alternative device architectures . . . . .	4
1.3 Alternative channel materials . . . . .	6
1.4 Graphene . . . . .	7
1.4.1 Graphene: why is it so remarkable? . . . . .	7
1.4.2 Graphene: critical issues . . . . .	9
1.5 Purpose of this work . . . . .	13
<b>2 Pseudospectral Method for the Simulation of Nanodevices</b>	<b>21</b>
2.1 Introduction . . . . .	22
2.2 Pseudospectral approach . . . . .	24
2.3 PS approach in one-dimensional domains . . . . .	24
2.3.1 Non periodic unknown function . . . . .	24
2.3.2 Approximation of a definite integral . . . . .	28
2.3.3 Treatment of boundary conditions . . . . .	28
2.3.4 Treatment of media discontinuities . . . . .	29
2.3.5 Periodic unknown function . . . . .	30
2.4 PS approach in two-dimensional domains . . . . .	31
2.4.1 PS approach for a rectangle . . . . .	31
2.4.2 PS approach for a disk . . . . .	31
2.4.3 PS approach for two-dimensional convex domains . . . . .	32
2.5 Application of the PS approach to the simulation of FinFETs and GAA nanowires	34
2.5.1 Electron quantization in nanowire FETs and FinFETs . . . . .	34
2.5.2 Self-consistent Schrödinger-Poisson solution . . . . .	37
2.5.3 Numerical results and comparison with other approaches . . . . .	38
2.6 Conclusions . . . . .	44
<b>3 Graphene</b>	<b>51</b>
3.1 Introduction . . . . .	52
3.2 Monolayer wide graphene sheet . . . . .	52
3.2.1 Atomic structure . . . . .	52
3.2.2 Calculation of the bandstructure . . . . .	53
3.2.3 Density of states, carrier statistics and ambipolarity . . . . .	56

3.2.4	Scattering mechanisms . . . . .	58
3.3	Generation/Recombination mechanisms . . . . .	60
3.3.1	Band-to-band tunneling . . . . .	61
3.3.2	Interband recombination assisted by phonons . . . . .	64
3.4	Graphene bilayer . . . . .	65
3.4.1	Atomic structure and bandstructure calculation . . . . .	65
3.4.2	Density of states . . . . .	70
3.4.3	Scattering mechanisms . . . . .	71
3.5	Conclusions . . . . .	72
<b>4</b>	<b>Linearization of the Boltzmann Transport Equation for the Calculation of the Low Field Mobility</b>	<b>77</b>
4.1	Introduction . . . . .	78
4.2	Linearization of the BTE . . . . .	78
4.2.1	Formulation based on the momentum relaxation time . . . . .	80
4.2.2	Mobility calculation . . . . .	80
4.3	Numerically efficient solution of the linearized BTE . . . . .	81
4.3.1	Anisotropic bands and scattering rates . . . . .	81
4.3.2	Isotropic scattering mechanisms . . . . .	84
4.3.3	Isotropic bands . . . . .	84
4.3.4	Multiple scattering mechanisms and Matthiessen's rule . . . . .	85
4.3.5	Some remarks about the numerical solution . . . . .	86
4.4	Numerical Results for mobility in graphene bilayers . . . . .	87
4.4.1	An isotropic energy relation . . . . .	87
4.4.2	Relaxation time and mobility for the isotropic energy relation . . . . .	87
4.4.3	Results for an anisotropic energy relation . . . . .	92
4.5	Conclusions . . . . .	96
<b>5</b>	<b>Monte Carlo Approach for the Simulation of Uniform Transport in Bilayer Graphene</b>	<b>101</b>
5.1	Introduction . . . . .	102
5.2	Model description . . . . .	102
5.2.1	Structure of the simulator . . . . .	102
5.2.2	Model for the bandstructure . . . . .	103
5.2.3	Scattering rates . . . . .	103
5.2.4	Monte Carlo implementation . . . . .	105
5.3	Simulation results . . . . .	107
5.3.1	Low-field mobility . . . . .	107
5.3.2	Saturation velocity . . . . .	109
5.3.3	Screening of remote phonons . . . . .	111
5.4	Conclusions . . . . .	114
<b>6</b>	<b>Monte Carlo Approach for the Simulation of Graphene Transistors</b>	<b>117</b>
6.1	Introduction . . . . .	118
6.2	Semi-classical Monte Carlo model . . . . .	119
6.3	Model validation . . . . .	124
6.4	Results . . . . .	129
6.4.1	Effect of scattering . . . . .	129
6.4.2	Effect of the scaling . . . . .	131
6.5	Conclusions . . . . .	135
<b>7</b>	<b>Concluding Remarks and Future Developments</b>	<b>141</b>

---

<b>A NanoTCAD ViDES full quantum simulator</b>	<b>145</b>
<b>B Simplifications of the MRT problem</b>	<b>149</b>
B.1 Isotropic scattering mechanisms . . . . .	150
B.2 Isotropic bands . . . . .	150
<b>C Monte Carlo approach for the solution of the Boltzmann Transport Equation</b>	<b>153</b>
<b>Publications of the Author</b>	<b>159</b>



# Abbreviations and Acronyms

BTBT	Band-To-Band-Tunneling
FBZ	First Brillouin Zone
DOS	Density Of State
GFET	Graphene Field Effect Transistor
GBL	Graphene BiLayer
EOT	Equivalent Oxide Thickness
SCE	Short Channel Effects
ITRS	International Technology Roadmap for Semiconductors
FinFET	fin shaped transistor
GAA	Gate-All-Around nanowire transistor
TEM	Transmission Electron Microscopy
FD	Finite-Difference method
FE	Finite-Element method
ACM	Alternative Channel Materials
HEMT	High Electron Mobility Transistors
RF	Radio-Frequency
CNT	Carbon NanoTube
GNR	Graphene NanoRibbon
MME	Micromechanical Exfoliation
HOPG	Highly Oriented Pyrolytic Graphite
CVD	Chemical Vapor Deposition
PS	PseudoSpectral approach
LBTE	Linearized Boltzmann Transport Equation
MC	Monte Carlo
S/D	Source/Drain
DGA	Discrete Geometric Approach
MOSFET	Metal Oxide Semiconductor Field Effect Transistor
BTE	Boltzmann Transport Equation
MRT	Momentum Relaxation Time
G/R	Generation/Recombination
RP	Remote Phonons
TB	Tight-Binding
ER	Edge Roughness



# Abstract

**T**HERE is a growing consensus in the electron device community that the 32nm node could be the last technology node based on the conventional silicon planar MOSFET, due to the physical limitations of this technology. Several new approaches are under investigation in order to reach the requirement of the International Technology Roadmap for Semiconductors beyond the 32nm technology node; some studies are focused on new device architectures that allow a better control of the gate over the channel, while other ones propose to substitute silicon in the channel with high-mobility materials. The physics-based modeling of these new devices is extremely important because it is supposed to guide the electron device industry in the choice of the best device structures for the future technology nodes. In this context, the aim of this PhD thesis is to investigate two of these innovative technology options: the FinFET and the nanowires device architectures and the graphene based transistors. To this purpose, we developed several TCAD simulation tools based on advanced modeling techniques.

In the first part of the thesis we developed a solver for the simulation of the electrostatics in the channel section of nanowires and FinFETs with realistic shape, based on an innovative numerical approach, the Pseudospectral method. Thanks to the remarkable accuracy of this approach (i.e. an exponential decrease of the approximating error with the number of discretization points), we were able to develop a very efficient simulator, which vastly outperforms solvers based on standard numerical approaches such as the finite differences. Moreover, we compared our approach with another innovative method, the Discrete Geometric Approach, in the simulation of the electrostatics of realistic devices.

The second part of the PhD was focused on the simulation of graphene, the innovative material with very interesting physical properties discovered in 2004. First we developed a novel and general approach for the exact solution of the linearized Boltzmann transport equation; we applied the proposed method to the calculation of the graphene bilayer low-field mobility: the obtained results are quite consistent with the experimental values found in the literature. We also demonstrate that the most common approach used in the literature for the estimation of the low-field mobility (i.e. the Momentum Relaxation Time approach) introduces non negligible errors in the considered case. We thus developed also a semi-classical transport simulator based on the Monte Carlo approach for the modeling of the uniform transport in bilayer graphene. Our simulations showed that the saturation velocity in this material is much higher than in silicon; moreover, with respect to monolayer graphene, the saturation velocity is higher in bilayer graphene only at high carrier densities.

Finally, we developed a semi-classical model for RF graphene FETs based on the Monte Carlo approach including a novel local model for band-to-band tunneling. The simulator, that was validated by comparison with full quantum results, improves the range of applications of semi-classical Monte Carlo models for graphene based transistors. Using this simulator we found that the band-to-band tunneling is responsible for the poor saturation of the current in GFETs transistors; moreover, we studied the effect of the scattering and of the gate length on the performance of this device and we found that the scattering has a non negligible influence on the main RF figures of merit even in short channel devices.



## Chapter 1

# Novel Device Architectures and New Materials for CMOS and Beyond CMOS Transistors



where  $Q_{sw}$  is the switched charge at the output node. As it can be seen in Eqs.1.1 and 1.2, an increase of  $v_{VS}$  improves the performance of the transistor by enhancing the  $I_{on}$  and reducing the  $t_p$ . The geometrical scaling has been the main enabler of the enhancement of the performance of silicon CMOS technologies down to the 130nm technology node, as can be seen in Fig.1.2, reporting the evolution along the technology nodes of the gate length ( $L_G$ ) and the Equivalent Oxide Thickness (EOT) of the gate dielectric, that are two of the most important geometrical parameters of the MOS transistor.

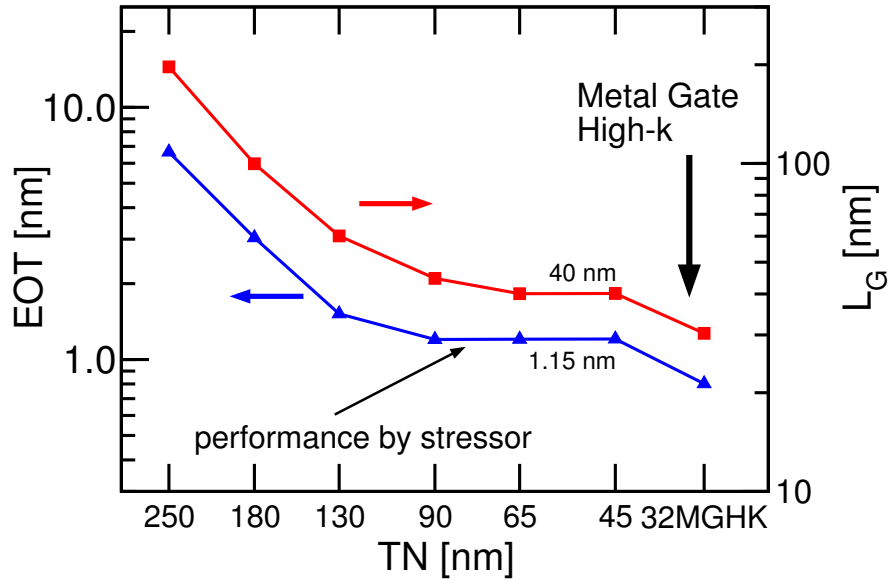


Figure 1.2: Evolution of the gate dielectric Equivalent Oxide Thickness (EOT) and of the gate length  $L_G$  with the technology nodes (data from [5]).

However, further scaling of the device dimensions is today very challenging because it may result in an unacceptable degradation of the device performance, due to the so-called Short Channel Effects (SCE) [6]. A lot of studies have been carried out both by the main players of the silicon industry and by the academic community in order to find new ways to improve the device performance that may complement or take the place of the geometrical scaling. These studies led to the introduction of new solutions into the device fabrication, called *technology boosters*. One of the most effective technology boosters has been the strain engineering. In fact by introducing appropriate strain conditions it was possible to improve the mobility and  $v_{VS}$  of silicon MOSFETs very remarkably. Thanks to the improvements given by the strained silicon, the manufacturers were able to meet the requirements set by the International Technology Roadmap for Semiconductors (ITRS) down to the 45nm technology node without any physical scaling (see Fig.1.2).

Since the mobility and carriers velocity enhancements provided by the strain tend to saturate above 3GPa, new technology boosters were needed to track the ITRS projections for the 32nm node. Hence, two other technology boosters were introduced: firstly, the standard silicon dioxide gate dielectric was replaced with high-k materials; secondly, a metal gate was employed. These innovations allowed to reduce the equivalent oxide thickness while keeping the gate leakage under control, which resulted in an improved electrostatic integrity of the device. Thanks to these solutions, a scaling of the device gate length was possible for the 32nm technology node.

It is a common belief in the electron device community that the 32nm node will be the last technology node based on the conventional silicon planar MOSFET, due to the physical limitations of this technology. Several new approaches are under investigation in order to reach

the requirement of the ITRS beyond the 32nm technology node (see for example [7]); some studies are focused on new device architectures that allow a better control of the gate over the channel, while other ones propose to substitute silicon in the channel with high-mobility materials. In the next sections we will introduce briefly these two different approaches.

## 1.2 Alternative device architectures

As mentioned in the previous section, in the last decade the electron device community made a strong effort in developing new device architectures able to fulfill the requirements of the ITRS beyond the 32nm technology node. The most promising alternatives to the standard planar MOSFET architecture are the so-called fin shaped transistor (FinFET) and the Gate-All-Around nanowire transistor (GAA). Fig.1.3 and Fig.1.4 show respectively a Transmission Electron Microscopy (TEM) photo and a sketch of the channel section of a FinFET and of a GAA transistor. As it can be seen, in these devices the channel is partly (in the FinFET)

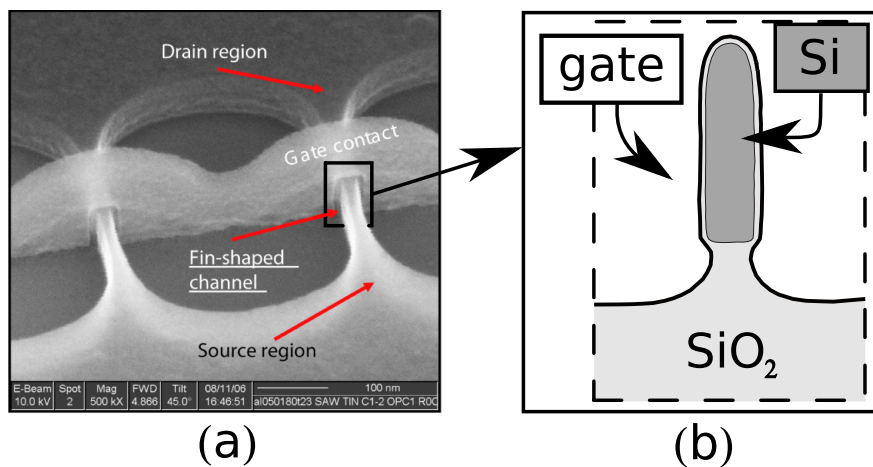


Figure 1.3: (a) TEM photo (courtesy of NXP Semiconductors, Leuven, Belgium) and (b) sketch of a section of the channel of a FinFET.

or completely (in the GAA) surrounded by the gate. The effect of this particular structure is twofold: firstly, it significantly improves the electrostatic integrity with respect to the planar devices, thus reducing the SCEs; secondly, it allows high on-currents [9, 10, 11]. The performance reached in the experiments by these type of devices have convinced some of the major players in the nano-electronic industry to invest on them. Indeed, in spring 2011, after 10 years of development, Intel announced the introduction of FinFET transistors (called by Intel Tri-Gate or 3D Transistors) for the 22nm technology node [7]. Moreover, the Intel Ivy Bridge processor that reached the market in April 2012 is already based on FinFETs transistors. The compatibility of FinFETs with the standard CMOS fabrication process has been one of the most important reasons that lead Intel to significantly invest in their development.

It is clear now that the FinFET will become the device architecture allowing for a further scaling of the transistor dimensions. Thus, it is very important to develop novel simulators able to model the behavior of this kind of devices, in order to give to the device designers appropriate tools to optimize the performance. Moreover, accurate and yet computationally efficient simulators of nanoscale FinFETs are an important target, also for the modeling of the electron device variability, which typically demands the simulation of large sets of devices with slightly modified physical or geometric parameters. However, a lot of problems for the device modeling community arise with the introduction of new architectures. First of all, there is an increase of the dimension of the quantization problem with respect to the standard

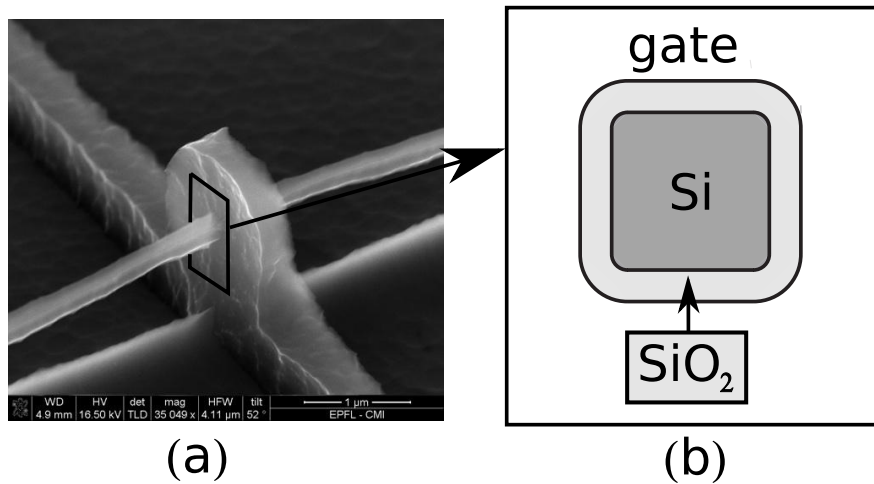


Figure 1.4: (a) TEM photo (adapted from [8]) and (b) sketch of a section of the channel of a GAA transistor.

transistor. Indeed, in the planar devices, the carriers are confined near the gate dielectric along the direction perpendicular to the transport (the  $z$  direction in figure Fig.1.5) by the electric field imposed by the gate stack, thus resulting in one-dimensional quantization. The carriers form a so-called two-dimensional gas. In nanowires and FinFETs with a narrow fin, instead, the

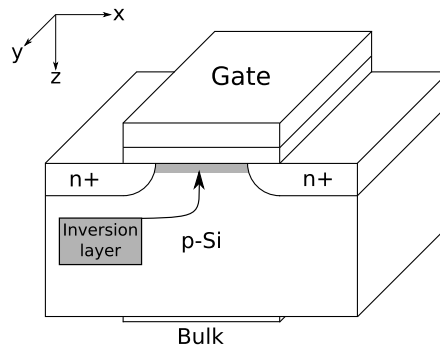


Figure 1.5: Sketch of a traditional planar  $n$ -MOSFET; the carriers are confined along the  $z$  direction and form a two-dimensional gas in the  $(x, y)$  plane.

carriers are confined in a two-dimensional well both by the electrostatics and by the geometry of the device (see the sketches in Figs.1.3 and 1.4) and form a one-dimensional gas. In the electron device community, the numerical solution of the eigenvalue problems related to the quantization of the carriers is most frequently tackled by using the Finite-Difference (FD) or Finite-Element (FE) methods, which are robust and easy to implement but feature a fixed (and usually low) order convergence of the approximation error with respect to the size of the discretization grid. For example, the FD method applied to a one-dimensional problem allows a convergence of the error that goes as  $\mathcal{O}(\mathcal{N}_{FD}^{-2})$ , where  $\mathcal{N}_{FD}$  is the number of discretization points used. This low order of convergence of the approximation error is not a problem when simple one-dimensional equations have to be solved. On the contrary, when the equations are defined on multi-dimensional domains, the low order of convergence translates into a very high and often unacceptable number of discretization points to be used in order to obtain a sufficient accuracy. Thus, it is very important to find novel numerical methods to accurately solve in a

computationally efficient way the quantization problems related to the new device architectures.

### 1.3 Alternative channel materials

As already mentioned in Sec.1.1, an innovative route to continue the progress of the integrated circuit technology is the replacement of silicon with Alternative Channel Materials (ACM). Indeed, new channel materials with large carrier mobility and carriers velocity  $v_{VS}$  can reduce significantly the gate delays for a given  $V_{DD}$ , offering potential advantages for highly energy efficient signal processing. The interest of the research community and of the semiconductor industries for ACM CMOS transistors has increased substantially in the recent years. SiGe and Ge are probably the strongest competitor of silicon for  $p$ -type MOSFETs [12, 13], whereas III-V semiconductors, such as InGaAs and GaSb, are being seriously investigated for  $n$ -type transistors (High Electron Mobility Transistors, HEMTs) [14, 15, 16, 17, 18, 19, 20]. As it can be seen in Fig.1.6, the  $v_{VS}$  is much larger in transistors based on III-V materials with respect to the silicon and strained silicon ones. However, up to now it is not clear if these materials

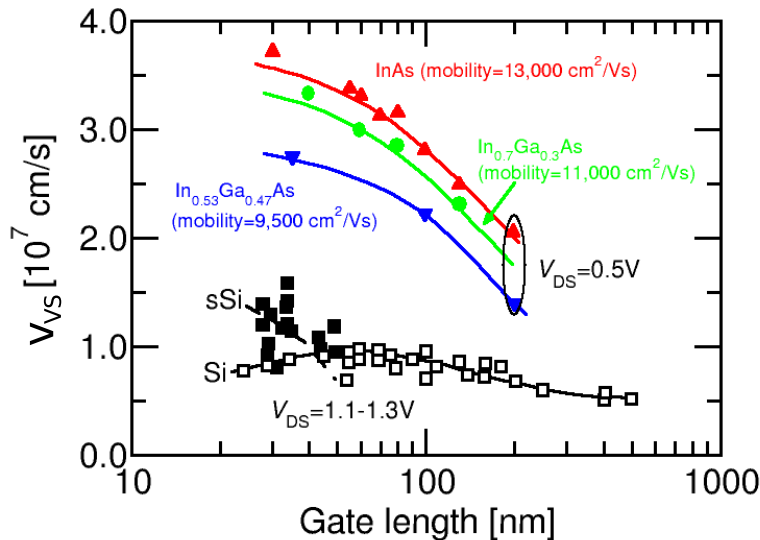


Figure 1.6: Experimentally extracted carrier velocity at the virtual source  $v_{VS}$  in silicon and strained silicon MOSFETs versus the channel length for  $V_{DS}$  ranging from 1.1V to 1.3V, and for III-V HEMTs at smaller  $V_{DS}=0.5V$ . The corresponding mobility values are also reported. Data from [21] and references therein.

will lead to an effective improvement of the performance for the technology nodes below 32nm, because the large carrier velocities are coupled with very small density of states that contribute negatively on the current (see for example the theoretical work [22]).

Besides III-V, SiGe and Ge, a new high mobility material came into the scene a few years ago. Indeed, in 2004 a breakthrough in solid state physics was achieved thanks to a discovery made at the Manchester University by Konstantin Novoselov and Andre Geim: the isolation of nearly perfect two-dimensional graphene monolayers. We will describe graphene in more details in Chap.3; in the next section we want just to briefly present its astounding properties, that make graphene a possible candidate as high mobility channel material in transistors beyond the 32nm technology node, and also list the potential limitations.

## 1.4 Graphene

### 1.4.1 Graphene: why is it so remarkable?

Graphene has been first isolated in its freestanding form by Konstantin Novoselov and Andre Geim in 2004 at the Manchester University [23]. Thanks to this discovery, they have been awarded the Nobel Prize in physics in 2010 [24]. Geim gives the following definition of graphene [25]:

*Graphene is a flat monolayer of carbon atoms tightly packed into a two-dimensional honeycomb lattice, and is a basic building block for graphitic materials of all other dimensionalities.*

Its particular atomic structure, reported in Fig.1.7, translates into a unique combination of

Figure 1.7: Atomic structure of the monolayer graphene: the carbon atoms are placed according to a two-dimensional honeycomb lattice.

exceptional properties:

- it is an excellent conductor, because its holes and electron mobilities can reach  $10^6 \text{cm}^2/(\text{Vs})$  [26] (for suspended monolayer graphene in vacuum); moreover, its saturation velocity is about  $5 \times 10^7 \text{cm/s}$ , twice the one of GaAs and five times higher than that of silicon; finally, it can sustain a maximum current density greater than  $10^8 \text{A/cm}^2$  [27];
- it is the first two-dimensional material ever created;
- it is the thinnest and lightest object ever created;
- it is “the strongest material ever created” (300 times stronger than steel); its Young’s modulus is about 1.1TPa, one order of magnitude higher than silicon;
- it is extremely bendable; it can sustain a reversable strain up to 25%;
- it is transparent; but, actually, its opacity can be controlled;
- it has a very high thermal conductivity: about  $5000 \text{W}/(\text{mK})$  at room temperature, that is ten times higher than in Cu and Al, and twice than in diamond.

This list helps to understand why graphene is so studied both by the academic community and by the industry. Some of the possible practical applications of graphene are summarized in Fig.1.8. In electronics, a graphene based transistor (GFETs) should benefit from the huge mobility and group velocity of graphene sheets. For example, one of the possible and most promising applications of graphene is using it as the channel material of radio-frequency (RF) transistors. In the last years a lot of work has been carried out by the scientific community to boost the performance of this kind of devices; this effort translated in a very fast improvement

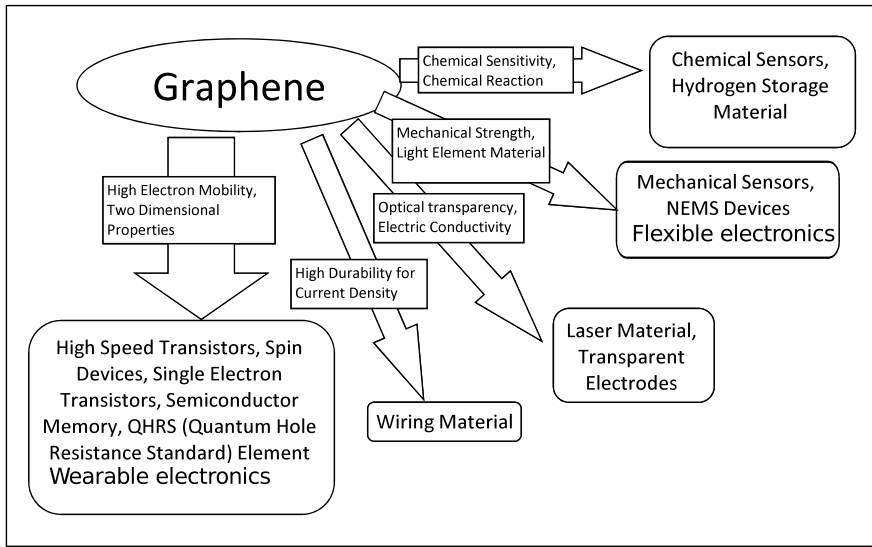


Figure 1.8: Possible applications of graphene. Adapted from [28].

of the performance of RF GFETs with respect to other technologies, as can be seen in Fig.1.9, where the evolution of the RF transistors based on graphene and on Carbon NanoTube (CNT) is compared. Indeed, in less than 5 years the scientific community was able to develop a transistor

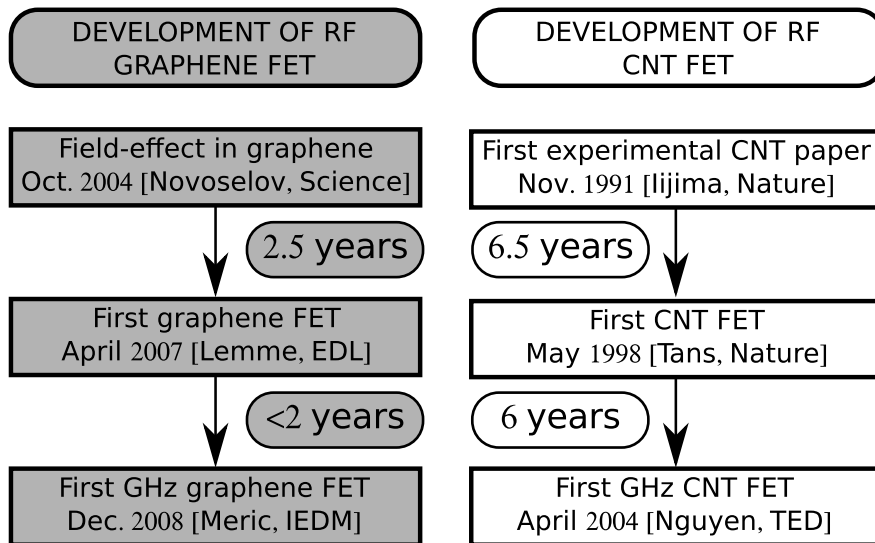


Figure 1.9: Progress in graphene RF MOSFET development compared with the evolution of nanotube FETs. Adapted from [29].

with a cut off frequency above the GHz limit, starting from scratch; in comparison, the same result was obtained for the CNT technology in more than 12 years. This fast growth is still continuing today, as can be seen in Fig.1.10, that compares the best cut-off frequencies obtained by GFETs in 2010 and 2011 versus the best performance given by other technologies. As can be seen, the growth is impressive: in only one year the record cut-off frequency tripled, passing from 100GHz [30] to 300GHz [31]. Moreover, in 2012 the record cut-off frequency has been further improved to 427 GHz [32]; thanks to these results GFETs have almost reached the best

performance given by more well-established technologies.

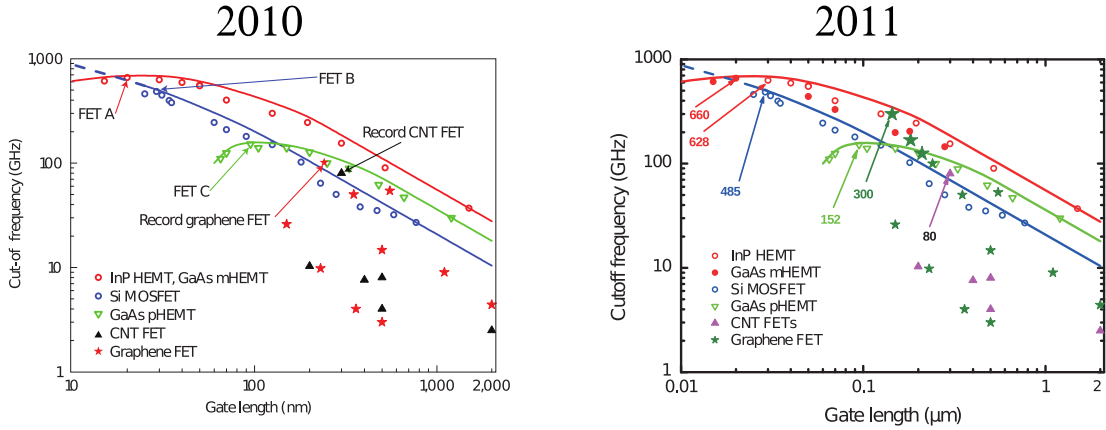


Figure 1.10: Comparison between the best unity current gain cut-off frequencies reached by GFETs transistors in 2010 (left, adapted from [29]) and 2011 (right, adapted from [33]) versus the best performance obtained by using other technologies.

However, besides all these amazing properties, graphene has also strong drawbacks and issues that have to be addressed in order to allow GFETs to outperform transistors based on other materials and technologies. The next section analyzes these critical issues.

### 1.4.2 Graphene: critical issues

As previously mentioned, there are some critical issues that must be solved in order to make GFETs competitive with transistors based on conventional semiconductors. The main issues are:

- graphene is gapless thus resulting in GFETs with very low  $I_{on}/I_{off}$  ratios and poor current saturation;
- there is a strong mobility reduction due to the influences of the substrate and the top gate dielectric on graphene; moreover, the mobility strongly depends on the fabrication process;
- GFETs have very high contact resistance (hundreds of  $\Omega \cdot \mu\text{m}$ ).

In the next subsections we will discuss these issues one by one.

#### Graphene is gapless

As can be seen in Fig.1.11, the huge mobility measured in suspended monolayer graphene (which is orders of magnitude higher with respect to all the other semiconductors considered in electronics) is coupled with a gapless energy dispersion relation. A gapless energy dispersion relation results in ambipolar FETs with very low  $I_{on}/I_{off}$  ratios and no current saturation, as can be seen in Fig.1.12. In order to solve this issue, ways to induce an energy gap have to be devised. Different techniques have been proposed to open a gap in graphene, among which we here recall:

- *Graphene NanoRibbons* (GNRs): an energy gap is created by size-induced quantization when graphene is cut in nanoribbons. Indeed, experiments show that this approach is able to induce a bandgap and thus increase the  $I_{on}/I_{off}$  ratio (see Fig.1.13-(a)), but at the cost of a strong reduction of the mobility (see Fig.1.13-(b)). Due to the strong decrease

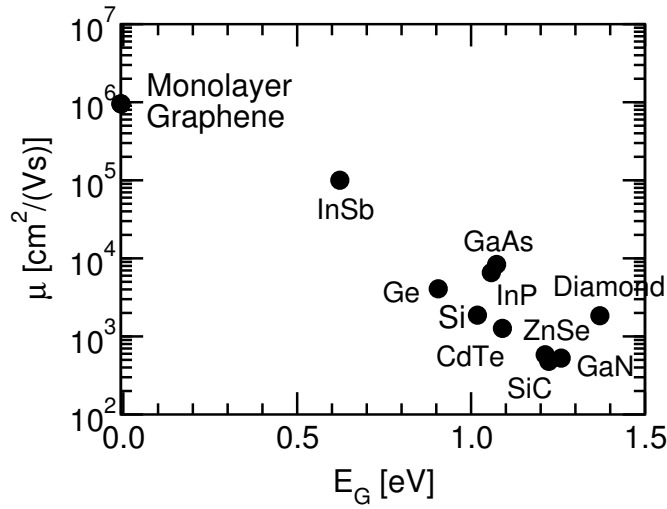


Figure 1.11: Electron low-field mobility and bandgap of several bulk semiconductors at 300K. Adapted from [28]. The graphene data is taken from [26].

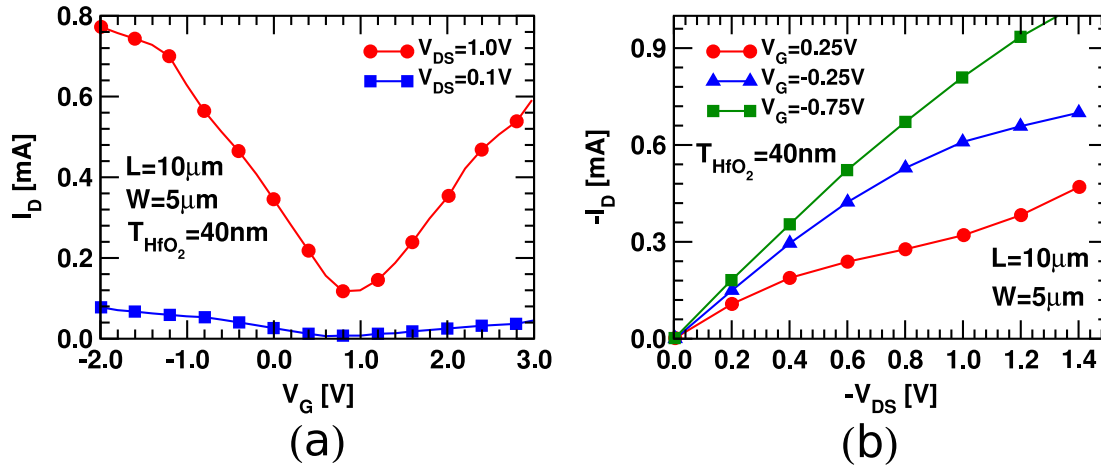


Figure 1.12: Experimental transcharacteristics (a) and output characteristics (b) of transistors based on a large graphene sheet: the  $I_{on}/I_{off}$  ratios are very low due to the ambipolar behavior; moreover, the devices do not exhibit a current saturation region. Adapted from [34].

of the mobility shown in Fig.1.13, today GNRs do not seem to be a convenient solution to induce a bandgap in graphene.

- *Strained graphene*: according to several theoretical studies, the stress can modify graphene bandstructure, making the transport anisotropic, changing the resistivity of the graphene sheet and inducing a bandgap [37, 38]. Only the first two effects have been already observed in experiments [39, 40, 41] and have been exploited for practical applications, like pressure sensors [42, 43]; regarding the bandgap opening, even theoretical calculations estimate a huge amount of suitable-directed strain in order to induce a bandgap in graphene: 23% in the zig-zag direction in [37], see Fig.1.14, and a combination of a 15% shear and uniaxial strains in [38]. Thus also strain seems to be an unpractical solution for the problem of the gapless bandstructure of graphene.

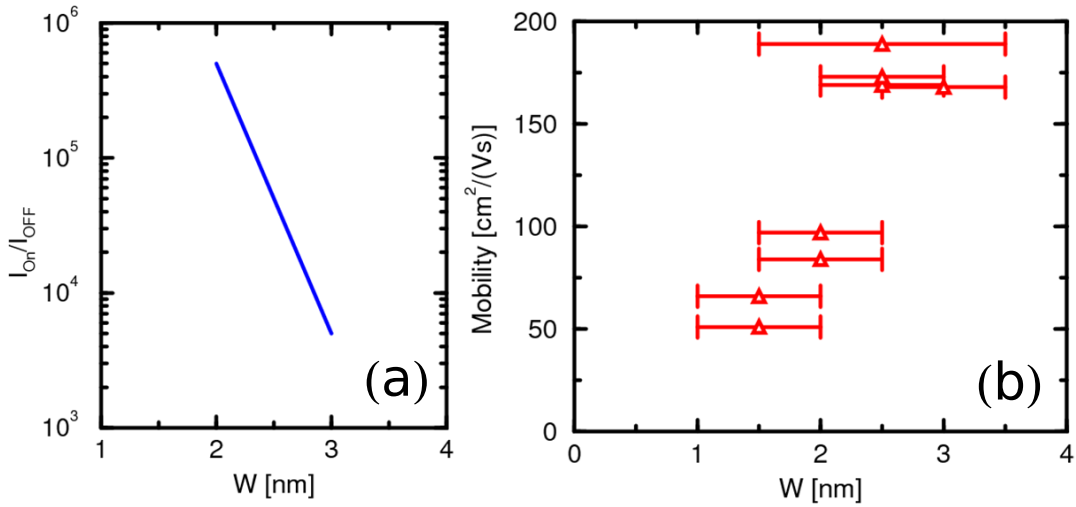


Figure 1.13: Experimental  $I_{on}/I_{off}$  ratio (a) and low-field mobility (b) versus the GNR width. Adapted from [35] and [36].

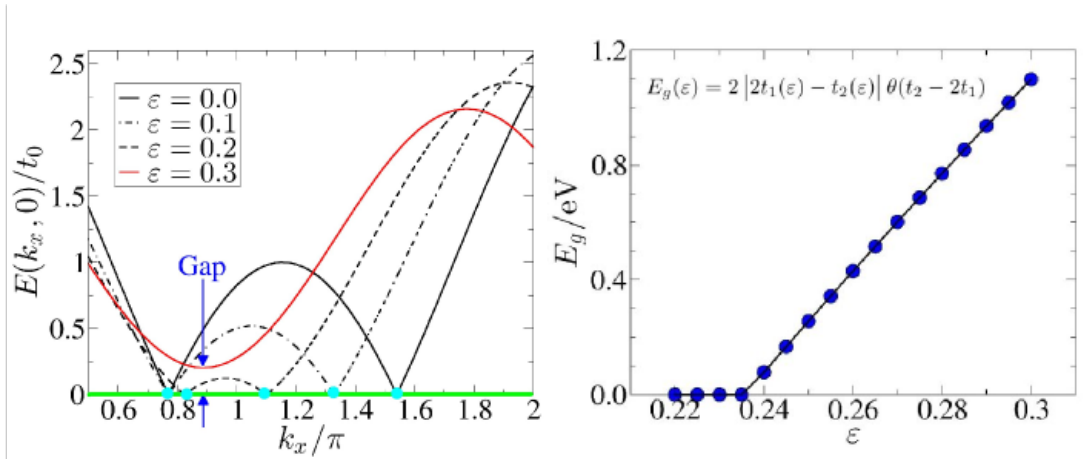


Figure 1.14: Theoretical estimation of the dependence on the strain of the bandstructure along the direction  $k_x$  (for  $k_y = 0\text{m}^{-1}$ ) (left) and induced energy gap (right). Adapted from [37].

- *Graphene BiLayer* (GBL): the GBL consists of two interacting sheets of graphene arranged according to the Bernal stacking [44, 45, 46] (see Fig.1.15), and it is a very interesting material because the potential difference  $V$  between the two layers controls the energy bandgap [44, 45, 46]. An energy gap has been already measured in several experiments [47, 48, 49, 50, 51, 52]; moreover, large  $I_{on}/I_{off}$  ratios [53] and very good current saturations have been observed [54] in GFETs based on GBL. Hence, GBL is a very promising approach that can be used in order to induce a bandgap in graphene.

#### Mobility dependence on the process, on the substrate and on the top gate dielectric

In 2004, Novoselov and Geim were able to peel graphene flakes off a graphite crystal using simple scotch tape. Indeed, graphite is made by a huge number of graphene monolayers bonded by the weak Van der Waals force. The removal of the tape breaks the Van der Waals bonds:

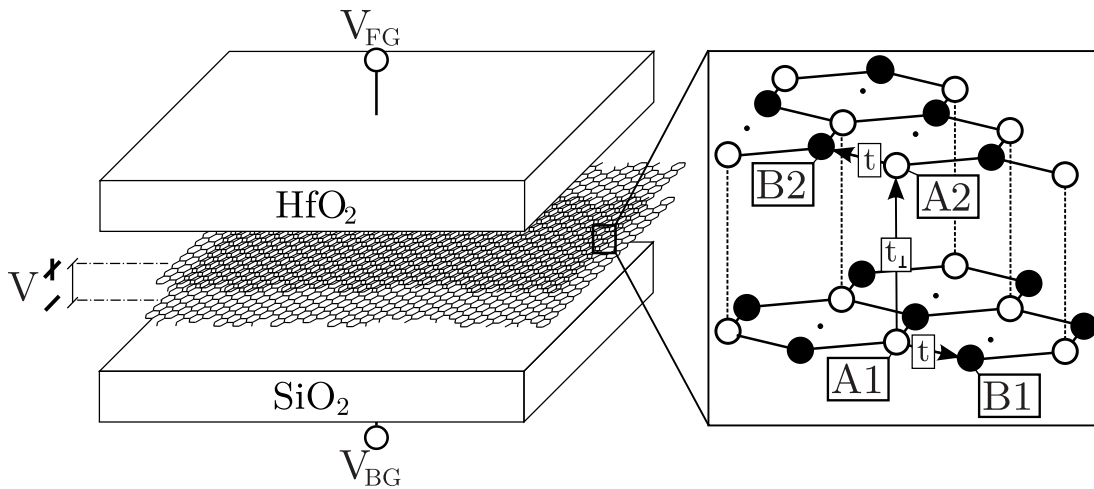


Figure 1.15: Structure of a double gate transistor based on GBL: an energy gap is induced by the electric field between the two graphene layers, that is controlled by biasing the gate stack; the inset on the right shows the four atoms unit cell of the material: the atoms A1 and A2 are aligned, according to the Bernal stacking.

by repeating several times the procedure, there is a chance that few or even a single layer of graphene remain isolated (see Fig.1.16). This procedure is called Micromechanical Exfoliation (MME): if it is applied to other sample materials, other two-dimensional crystals different from graphene can be obtained [55]. Moreover, different two-dimensional materials can be tailored together in order to obtain novel artificial structures with unique physical properties [56], thus opening a novel and extremely interesting field of physics and material science. However, the MME procedure is well suited only for scientific purposes, because it cannot be efficiently scaled for mass production.

Several alternative approaches have been developed in the recent years in order to overcome these difficulties; for example, it is possible to produce graphene by thermal decomposition of SiC (epitaxial graphene) [57] or by the Chemical Vapor Deposition (CVD) on a metal (for example, on copper) [58, 59, 60]. The former approach has a limited scalability, requires high temperatures ( $\approx 1500^\circ\text{C}$ ) and it is expensive. The latter instead is highly scalable, has high potential for large areas (thanks to the roll-to-roll production, see [61]) and allows for graphene transfer to arbitrary substrates: hence, it is much more attractive for the industry with respect to the other approaches. The problem is that CVD typically induces a high defect density in the crystal, that drastically degrades the quality and the physical properties of the CVD graphene samples with respect to the sheets obtained by MME. Up to now, the CVD graphene samples have a record low-field mobility at room temperature that is about  $4000\text{cm}^2/(\text{Vs})$  [28], that is much smaller with respect to that of the MME graphene.

Moreover, even the substrate and the top gate dielectric have a strong influence on the graphene mobility. For example, when graphene is placed on  $\text{SiO}_2$  the mobility at room temperature decreases to  $40000\text{cm}^2/(\text{Vs})$  for MME graphene due to the remote phonons [62, 63, 64]. The effect is stronger if the top gate dielectric is an high-k material [65]. Also the charged impurities have a strong influence, reducing the mobility of MME graphene to  $10000\text{cm}^2/(\text{Vs})$  [23, 62].

### Very high contact resistance

The contact resistance is a crucial parameter that has to be minimized in order to have good performing devices. Indeed, a high contact resistance degrades both the digital performance

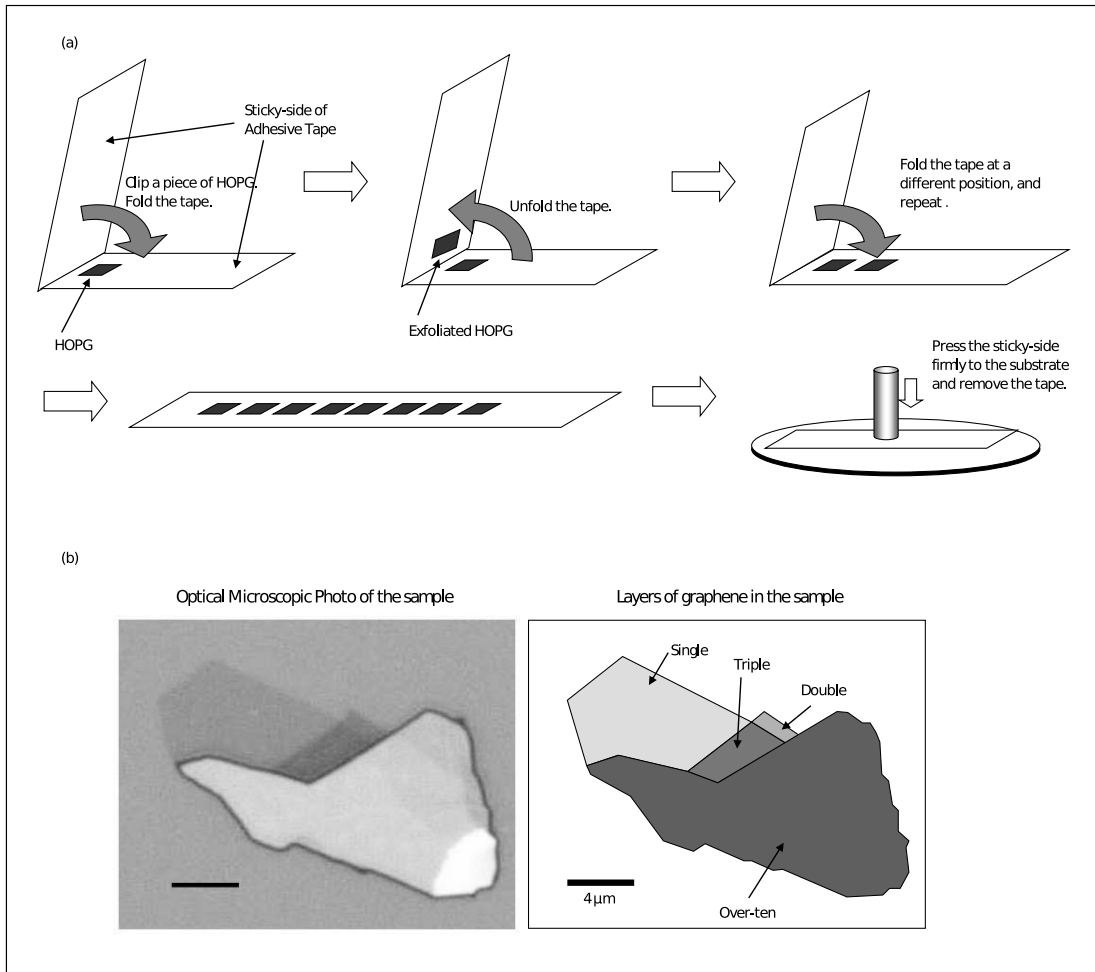


Figure 1.16: Mechanical exfoliation of graphene monolayer: Highly Oriented Pyrolytic Graphite (HOPG) are exfoliated using a simple scotch tape. The repetition of the process allows to isolate few or even single layer graphene. Adapted from [28].

(by reducing the  $I_{on}$  current) and the analog performance (by reducing important parameters as the cut-off frequency [29]) of the transistor. The ITRS sets the contact resistivity maximum limit to  $10^{-8}\Omega\text{cm}^2$  for graphene devices; however, the resistivity measured in the experiments is in the range of  $10^{-7} < \rho < 6 \times 10^{-6}\Omega\text{cm}^2$  [66, 67], well above the ITRS limit. These huge values of the contact resistivity are due to the weak interaction that exists between metals and graphene; indeed, it seems that all metals favor sites on the omnipresent hydrocarbon surface contamination rather than on the clean graphene surface and present nonuniform distributions, which never result in continuous films but instead in clusters or nanocrystals [68], thus resulting in a very high contact resistivity.

## 1.5 Purpose of this work

As mentioned in Sec.1.2, it is very important to develop novel numerical methods for a computationally efficient solution of the quantization problems related to new device architectures like FinFET and GAA transistors. To this purpose, during my PhD course we studied the application of the so-called PseudoSpectral (PS) approach to the solution of quantization prob-

lems relevant to nanodevice simulations. In a one-dimensional case, PS method approximates the *unknown function* using an appropriate polynomial. The decay of the approximation error of this approach with respect to the degree  $N$  of the polynomial depends on the degree of smoothness of the unknown function: the more regular the unknown function is, the more rapidly the error decreases. In particular for analytical functions, the PS method can achieve the so-called *spectral accuracy*, that is an exponential decrease of the error that goes as  $c^N$ , with  $c \in (0, 1)$ . This behavior is expected to yield a remarkable reduction of the CPU time with respect to the conventional FD and FE approaches that result in a fixed order accuracy (e.g.  $\mathcal{N}_{FD}^{-2}$  for the FD), because the convergence is attained by decreasing the mesh size while keeping the approximating polynomial degree constant. Chap. 2 presents a detailed explanation on how PS methods can be applied to the simulation of the carrier quantization in the channel of nanowires and FinFETs with arbitrary geometry.

Moreover, in the second part of the PhD program, we developed several models to study different transport properties and applications of graphene. Firstly, we developed a new approach for an exact solution of the Linearized Boltzmann Transport Equation (LBTE) (see Chap.4). Using this novel approach we studied the low field mobility of graphene bilayer, considering both the intrinsic graphene phonons and the remote phonons stemming from the top gate and substrate dielectrics (see Sec.4.4). Secondly, we developed a novel Monte Carlo (MC) model for the simulation of uniform transport in bilayer graphene (see Chap.5). With this tool we estimated the saturation velocity of this material. Finally, we developed a self-consistent MC model able to simulate long as well as short channel transistors based on wide sheets of graphene, including the Band-To-Band Tunneling (BTBT) and the main scattering mechanisms (see Chap.6). We first validated our model by comparison with the full quantum simulator NanoTCAD ViDES [69]; then we used our MC model to estimate the effect of the BTBT and scattering mechanisms on the output characteristics and RF figures of merit of GFETs with different channel lengths and source/drain (S/D) to channel underlaps.

# Bibliography

- [1] G. E. Moore, "Cramming More Components onto Integrated Circuits," *Electronics*, vol. 38, no. 8, Apr 1965.
- [2] M. Lundstrom, "Elementary scattering theory of the Si MOSFET," *Electron Device Letters, IEEE*, vol. 18, no. 7, pp. 361–363, July 1997.
- [3] A. Rahman and M. Lundstrom, "A compact scattering model for the nanoscale double-gate MOSFET," *Electron Devices, IEEE Transactions on*, vol. 49, no. 3, pp. 481–489, Mar 2002.
- [4] D. Esseni, P. Palestri, and L. Selmi, *Nanoscale MOS Transistors*. Cambridge University Press, 2011.
- [5] M. Horstmann, M. Wiatr, A. Wei, J. Hoentschel, T. Feudel, M. Gerhardt, R. Stephan, S. Krügel, D. Greenlaw, and M. Raab, "Advanced SOI CMOS transistor technology for high performance microprocessors," in *Proceedings Workshop ULIS*, 2009, pp. 81–84.
- [6] Y. Taur and T. Ning, *Fundamentals of Modern VLSI Devices*. Cambridge University Press, 2010.
- [7] Intel. 22nm technology, 2011. <http://www.intel.com/content/www/us/en/silicon-innovations/intel-22nm-technology.html>.
- [8] D. Sacchetto, M. Ben-Jamaa, G. De Micheli, and Y. Leblebici, "Fabrication and characterization of vertically stacked Gate-All-Around Si Nanowire FET arrays," in *Solid State Device Research Conference, 2009. ESSDERC '09. Proceedings of the European*, Sept. 2009, pp. 245–248.
- [9] Y. Taur, D.A. Buchanan, W. Chen, D.J. Frank, K.E. Ismail, S-H. Lo, G. A. Sai-Halasz, R.G.Viswanathan, H.C. Wann, S.J.Wind, and H-S. Wong, "CMOS Scaling into the Nanometer Regime," *IEEE Proceedings*, vol. 85, no. 4, pp. 486–503, 1997.
- [10] C-T. Chuang, P-F. Lu, and C.J.Anderson, "SOI for Digital VLSI: Design Consideration and Advances," *IEEE Proceedings*, vol. 86, no. 4, pp. 689–720, 1998.
- [11] G. Vellianitis, M. van Dal, L. Witters, G. Curatola, G. Doornbos, N. Collaert, C. Jonville, C. Torregiani, L.-S. Lai, J. Petty, B. Pawlak, R. Duffy, M. Demand, S. Beckx, S. Mertens, A. Delabie, T. Vandeweyer, C. Delvaux, F. Leys, A. Hikavy, R. Rooyackers, M. Kaiser, R. Weemaes, F. Voogt, H. Roberts, D. Donnet, S. Biesemans, M. Jurczak, and R. Lander, "Gatestacks for Scalable High-performance FinFETs," in *IEEE IEDM Technical Digest*, Dec. 2007, pp. 681–684.
- [12] C. Le Royer, A. Villalon, M. Casse, D. Cooper, J. Mazurier, B. Previtali, C. Tabone, P. Perreau, J.-M. Hartmann, P. Scheiblin, F. Allain, F. Andrieu, O. Weber, P. Batude, O. Faynot, and T. Poiroux, "First demonstration of ultrathin body c-SiGe channel FDSOI

- pMOSFETs combined with SiGe(:B) RSD: Drastic improvement of electrostatics ( $V_{th}$ ,  $\mu$ ,  $I_{sat}$ ) tuning, DIBL) and transport ( $\mu$ ,  $I_{sat}$ ) properties down to 23nm gate length,” in *Electron Devices Meeting (IEDM), 2011 IEEE International*, dec. 2011, pp. 16.5.1–16.5.4.
- [13] L. Witters, J. Mitard, A. Veloso, A. Hikavy, J. Franco, T. Kauerauf, M. Cho, T. Schram, F. Sebai, S. Yamaguchi, S. Takeoka, M. Fukuda, W.-E. Wang, B. Duriez, G. Eneman, R. Loo, K. Kellens, H. Tielens, P. Favia, E. Rohr, G. Hellings, H. Bender, P. Roussel, Y. Crabbe, S. Brus, G. Mannaert, S. Kubicek, K. Devriendt, K. De Meyer, L.-A. Ragnarsson, A. Steegen, and N. Horiguchi, “Dual-channel technology with cap-free single metal gate for high performance CMOS in gate-first and gate-last integration,” in *Electron Devices Meeting (IEDM), 2011 IEEE International*, dec. 2011, pp. 28.6.1–28.6.4.
- [14] G. Doornbos and M. Passlack, “Benchmarking of III-V n-MOSFET Maturity and Feasibility for Future CMOS,” *Electron Device Letters, IEEE*, vol. 31, no. 10, pp. 1110–1112, Oct. 2010.
- [15] M. Yokoyama, R. Iida, S. Kim, N. Taoka, Y. Urabe, T. Yasuda, H. Takagi, H. Yamada, N. Fukuhara, M. Hata, M. Sugiyama, Y. Nakano, M. Takenaka, and S. Takagi, “Extremely-thin-body InGaAs-on-insulator MOSFETs on Si fabricated by direct wafer bonding,” in *Electron Devices Meeting (IEDM), 2010 IEEE International*, dec. 2010, pp. 3.1.1–3.1.4.
- [16] M. Rodwell, W. Frensley, S. Steiger, E. Chagarov, S. Lee, H. Ryu, Y. Tan, G. Hegde, L. Wang, J. Law, T. Boykin, G. Klimek, P. Asbeck, A. Kummel, and J. Schulman, “III-V FET channel designs for high current densities and thin inversion layers,” in *Device Research Conference (DRC), 2010*, june 2010, pp. 149–152.
- [17] M. Luisier, “Performance Comparison of GaSb, Strained-Si, and InGaAs Double-Gate Ultrathin-Body n-FETs,” *Electron Device Letters, IEEE*, vol. 32, no. 12, pp. 1686–1688, dec. 2011.
- [18] M. Heyns, A. Alian, G. Brammertz, M. Caymax, Y. Chang, L. Chu, B. De Jaeger, G. Eneman, F. Gencarelli, G. Groeseneken, G. Hellings, A. Hikavy, T. Hoffmann, M. Houssa, C. Huyghebaert, D. Leonelli, D. Lin, R. Loo, W. Magnus, C. Merckling, M. Meuris, J. Mitard, L. Nyns, T. Orzali, R. Rooyackers, S. Sioncke, B. Soree, X. Sun, A. Vandooren, A. Verhulst, B. Vincent, N. Waldron, G. Wang, W. Wang, and L. Witters, “Advancing CMOS beyond the Si roadmap with Ge and III/V devices,” in *Electron Devices Meeting (IEDM), 2011 IEEE International*, dec. 2011, pp. 13.1.1–13.1.4.
- [19] S. Kim, M. Yokoyama, N. Taoka, R. Nakane, T. Yasuda, O. Ichikawa, N. Fukuhara, M. Hata, M. Takenaka, and S. Takagi, “Enhancement technologies and physical understanding of electron mobility in III-V n-MOSFETs with strain and MOS interface buffer engineering,” in *Electron Devices Meeting (IEDM), 2011 IEEE International*, dec. 2011, pp. 13.4.1–13.4.4.
- [20] M. Radosavljevic, G. Dewey, D. Basu, J. Boardman, B. Chu-Kung, J. Fastenau, S. Kabehie, J. Kavalieros, V. Le, W. Liu, D. Lubyshev, M. Metz, K. Millard, N. Mukherjee, L. Pan, R. Pillarisetty, W. Rachmady, U. Shah, H. Then, and R. Chau, “Electrostatics improvement in 3-D tri-gate over ultra-thin body planar InGaAs quantum well field effect transistors with high-K gate dielectric and scaled gate-to-drain/gate-to-source separation,” in *Electron Devices Meeting (IEDM), 2011 IEEE International*, dec. 2011, pp. 33.1.1–33.1.4.
- [21] J. A. del Alamo, “Nanometre-scale electronics with III-V compound semiconductors,” *Nature*, vol. 479, pp. 317–323, 2011.
- [22] M. V. Fischetti, T. O’Regan, S. Narayanan, C. Sachs, S. Jin, J. Kim, and Y. Zhang, “Theoretical Study of Some Physical Aspects of Electronic Transport in nMOSFETs at

- the 10-nm Gate-Length,” *Electron Devices, IEEE Transactions on*, vol. 54, no. 9, pp. 2116–2136, Sep. 2007.
- [23] K. S. Novoselov, A. K. Geim, S. V. Morozov, D. Jiang, Y. Zhang, S. V. Dubonos, I. V. Grigorieva, and A. A. Firsov, “Electric Field Effect in Atomically Thin Carbon Films,” *Science*, vol. 306, no. 5696, pp. 666–669, 2004.
- [24] [http://www.nobelprize.org/nobel\\_prizes/physics/laureates/2010/](http://www.nobelprize.org/nobel_prizes/physics/laureates/2010/).
- [25] A. K. Geim and K. S. Novoselov, “The rise of graphene,” *Nature Materials*, vol. 6, no. 3, pp. 183–191, 2007.
- [26] A. Geim, “Graphene update,” *Bulletin of the American Physical Society*, vol. 55, 2010.
- [27] R. Murali, Y. Yang, K. Brenner, T. Beck, and J. D. Meindl, “Breakdown current density of graphene nanoribbons,” *Applied Physics Letters*, vol. 94, no. 24, p. 243114, 2009.
- [28] Y. Iyechika, “Application of Graphene to High-Speed Transistors: Expectations and Challenges,” *Science and technology trends*, vol. 37, pp. 76 – 92, Oct 2010.
- [29] F. Schwierz, “Graphene Transistors,” *Nat. Nano.*, vol. 5, no. 7, pp. 487–496, 2010.
- [30] Y.-M. Lin, C. Dimitrakopoulos, K. A. Jenkins, D. B. Farmer, H.-Y. Chiu, A. Grill, and P. Avouris, “100-GHz Transistors from Wafer-Scale Epitaxial Graphene,” *Science*, vol. 327, no. 5966, p. 662, 2010.
- [31] L. Liao, Y.-C. Lin, M. Bao, R. Cheng, J. Bai, Y. Liu, Y. Qu, K. L. Wang, Y. Huang, and X. Duan, “High-Speed Graphene Transistors With a Self-Aligned Nanowire Gate,” *Nature*, vol. 467, pp. 305–308, 2010.
- [32] R. Cheng, J. Bai, L. Liao, H. Zhou, Y. Chen, L. Liu, Y.-C. Lin, S. Jiang, Y. Huang, and X. Duan, “High-frequency self-aligned graphene transistors with transferred gate stacks,” *Proceedings of the National Academy of Sciences*, 2012.
- [33] F. Schwierz, “Graphene transistors 2011,” in *VLSI Technology, Systems and Applications (VLSI-TSA), 2011 International Symposium on*, april 2011, pp. 1–2.
- [34] J. Kedzierski, P.-L. Hsu, A. Reina, J. Kong, P. Healey, P. Wyatt, and C. Keast, “Graphene-on-Insulator Transistors Made Using C on Ni Chemical-Vapor Deposition,” *Electron Device Letters, IEEE*, vol. 30, no. 7, pp. 745–747, july 2009.
- [35] X. Li, X. Wang, L. Zhang, S. Lee, and H. Dai, “Chemically Derived, Ultrasoft Graphene Nanoribbon Semiconductors,” *Science*, vol. 319, no. 5867, pp. 1229–1232, 2008.
- [36] X. Wang, Y. Ouyang, X. Li, H. Wang, J. Guo, and H. Dai, “Room-Temperature All-Semiconducting Sub-10-nm Graphene Nanoribbon Field-Effect Transistors,” *Phys. Rev. Lett.*, vol. 100, p. 206803, May 2008.
- [37] V. M. Pereira, A. H. Castro Neto, and N. M. R. Peres, “Tight-binding approach to uniaxial strain in graphene,” *Phys. Rev. B*, vol. 80, p. 045401, Jul 2009.
- [38] G. Cocco, E. Cadelano, and L. Colombo, “Gap opening in graphene by shear strain,” *Phys. Rev. B*, vol. 81, p. 241412, Jun 2010.
- [39] K. S. Kim, Y. Zhao, H. Jang, S. Y. Lee, J. M. Kim, K. S. Kim, J.-H. Ahn, P. Kim, J.-Y. Choi, and B. H. Hong, “Large-scale pattern growth of graphene films for stretchable transparent electrodes,” *Nature*, vol. 457, pp. 706–710, Feb. 2009.

- [40] M. Huang, T. A. Pascal, H. Kim, W. A. Goddard, and J. R. Greer, “Electronic-Mechanical Coupling in Graphene from in situ Nanoindentation Experiments and Multiscale Atomistic Simulations,” *Nano Letters*, vol. 11, no. 3, pp. 1241–1246, 2011.
- [41] X.-W. Fu, Z.-M. Liao, J.-X. Zhou, Y.-B. Zhou, H.-C. Wu, R. Zhang, G. Jing, J. Xu, X. Wu, W. Guo, and D. Yu, “Strain dependent resistance in chemical vapor deposition grown graphene,” *Applied Physics Letters*, vol. 99, no. 21, p. 213107, 2011.
- [42] X. Chen, X. Zheng, J.-K. Kim, X. Li, and D.-W. Lee, “Investigation of graphene piezoresistors for use as strain gauge sensors,” *Journal of Vacuum Science Technology B: Microelectronics and Nanometer Structures*, vol. 29, no. 6, pp. 06FE01–06FE01–5, nov 2011.
- [43] A. Smith, S. Vaziri, A. Delin, M. Ostling, and M. Lemme, “Strain engineering in suspended graphene devices for pressure sensor applications,” in *Ultimate Integration on Silicon (ULIS), 2012 13th International Conference on*, march 2012, pp. 21–24.
- [44] E. McCann, “Asymmetry gap in the electronic band structure of bilayer graphene,” *Phys. Rev. B*, vol. 74, no. 16, p. 161403, Oct 2006.
- [45] J. Nilsson, A. H. Castro Neto, F. Guinea, and N. M. R. Peres, “Electronic properties of bilayer and multilayer graphene,” *Phys. Rev. B*, vol. 78, p. 045405, Jul 2008.
- [46] L. A. Falkovsky, “Screening in gated bilayer graphene,” *Phys. Rev. B*, vol. 80, no. 11, p. 113413, Sep 2009.
- [47] J. B. Oostinga, H. B. Heersche, X. Liu, A. F. Morpurgo, and L. M. K. Vandersypen, “Gate-induced insulating state in bilayer graphene devices,” *Nature Materials*, vol. 7, no. 2, pp. 151–157, 2007.
- [48] Y. Zhang, T.-T. Tang, C. Girit, Z. Hao, M. C. Martin, A. Zettl, M. F. Crommie, Y. R. Shen, and F. Wang, “Direct observation of a widely tunable bandgap in bilayer graphene,” *Nature*, vol. 459, no. 7248, pp. 820–823, 2009.
- [49] F. Xia, D. B. Farmer, Y.-m. Lin, and P. Avouris, “Graphene Field-Effect Transistors with High On/Off Current Ratio and Large Transport Band Gap at Room Temperature,” *Nano Letters*, vol. 10, no. 2, pp. 715–718, 2010, pMID: 20092332.
- [50] L. Jing, J. Velasco Jr., P. Kratz, G. Liu, W. Bao, M. Bockrath, and C. N. Lau, “Quantum Transport and Field-Induced Insulating States in Bilayer Graphene pnp Junctions,” *Nano Letters*, vol. 10, no. 10, pp. 4000–4004, 2010.
- [51] T. Taychatanapat and P. Jarillo-Herrero, “Electronic Transport in Dual-Gated Bilayer Graphene at Large Displacement Fields,” *Phys. Rev. Lett.*, vol. 105, p. 166601, Oct 2010.
- [52] B. N. Szafranek, D. Schall, M. Otto, D. Neumaier, and H. Kurz, “Electrical observation of a tunable band gap in bilayer graphene nanoribbons at room temperature,” *Applied Physics Letters*, vol. 96, no. 11, p. 112103, 2010.
- [53] —, “High On/Off Ratios in Bilayer Graphene Field Effect Transistors Realized by Surface Dopants,” *Nano Letters*, vol. 11, no. 7, pp. 2640–2643, 2011.
- [54] B. N. Szafranek, G. Fiori, D. Schall, D. Neumaier, and H. Kurz, “Current Saturation and Voltage Gain in Bilayer Graphene Field Effect Transistors,” *Nano Letters*, vol. 12, no. 3, pp. 1324–1328, 2012.
- [55] K. S. Novoselov, D. Jiang, F. Schedin, T. J. Booth, V. V. Khotkevich, S. V. Morozov, and A. K. Geim, “Two-dimensional atomic crystals,” in *Proceedings of the National Academy of Sciences*, vol. 102, no. 30, jul. 2005, pp. 10 451–10 453.

- [56] K. S. Novoselov and A. H. C. Neto, "Two-dimensional crystals-based heterostructures: materials with tailored properties," *Physica Scripta*, vol. 2012, no. T146, p. 014006, 2012.
- [57] C. Berger, Z. Song, T. Li, X. Li, A. Y. Ogbazghi, R. Feng, Z. Dai, A. N. Marchenkov, E. H. Conrad, P. N. First, and W. A. de Heer, "Ultrathin Epitaxial Graphite: 2D Electron Gas Properties and a Route toward Graphene-based Nanoelectronics," *The Journal of Physical Chemistry B*, vol. 108, no. 52, pp. 19 912–19 916, 2004.
- [58] H. Cao, Q. Yu, L. A. Jauregui, J. Tian, W. Wu, Z. Liu, R. Jalilian, D. K. Benjamin, Z. Jiang, J. Bao, S. S. Pei, and Y. P. Chen, "Electronic transport in chemical vapor deposited graphene synthesized on Cu: Quantum Hall effect and weak localization," *Applied Physics Letters*, vol. 96, no. 12, p. 122106, 2010.
- [59] Y. Lee, S. Bae, H. Jang, S. Jang, S.-E. Zhu, S. H. Sim, Y. I. Song, B. H. Hong, and J.-H. Ahn, "Wafer-Scale Synthesis and Transfer of Graphene Films," *Nano Letters*, vol. 10, no. 2, pp. 490–493, 2010, pMID: 20044841.
- [60] F. Schwierz, "Electronics: Industry-compatible graphene transistors," *Nature*, vol. 472, pp. 41–42, 2011.
- [61] S. Bae, H. Kim, Y. Lee, X. Xu, J.-S. Park, Y. Zheng, J. Balakrishnan, T. Lei, H. Ri Kim, Y. I. Song, Y.-J. Kim, K. S. Kim, B. Ozyilmaz, J.-H. Ahn, B. H. Hong, and S. Iijima, "Roll-to-roll production of 30-inch graphene films for transparent electrodes," *Nature Nanotechnology*, vol. 5, no. 8, pp. 574–578, 2010.
- [62] J.-H. Chen, C. Jang, S. Xiao, M. Ishigami, and M. S. Fuhrer, "Intrinsic and extrinsic performance limits of graphene devices on SiO<sub>2</sub>," *Nature Nanotechnology*, vol. 3, no. 4, pp. 206–209, 2008.
- [63] S. Fratini and F. Guinea, "Substrate-limited electron dynamics in graphene," *Physical Review B (Condensed Matter and Materials Physics)*, vol. 77, no. 19, p. 195415, 2008.
- [64] M. Bresciani, A. Paussa, P. Palestri, D. Esseni, and L. Selmi, "Low-Field Mobility and High-Field Drift Velocity in Graphene Nanoribbons and Graphene Bilayers," in *Electron Devices Meeting (IEDM), 2010 IEEE International*, dec. 2010, pp. 724 –727.
- [65] A. Konar, T. Fang, and D. Jena, "Effect of high- $\kappa$  gate dielectrics on charge transport in graphene-based field effect transistors," *Phys. Rev. B*, vol. 82, p. 115452, Sep 2010.
- [66] W. Liu, H. Yu, S. Xu, Q. Zhang, X. Zou, J. Wang, K. Pey, J. Wei, H. Zhu, and M. Li, "Understanding Asymmetric Transportation Behavior in Graphene Field-Effect Transistors Using Scanning Kelvin Probe Microscopy," *Electron Device Letters, IEEE*, vol. 32, no. 2, pp. 128 –130, feb. 2011.
- [67] D. Berdebes, T. Low, Y. Sui, J. Appenzeller, and M. Lundstrom, "Substrate Gating of Contact Resistance in Graphene Transistors," *Electron Devices, IEEE Transactions on*, vol. 58, no. 11, pp. 3925 –3932, nov. 2011.
- [68] R. Zan, U. Bangert, Q. Ramasse, and K. S. Novoselov, "Interaction of Metals with Suspended Graphene Observed by Transmission Electron Microscopy," *The Journal of Physical Chemistry Letters*, vol. 3, no. 7, pp. 953–958, 2012.
- [69] G. Fiori; G. Iannaccone (2009), "NanoTCAD ViDES," <http://nanohub.org/resources/vides>. (doi:10254/nanohub-r5116.5).



## Chapter 2

# Pseudospectral Method for the Simulation of Nanodevices

## 2.1 Introduction

As already mentioned in Sec.1.2, the nanowire GAA FET and the FinFET architectures can improve significantly the electrostatic integrity of the planar devices and have good potentials for high on currents [1, 2, 3]. Moreover, the transport in silicon transistors can be improved also by optimizing the crystallographic orientation [4, 5].

The above engineering options affect the characteristics of the MOSFETs mainly through the band-structure of the carriers, which form a two-dimensional (2D) gas in planar MOSFETs and a one-dimensional (1D) gas in nanowire FETs or in very narrow FinFETs. Thus an accurate and yet computationally efficient description of the carrier quantization in nanoscale transistors is an important modeling target, also in the viewpoint of the modeling of the electron device variability which typically demands the simulation of large sets of devices with slightly modified physical or geometrical parameters.

In the electron device community the numerical solution of the eigenvalue problems is most frequently tackled by using the finite difference (FD) or the finite element (FE) method, which are robust and easy to implement, but feature a fixed (and usually low) order convergence of the approximation error with respect to the size of the discretization grid.

In this latter respect, it should be also emphasized that, when dealing with transport modeling, the refinement of the discretization grid for the quantization model is frequently imposed not much by the precision of the calculation of the eigenvalues but rather by the accuracy needed for some relevant features of the wave-functions. As an example, the matrix elements for the surface roughness scattering are related to the first derivative of the wave-functions at the semiconductor-oxide interface [6, 7]. Thus, a dense discretization grid must be used close to such interface to reduce the approximation error.

Recent investigations of numerical methods alternative to the standard FD approach for electron device applications include the combined use of frequency domain Fourier series and real space domain polynomial expansions for high-frequency devices [8], the pseudo-spectral (PS) method for the 1D effective mass Schrödinger equation in electron inversion layers [9], as well as the spectral element method for 3D effective mass Schrödinger equations [10, 11]; the reader may also refer to [9] for an excellent review of analytical and numerical methods for the solution of the effective mass Schrödinger equation.

This chapter gives a brief introduction to PS methods; then, it presents a systematic comparison between the numerical efficiency of the PS versus the FD method obtained by implementing with both approaches self-consistent Schrödinger-Poisson solvers for the 2D quantization problem in polar coordinates for a circular cylindrical nanowire FET (see Fig.2.1-(a)).

Then, we compare PS method with another innovative numerical method, the Discrete Geometric Approach (DGA), for the simulation of the 2D quantization problem in domains with more complex geometries, i.e. (a) a squared with rounded corner nanowire FET (see Fig.2.1-(b)) and (b) a FinFET with a realistic shape obtained from a TEM photo (see Fig.2.1-(c)). DGA is based on the geometrical structure behind a physical theory [12, 13, 14, 15]; thanks to this theoretical basis, it allows both a fast convergence of the approximating error and a strong flexibility concerning the geometry of the problem. Thus, DGA can be a very good reference in order to study the computational efficiency of the PS approach. The DGA simulations have been carried out by using the GAME software [16].

The three methods (PS, FD and DGA) are benchmarked in terms of discretization points and CPU time by inspecting the accuracy of not only the subband energies and wave-functions in the low dimensional carrier gas, but also the calculation of some scattering matrix elements that are crucially important for the transport modeling in the considered device structures. In all the cases considered in this study the PS method offers remarkable advantages in terms of CPU time with respect to the FD method; the difference in the CPU time between the PS and the FD approach increases with the accuracy required for the numerical solution.

Regarding the comparison between the PS and DGA approaches, we demonstrate that both

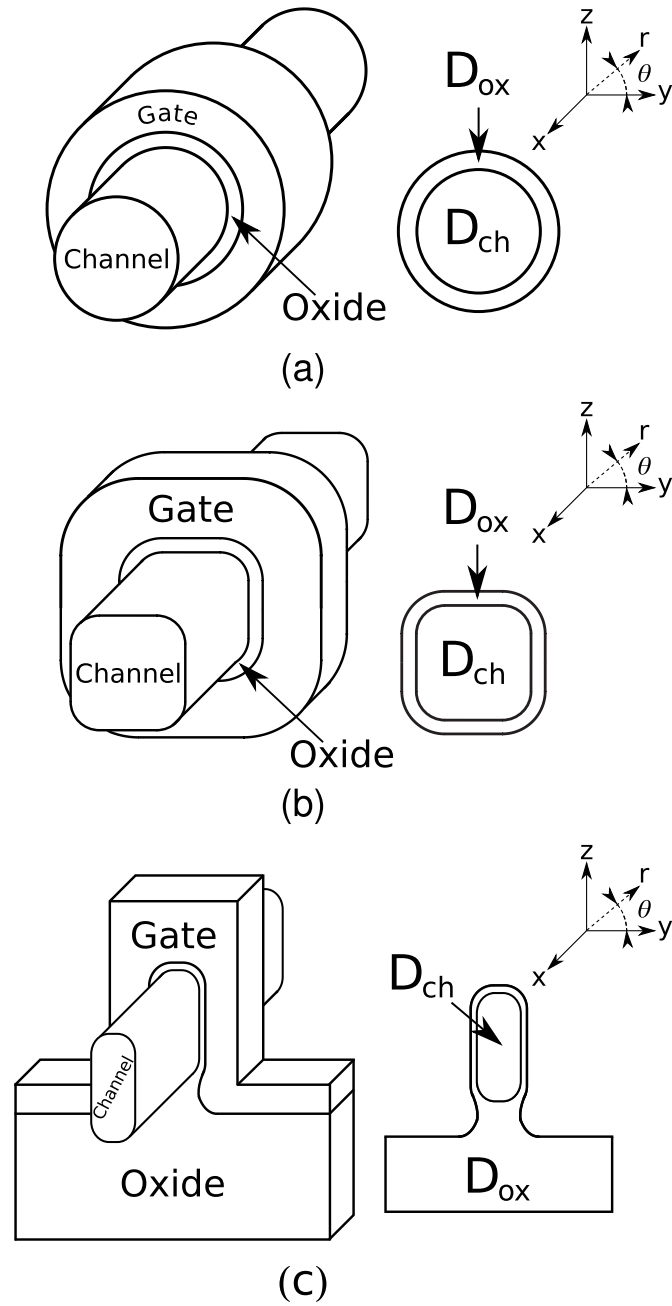


Figure 2.1: DCS  $(x, y, z)$  for different MOS transistors: (a) cylindrical nanowire; (b) cylindrical nanowire with a squared section with rounded corners; (c) SOI FinFET.  $(r, \theta)$  are the polar coordinates used in the device section normal to the transport direction  $x$ . In all the considered geometries, an inner silicon core  $D_{ch}$  is surrounded by the gate dielectric  $D_{ox}$ .

methods can be used for the efficient solution of the Schrödinger–Poisson problem. On the one hand, the PS method is more effective when the domain is convex, smooth and simply connected; on the other hand, DGA can handle complicated geometries like those of the real devices, and may be thus suitable for the study of the device variability produced by process induced variations of the geometrical dimensions.

## 2.2 Pseudospectral approach

The PS approach for a differential equation or a differential eigenvalue problem approximates the *unknown* function by using algebraic polynomials or trigonometric polynomials. The decay of the approximation error of this approach with respect to the degree  $N$  of the polynomial depends on the degree of smoothness of the unknown function: the more regular the unknown function is, the more rapidly the error decreases. In particular, the PS method can achieve the so-called *spectral accuracy*, that consists in a decreasing of the approximation error according to [17]:

- $c^N$ , with  $c \in (0, 1)$  for analytic functions<sup>1</sup>, as it is the case of the eigenfunctions of the Schrödinger problem (see Sec.2.5.1);
- $N^{-m}$  for every  $m$  if the unknown function is infinitely-differentiable;
- $N^{-(q+1)}$  if the unknown function has  $q$  continuous derivatives.

Hence, the regularity of the unknown function is very important, as can be seen in Fig.2.2, that shows an exponential decrease of the approximating error for the infinitely-differentiable  $\alpha_1$  function, and a linear decrease (in logarithmic scales) for the function  $|y|$ , which has a derivative that is not continuous.

The spectral accuracy is expected to yield a remarkable reduction of CPU time with respect to the conventional FD and FE methods that result in a fixed order accuracy (typically second order in the one-dimensional case, see Sec.2.5.3), since the convergence is attained by decreasing the mesh size while keeping the polynomial degree constant (see Fig.2.3).

## 2.3 PS approach in one-dimensional domains

### 2.3.1 Non periodic unknown function

The main features of the PS method can be introduced by considering first a one-dimensional case, where  $\alpha(y)$ , with  $y \in [a, b]$ , is the unknown solution of the differential equation

$$\frac{d\alpha}{dy}(y) = v(y), \quad (2.1)$$

with appropriate boundary conditions at  $y=a$  and  $y=b$ ;  $v(y)$  is an appropriate known function defined in  $[a, b]$ ; both  $\alpha(y)$  and  $v(y)$  can in general take complex values. Let  $\{y_0, y_1, \dots, y_N\}$  be a grid of distinct nodes in  $[a, b]$ , with  $a = y_0 < y_1 < \dots < y_N = b$ , and let  $\boldsymbol{\alpha}_N = (\alpha_0, \alpha_1, \dots, \alpha_N)^T \in \mathbb{C}^{N+1}$  be the vector of entries  $\alpha_i = \alpha(y_i)$ ,  $i = 0, \dots, N$ . The  $N$ -degree polynomial  $p_N$  interpolating the values of  $\boldsymbol{\alpha}_N$  can be represented in the Lagrange form as

$$p_N(y) = \sum_{j=0}^N \ell_j(y) \alpha_j, \quad (2.2)$$

<sup>1</sup>An analytic function  $\alpha(y)$  is an infinitely differentiable function such that the Taylor series at any point  $y_0$  in its domain converges to  $\alpha(y)$  for  $y$  in a neighborhood of  $y_0$

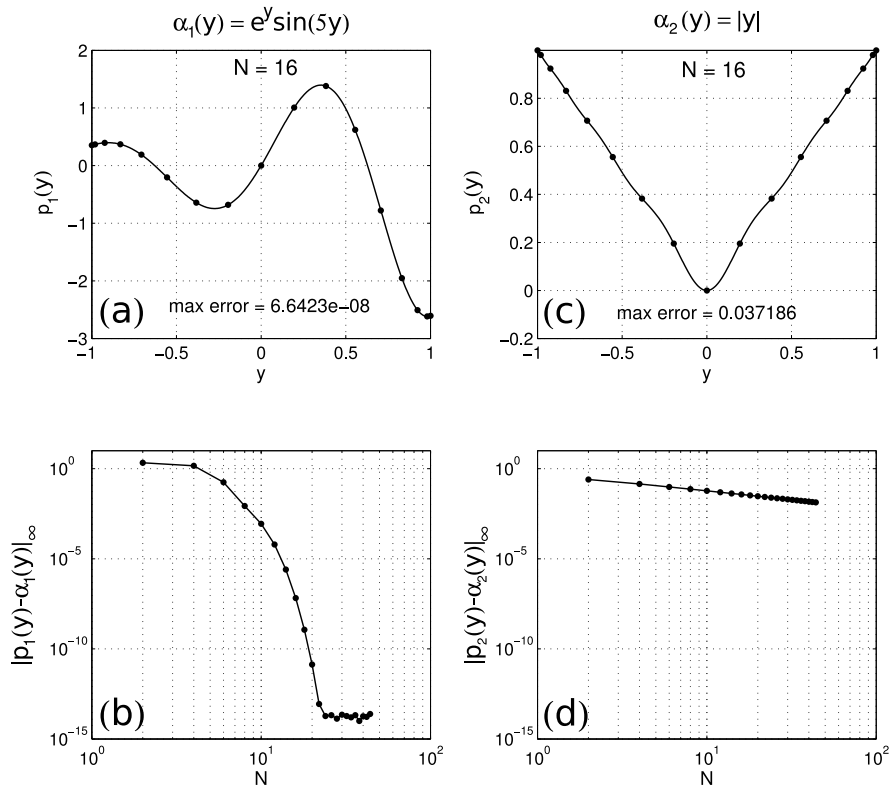


Figure 2.2: Approximating polynomial of the function  $\alpha_1(y) = e^y \sin(5y)$  (a) and  $\alpha_2(y) = |y|$  (c) in the domain  $[-1, 1]$  using the PS method. The spectral accuracy is achieved only in the former case, as can be seen in (b), that shows an exponential decrease of the approximating error versus the order  $N$  of the approximating polynomial. Conversely, the approximating error decreases very slowly (i.e. a linear decrease in logarithmic scales) for the function  $\alpha_2(y)$  (d).

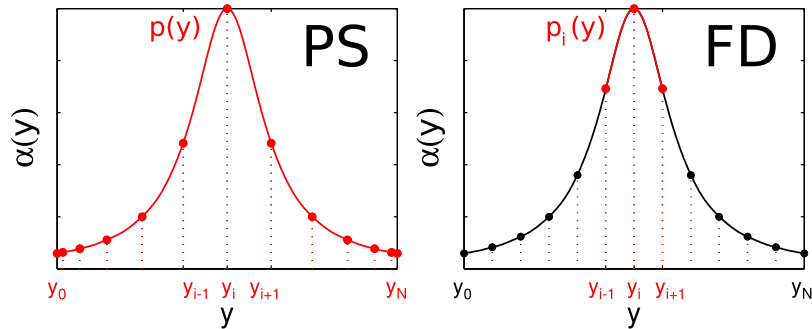


Figure 2.3: The main difference between PS (left) and FD (right) approaches are that the former approximates the unknown function  $\alpha(y)$  using a single global polynomial with an order  $N$  dependent on the number of discretization points, while the latter uses fixed (and generally low) order local polynomials linked together.

where the set of

$$\ell_j(y) = \prod_{\substack{i=0 \\ i \neq j}}^N \frac{y - y_i}{y_j - y_i} \quad j = 0, \dots, N \quad (2.3)$$

are the Lagrange basis polynomials [18]; each  $\ell_j(y)$  fulfills the condition

$$\ell_j(y_i) = \delta_{ij} = \begin{cases} 1, & i = j \\ 0, & i \neq j. \end{cases} \quad (2.4)$$

An example of Lagrange basis polynomial is shown in Fig.2.4: as can be seen,  $\ell_6(y)$  is equal to 1 in  $y_6$  and is zero in the other  $y_i$  points, with  $i \neq 6$  (indicated in the figure by the red circles) as prescribed by Eq.2.4. In virtue of Eq.2.4, the value taken by the unknown function in the

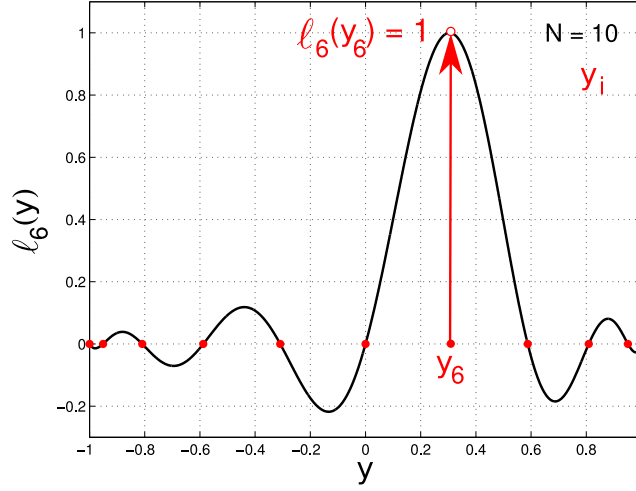


Figure 2.4: Lagrange basis polynomial defined on the set of points  $y_i$  indicated by the filled red circles, on the domain  $[-1, 1]$ .

node  $y_j$  is the coefficient  $\alpha_j$  of the  $p_N(y)$  written in Eq.2.2.

The idea at the base of PS approach is to approximate the derivative of the unknown function  $\alpha$  at  $y_i$  with the derivative of  $p_N$  as

$$\alpha'(y_i) \approx p'_N(y_i) = \sum_{j=0}^N \ell'_j(y_i) \alpha_j, \quad i = 0, \dots, N. \quad (2.5)$$

If we let now  $\alpha'_N = (\alpha'_0, \alpha'_1, \dots, \alpha'_N)^T \in \mathbb{C}^{N+1}$  be the vector of values  $\alpha'_i = p'_N(y_i)$ ,  $i = 0, \dots, N$ , we can write

$$\alpha'_N = \mathbf{D}_{N,y} \alpha_N, \quad (2.6)$$

where  $\mathbf{D}_{N,y} \in \mathbb{R}^{(1+N) \times (1+N)}$  is the so-called differentiation matrix, which has entries

$$[\mathbf{D}_{N,y}]_{ij} = \ell'_j(y_i), \quad i, j = 0, \dots, N, \quad (2.7)$$

and represents the PS discretization of the first derivative operator. The choice of Chebyshev extremal nodes

$$y_i = \frac{b+a}{2} - \frac{b-a}{2} \cos\left(\frac{i\pi}{N}\right), \quad i = 0, \dots, N, \quad (2.8)$$

is usually appropriate [18] and the differentiation matrix can be explicitly and efficiently computed [17]. The Chebyshev extremal nodes are the points in which the  $N$ -degree Chebyshev polynomial defined in the interval  $[a, b]$  assumes its maximum and minimum values. As reported in Fig.2.5, they can be seen as the projections on the real axis of  $N+1$  equally spaced points defined on a semi-circle centered in  $(b+a)/2$  and with radius  $(b-a)/2$ . Fig.2.5 shows also that the resulting discretization is more dense at the edges of the considered domain. The

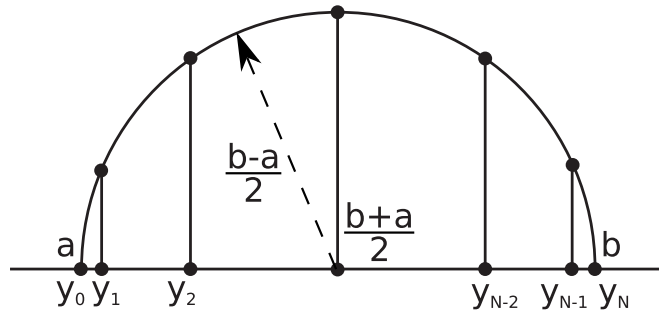


Figure 2.5: The Chebyshev extremal nodes are the projections on the real axis of equally spaced points along a semi-circle with radius  $(b - a)/2$  and centered in  $(b + a)/2$ .

Chebyshev points have to be used because polynomial interpolations based on sets of equally spaced points lead to very high interpolation error near the boundaries of the domain, as can be seen in Fig.2.6; the error increases with the degree  $N$  of the interpolating polynomial, due to the so-called Runge’s phenomenon [17]. It is possible to demonstrate that the interpolating

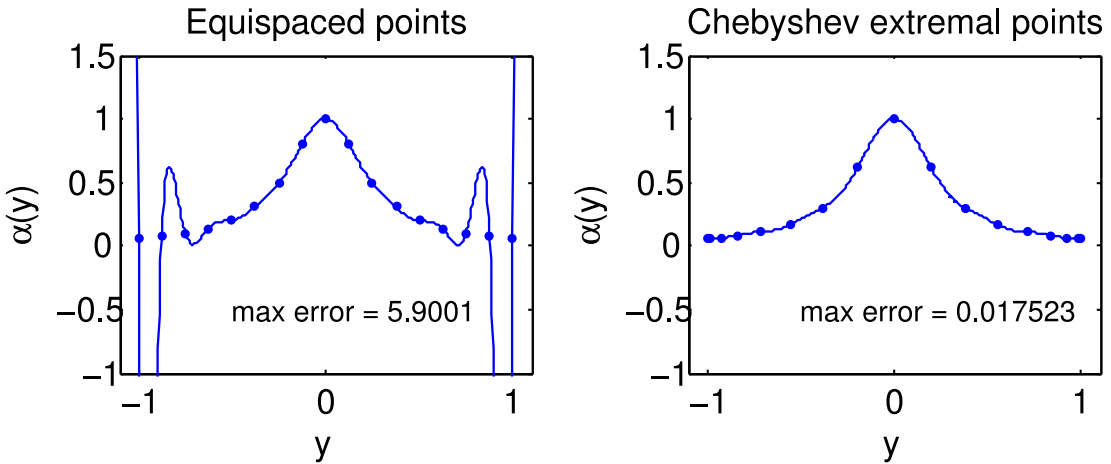


Figure 2.6: A polynomial interpolation (in this case the interpolated function is  $\alpha(y) = 1/(1 + 16y^2)$ ) based on an equally spaced grid results in a very high interpolating error near the boundaries of the domain; this error increases with the degree  $N$  of the interpolating polynomial, due to the Runge’s phenomenon (left); conversely, the error decreases with  $N$  when a grid based on the Chebyshev extremal nodes is employed.

error decreases with  $N$  if the discretization points are distributed according to the following density [17]

$$g \sim \frac{N}{\pi \sqrt{1 - \left(\frac{2y-b-a}{b-a}\right)^2}}, \tag{2.9}$$

depicted in Fig.2.7. The polynomial interpolation based on the Chebyshev extremal nodes is not affected by the Runge’s phenomenon since this particular set of points satisfy the condition expressed by Eq.2.9 [17].

Using Eq.2.5 it is possible to approximate the first derivative of the unknown function and higher order derivatives can be approximated using similar expressions; moreover, the associated

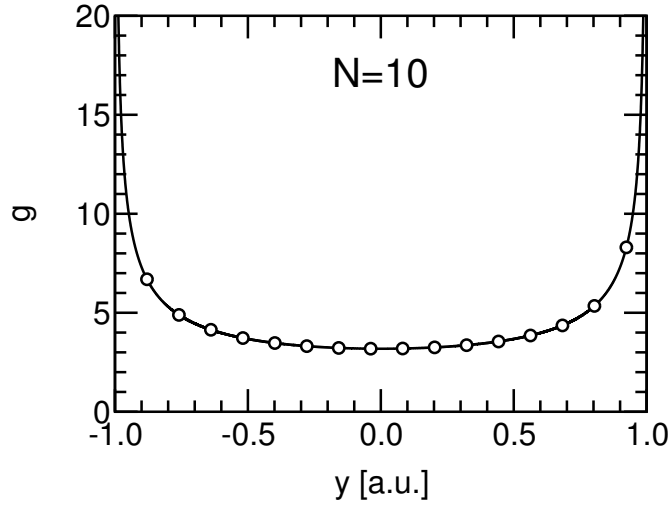


Figure 2.7: Density of the discretization points given by Eq.2.9 calculated in  $[-1, 1]$  with  $N = 10$ . The resulting discretization grid is more dense at the edges of the domain.

differentiation matrix of  $k$ -th order can be calculated as<sup>2</sup>

$$\mathbf{D}_{N,y}^{(k)} = (\mathbf{D}_{N,y})^k, k < N. \quad (2.10)$$

Therefore, in a one-dimensional domain Eq.2.1 is discretized as

$$\mathbf{D}_{N,y} \boldsymbol{\alpha}_N = \mathbf{v}_N, \quad (2.11)$$

where  $\mathbf{v}_N = (v_0, v_1, \dots, v_N)^T \in \mathbb{C}^{N+1}$ .

### 2.3.2 Approximation of a definite integral

The PS principle of substituting the unknown function  $\alpha$  with  $p_N$  can be also used to approximate the definite integral of  $\alpha$

$$\int_a^b \alpha(y) dy \approx \int_a^b p_N(y) dy = \sum_{j=0}^N h_j \alpha_j, \quad (2.12)$$

where  $h_j = \int_a^b \ell_j(y) dy$  are the weights of the quadrature, known as Clenshaw–Curtis formula [17]. This may result extremely useful because the same vector  $\boldsymbol{\alpha}_N$  can be employed for different computational purposes.

### 2.3.3 Treatment of boundary conditions

The PS discretization leads to an easy treatment of the boundary conditions of differential problems. Consider for example the following one-dimensional boundary value problem:

$$\frac{d^2 w}{dy^2}(y) = -\beta(y), \quad (2.13)$$

<sup>2</sup>For the second order derivative:

$$\alpha''(y_i) \approx \sum_{j=0}^N \ell'_j(y_i) \alpha'(y_j) = \sum_{j=0}^N \sum_{m=0}^N \ell'_j(y_i) \ell'_m(y_j) \alpha_m \Rightarrow \mathbf{D}_{N,y}^{(2)} = (\mathbf{D}_{N,y})^2$$

with general Robin-type condition

$$\begin{cases} \xi_0 w(a) + \mu_0 w'(a) = \gamma_0 \\ \xi_N w(b) + \mu_N w'(b) = \gamma_N. \end{cases} \quad (2.14)$$

Eq.2.13 is discretized as

$$\mathbf{D}_{N,y}^2 \mathbf{w}_N = -\boldsymbol{\beta}_N \quad (2.15)$$

with  $\mathbf{w}_N = (w_0, w_1, \dots, w_N)^T \in \mathbb{C}^{N+1}$  and  $\boldsymbol{\beta}_N = (\beta_0, \beta_1, \dots, \beta_N)^T \in \mathbb{C}^{N+1}$ . By substituting Eq.2.2 for  $w$  in Eq.2.14, we get the discretized boundary conditions

$$\begin{cases} \xi_0 w_0 + \mu_0 \sum_{j=0}^N \ell'_j(a) w_j = \gamma_0 \\ \xi_N w_N + \mu_N \sum_{j=0}^N \ell'_j(b) w_j = \gamma_N. \end{cases} \quad (2.16)$$

Therefore, in order to take into account for the boundary conditions, it is enough to substitute the first and last row of  $\mathbf{D}_{N,y}^2$  accordingly and consider the modified right-hand side vector to eventually get the linear system

$$\begin{pmatrix} \xi_0 + \mu_0 \ell'_0(a) & \mu_0 \ell'_1(a) & \cdots & \mu_0 \ell'_N(a) \\ [\mathbf{D}_{N,y}^2]_{1,0} & \cdots & \cdots & [\mathbf{D}_{N,y}^2]_{1,N} \\ \vdots & & & \vdots \\ [\mathbf{D}_{N,y}^2]_{N-1,0} & \cdots & \cdots & [\mathbf{D}_{N,y}^2]_{N-1,N} \\ \mu_N \ell'_0(b) & \cdots & \mu_N \ell'_{N-1}(b) & \xi_N + \mu_N \ell'_N(b) \end{pmatrix} \begin{pmatrix} w_0 \\ w_1 \\ \vdots \\ w_{N-1} \\ w_N \end{pmatrix} = \begin{pmatrix} \gamma_0 \\ -\beta(y_1) \\ \vdots \\ -\beta(y_{N-1}) \\ \gamma_N \end{pmatrix}. \quad (2.17)$$

It should be noticed that for homogeneous Dirichlet boundary conditions, the first and last rows and the first and last columns can be simply omitted and the number of unknowns reduces to  $N - 1$  since  $w_0 = w_N = 0$ .

### 2.3.4 Treatment of media discontinuities

In general, PS methods assure a fast decay of the approximating error in domain  $D$  with homogeneous media properties. However in the case of discontinuities between different media in  $D$ , PS method yields solutions with low-order of convergence (see Sec.2.2). In order to preserve all the advantages of the PS approach also in a non homogeneous domain  $D$ , it is necessary to revisit PS approach in a piecewise point formulation, taking into account the continuity conditions to be imposed at the boundaries between the different domains. Let us consider, for example, the Poisson's problem over one-dimensional non-homogeneous multi-domains

$$\frac{d}{dy} \left( -m(y) \frac{d\alpha(y)}{dy} \right) = \beta(y) \quad (2.18)$$

with  $m(y) = m_-$  for  $y \in [a, c[$  and  $m(y) = m_+$  for  $y \in ]c, b]$  being the dielectric permittivity that is different in the two sub-domains (see Fig.2.8). We require the functions  $\alpha$  and  $m\alpha'$  to be continuous over the entire interval  $[a, b]$ , which imposes the conditions

$$\begin{cases} \alpha(c_-) = \alpha(c_+) \\ m_- \alpha'(c_-) = m_+ \alpha'(c_+). \end{cases} \quad (2.19)$$

Then we consider one interpolating polynomial for each semi-interval, namely  $p_{N,-}$  built on the nodes  $a = y_{N,-} < \dots < y_{0,-} = c$  and  $p_{N,+}$  built on the nodes  $c = y_{0,+} < \dots < y_{N,+} = b^3$  (see Fig.2.8).

<sup>3</sup>In general the number of nodes in each semi-interval can be different.

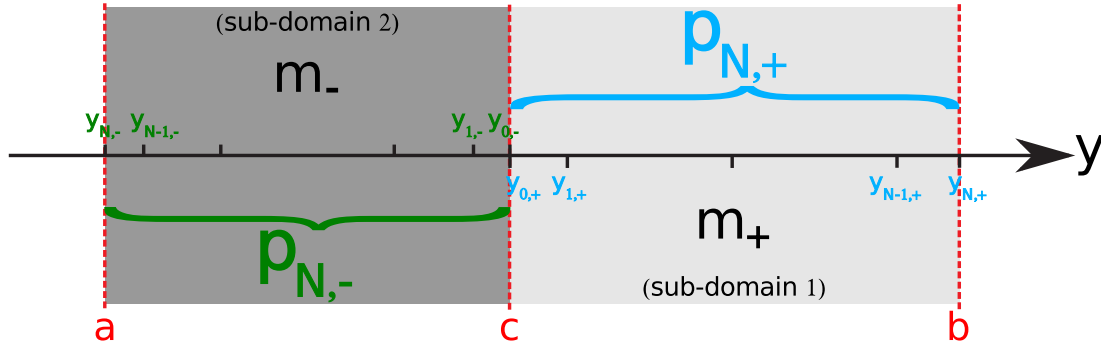


Figure 2.8: Sketch of the domain with non homogeneous media properties considered in Sec.2.3.4: two approximating polynomials are employed, one for each domain, and appropriate continuity conditions are imposed at the point  $c$  (see Eq.2.19).

The conditions in Eq.2.19 are discretized as

$$\begin{cases} \alpha_{0,-} = \alpha_{0,+} \\ m_- (\mathbf{D}_{N,y-})_1 \boldsymbol{\alpha}_{N,-} = m_+ (\mathbf{D}_{N,y+})_1 \boldsymbol{\alpha}_{N,+}, \end{cases} \quad (2.20)$$

where  $\boldsymbol{\alpha}_{N,-} = (\alpha_{N,-}, \dots, \alpha_{0,-})^T \in \mathbb{C}^{N+1}$ ,  $\boldsymbol{\alpha}_{N,+} = (\alpha_{0,+}, \dots, \alpha_{N,+})^T \in \mathbb{C}^{N+1}$  and  $(\mathbf{D}_{N,y-})_1$  and  $(\mathbf{D}_{N,y+})_1$  are the first rows of the differentiation matrices defined in the two sub-domains. Therefore, the original  $2N + 2$  unknowns are reduced to  $2N$  by using the above relation. In such a way, the continuity constraints along the discontinuity surfaces are implicitly included into the scheme, leading to modified differentiation matrices.

### 2.3.5 Periodic unknown function

For a sufficiently smooth periodic function  $\alpha(\theta) \in \mathbb{C}$  defined in the domain  $[0, 2\pi]$ , the PS approach considers trigonometric interpolating polynomial  $t_M(\theta)$  defined on the uniform periodic grid  $\theta_j = \frac{j2\pi}{M}, j = 1, \dots, M$ . We assume for simplicity that  $M$  is even and that  $\boldsymbol{\alpha}_M = (\alpha_1, \dots, \alpha_M)^T \in \mathbb{C}^M$  is the vector of entries  $\alpha_j = \alpha(\theta_j), j = 1, \dots, M$ . A trigonometric polynomial of degree  $M/2$  is obtained by a linear combination of  $1, \sin(\theta), \cos(\theta), \dots, \sin[(M/2 - 1)\theta], \cos[(M/2 - 1)\theta], \cos[(M/2)\theta]$ . The interpolating trigonometric polynomial  $t_M$  of degree  $M/2$  can be rewritten in analogy to Eq.2.2 as

$$t_M(\theta) = \sum_{j=1}^M S(\theta - \theta_j) \alpha_j, \quad (2.21)$$

where  $S(\theta) = \frac{\sin(M\theta/2)}{M \tan(\theta/2)}$ . Similarly to the property of the Lagrange basis polynomials, also in this case  $S(\theta_i - \theta_j) = \delta_{ij}$ . The differentiation matrix can be explicitly and efficiently computed by

$$[\mathbf{D}_{M,\theta}]_{ij} = S'(\theta_i - \theta_j), \quad i, j = 1, \dots, M. \quad (2.22)$$

Similar to the case of Sec.2.3.1, the differentiation matrix of any order smaller than  $M$  can be calculated by further differentiation of  $S$ . It is important to observe that the derivatives of the interpolating trigonometric polynomial can be also calculated by FFT in  $O(M \log M)$  floating point operations [17].

The periodic rectangular method can be used to approximate the definite integral of  $\alpha(\theta)$ :

$$\int_0^{2\pi} \alpha(\theta) d\theta \approx \frac{2\pi}{M} \sum_{j=1}^M \alpha_j. \quad (2.23)$$

For smooth periodic integrands the error related to this approach decreases very rapidly as  $M$  increases.

## 2.4 PS approach in two-dimensional domains

### 2.4.1 PS approach for a rectangle

The basic definitions and properties of the PS method are extended quite naturally to the two-dimensional case (or even to more dimensions). The unknown solution  $\alpha(y, z)$  of a differential equation or an eigenvalue differential problem (with  $y$  and  $z$  belonging to  $[a_y, b_y]$  and  $[a_z, b_z]$ , respectively), is expressed as

$$\alpha(y, z) \approx \sum_{n=0}^N \sum_{m=0}^M \ell_{y,n}(y) \ell_{z,m}(z) \alpha_{n,m}, \quad (2.24)$$

where  $\ell_{y,n}(y)$  and  $\ell_{z,m}(z)$  are respectively the  $N$  and  $M$ -degree Lagrange basis polynomials defined in the  $y$  and  $z$  directions (see Eq.2.3) and  $\alpha_{n,m}$  are in general complex numbers.

Since the  $y$  and  $z$  dependence of  $\alpha(y, z)$  in Eq.2.24 is separately given by  $\ell_{y,n}(y)$  and  $\ell_{z,m}(z)$ , the matrices representative of the partial differential equations can be expressed in terms of the differentiation matrices with respect to  $y$  and  $z$ , which is very useful for implementation. As an example, if the discretization points are sorted according to the lexicographical order, so that the column vector  $\alpha_{N,M}$  of the unknown function values reads [17]

$$\alpha_{N,M} = (\alpha_{0,0} \dots \alpha_{0,M}, \alpha_{1,0} \dots \alpha_{1,M} \dots \alpha_{N,1} \dots \alpha_{N,M})^T \quad (2.25)$$

where  $\mathbf{a}^T$  is the transpose of  $\mathbf{a}$ , then the differentiation matrix  $\mathbf{D}_{NM}^{(2)}$  for the first mixed derivative  $\frac{\partial^2 \alpha(y,z)}{\partial y \partial z}$  reads

$$\mathbf{D}_{NM}^{(2)} = \mathbf{D}_N^{(1)} \otimes \mathbf{D}_M^{(1)}, \quad (2.26)$$

where the  $\otimes$  sign denotes the Kronecker product [17].

All the results concerning the quadrature for the integrals are readily extended to the two-dimensional case.

### 2.4.2 PS approach for a disk

The PS method can be successfully applied to a disk of radius  $R$  by using polar coordinates  $(r, \theta)$  [19], with  $r \in [0, R]$ ,  $\theta \in [0, 2\pi]$ , by combining a Chebyshev expansion in  $r$  (Sec.2.3.1) with a periodic Fourier expansion in  $\theta$  (Sec.2.3.5). Hence, the unknown function  $\alpha(r, \theta)$  is approximated by the interpolating polynomial  $Q_{N,M}(r, \theta)$  defined as

$$Q_{N,M}(r, \theta) = \sum_{n=0}^N \sum_{m=1}^M \ell_n(r) S(\theta - \theta_m) \alpha_{nm}, \quad (2.27)$$

where  $\alpha_{nm} = \alpha(r_n, \theta_m)$ ,  $i = 0, \dots, N$ ,  $j = 1, \dots, M$ . As an example, the lowest order mixed derivative in  $(r_i, \theta_j)$  can be approximated as:

$$\frac{\partial^2 \alpha}{\partial r \partial \theta}(r_i, \theta_j) \approx \frac{\partial^2 Q_{N,M}}{\partial r \partial \theta}(r_i, \theta_j) = \sum_{n=0}^N \sum_{m=1}^M \frac{d\ell_n}{dr}(r_i) \frac{dS}{d\theta}(\theta_j - \theta_m) \alpha_{nm} \quad (2.28)$$

for  $i = 0, \dots, N$ ,  $j = 1, \dots, M$ . This latter can be conveniently represented by resorting to the lexicographical order of the grid values  $\alpha_{nm}$  [17]:

$$\alpha_{N,M} = (\alpha_{0,1}, \dots, \alpha_{0,M}, \alpha_{1,1}, \dots, \alpha_{1,M}, \dots, \alpha_{N,1}, \dots, \alpha_{N,M})^T \in \mathbb{C}^{(1+N)M}. \quad (2.29)$$

We can thus write

$$\frac{\partial^2 \alpha}{\partial r \partial \theta}(r_i, \theta_j) \approx [(\mathbf{D}_{N,r} \otimes \mathbf{D}_{M,\theta}) \boldsymbol{\alpha}_{N,M}]_{ij}, \quad i = 0, \dots, N, \quad j = 1, \dots, M, \quad (2.30)$$

where

$$[\mathbf{D}_{N,r}]_{ij} = \left. \frac{\ell_j(r)}{dr} \right|_{r_i} \quad (2.31)$$

and

$$[\mathbf{D}_{M,\theta}]_{ij} = \left. \frac{dS(\theta - \theta_j)}{d\theta} \right|_{\theta_i}. \quad (2.32)$$

Moreover, also the integral on the disk can be approximated by combining two quadrature rules: periodic trapezoid rule in  $\theta$  and Clenshaw-Curtis formula in  $r$ .

The transformation in polar coordinates of the Schrödinger–Poisson problem leads to a singularity at  $r = 0$  [19] (see Sec.2.5.1). Different approaches can be found in the literature to overcome this difficulty [17]: here we follow the so called diameter approach. The idea is to take  $r \in [-R, R]$  and  $\theta \in [0, 2\pi]$  and to use the symmetry condition

$$\alpha(r, \theta) = \alpha(-r, \theta + \pi) \quad (2.33)$$

to eliminate the redundant information. The discretization  $\{(r_i, \theta_j), i = 0, \dots, N, j = 1, \dots, M\}$  of the disk of radius  $R$  is obtained by choosing the Chebyshev grid in  $r$ , and the periodic uniform grid in  $\theta$ . The difficulty at  $r = 0$  is circumvented by taking an even number of discretization points in the radial direction so that  $r = 0$  is avoided (see Fig.2.9). Moreover, the number of discretization points in the angular direction must be even. The resulting grid is highly clustered near  $\partial D$  yielding to a finer description of the solution  $\alpha(r, \theta)$  close to the boundary of the domain.

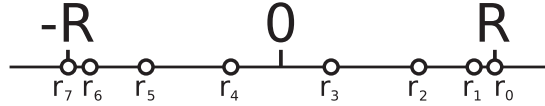


Figure 2.9: The origin of the axis  $r=0$  is avoided employing an even number of discretization points in the radial direction. The resulting grid is highly clustered near the boundary.

### 2.4.3 PS approach for two-dimensional convex domains

We have also applied PS method to convex, two-dimensional domains with smooth boundaries following the approach presented in [20]. Fig.2.10 shows the considered geometry: an inner domain  $D_{ch}$ , described by the function  $d_{int}(\theta)$ , is surrounded by the domain  $D_{ox}$ , whose external limit is defined by  $d_{ext}(\theta)$ ;  $d_{int}(\theta)$  and  $d_{ext}(\theta)$  are respectively the distances of the inner and the outer contours from the origin. The approximation of the solution of differential equations defined on these type of domains has been obtained using appropriate mappings based on polar coordinates.

To this purpose we mapped the inner domain  $D_{ch}$  onto a unitary disk

$$\begin{cases} y = [rh(\theta) + k(\theta)] \cos(\theta) \\ z = [rh(\theta) + k(\theta)] \sin(\theta), \end{cases} \quad (2.34)$$

where  $r \in [-1, 1]$ ,  $\theta \in [0, 2\pi]$ , and

$$h(\theta) = \frac{d_{int}(\theta) + d_{int}(\theta + \pi)}{2} \quad (2.35)$$

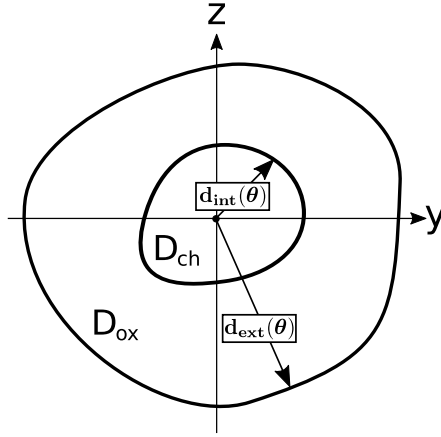


Figure 2.10: Two-dimensional domain with smooth boundaries. The functions  $d_{int}(\theta)$  and  $d_{ext}(\theta)$  define the limits of the two regions: an inner core  $D_{ch}$  surrounded by the the region  $D_{ox}$ .

$$k(\theta) = \frac{d_{int}(\theta) - d_{int}(\theta + \pi)}{2}. \quad (2.36)$$

The outer domain  $D_{ox}$  was mapped onto an annulus with the internal and external radii 1 and  $R$  respectively

$$\begin{cases} y = \left[ d_{int}(\theta) + \frac{r-1}{R-1} (d_{ext}(\theta) - d_{int}(\theta)) \right] \cos(\theta) \\ z = \left[ d_{int}(\theta) + \frac{r-1}{R-1} (d_{ext}(\theta) - d_{int}(\theta)) \right] \sin(\theta), \end{cases} \quad (2.37)$$

where  $r \in [1, R]$ , and  $\theta \in [0, 2\pi]$ . Eqs.2.34 and 2.37 transform the original differential problem expressed in Cartesian coordinates and defined on a complex domain into a differential problem based on polar coordinates, defined on a disk, that can be very efficiently solved using PS methods [17] when the functions  $d_{int}(\theta)$  and  $d_{ext}(\theta)$  are smooth. The same transformations must be applied to the continuity conditions between subdomains and to the boundary conditions. A similar approach applies also to the calculation of definite integrals.

## 2.5 Application of the PS approach to the simulation of FinFETs and GAA nanowires

### 2.5.1 Electron quantization in nanowire FETs and FinFETs

In order to introduce the quantization problems investigated in this section and their mathematical formulation, we have illustrated in Fig.2.11 the devices and the relevant coordinate systems. In particular,  $(x, y, z)$  denotes the device coordinate system (DCS), where  $x$  is the

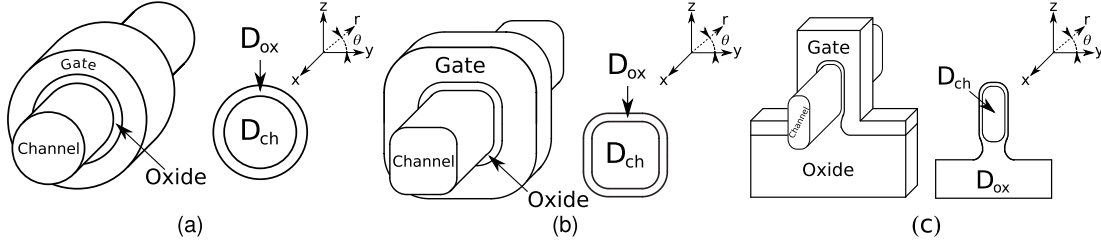


Figure 2.11: DCS  $(x, y, z)$  for different MOS transistors: (a) cylindrical nanowire; (b) cylindrical nanowire with a squared section with rounded corners; (c) SOI FinFET.  $(r, \theta)$  are the polar coordinates used in the device section normal to the transport direction  $x$ . In all the considered geometries, an inner silicon core  $D_{ch}$  is surrounded by the gate dielectric  $D_{ox}$ .

transport direction. Furthermore, we will hereafter make use also of the crystal coordinate system (CCS), where  $k_{c,x}$ ,  $k_{c,y}$  and  $k_{c,z}$  lie along the three equivalent  $\langle 100 \rangle$  crystallographic directions [21].

The ellipsoid coordinate system (ECS,  $(k_l, k_{t_1}, k_{t_2})$ ) for a given conduction band minimum is identified by the principal axes of the ellipsoid describing the electron energy close to such minimum according to the parabolic EMA [22, 21]. In the ECS the electron energy close to the minimum  $\nu$  can be written as

$$E_\nu(k_l, k_{t_1}, k_{t_2}) = E_{\nu_0} + \frac{\hbar^2}{2} \left[ \frac{k_l^2}{m_l} + \frac{k_{t_1}^2 + k_{t_2}^2}{m_t} \right], \quad (2.38)$$

where  $m_l$  and  $m_t$  are the effective masses respectively in the longitudinal and in the transverse direction and  $E_{\nu_0}$  is the reference energy of the valley  $\nu$ . In the DCS, where  $x$  is the transport direction (see Fig.2.11),  $E_\nu(k_x, k_y, k_z)$  can be written as

$$E_\nu(k_x, k_y, k_z) = E_{\nu_0} + \frac{\hbar^2}{2} (k_x, k_y, k_z) \mathbf{W}_\nu (k_x, k_y, k_z)^T, \quad (2.39)$$

where  $\mathbf{W}_\nu$  is the matrix of the inverse masses in the DCS, that can be written as

$$\mathbf{W}_\nu = \begin{pmatrix} w_{xx} & w_{xy} & w_{xz} \\ w_{yx} & w_{yy} & w_{yz} \\ w_{zx} & w_{zy} & w_{zz} \end{pmatrix} = \mathbf{R}_{DE}^T \begin{pmatrix} \frac{1}{m_l} & 0 & 0 \\ 0 & \frac{1}{m_t} & 0 \\ 0 & 0 & \frac{1}{m_t} \end{pmatrix} \mathbf{R}_{DE}, \quad (2.40)$$

with  $\mathbf{R}_{DE}$  being the unitary rotation matrix from the DCS to the ECS. Eq.2.40 allows one to calculate the elements of  $\mathbf{W}_\nu$  directly from the longitudinal and transverse masses  $m_l$  and  $m_t$ . According to the EMA quantization model [23, 24], the Schrödinger-like equation for an electron gas confined in the plane normal to the transport direction is obtained, for each valley  $\nu$ , by using the standard prescription ( $\mathbf{K} \rightarrow -i\nabla_{\mathbf{R}}$ ) in the  $E_\nu(k_x, k_y, k_z)$  given by Eq.2.39, where  $\mathbf{K} = (k_x, k_y, k_z)$  and  $\nabla_{\mathbf{R}}$  denotes the gradient with respect to  $\mathbf{R} = (x, y, z)$ . Eq.2.40 shows that in general the matrix  $\mathbf{W}_\nu$  is not diagonal, consequently the operator  $\hat{E}_\nu(-i\nabla_{\mathbf{R}})$  obtained by the prescription above contains mixed derivatives.

Table 2.1: Expression for the terms  $w_{yy}$ ,  $w_{zz}$  and  $w_{yz}$  of the matrix  $\mathbf{W}_\nu$  entering Eqs.2.43, 2.46 and 2.47 as well as for the corresponding effective mass  $m_x$  in the transport direction defined in Eq.2.45. The expressions are given for the [100] and the  $[\bar{1}10]$  transport direction and in terms of the longitudinal  $m_l$  and transverse mass  $m_t$  of the silicon  $\Delta$  minima. The index  $\nu$  denotes the different valleys.

$x$	$y$	$z$	$\nu$	$w_{yy}$	$w_{zz}$	$w_{yz}$	$m_x$	$g_\nu$
$[\bar{1}10]$	[110]	$[00\bar{1}]$	1	$\frac{1}{m_t}$	$\frac{1}{m_l}$	0	$m_t$	2
			2	$\frac{m_t+m_l}{2m_t m_l}$	$\frac{1}{m_t}$	0	$\frac{m_t+m_l}{2}$	4
[100]	[010]	[001]	1	$\frac{1}{m_l}$	$\frac{1}{m_t}$	0	$m_t$	2
			2	$\frac{1}{m_t}$	$\frac{1}{m_l}$	0	$m_t$	2
			3	$\frac{1}{m_t}$	$\frac{1}{m_t}$	0	$m_l$	2

The Schrödinger-like equation governed by  $\hat{E}_\nu(-i\nabla_{\mathbf{R}})$  can be solved by following the approach proposed in [25], namely by introducing the *ansatz* for the unknown wave-function  $\Psi_{\nu,j}(x, y, z)$ :

$$\Psi_{\nu,j}(x, y, z) = \sigma_{\nu,j}(y, z) \frac{e^{ik_x(\alpha_\nu y + \beta_\nu z + x)}}{\sqrt{L_x}}. \quad (2.41)$$

In Eq.2.41  $L_x$  is a normalization length in the transport direction,  $\alpha_\nu$  and  $\beta_\nu$  are expressed as

$$\alpha_\nu = \frac{w_{yz}w_{xz} - w_{xy}w_{zz}}{w_{yy}w_{zz} - w_{yz}^2}, \quad \beta_\nu = \frac{w_{yz}w_{xy} - w_{yy}w_{xz}}{w_{yy}w_{zz} - w_{yz}^2} \quad (2.42)$$

and  $\sigma_{\nu,j}(y, z)$  is obtained solving the eigenvalue problem

$$-\frac{\hbar^2}{2} \left[ w_{yy} \frac{\partial^2 \sigma_{\nu,j}(y, z)}{\partial y^2} + 2w_{yz} \frac{\partial^2 \sigma_{\nu,j}(y, z)}{\partial y \partial z} + w_{zz} \frac{\partial^2 \sigma_{\nu,j}(y, z)}{\partial z^2} \right] + U(y, z) \sigma_{\nu,j}(y, z) = \varepsilon_{\nu,j} \sigma_{\nu,j}(y, z). \quad (2.43)$$

Thanks to the *ansatz* in Eq.2.41 the eigenvalue problem in Eq.2.43 is independent of the wave-vector  $k_x$  in the transport direction. The electron energy  $E_{\nu,j}(k_x)$  in the subband  $j$  of the valley  $\nu$  is then given by

$$E_{\nu,j}(k_x) = E_{\nu_0} + \varepsilon_{\nu,j} + \frac{\hbar^2 k_x^2}{2m_x}, \quad (2.44)$$

where

$$m_x = \frac{w_{yy}w_{zz} - w_{yz}^2}{w_t^2 w_l} \quad (2.45)$$

is the effective mass in the transport direction. Tab.2.1 reports the effective masses related to the silicon devices considered in the following of this section.

The continuity equations for the wave-function  $\Psi(x, y, z)$  at an interface  $\partial D$  between silicon and the gate oxide can be set according to the Ben Daniel-Duke condition [26], which prescribes the continuity of  $\Psi(x, y, z)$  and of the component in the direction normal to  $\partial D$  of the vector  $[\mathbf{W}\nabla\Psi(x, y, z)]$ , where  $\mathbf{W}$  is the inverse mass matrix defined in Eq.2.40 and  $\nabla\Psi(x, y, z)$  is the gradient of  $\Psi(x, y, z)$ .

By recalling the  $\Psi(x, y, z)$  expression in Eq.2.41, we see that the continuity of the normal component of  $\mathbf{W}\nabla\Psi(x, y, z)$  is in general problematic, because, for arbitrary crystal orientations, the  $\mathbf{W}$  in silicon has off-diagonal terms, thus the  $\alpha_\nu$  and  $\beta_\nu$  coefficients in Eq.2.41 are not null and, consequently, the component  $k_x$  of the wave-vector in the transport direction enters the

Table 2.2: Expression for the terms  $w_{i,j}$  (with  $i, j$  being  $r$  or  $\theta$ ) of Eq.2.46 and for the [100] transport direction. The index  $\nu$  denotes the different valleys.

	$\nu=1$	$\nu=2$	$\nu=3$
$w_{rr}$	$\frac{\cos^2(\theta)}{m_l} + \frac{\sin^2(\theta)}{m_t}$	$\frac{\cos^2(\theta)}{m_t} + \frac{\sin^2(\theta)}{m_l}$	$\frac{1}{m_t}$
$w_r$	$\frac{1}{r} \left( \frac{\sin^2(\theta)}{m_l} + \frac{\cos^2(\theta)}{m_t} \right)$	$\frac{1}{r} \left( \frac{\sin^2(\theta)}{m_t} + \frac{\cos^2(\theta)}{m_l} \right)$	$\frac{1}{r m_t}$
$w_{r\theta}$	$\frac{2 \cos(\theta) \sin(\theta) (m_l - m_t)}{r m_t m_l}$	$\frac{2 \cos(\theta) \sin(\theta) (m_t - m_l)}{r m_t m_l}$	0
$w_\theta$	$\frac{2 \cos(\theta) \sin(\theta) (m_t - m_l)}{r^2 m_t m_l}$	$\frac{2 \cos(\theta) \sin(\theta) (m_l - m_t)}{r^2 m_t m_l}$	0
$w_{\theta\theta}$	$\frac{1}{r^2} \left( \frac{\sin^2(\theta)}{m_l} + \frac{\cos^2(\theta)}{m_t} \right)$	$\frac{1}{r^2} \left( \frac{\sin^2(\theta)}{m_t} + \frac{\cos^2(\theta)}{m_l} \right)$	$\frac{1}{r^2 m_t}$

continuity equations. Strictly speaking this results in a  $k_x$  dependent  $\sigma(y, z)$  which increases dramatically the complexity of the problem.

To circumvent this issue, in our work we adopted a single material approximation and used the silicon effective masses also in the oxide domain. By doing so the continuity conditions for  $\Psi(x, y, z)$  and for the component in the direction normal to  $\partial D$  of the vector  $[\mathbf{W} \nabla \Psi(x, y, z)]$  result in simple continuity conditions for  $\sigma(y, z)$  and its first derivatives.

For the device sketched in Fig.2.11-(a) it is convenient to use the polar coordinates  $(r, \theta)$  in the quantization plane by setting  $y=r \cos(\theta)$  and  $z=r \sin(\theta)$ . The Schrödinger equation is readily obtained by introducing in Eq.2.43 the appropriate transformations of the differential operators and it reads

$$\begin{aligned}
& -\frac{\hbar^2}{2} \left[ w_{rr} \frac{\partial^2 \tilde{\sigma}_{\nu,j}(r, \theta)}{\partial r^2} + w_r \frac{\partial \tilde{\sigma}_{\nu,j}(r, \theta)}{\partial r} + w_{r\theta} \frac{\partial^2 \tilde{\sigma}_{\nu,j}(r, \theta)}{\partial r \partial \theta} + w_\theta \frac{\partial \tilde{\sigma}_{\nu,j}(r, \theta)}{\partial \theta} \right. \\
& \left. + w_{\theta\theta} \frac{\partial^2 \tilde{\sigma}_{\nu,j}(r, \theta)}{\partial \theta^2} \right] + \tilde{U}(r, \theta) \tilde{\sigma}_{\nu,j}(r, \theta) = \tilde{\varepsilon}_{\nu,j} \tilde{\sigma}_{\nu,j}(r, \theta),
\end{aligned} \tag{2.46}$$

where  $w_{rr}$ ,  $w_r$ ,  $w_{r\theta}$ ,  $w_\theta$  and  $w_{\theta\theta}$  are  $r$  and  $\theta$  dependent coefficients defined as

$$\begin{aligned}
w_{rr} &= w_{yy} \cos^2(\theta) + 2w_{yz} \sin(\theta) \cos(\theta) + w_{zz} \sin^2(\theta), \\
w_r &= \frac{1}{r} (w_{yy} \sin^2(\theta) - 2w_{yz} \sin(\theta) \cos(\theta) + w_{zz} \cos^2(\theta)), \\
w_{r\theta} &= \frac{1}{r} [2 \cos(\theta) \sin(\theta) (w_{zz} - w_{yy}) + 2(\cos^2(\theta) - \sin^2(\theta)) w_{yz}], \\
w_\theta &= -\frac{w_{r\theta}}{r}, \quad w_{\theta\theta} = \frac{w_r}{r}.
\end{aligned} \tag{2.47}$$

Tab.2.2 reports the terms  $w_{i,j}$  (with  $i, j$  being  $r$  and  $\theta$ ) of Eq.2.46 for a [100] transport orientation and in terms of the effective masses  $m_t$  and  $m_l$  of the bulk material ellipsoids. Eqs.2.46 and 2.47 show that the Schrödinger equation for the 1D electron gas has a radial symmetry only if  $w_{yz}$  is null and, furthermore,  $w_{yy}$  and  $w_{zz}$  are equal. Tabs.2.1 and 2.2 show that, for a [100] transport direction, this is the case for the valley  $\nu=3$ . As it can be seen, in general the Schrödinger equation and the corresponding wave-functions do not have a radial symmetry, in fact the Schrödinger equation cannot be simply expressed in terms of the Laplacian of the unknown wave-function  $\sigma$ . We will return to this point in Sec.2.5.3.

For the devices of Figs.2.11-(b) and (c) we have transformed the Schrödinger's equation in Cartesian coordinate expressed by Eq.2.43 using the approach based on the mappings presented in Sec.2.4.3 (see [20] for further details). Since it is impossible to obtain a simple analytic expression in this case, all the equations used in our simulators were numerically calculated. Here we want just to underline that the resulting transformed Schrödinger's equation depends

also on the first and second derivatives of the functions  $d_{int}(\theta)$  and  $d_{ext}(\theta)$  defined in Sec.2.4.3. Since the functions  $d_{int}(\theta)$  and  $d_{ext}(\theta)$  describing the considered geometries are not smooth, in order to preserve the spectral accuracy given by the PS method, we have approximated them using a smoothing spline (calculated using the MATLAB function *spaps*). The approximated contours are high-order differentiable functions while their values are still very close to the exact ones (see Fig.2.12).

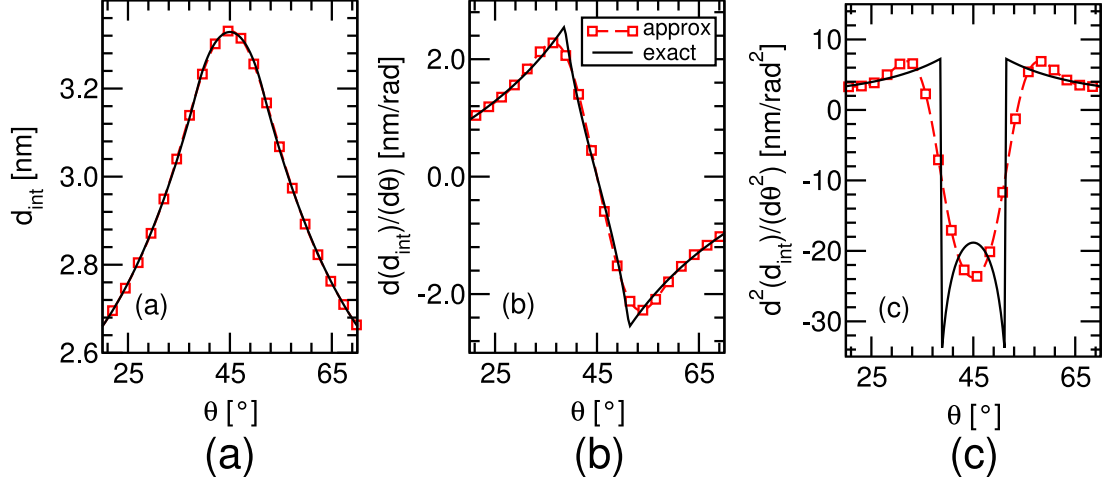


Figure 2.12: (a) Comparison between the function  $d_{int}(\theta)$  defined for the geometry shown in figure 2.11-(b) and its smoothed approximation: the approximated function is very close to the exact one. (b,c) Comparisons between the exact and the approximated first and second derivatives of  $d_{int}(\theta)$  with respect to the angular direction  $\theta$ : in the approximated case the contour is more regular, allowing the PS method to achieve the spectral accuracy.

### 2.5.2 Self-consistent Schrödinger-Poisson solution

The electrostatic behavior of the devices in Fig.2.11 was simulated solving the Schrödinger problems self-consistently with the Poisson equation [27]. The latter equation is solved considering two different materials and imposing the fulfillment of the Gauss's theorem on the separation surface. Moreover the Poisson's equation is solved using the Newton-Raphson's method. The loop is built as follow: a potential energy is chosen as an initial guess; then a Schrödinger's equation is solved. The obtained wave-functions have been used into the calculation of the charge density. The link between the Schrödinger and the Poisson equations is given by the expressions of the carrier densities.

For the  $n$ -type nanowire FETs and FinFETs at the equilibrium the electron concentration in a device section is given by

$$n(y, z) = \sum_{\nu} \sum_i N_{\nu,i} |\sigma_{\nu,i}(y, z)|^2, \quad (2.48)$$

with

$$N_{\nu,i} = g_{\nu} \sqrt{\frac{2m_x K_B T}{\pi \hbar^2}} \mathcal{F}_{-\frac{1}{2}} \left( \frac{E_F - \varepsilon_{\nu,i}}{K_B T} \right), \quad (2.49)$$

where  $g_{\nu}$  is the valley degeneracy (see Tab.2.1),  $E_F$  is the Fermi energy and  $\mathcal{F}_{-\frac{1}{2}}$  is the complete Fermi-Dirac's integral of order -1/2 into the Dingle notation [28]. In order to obtain an efficient convergence of the Schrödinger-Poisson loop we have employed the so called non-linear formulation of the Poisson equation [27, 29].

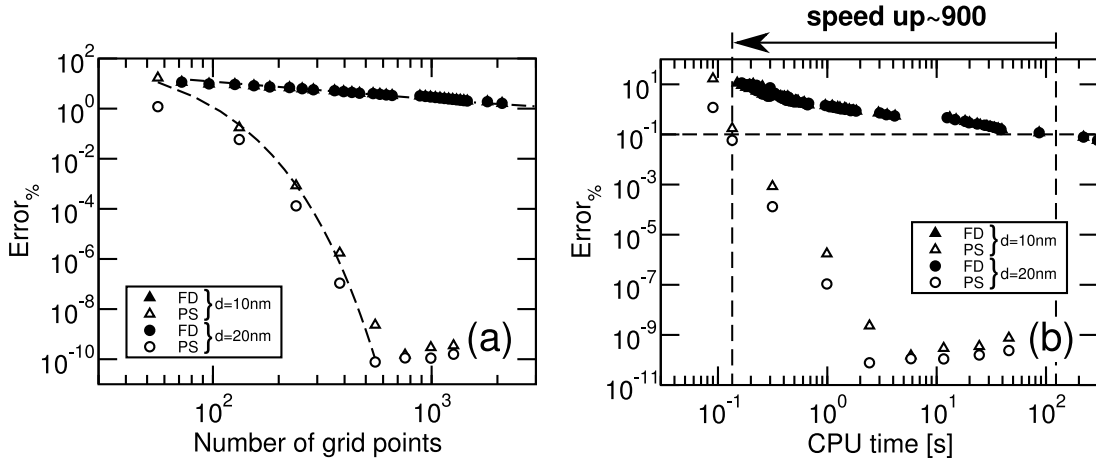


Figure 2.13: Solution of the two-dimensional Schrödinger problem in the ideal circular well presented in Sec.2.5.3: maximum relative error calculated with respect to the analytic solutions of Eqs.2.43 and 2.46 over the 10 lowest eigenvalues for the PS (open symbols) and the FD methods (closed symbols) versus the CPU time in (a) two squared ( $x=[\bar{1}10]$ ) and (b) two circular ( $x=[100]$ ) well confining potentials; the exact eigenvalues used to calculate the approximation errors are expressed by Eq.2.50. The speed-up obtained at a relative error of 0.1% using PS method with respect to FD method is remarkable in both cases.

### 2.5.3 Numerical results and comparison with other approaches

In this section, the computational efficiency of the PS method is compared with that of the FD and DGA approaches for the devices shown in Fig.2.11.

#### Circular nanowire (Fig.2.11-(a))

Firstly, the computational efficiency of the PS method is compared to the one of the FD approach in an ideal circular well, that is with  $\tilde{U}(r, \theta) = 0$  in Eq.2.46, with  $w_{yz}=0$  and  $w_{yy}=w_{zz}=w$ , for which the analytical expression for the eigenvalues of the Schrödinger equation is known. In fact, Eq.2.46 results in eigenvalues of the form

$$\tilde{\epsilon}_\nu(m, n) = \frac{\hbar^2 w}{2} \left( \frac{2\mu_{m,n}}{d} \right)^2, \quad (2.50)$$

where  $d$  is the diameter of the device section and  $\mu_{m,n}$  is the  $n$ -th zero of the Bessel function of the first kind and order  $m$ , with  $m=0, \pm 1, \pm 2, \pm 3, \dots$ . The exact solutions of the problem have been used as the reference to evaluate the accuracy of the numerical methods.

We have compared the PS and FD methods considering the maximum relative error over the lowest 10 eigenvalues versus the number of discretization points and average CPU time<sup>4</sup>. Fig.2.13-(a) shows the percentage error as a function of the number of grid points for the PS and the FD methods. As it can be seen by the comparison of the PS curves to the dashed lines proportional to  $c^N$ , the PS method can achieve the spectral accuracy, which results in a dramatic improvement of the numerical efficiency with respect to the FD method, whose error decreases only linearly in logarithmic scales (see the dot-dashed line in Fig.2.13-(a)). It should be noticed that the machine precision is reached by the PS method using about 600 grid points. Fig.2.13-(b) reports the percentage error as a function of the CPU time: the PS

<sup>4</sup>The simulations were run on a notebook with an Intel Core2 Duo P9500 (2.53GHz) processor and a 4GB DDR2-667 RAM

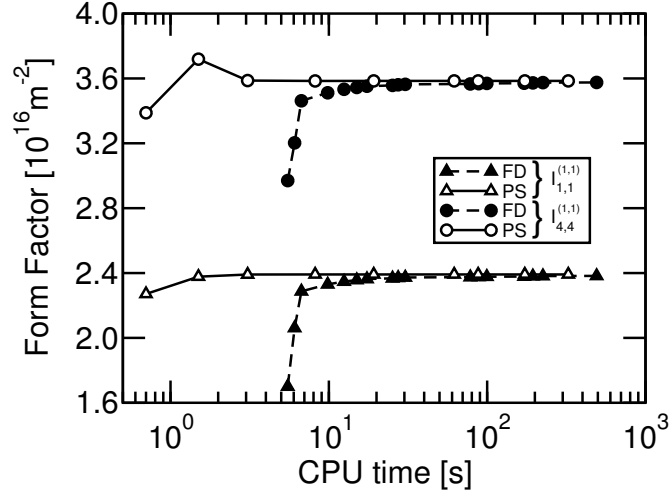


Figure 2.14: Self-consistent Schrödinger-Poisson solution of the cylindrical nanowire sketched in Fig.2.11-(a), with a [100] channel orientation,  $d=8.4\text{nm}$ ,  $EOT=0.8\text{nm}$  and a gate potential  $V_G=0.5\text{V}$ . Intra-subband phonon scattering form factors defined in Eq.2.51 for the first and the fourth wave-functions of the valley  $\nu=3$  (see Tab.2.2) versus the CPU time calculated with either the PS (open symbols) or the FD methods (closed symbols). The number of discretization points varies respectively between 70 and 1480 for the PS method and between 70 and 270000 for the FD method.

method gives a remarkable speed-up over the FD approach for all the considered percentage errors. In particular, an amazing speed-up of about 900 is obtained for a percentage error of 0.1%; moreover, the gap between the two methods increases significantly for decreasing relative errors, namely for a higher accuracy.

In the practice of the electron device modeling the quantization problems are solved self-consistently with the Poisson equation and the refinement of the grid is frequently imposed by the precision necessary to describe some physically relevant quantities. An accurate calculation of the matrix elements for the surface roughness scattering, for example, may be challenging for the self-consistent numerical procedure, because it is related to the first derivative of the wave-functions at the semiconductor-oxide interface [23, 6, 7]. As a second example related to physical quantities relevant for the transport modeling, we have analyzed the form factors of the acoustic and optical phonon scattering, which, for a 1D electron gas in a FinFET or a nanowire transistor, are defined as [30]:

$$I_{i,j}^{(\nu,\nu')} = \iint_D dydz |\Psi_{\nu,i}(y,z)|^2 |\Psi_{\nu',j}(y,z)|^2, \quad (2.51)$$

where  $D$  is the device section normal to the transport direction  $x$ . Fig.2.14 reports the  $I_{i,j}^{(\nu,\nu')}$  for a circular nanowire versus the CPU time. As expected the PS and FD methods tend to the same  $I_{i,j}^{(\nu,\nu')}$  values with the increase of the CPU time (hence of the discretization points), however the PS method reaches an acceptable accuracy with a much shorter CPU time.

To introduce the last case study we reconsider the Schrödinger Eq.2.46 for cylindrical nanowires. As already said in Sec.2.5.1 the equation has a radial symmetry only if  $w_{yz}$  is null and  $w_{yy}=w_{zz}$  (as for the valley  $\nu=3$  of Tab.2.2). This observation suggested to use an approximated formulation of the Schrödinger equation based on an isotropic effective mass  $m_{eff}$ , because the solution of such an isotropic Schrödinger equation is computationally very efficient when the separation of the radial and angular variables is used [31, 32]. We have used the self-consistent Schrödinger-Poisson solver based on the PS approach to compare the exact solution of Eq.2.46

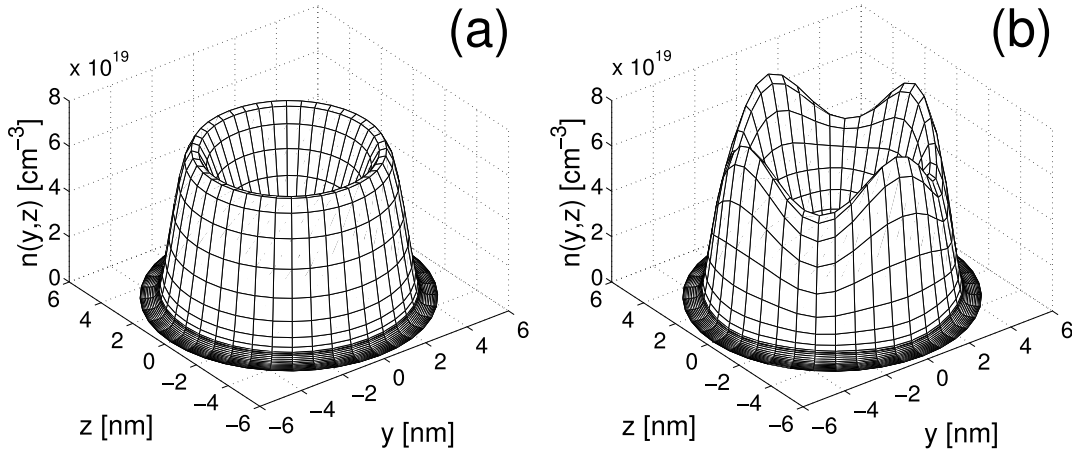


Figure 2.15: Self-consistent Schrödinger-Poisson solution for the cylindrical nanowire sketched in Fig.2.11-(a), with  $d=10\text{nm}$  and a  $[100]$  transport orientation: electron concentration  $n(y, z)$  simulated with the PS method (a) using and (b) non using the isotropic effective mass approximation. In the non-approximated case (b), the electron concentration is clearly anisotropic, reflecting the anisotropy of the electron energy dispersion. A doping density  $N_A=1 \times 10^{15}\text{cm}^{-3}$ , a  $\text{SiO}_2$  oxide thickness  $T_{ox}=0.7\text{nm}$ , a gate work function  $\phi_m=4.05\text{eV}$  and a  $N_{inv} \approx 3.1 \times 10^7\text{cm}^{-1}$  have been considered in both cases.

with the approximated solution obtained imposing  $w_{yy}=w_{zz}=m_{eff}^{-1}$ . For the valleys  $\nu=1, 2$  of the  $[100]$  transport direction (see Tab.2.1), the approximation is  $m_{eff}=(2m_t m_l)/(m_t + m_l)$ .

Fig.2.15 shows the electron concentration at the equilibrium in the section of a nanowire with a diameter  $d=10\text{nm}$  and a  $[100]$  transport orientation, obtained with a self-consistent Schrödinger-Poisson solution, by using (Fig.2.15-(a)) and by non using (Fig.2.15-(b)) the isotropic effective mass approximation. As it can be seen, the electron concentration is appreciably anisotropic in the latter case (see Fig.2.15-(b)), because the squared magnitude of the wavefunctions is strongly anisotropic for the lowest valleys featuring  $m_y=0.92m_0$  and  $m_z=0.19m_0$  (or  $m_y=0.19m_0$  and  $m_z=0.92m_0$ ). For smaller diameters, however, the effects induced by the anisotropy of the energy relation become progressively smaller.

In order to further investigate the effects of the isotropic approximation, Fig.2.16 compares the subband minima for the lowest subbands versus  $V_G$  for a  $d=4\text{nm}$  nanowire with a  $[100]$  transport direction: filled symbols show the results obtained by the exact formulation of the Schrödinger problem and open symbols are the results corresponding to the isotropic effective mass approximation (the valley indexes  $\nu$  are consistent with the ones of Tab.2.1). Note that the eigenvalues  $\varepsilon_{1,i}$  associated with the valley  $\nu=1$  are equal to the corresponding  $\varepsilon_{2,i}$ . Fig.2.17 reports the corresponding contribution  $N_{\nu,i}$  of the subbands to the total inversion density  $N_{inv}$  in the nanowire (see Eq.2.49). As it can be seen in Fig.2.16, the second lowest eigenvalue  $\varepsilon_{1,2}$  of the valley  $\nu=1$  is heavily overestimated by the approximated method for all  $V_G$  values (compare the open triangles with the filled ones). At low  $V_G$  the other eigenvalues are, instead, well approximated by the isotropic model. When the contribution of the subband related to  $\varepsilon_{1,2}$  becomes appreciable in the results of the non-approximated solution (for  $V_g > 0.4\text{V}$ , see the filled triangles in Fig.2.17), all the subband minima  $\varepsilon_{i,j}$  of the approximated case start to deviate from their exact counterparts, because the self-consistent Schrödinger-Poisson solution forces somewhat different electrostatic potentials in the isotropic with respect to the exact model. We verified that for a diameter of  $3\text{nm}$  or smaller, only the lowest subbands of each valley contribute significantly to the inversion density and the results of the approximated isotropic model are in

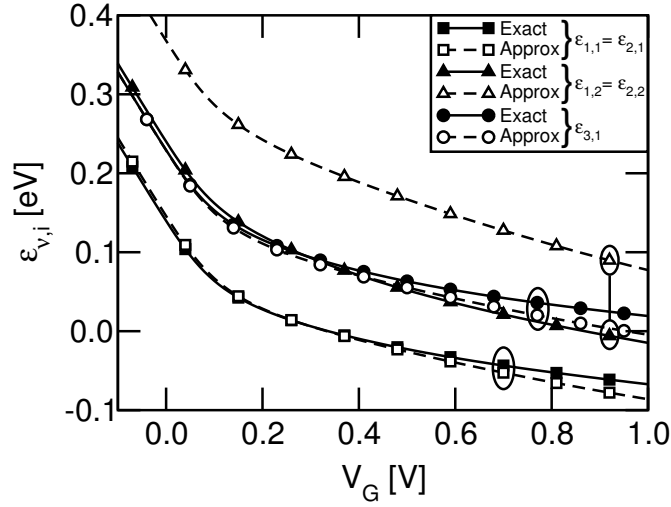


Figure 2.16: Self-consistent Schrödinger-Poisson solution for a cylindrical nanowire sketched in Fig.2.11-(a), with  $d=4\text{nm}$  and a  $[100]$  transport orientation: minimum of the subbands that give an appreciable contribution to the  $N_{inv}$  as a function of  $V_G$ , using (open symbols) and non-using (closed symbols) the isotropic effective mass approximation. Note that the Fermi level  $E_F$  is taken as the reference energy. A doping density  $N_A=1 \times 10^{15}\text{cm}^{-3}$ , a  $\text{SiO}_2$  oxide thickness  $T_{ox}=0.7\text{nm}$  and a gate work function  $\phi_m=4.05\text{eV}$  have been considered.

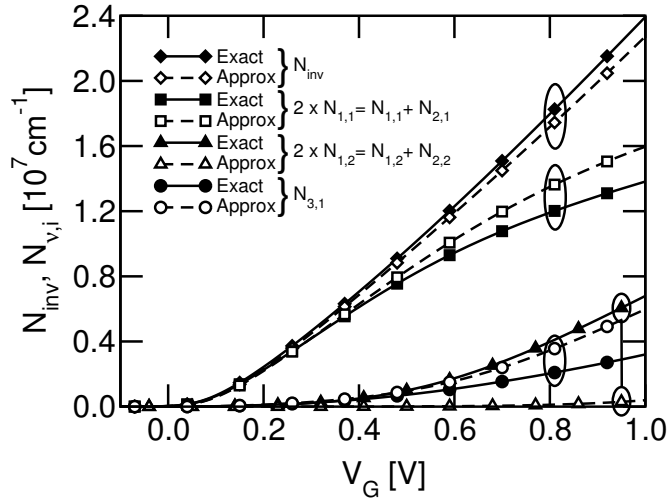


Figure 2.17: Self-consistent Schrödinger-Poisson solution for the cylindrical nanowire considered in Fig.2.16: contributions  $N_{\nu,i}$  (see Eq.2.49) of different subbands to the total inversion charge  $N_{inv}$  versus the gate voltage  $V_G$ . Results obtained either with the exact formulation of Eq.2.46 (closed symbols) or with the isotropic effective mass approximation (open symbols). Note that  $N_{1,1}=N_{2,1}$  and  $N_{1,2}=N_{2,2}$  in both cases. The contribution  $(N_{1,2}+N_{2,2})$  is negligible in the approximated case even at high  $V_G$ .

closer agreement to the results of the exact model.

### Rectangular nanowire with rounded corners (Fig.2.11-(b))

We solved the coupled Schrödinger-Poisson's problem for the squared cylindrical nanowire with rounded corners represented in Fig.2.11-(b) using both the DGA and the PS methods. The DGA simulations have been carried out by using the GAME software [16]. A doping density  $N_A = 1 \times 10^{18} \text{cm}^{-3}$  and an equivalent oxide thickness (EOT) of 1 nm have been considered in this simulation. We have considered a [100] transport orientation as described in Tab.2.1.

Fig. 2.18 compares the convergence of the maximum error of the three smallest eigenvalues of the first and second valley for an increasing number of discretization points computed by means of the DGA and PS approaches respectively for a gate voltage  $V_G = 1\text{V}$ . Since the

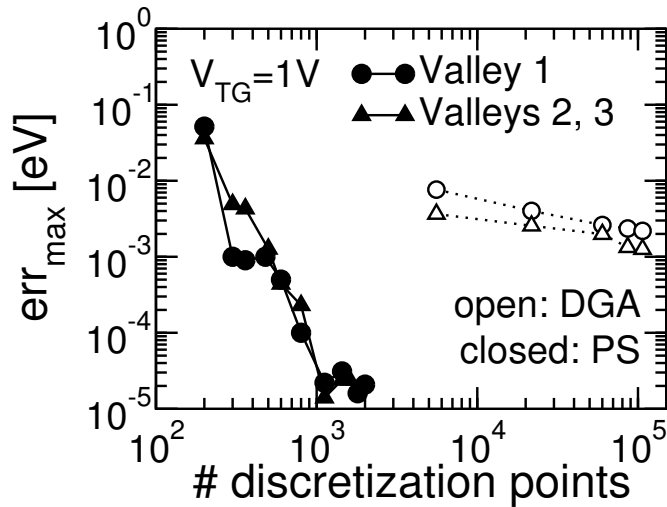


Figure 2.18: Error on the three smallest eigenvalues for each valley for the nanowire FET sketched in Fig.2.11-(b).  $V_G = 1\text{V}$ .

analytical solution of the problem is not available, the error has been calculated taking as the reference solution the one obtained by the PS method with a huge number of discretization points. The results obtained by the two methods are in good agreement; moreover, we note that the PS method converges at a much faster rate when the number of discretization points is increased. The convergence of the total charge concentration  $n + N_A$  with respect to an increasing number of discretization points is shown in Fig.2.19.

Fig.2.20 shows the total charge concentration  $n + N_A$  variation with respect to the gate voltage  $V_G$ : as can be seen the two methods give the same results over a wide range of gate voltages.

Finally, Fig.2.21 shows a 3D view of the charge density distribution in the cylindrical nanowire shown in Fig.2.11-(b), calculated by the PS method. We can conclude that the results obtained with the PS or DGA methods are in very good agreement.

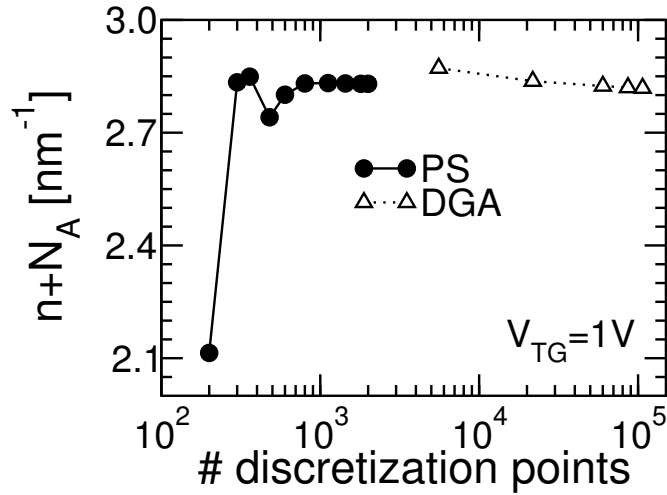


Figure 2.19: Total charge concentration  $n + N_A$  in the nanowire FET sketched in Fig.2.11-(b).  $V_G = 1V$ .

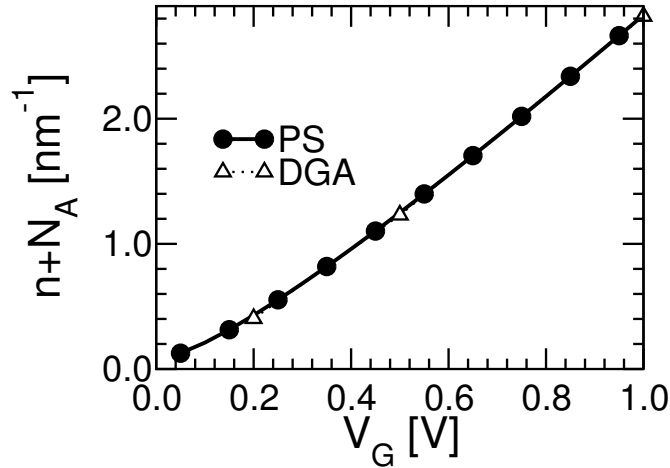


Figure 2.20: Total charge concentration  $n + N_A$  for the nanowire FET sketched in Fig.2.11-(b) for increasing gate voltages.

### FinFET transistor (Figs.2.11-(c) and 2.22)

We solved the coupled Schrödinger-Poisson's problem for the FinFET presented in Fig.2.11-(c) using both the DGA and the PS methods. The DGA simulations have been carried out by using the GAME software [16]. A doping density  $N_A = 1 \times 10^{15} \text{cm}^{-3}$  and an equivalent oxide thickness of about 2 nm have been considered in this simulation. It is worth noting that the geometry of the FinFET has been obtained by tracing the TEM image shown in Fig.2.22-(c). A  $[\bar{1}10]$  transport orientation (see Tab.2.1) and a gate voltage  $V_G = 1V$  have been considered. Fig.2.23 compares the convergence of the lowest eigenvalue of the first and second valley for an increasing number of discretization points computed for both the DGA and the PS approaches. Fig.2.24 illustrates the total charge concentration ( $n + N_A$ ) with respect to the gate voltage  $V_G$ . The results obtained with the PS or DGA methods are similar but not exactly the same due to the difference in the simulated domain, as shown in Fig. 2.22.

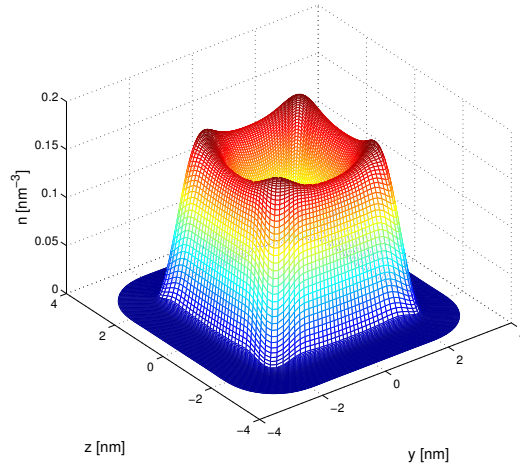


Figure 2.21: A 3D view of the electron concentration  $n$  in the nanowire FET sketched in Fig.2.11-(b) computed by the PS method,  $V_G = 1V$ .

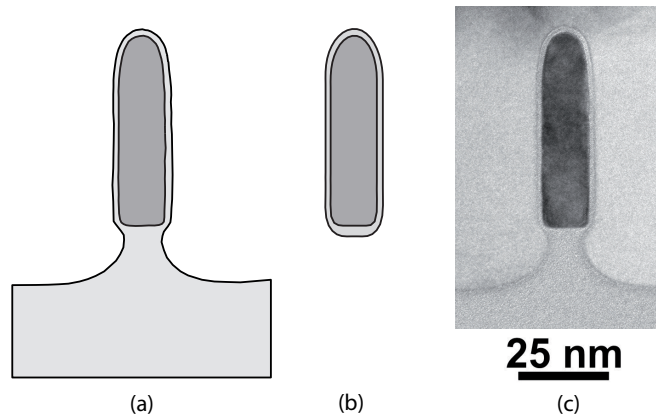


Figure 2.22: Simulation domains used for the FinFET problem (a) with DGA method (b) with PS method. The domains are different since PS method is not able to handle non-convex domains. The reference FinFET structure is illustrated in (c), that is a picture obtained with the TEM technique (courtesy of NXP Semiconductors, Leuven, Belgium).

## 2.6 Conclusions

This chapter has studied the possible advantages of the PS method compared to the FD and DGA approaches for the modeling of quantization in nanoscale devices. We have implemented, by using the FD, the PS and the DGA methods, self-consistent Schrödinger-Poisson solvers for a 1D electron gas based on the effective mass approximation model (suitable for FinFETs and nanowire FETs). We have systematically compared the errors obtained with the different approaches by varying the discretization points and, furthermore, we have benchmarked the methods for the calculation of some relevant scattering matrix elements.

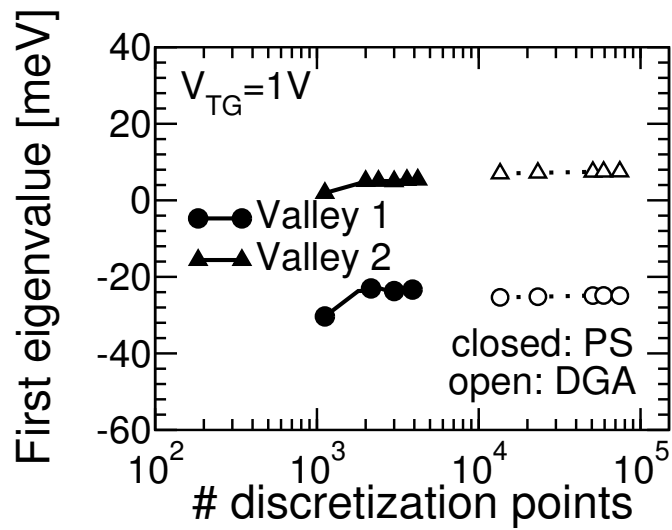


Figure 2.23: First eigenvalue for each valley for the FinFET transistor,  $V_G = 1V$ .

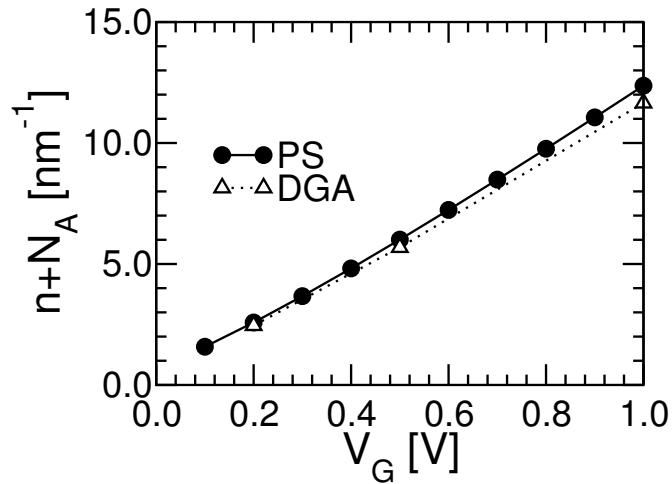


Figure 2.24: Total charge concentration ( $n + N_A$ ) for the FinFET transistor for increasing gate voltages.

All the figures of merit show a remarkable reduction in the CPU time for the PS with respect to the FD method, which makes the PS method very attractive for the electron device modeling. Moreover, thanks to the comparison with the DGA approach, we have demonstrated that also devices with a complex shape can be efficiently simulated by the PS method. Our results show that the PS method is more effective when the domain is convex, smooth and simply connected while DGA can handle complicated geometries (like those of real devices), and may be thus suitable for the study of the device variability produced by the process induced variations of the geometrical features.



# Bibliography

- [1] Y. Taur, D.A. Buchanan, W. Chen, D.J. Frank, K.E. Ismail, S-H. Lo, G. A. Sai-Halasz, R.G.Viswanathan, H.C. Wann, S.J.Wind, and H-S. Wong, "CMOS Scaling into the Nanometer Regime ," *IEEE Proceedings*, vol. 85, no. 4, pp. 486–503, 1997.
- [2] C-T. Chuang, P-F. Lu, and C.J.Anderson, "SOI for Digital VLSI: Design Consideration and Advances," *IEEE Proceedings*, vol. 86, no. 4, pp. 689–720, 1998.
- [3] G. Vellianitis, M. van Dal, L. Witters, G. Curatola, G. Doornbos, N. Collaert, C. Jonville, C. Torregiani, L.-S. Lai, J. Petty, B. Pawlak, R. Duffy, M. Demand, S. Beckx, S. Mertens, A. Delabie, T. Vandeweyer, C. Delvaux, F. Leys, A. Hikavy, R. Rooyackers, M. Kaiser, R. Weemaes, F. Voogt, H. Roberts, D. Donnet, S. Biesemans, M. Jurczak, and R. Lander, "Gatestacks for Scalable High-performance FinFETs," in *IEEE IEDM Technical Digest*, Dec. 2007, pp. 681–684.
- [4] M. Yang, V.W.C. Chan, K.K. Chan, L. Shin, D.M. Fried, J.H. Stathis, A.I. Chou, E. Gusev, J.A. Ott, L.E. Burns, M.V. Fischetti, and M. Jeong, "Hybrid-orientation Technology (HOT): Opportunitites and Challanges," *IEEE Trans. on Electron Devices*, vol. 53, no. 5, pp. 965–978, 2006.
- [5] L. Weber, J. Damlencourt, F. Andrieu, F. Ducroquet, T. Ernst, J. Hartmann, A. Papon, O. Renault, B. Guillaumot, and S. Deleonibus, "Fabrication and Mobility Characteristics of SiGe Surface Channel *p*MOSFETs with a HfO<sub>2</sub>/TiN Gate Stack," *IEEE Trans. on Electron Devices*, vol. 53, no. 3, pp. 449–455, 2006.
- [6] D. Esseni, "On the Modeling of Surface Roughness Limited Mobility in SOI MOSFETs and its Correlation to the Transistor Effective Field ," *IEEE Trans. on Electron Devices*, vol. 51, no. 3, pp. 394–401, 2004.
- [7] M. V. Fischetti, Z. Ren, P. M. Solomon, M. Yang, and K. Rim, "Six-band  $\mathbf{k} \cdot \mathbf{p}$  Calculation of the Hole Mobility in Silicon Inversion Layers: Dependence on Surface Orientation, Strain, and Silicon Thickness," *Journal of Applied Physics*, vol. 94, no. 2, pp. 1079–1095, 2003.
- [8] G. Leuzzi and V. Stornelli, "A Frequency- and Space-Domain Series-Expansion Approach for Efficient Numerical Modeling of Semiconductor Devices," *IEEE Trans. on Electron Devices*, vol. 55, no. 12, pp. 3525 –3531, dec. 2008.
- [9] Q. H. Liu, C. Cheng, and H. Massoud, "The Spectral Grid Method: a Novel Fast Schrödinger-Equation Solver for Semiconductor Nanodevice Simulation," *IEEE Trans. on Computer-Aided Design of Integrated Circuits and Systems*, vol. 23, no. 8, pp. 1200–1208, Aug. 2004.
- [10] J.-H. Lee and Q. H. Liu, "An Efficient 3-D Spectral-Element Method for Schrödinger Equation in Nanodevice Simulation," *IEEE Trans. on Computer-Aided Design of Integrated Circuits and Systems*, vol. 24, pp. 1848–1858, 2005.

- [11] C. Cheng, J.-H. Lee, H. Z. Massoud, and Q. H. Liu, “3-D Self-Consistent Schrödinger-Poisson Solver: the Spectral Element Method,” *Journal of Computational Electronics*, vol. 7, pp. 337–341, 2008.
- [12] E. Tonti, *On the formal structure of physical theories*. Quaderni dei Gruppi di Ricerca Matematica del CNR, 1975.
- [13] —, “Algebraic topology and computational electromagnetism,” in *International Workshop on Electric and Magnetic Fields, 1998*, May 1998, pp. 284–294.
- [14] A. Bossavit, *Computational Electromagnetism*. Academic Press, 1998.
- [15] R. Specogna and F. Trevisan, “A discrete geometric approach to solving time independent Schrödinger equation,” *Journal of Computational Physics*, vol. 230, no. 4, pp. 1370–1381, 2011.
- [16] —, “GAME (Geometric Approach to Maxwell’s Equations) code,” Copyright 2003-2012. [Online]. Available: <http://www.comphys.com>
- [17] L. N. Trefethen, *Spectral Methods in MATLAB*. SIAM, Philadelphia, USA, 2000.
- [18] P. J. Davis, *Interpolation & Approximation*. Dover, New York, USA, 1975.
- [19] A. Paussa, F. Conzatti, D. Breda, R. Vermiglio, D. Esseni, and P. Palestri, “Pseudospectral Methods for the Efficient Simulation of Quantization Effects in Nanoscale MOS Transistors,” *Electron Devices, IEEE Transactions on*, vol. 57, no. 12, pp. 3239–3249, dec. 2010.
- [20] W. Heinrichs, “Spectral collocation schemes on the unit disc,” *Journal of Computational Physics*, vol. 199, no. 1, pp. 66–86, 2004.
- [21] D. Esseni, F. Conzatti, M. De Michielis, N. Serra, P. Palestri, L. Selmi, “Semi-classical Transport Modelling of CMOS Transistors with Arbitrary Crystal Orientations and Strain Engineering,” *Journal of Computational Electronics*, vol. 8, pp. 209–224, 2009.
- [22] S.M. Sze, *Physics of Semiconductor Devices*. J.Wiley, 1981, p. 316.
- [23] T. Ando, A. B. Fowler, and F. Stern, “Electronic Properties of Two-dimensional Systems,” *Rev. Mod. Phys.*, vol. 54, no. 2, pp. 437–672, Apr 1982.
- [24] F. Stern and W. E. Howard, “Properties of Semiconductor Surface Inversion Layers in the Electric Quantum Limit,” *Phys. Rev.*, vol. 163, no. 3, pp. 816–835, Nov 1967.
- [25] M. Bescond, N. Cavassilas, and M. Lannoo, “Effective-mass Approach for n-type Semiconductor Nanowire MOSFETs Arbitrarily Oriented,” *Nanotechnology*, vol. 18, no. 25, p. 255201 (6pp), 2007.
- [26] P. Harrison, *Quantum Wells, Wires and Dots. Theoretical and Computational Physics of Semiconductor Nanostructures*. John Wiley & Sons, Chichester, 2000.
- [27] A. Pacelli, “Self-consistent Solution of the Schrodinger Equation in Semiconductor Devices by Implicit Iteration,” *IEEE Trans. on Electron Devices*, vol. 44, no. 7, pp. 1169–1171, jul 1997.
- [28] J. Blakemore, “Approximations for Fermi-Dirac Integrals, Especially the Function Used to Describe Electron Density in a Semiconductor,” *Solid-State Electronics*, vol. 25, no. 11, pp. 1067–1076, 1982.

- 
- [29] A. Trellakis, A. T. Galick, A. Pacelli, and U. Ravaioli, "Iteration Scheme for the Solution of the Two-dimensional Schrödinger-Poisson Equations in Quantum Structures," *Journal of Applied Physics*, vol. 81, no. 12, pp. 7880–7884, 1997.
- [30] M. Lenzi, P. Palestri, E. Gnani, S. Reggiani, A. Gnudi, D. Esseni, L. Selmi, and G. Bacarani, "Investigation of the Transport Properties of Silicon Nanowires Using Deterministic and Monte Carlo Approaches to the Solution of the Boltzmann Transport Equation," *IEEE Trans. on Electron Devices*, vol. 55, no. 8, pp. 2086–2096, aug. 2008.
- [31] A. Marchi, E. Gnani, S. Reggiani, M. Rudan, and G. Bacarani, "Investigating the Performance Limits of Silicon-nanowire and Carbon-nanotube FETs," *Solid-State Electronics*, vol. 50, no. 1, pp. 78–85, 2006.
- [32] S. Jin, M. V. Fischetti, and T. wei Tang, "Modeling of Electron Mobility in Gated Silicon Nanowires at Room Temperature: Surface Roughness Scattering, Dielectric Screening, and Band Nonparabolicity," *Journal of Applied Physics*, vol. 102, no. 8, p. 083715, 2007.



## Chapter 3

# Graphene

## 3.1 Introduction

As already mentioned in Sec.1.4, thanks to its amazing physical properties the number of potential applications of graphene is huge. For example, it is possible to exploit the excellent mobility and saturation velocity of monolayer graphene by using it as channel material in field effect transistors. Moreover, the low  $I_{on}/I_{off}$  ratio and poor saturation behavior observed in gapless monolayer graphene FETs can be improved by using bilayer graphene; indeed, in this material it is possible to induce an energy gap by applying a potential difference between the two layers; this energy gap is expected to improve both  $I_{on}/I_{off}$  and the output conductance in saturation.

In this chapter we will give a theoretical presentation of monolayer and bilayer graphene by describing their atomic structure, bandstructure, and Density Of States (DOS) and by presenting the main scattering mechanisms that limit the low-field mobility in these materials. We will also present the main Generation/Recombination (G/R) mechanisms in monolayer graphene, that are essential in the GFETs simulation.

## 3.2 Monolayer wide graphene sheet

### 3.2.1 Atomic structure

As already mentioned in Sec.1.4, a monolayer graphene sheet is made by carbon atoms displaced according to a two-dimensional honeycomb lattice, bonded together by very strong covalent bonds (see Fig.3.1). The two atoms unit cell of graphene monolayer is shown in Fig.3.2. The

Figure 3.1: Atomic structure of the monolayer graphene: the carbon atoms are placed according to a two-dimensional honeycomb lattice.

carbon-carbon bond length  $a_0$  is 1.43Å [1], while the direct lattice vectors are

$$\begin{aligned}\mathbf{a}_1 &= a\hat{x} + b\hat{y} \\ \mathbf{a}_2 &= a\hat{x} - b\hat{y},\end{aligned}\tag{3.1}$$

where

$$\begin{aligned}a &= \frac{3a_0}{2} \\ b &= \frac{\sqrt{3}a_0}{2}.\end{aligned}\tag{3.2}$$

Starting from the real space lattice vectors, it is possible to calculate the reciprocal space

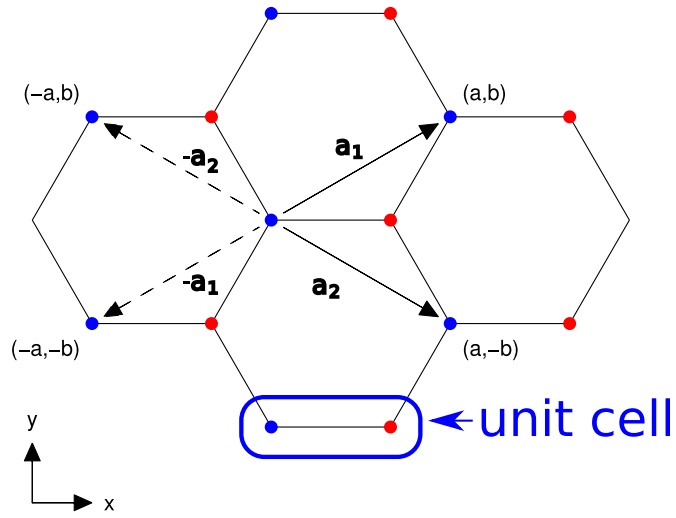


Figure 3.2: Real space lattice of monolayer graphene. The real space lattice vectors and the two atoms unit cell are highlighted.

lattice vectors  $\mathbf{A}_1$  and  $\mathbf{A}_2$  and the First Brillouin Zone (FBZ).  $\mathbf{A}_1$  and  $\mathbf{A}_2$  can be calculated as

$$\begin{aligned}\mathbf{A}_1 &= \frac{2\pi(\mathbf{a}_2 \times \hat{z})}{\mathbf{a}_1 \cdot (\mathbf{a}_2 \times \hat{z})} = \frac{\pi}{a} \hat{k}_x + \frac{\pi}{b} \hat{k}_y \\ \mathbf{A}_2 &= \frac{2\pi(\hat{z} \times \mathbf{a}_1)}{\mathbf{a}_2 \cdot (\hat{z} \times \mathbf{a}_1)} = \frac{\pi}{a} \hat{k}_x - \frac{\pi}{b} \hat{k}_y\end{aligned}\quad (3.3)$$

where  $\hat{z}$  is the direction perpendicular to the plane  $(x, y)$  and  $(k'_x, k'_y)$  is the reciprocal space. The FBZ is hexagonal and is identified by the following vertices (called K points):

$$\begin{pmatrix} 0, +\frac{2\pi}{3b} \\ 0, -\frac{2\pi}{3b} \\ +\frac{\pi}{a}, +\frac{\pi}{3b} \\ -\frac{\pi}{a}, -\frac{\pi}{3b} \\ +\frac{\pi}{a}, -\frac{\pi}{3b} \\ -\frac{\pi}{a}, +\frac{\pi}{3b} \end{pmatrix}\quad (3.4)$$

The vectors  $\mathbf{A}_1$  and  $\mathbf{A}_2$  and the hexagonal FBZ are shown in Fig.3.3.

### 3.2.2 Calculation of the bandstructure

The bandstructure can be calculated by solving the Schrödinger equation using a tight-binding (TB) approach

$$E(\mathbf{k}') \Psi_{\mathbf{k}'} = [h(\mathbf{k}')] \Psi_{\mathbf{k}'} \quad (3.5)$$

where  $[h(\mathbf{k}')]$  is the matrix form of the Hamiltonian operator. The obtained energy dispersion relation have  $s$  branches, where  $s$  is the rank of the matrix  $[h(\mathbf{k}')]$ . The rank of the matrix depends on the number of atoms of the unit cell (2 in the case of graphene, see Sec.3.2.1) and on the number of the considered orbitals. In graphene there are 4 valence orbital for each carbon atom:  $2s$ ,  $2p_x$ ,  $2p_y$  and  $2p_z$ . The orbitals  $2s$ ,  $2p_x$ ,  $2p_y$  can be neglected since their energetic levels are very far from the Fermi energy. Hence, since it is possible to calculate the energy dispersion relation just by considering the effect of the  $2p_z$  orbital, the rank  $s$  of the matrix  $[h(\mathbf{k}')]$  is 2. When only the effect of the nearest-neighbors are considered, the matrix  $[h(\mathbf{k}')]$  takes the form:

$$[h(\mathbf{k}')] = \begin{pmatrix} 0 & h_0^* \\ h_0 & 0 \end{pmatrix} \quad (3.6)$$

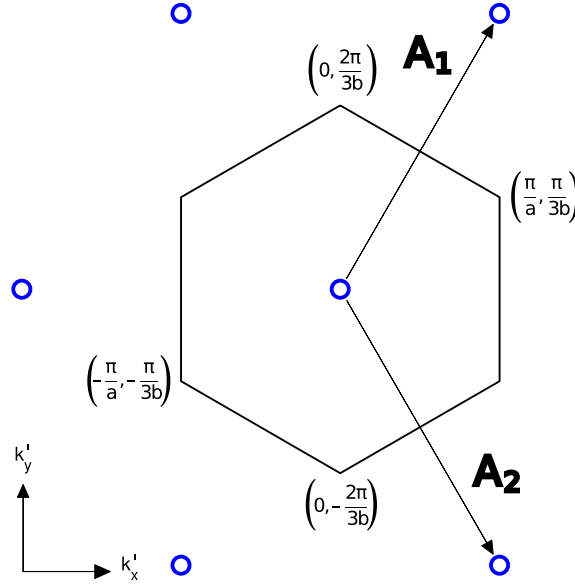


Figure 3.3: Hexagonal first Brillouin zone of monolayer graphene and the related reciprocal space lattice vectors.

where

$$h_0 = -t [1 + 2 \exp(ik'_x a) \cos(k'_y b)], \quad (3.7)$$

where  $t = 2.7\text{eV}$  is the hopping integral between two nearest neighbors [2]. The branches of the energy dispersion relation, obtained by calculating the eigenvalues of the matrix  $[h(\mathbf{k}')$ ], are expressed by

$$E(k'_x, k'_y) = \pm t \sqrt{1 + 4 \cos(k'_y b) \cos(k'_x a) + 4 \cos^2(k'_y b)}. \quad (3.8)$$

The conduction and the valence band edges in the FBZ are shown in Fig.3.4-(a) respectively by the red and the blue surface, while a contour of the conduction band is shown in Fig.3.4-(b). Two very important characteristics of the graphene bandstructure can be observed: firstly, the conduction band touches the valence band in the six vertices of the hexagonal FBZ (i.e. the six K points), thus *the monolayer graphene energy dispersion relation is gapless*. These points of the  $k$  space are called Dirac points. The energy at which the bands touch is always taken as the energy reference in this work and it is called Dirac energy. Secondly, *the conduction and the valence bands are symmetric with respect to the Dirac energy*.

Another important feature of monolayer graphene is the linearity of its bandstructure with respect to the magnitude of the wave-vector near the edges of the conduction and valence bands. Indeed, near the Dirac energy the energy dispersion relation can be approximated as

$$E(k_x, k_y) \approx \pm \hbar v_f \sqrt{k_x^2 + k_y^2} = \pm \hbar v_f k \quad (3.9)$$

where  $k_x$  and  $k_y$  are the components of the wave-vectors referred to one of the six Dirac points, and

$$v_f = \frac{3a_0 t}{2\hbar} \approx 8.8 \cdot 10^5 \quad \left[ \frac{m}{s} \right] \quad (3.10)$$

is the Fermi velocity. Fig.3.5 compares the isotropic energy relation of Eq.3.9 with the one given by Eq.3.8 close to a K point: as can be seen, the linearized approximation holds up to  $\sim 1\text{eV}$ . Thus, it is correct to say that *the energy dispersion relation near the Dirac energy is*

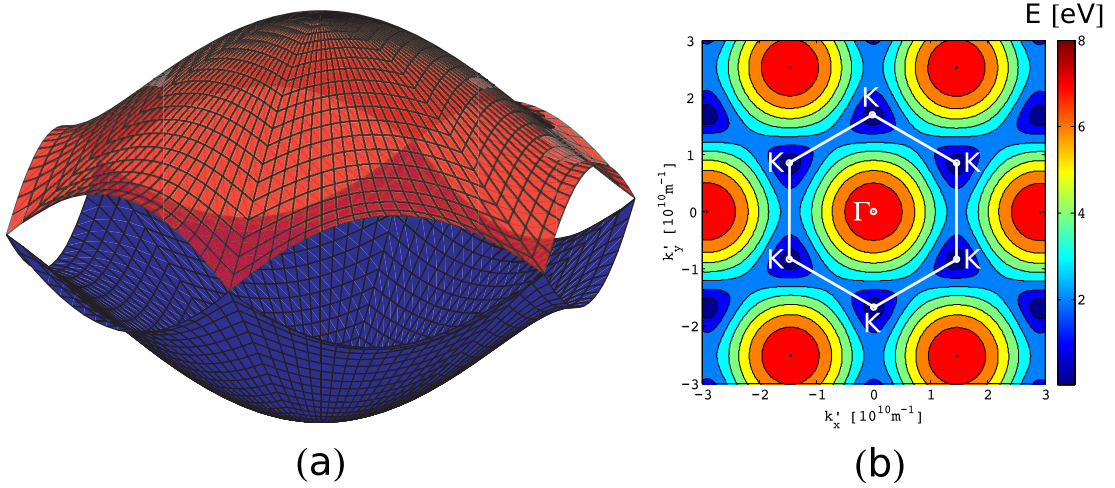


Figure 3.4: Conduction (red) and valence (blue) band edges in the FBZ for a monolayer graphene large sheet (a). Contour of the conduction band: the minima are located at the 6 vertices of the FBZ, i.e. the 6 K points (b).

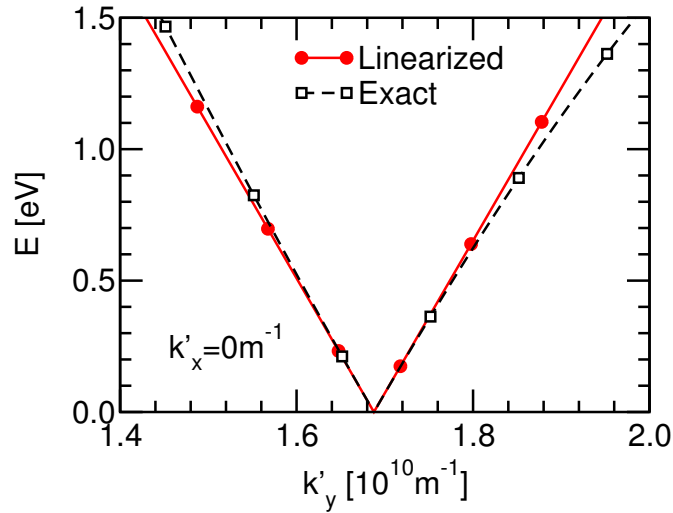


Figure 3.5: Comparison between the energy dispersion relations calculated along  $k_y$  for  $k_x = 0\text{m}^{-1}$  and given by Eq.3.8 (black curve) and Eq.3.9 (red curve).

*linear and isotropic.* Thanks to this feature, close to the Dirac energy the group velocity of graphene is isotropic, constant and equal to  $v_f$ :

$$v_g = \frac{1}{\hbar} \frac{\partial E}{\partial k} = v_f. \quad (3.11)$$

Moreover, the effective masses of electrons and holes are very low, and are even null if calculated at the Dirac point (*massless Dirac fermions*). This peculiar characteristic, joined to the very high quality of the graphene samples obtained by mechanical exfoliation (see Sec.1.4.2), are the main factors responsible for the huge low-field mobility values measured in monolayer graphene (up to  $10^6\text{cm}^2/(\text{Vs})$  in suspended samples [3]).

Finally, the eigenvectors obtained by the solution of Eq.3.5 close to the K points are ex-

pressed by [4]:

$$\Psi_{\mathbf{k}} = \frac{1}{\sqrt{2}} \begin{pmatrix} \exp\left(-i\frac{\alpha_{\mathbf{k}}}{2}\right) \\ \pm \exp\left(i\frac{\alpha_{\mathbf{k}}}{2}\right) \end{pmatrix} \quad (3.12)$$

where  $\mathbf{k} = (k_x, k_y)$ ,  $\alpha_{\mathbf{k}} = k_y/k_x$  and the upper and minus signs stands for the conduction and the valence bands respectively. The spinor-overlap  $F_{\mathbf{k},\mathbf{k}'}$  between two states  $\mathbf{k}$  and  $\mathbf{k}'$  both belonging to the conduction band is expressed by:

$$F_{\mathbf{k},\mathbf{k}'} = \Psi_{\mathbf{k}}^\dagger \cdot \Psi_{\mathbf{k}'} = \frac{1 + \cos\theta}{2} \quad (3.13)$$

where  $\theta$  is the angle between  $\mathbf{k}$  and  $\mathbf{k}'$  and  $\dagger$  is the conjugate transpose.

In summary, the graphene bandstructure is very different with respect to the one of silicon, because near the Dirac energy it is linear, isotropic, gapless and the conduction and the valence bands are symmetric. Similar results are obtained by employing more accurate TB models (for example, by considering also the effects of the next-nearest-neighbor atoms as in [4]).

### 3.2.3 Density of states, carrier statistics and ambipolarity

The DOS of the conduction band at low energies can be calculated as

$$DOS(E) = \frac{n_s n_v}{(2\pi)^2} \int_{\mathbf{k}} d\mathbf{k} \delta[E - E'(\mathbf{k})] = \frac{2}{\pi} \left( \frac{e}{\hbar v_f} \right)^2 E \quad (3.14)$$

where  $e$  is the modulus of the electron charge,  $n_s = 2$  is given by the spin and  $n_v$  is the number of the valleys;  $n_v = 2$  because, as can be seen in Fig.3.6, the 6 minimum of the FBZ can be grouped in two degenerate valleys. As it can be seen from Eq.3.14, the monolayer graphene DOS close to the band edge is linear in energy. Due to the symmetric energy dispersion relation, the DOS in the valence band is the same as in the conduction band.

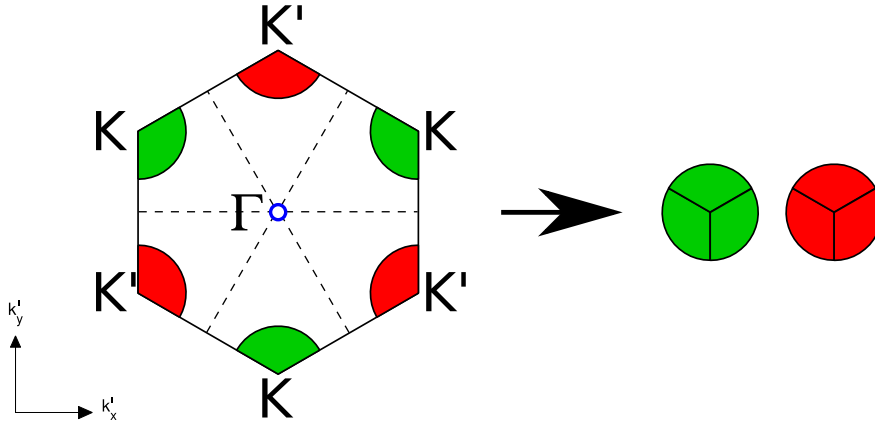


Figure 3.6: In monolayer graphene, the 6 minimum of the FBZ can be grouped in two degenerate valleys, highlighted in the figure by the green and red circles.

The electron and hole densities can be calculated as [5]

$$n = \int_0^\infty dE DOS(E) f(E) = \frac{2}{\pi} \left( \frac{K_B T}{\hbar v_f} \right)^2 \mathcal{F}_1(\eta) \quad (3.15)$$

$$p = \int_{-\infty}^0 dE DOS(E) [1 - f(E)] = \frac{2}{\pi} \left( \frac{K_B T}{\hbar v_f} \right)^2 \mathcal{F}_1(-\eta) \quad (3.16)$$

where

$$f(E) = \frac{1}{1 + \exp\left[\frac{e(E-E_F)}{K_B T}\right]} \quad (3.17)$$

is the Fermi-Dirac distribution,  $E_F$  is the Fermi energy,  $K_B$  is the Boltzmann constant,  $T$  is the temperature,  $\mathcal{F}$  is the complete Fermi-Dirac integral of order 1 [6], and

$$\eta = \frac{eE_F}{K_B T}. \quad (3.18)$$

When  $E_F = 0$ eV, the electron and hole densities are equal to the so-called intrinsic density:

$$n_i = p_i = \frac{\pi}{6} \left( \frac{K_B T}{\hbar v_f} \right)^2 \approx 10^{11} \text{ cm}^{-2} @ T = 300\text{K}. \quad (3.19)$$

Now it is possible to understand the ambipolar behavior of GFETs. Fig.3.7 shows on the left an experimental transcharacteristic  $I_D(V_G)$  of one of the GFETs reported in [7]. The very low

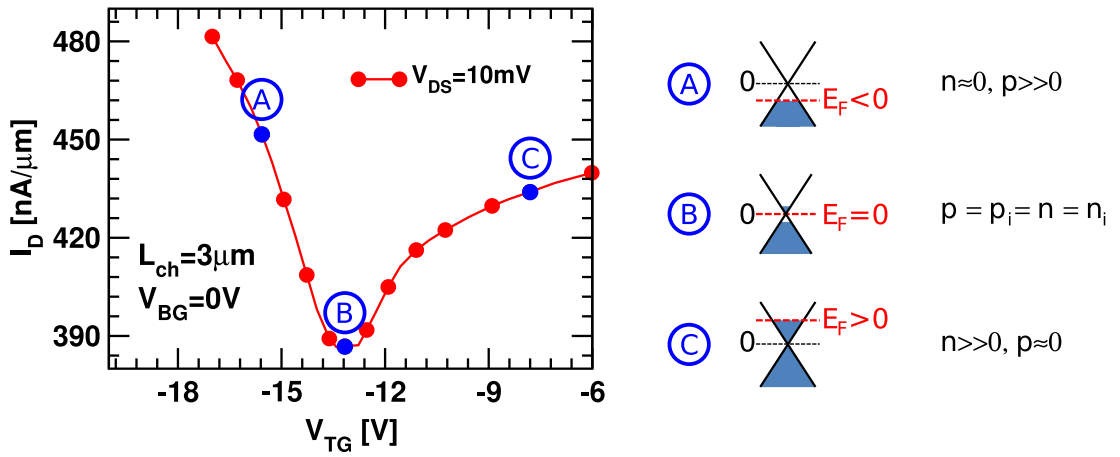


Figure 3.7: Typical experimental transcharacteristic of a GFET based on a large graphene sheet (adapted from [7]). The gapless energy dispersion relation results in unacceptable  $I_{on}/I_{off}$  ratios. A sketch explaining the origin of the ambipolarity of GFETs is reported on the right.

$I_{on}/I_{off}$  ratio ( $\approx 7$ ) limits the digital performance of this transistor. The gate voltage that corresponds to the minimum output current is called Dirac voltage ( $V_{Dirac}$ ). When  $V_G < V_{Dirac}$  (case A) the Fermi level is below 0, thus resulting in a high hole and a negligible electron densities. The channel in this case is completely populated by holes. When  $V_G = V_{Dirac}$  instead (case B), if we neglect the effect of the defects, since the considered  $V_{DS}$  is very low the concentrations of electrons and holes in the channel are approximately equal to the intrinsic concentration (see Eq.3.19), that is low but not zero, thus resulting in a high off-current. The final case ( $V_G > V_{Dirac}$ , case C) is dual with respect to case A and the current is completely due to electrons. Hence, the gapless graphene energy dispersion relation results into devices that cannot be efficiently turned off, thus limiting the possible application to digital electronics of FETs based on large sheets of monolayer graphene.

### 3.2.4 Scattering mechanisms

According to the literature, different mechanisms appear to limit the mobility in monolayer graphene sheets depending on the temperature and on the sample preparation conditions. At low temperature the mobility is typically limited by scattering with ionized impurities in the dielectric and with neutral defects in the graphene [8, 9]; however at room temperature intrinsic as well as remote phonons (RP) still play an important role [10].

In this work we have considered both the phonons intrinsic to graphene and the RP stemming from the gate dielectrics. In the next subsections we will describe the calculation of the scattering rates related to these mechanisms.

#### Intrinsic graphene phonons

Due to the two valley nature of graphene (i.e. 6  $K$ -valleys each contributing for 1/3, see Fig.3.6), phonons can assist intra-valley as well as inter-valley transitions. However, selection rules [11] reduce the number of allowed transitions. In particular we consider elastic transitions due to acoustic phonons and inelastic transitions due to zone boundary phonons. Flexural phonon modes are not expected to play an important role when the graphene sheets are sandwiched between two oxide layers as it is the case of GFETs [12, 13]. The scattering rate for the elastic intra-valley acoustic phonons is expressed by [6, 2]

$$S_{AP}(\mathbf{k}_i, \mathbf{k}_f) = \frac{2\pi K_B T D_{ac}^2}{\rho A \hbar v_s^2} |F_{\mathbf{k}_i, \mathbf{k}_f}|^2 \delta[E(\mathbf{k}_i) - E(\mathbf{k}_f)] \quad (3.20)$$

where  $\mathbf{k}_i$  and  $\mathbf{k}_f$  are respectively the initial and the final wave-vectors,  $A$  is the normalization area,  $D_{ac}=14\text{eV}$  is the deformation potential [14],  $\rho=7.6\text{kg/m}^2$  and  $v_s=2 \times 10^6\text{cm/s}$  are respectively the density of monolayer graphene [15] and the sound velocity in graphene [16, 17], and  $F_{\mathbf{k}_i, \mathbf{k}_f}$  is the spinor-overlap defined in Eq.3.13.

The scattering rate for inelastic phonons is [6, 2]

$$S_{OP}(\mathbf{k}_i, \mathbf{k}_f) = \frac{\pi D_{op}^2}{\omega_{OP} \rho A} |F_{\mathbf{k}_i, \mathbf{k}_f}|^2 \left( n_{op} + \frac{1}{2} \mp \frac{1}{2} \right) \delta[E(\mathbf{k}_i) - E(\mathbf{k}_f) \pm \hbar\omega_{OP}] \quad (3.21)$$

where  $D_{op}=10^{11}\text{eV/m}$  is the deformation potential [14],  $\hbar\omega_{OP}=0.152\text{eV}$  is the energy of the phonon [14], and  $n_{op}$  is the phonon occupation [6], i.e.:

$$n_{op} = \frac{1}{\exp\left(\frac{\hbar\omega_{OP}}{K_B T}\right) - 1}. \quad (3.22)$$

The upper and lower signs in Eq.3.21 are related respectively to phonon absorption and phonon emission. We simplify the treatment of in-plane phonons by considering only the associated scalar perturbation potential and not the vector potential contribution [4]. The deformation potentials used in the elastic and in the inelastic zone boundary phonon should be considered as effective values that collectively describe both longitudinal and transverse phonons as well as acoustic phonon screening [14]. The results shown in the next chapters (see for example Sec.5.3.1) show that the scattering with remote phonons is way dominant with respect to local graphene phonons for the determination of the overall mobility, hence the undeniable uncertainties in the values of the deformation potentials  $D_{ac}$  and  $D_{op}$  are not expected to affect critically the main results for mobility calculations.

Finally, since in all the forthcoming simulations we consider wide graphene sheets, we consistently neglect edge roughness scattering.

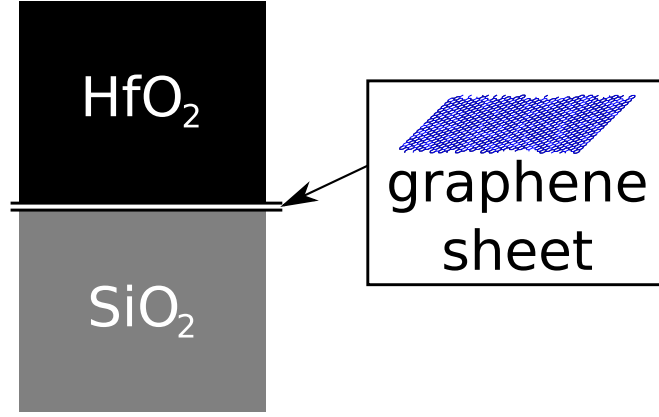


Figure 3.8: Structure considered in the calculation of the remote phonons scattering rate: the graphene monolayer is sandwiched between an high- $k$  top gate dielectric (in this case  $\text{HfO}_2$ ) and a  $\text{SiO}_2$  substrate. We have supposed for both the dielectrics an infinite thickness.

### Remote phonons

Let us start by considering a sheet of graphene between two dielectrics with an infinite thickness (see Fig.3.8). Following [6, 18], it is possible to demonstrate that the scattering rates of the remote phonons originating in each of the two dielectrics reported in Fig.3.8 are expressed by [10]:

$$S_{RP_m}(\mathbf{k}_i, \mathbf{k}_f) = \frac{2\pi}{\hbar A} |F_{\mathbf{k}_i, \mathbf{k}_f}|^2 e^2 \left( n_{RP_m} + \frac{1}{2} \mp \frac{1}{2} \right) \frac{\hbar \omega_{RP_m}}{2q \hat{\epsilon}_m} \exp(-2qd) \delta[E(\mathbf{k}_i) - E(\mathbf{k}_f) \pm \hbar \omega_{RP_m}] \quad (3.23)$$

where  $\theta$  is the angle between the initial  $\mathbf{k}_i$  and the final  $\mathbf{k}_f$  wave-vectors,  $m$  indicates the material originating the phonon (i.e.  $m = \text{SiO}_2$  or  $\text{HfO}_2$ , see Fig.3.8),  $q^2 = (k^2 + k_f^2 - 2kk_f \cos \theta)$  is the magnitude of the exchanged wave-vector  $\mathbf{q} = (\mathbf{k}_f - \mathbf{k}_i)$  (see Fig.3.9). Furthermore,  $n_{RP}$  is the phonon occupation given by [6]

$$n_{RP_m} = \frac{1}{\exp\left(\frac{\hbar \omega_{RP_m}}{K_B T}\right) - 1}; \quad (3.24)$$

$\hbar \omega_{RP_m}$  is the energy of the  $m$ -th remote phonon, and the upper and lower signs stand for absorption and emission, respectively. Finally,  $d$  is the distance between the dielectric and the graphene sheet. In the calculations we set  $d=0$  because we verified that  $d$  up to a few  $\text{\AA}$  does

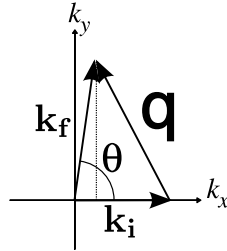


Figure 3.9: Exchanged wave-vector  $\mathbf{q}$  between the initial state  $\mathbf{k}_i$  and the final state  $\mathbf{k}_f$ .

not change the results. The phonon energies  $\hbar \omega_{RP_m}$  have been obtained by setting to zero the sum of the frequency dependent oxide polarizabilities [6]:

$$\epsilon_{\text{HfO}_2}(\omega) + \epsilon_{\text{SiO}_2}(\omega) = 0. \quad (3.25)$$

It should be noted that the graphene polarizability and thus the possible phonon to plasmon coupling have been neglected [19, 20]. The phonon-plasmon coupling is a delicate matter whose quantitative investigation demands an accurate determination of both the real and the imaginary part of the graphene polarizability. In this respect, the analytical results for the graphene polarizability reported in [20, 21] (and derived for  $T = 0\text{K}$ ) show that the imaginary part of the polarizability is non null in a wide region of the energy versus wave-vector plane. This implies that a large part of the coupled phonon-plasmon modes undergo strong Landau damping and cease to be collective excitations [19, 22]. In the region of Landau damping not only the phonon-plasmon coupling is suppressed but also the screening of the RP modes due to the electronic polarizability of the graphene layer should not be included in the calculation, so that it is questionable to describe the screening by simply dividing the RP matrix elements by the graphene static dielectric function [23, 24]. In this complicated theoretical framework we embraced a relatively simple picture and did not include the graphene polarization in our calculations, thus neglecting the phonon-plasmon coupling. A recent publication [22] has shown that phonon-plasmon coupling is essentially negligible in silicon devices with  $\text{SiO}_2$  or high- $k$  dielectrics in all cases of practical interest. While the same conclusion is not granted for graphene devices, still it suggests that using the static dielectric function for the screening of RP most likely leads to a significant overestimation of the screening effect.

We included in the calculations only the dominant remote phonon mode with the lowest energy and we neglected the possible coupling with the phonons of the other dielectric by assuming  $\text{SiO}_2$  working at low-frequency when computing the mode originating from  $\text{HfO}_2$ , and  $\text{HfO}_2$  at intermediate-frequency when computing the mode originating from the substrate. To be more explicit, in order to calculate the energy and the effective dielectric constants related to the remote phonon originating in the  $\text{HfO}_2$  top gate dielectric, we have solved

$$\epsilon_{\text{HfO}_2}^i + \frac{\epsilon_{\text{HfO}_2}^0 - \epsilon_{\text{HfO}_2}^i}{1 - \left(\frac{\omega_{\text{RP}_{\text{HfO}_2}}}{\omega_{\text{TO}_{\text{HfO}_2}}}\right)^2} = -\epsilon_{\text{SiO}_2}^0. \quad (3.26)$$

Using simple mathematical operations, we obtained:

$$\hbar\omega_{\text{RP}_{\text{SiO}_2}} = \hbar\omega_{\text{TO}_{\text{SiO}_2}} \sqrt{\frac{\epsilon_{\text{HfO}_2}^i + \epsilon_{\text{SiO}_2}^0}{\epsilon_{\text{HfO}_2}^i + \epsilon_{\text{SiO}_2}^i}}. \quad (3.27)$$

A similar expression has been obtained for the remote phonon originating in the  $\text{SiO}_2$  substrate:

$$\hbar\omega_{\text{RP}_{\text{HfO}_2}} = \hbar\omega_{\text{TO}_{\text{HfO}_2}} \sqrt{\frac{\epsilon_{\text{SiO}_2}^0 + \epsilon_{\text{HfO}_2}^0}{\epsilon_{\text{SiO}_2}^0 + \epsilon_{\text{HfO}_2}^i}}. \quad (3.28)$$

Using the values of the phonon energies expressed by Eqs.3.27 and 3.28, it is possible to calculate the effective dielectric constants  $\hat{\epsilon}_{\text{SiO}_2}$  and  $\hat{\epsilon}_{\text{HfO}_2}$  to be used in Eq.3.23, that are

$$\frac{1}{\hat{\epsilon}_{\text{SiO}_2}} = \frac{1}{\epsilon_{\text{HfO}_2}^i + \epsilon_{\text{SiO}_2}^i} - \frac{1}{\epsilon_{\text{HfO}_2}^i + \epsilon_{\text{SiO}_2}^0} \quad (3.29a)$$

$$\frac{1}{\hat{\epsilon}_{\text{HfO}_2}} = \frac{1}{\epsilon_{\text{SiO}_2}^0 + \epsilon_{\text{HfO}_2}^i} - \frac{1}{\epsilon_{\text{SiO}_2}^0 + \epsilon_{\text{HfO}_2}^0} \quad (3.29b)$$

where the values of  $\omega_{\text{TO}_m}$ ,  $\epsilon_m^i$ , and  $\epsilon_m^0$  have been taken from [19] and are reported in Tab.3.1.

### 3.3 Generation/Recombination mechanisms

The G/R mechanisms have a very strong impact on the performance of FETs based on a large sheet of graphene due to the gapless energy dispersion relation of this material. Hence, in

Table 3.1: Values of the parameters used for the calculation of the scattering rates due to remote phonons.

Parameter	Value [19]
$\hbar\omega_{TO_{SiO_2}}$	55.6meV
$\epsilon_{SiO_2}^0$	3.9
$\epsilon_{SiO_2}^i$	3.05
$\hbar\omega_{TO_{HfO_2}}$	12.43meV
$\epsilon_{HfO_2}^0$	22
$\epsilon_{HfO_2}^i$	6.58

order to estimate the performance of graphene FETs we modeled two of the main phenomena responsible of these mechanisms: the band-to-band tunneling and the interband recombination assisted by phonons.

### 3.3.1 Band-to-band tunneling

Concerning the BTBT, since wide graphene sheets have zero bandgap, we have employed a local model described in terms of generation-recombination [25]. The tunneling current density of electrons from the valence band to the conduction band is expressed by:

$$J = \frac{n_v n_s}{A} e \sum_{k_y} \sum_{k_x > 0} [f_v(E) - f_c(E)] v_x(E) T(E) \quad (3.30)$$

where  $E = \hbar v_f |\mathbf{k}|$  is the energy related to the state  $\mathbf{k} = (k_x, k_y)$ ,  $f_c(E)$  and  $f_v(E)$  are the occupation probabilities in the conduction and in the valence bands at  $E$ ,  $v_x(E)$  is the component of the electron velocity in the  $x$  direction, i.e.

$$v_x(E) = \frac{1}{\hbar} \frac{dE}{dk_x}, \quad (3.31)$$

and  $T(E)$  is the tunneling probability calculated according to the WKB approximation, i.e.

$$T(E) = \exp\left(-2 \int_{-\infty}^{+\infty} \text{Im}\{k_x\} dx\right). \quad (3.32)$$

By converting the sums over  $k_x$  and  $k_y$  in integrals according to the standard prescriptions [6], we obtained:

$$J = \frac{n_v n_s}{(2\pi)^2} e \int_{-\infty}^{+\infty} dk_y \int_0^{+\infty} [f_s(E) - f_d(E)] \frac{1}{\hbar} \frac{dE}{dk_x} T(E) dk_x. \quad (3.33)$$

At this point, in order to simplify the calculation and obtain an analytic expression for the BTBT rate, we assume an infinite device and employ the following approximation:

$$f_v(E) - f_c(E) = 1 \quad (3.34)$$

hence we consider the case of maximum generation due to the BTBT (the valence band is full of electrons while the conduction band is completely empty). Thanks to these hypothesis and under the assumption of a constant local electric field  $F_x$ , the current density is independent of the energy  $E$  and it is possible to obtain

$$\frac{J}{\Delta E} = \frac{n_v n_s}{(2\pi)^2} e \int_{-\infty}^{+\infty} dk_y T(k_y). \quad (3.35)$$

The maximum BTBT generation rate can be calculated as

$$G_{BTBT_{max}} = F_x \frac{J}{\Delta E} = F_x \frac{n_v n_s}{(2\pi)^2} e \int_{-\infty}^{+\infty} dk_y T(k_y). \quad (3.36)$$

Let us now consider the situation sketched in Fig.3.10: we have a constant electric field  $F_x$ , and we take  $x = 0$  as the point where the energy of the electron  $E_{tot}$  crosses the Dirac point. We

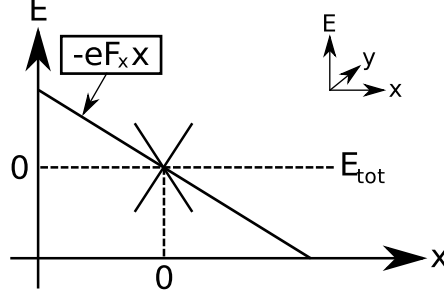


Figure 3.10: Sketch of the considered situation: under a constant electric field  $F_x$ , an electron with a total energy  $E_{tot}$  tunnels from the valence band on the left to the conduction band on the right.

can express the electron total energy as

$$E_{tot} = -eFx + \hbar v_f \sqrt{k_x^2 + k_y^2} \quad (3.37)$$

By setting  $E_{tot} = 0eV$ , after some calculations we obtain:

$$k_x = i \sqrt{k_y^2 - \left( \frac{eFx}{\hbar v_f} \right)^2} \quad (3.38)$$

Thanks to Eq.3.38, we can say that

$$\text{Im}\{k_x\} \neq 0 \Leftrightarrow |x| < \left| \frac{k_y \hbar v_f}{eF} \right|. \quad (3.39)$$

Thus, the integral in equation 3.32 has an analytic solution, i.e.

$$T(E) = T(k_y) = \exp \left[ -2 \int_{-\frac{k_y \hbar v_f}{eF}}^{+\frac{k_y \hbar v_f}{eF}} \sqrt{k_y^2 - \left( \frac{eFx}{\hbar v_f} \right)^2} dx \right] = \exp \left( -\frac{k_y^2 \hbar v_f \pi}{eF} \right). \quad (3.40)$$

By substituting Eq.3.40 in Eq.3.36 we obtain the analytic expression for the maximum<sup>1</sup> generation rate due to BTBT:

$$G_{BTBT_{max}} = F_x \frac{n_v n_s}{(2\pi)^2} e \int_{-\infty}^{+\infty} \exp \left( -\frac{k_y^2 \hbar v_f \pi}{eF} \right) dk_y = \frac{1}{\pi^2 \sqrt{v_f}} \left( \frac{eF_x}{\hbar} \right)^{3/2} \quad (3.41)$$

with  $n_v = 2$  and  $n_s = 2$  (see Sec.3.2.3). The obtained expression, that is consistent with previous works found in the literature [26, 27], has been validated against the result obtained using a state-of-the-art NEGF simulator based on a TB description of the graphene layer, NanoTCAD ViDES [28]. A brief description of this simulator can be found in Appx.A. We have compared Eq.3.41 with the results calculated by NanoTCAD ViDES in a simple uniform device characterized by a constant electric field and boundary conditions such that  $f_v = 1$  and

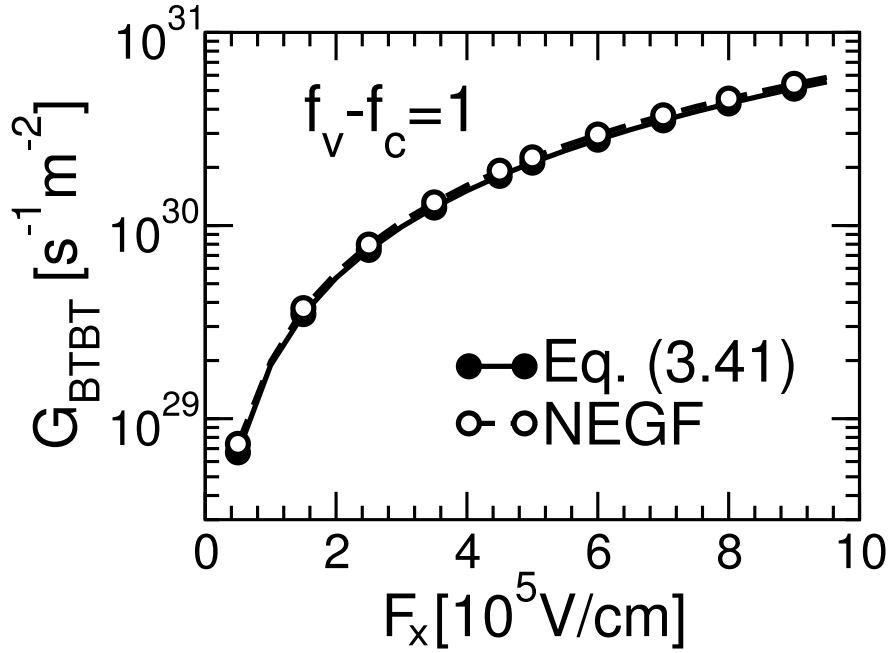


Figure 3.11: BTBT generation rate calculated by the semi-classical (closed symbols, Eq.3.41) and NEGF (open symbols) models under a uniform electric field  $F_x$ .

$f_c = 0$ . Fig.3.11 shows that the maximum generation rate of Eq.3.41 is in excellent agreement with the NEGF results over a wide range of electric fields.

As already mentioned, Eq.3.41 represents the maximum generation rate due to BTBT obtained when the valence band is completely filled of electrons while the conduction band is empty. However, in general the occupations of the initial and the final states limit the BTBT phenomena. In order to take this effect into account, we multiply Eq.3.41 by the term  $(f_v - f_c)$  without considering its dependence on  $\mathbf{k}$ , thus obtaining:

$$G_{BTBT} - R_{BTBT} \approx \frac{f_v - f_c}{\pi^2 \sqrt{v_f}} \left( \frac{eF}{\hbar} \right)^{3/2} \quad (3.42)$$

where  $f_v$  and  $f_c$  are, respectively, the local occupation probabilities of the particles impinging on the classical turning points in the valence and in the conduction bands. Here we want to remark that the formulation of the net BTBT rate reported in Eq.3.42 naturally includes the generation as well as the recombination, that are both important in GFETs.

Compared to more accurate models for chiral tunneling in graphene [29, 30] this model does not account for wave-functions mismatch [29], considers  $k_y$  ranging from  $-\infty$  to  $+\infty$ <sup>2</sup> and averages the dependence on the carriers angle of the term  $(f_v - f_c)$ . However, the good agreement with the NEGF simulations reported in Chap.6 suggests that these effects are of small relevance in practical, wide channel, GFETs designs.

As a final remark, our approach for the BTBT is similar to that of a recent paper [31], although the expression of the net generation rate appears to differ by a factor of 1/4 in the argument of the exponential in Eq.3.41. However, the consistency with [26, 27] and the good agreement with NEGF results shown in Fig.3.11 and in Chap.6 support the validity of Eq.3.42 of this work.

<sup>1</sup>It is the maximum value of the generation rate because we have set  $f_v(E) - f_c(E) = 1$  (see Eq.3.34).

<sup>2</sup>In the case of finite barriers a limited  $k_y$  range should be considered.

### 3.3.2 Interband recombination assisted by phonons

In the model used in the rest of the thesis, we also consider interband recombination assisted by phonons. We neglect the effect of the generation due to the same phenomena since in GFETs we expect always high carriers densities. The recombination rate is given by the following simplified expression, taken from [32]

$$R_{IR} = \frac{\min(n, p)}{\tau_r} \quad (3.43)$$

where  $n$  and  $p$  are respectively the electron and hole densities and  $\tau_r$  is the recombination time. The recombination time strongly depends on the temperature and on the densities of electrons and holes, as can be seen in Fig.3.12.

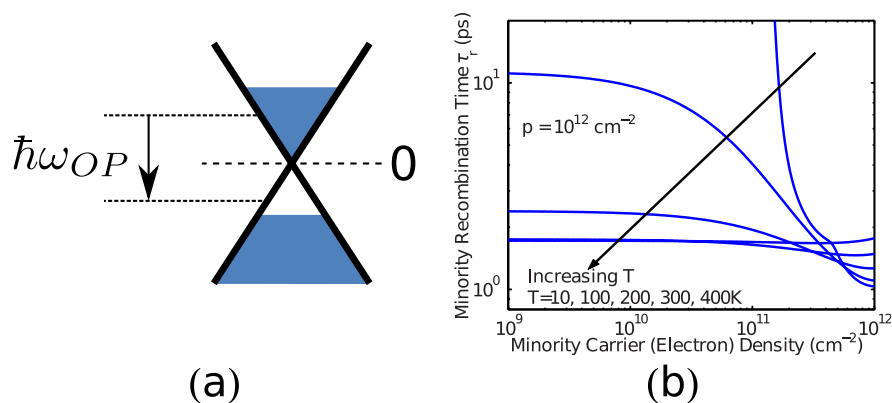


Figure 3.12: (a) Sketch illustrating the recombination assisted by optical phonons in mono-layer graphene. (b) Minority carrier (electron) average recombination times assisted by optical phonons are plotted as a function of the minority carrier density for different temperatures. The majority carrier (hole) density is assumed to be 10<sup>12</sup>cm<sup>-2</sup>. Adapted from [32].

### 3.4 Graphene bilayer

As already mentioned in Sec.1.4.2, in order to improve the  $I_{on}/I_{off}$  ratio and the current saturation behavior of GFETs a bandgap has to be induced in graphene [33]. A method to induce an energy gap is to insert a Graphene BiLayer (GBL) in a double-gate structure (see Fig.3.13), and apply an electric field across it [34, 35, 1]. This is a very promising approach,

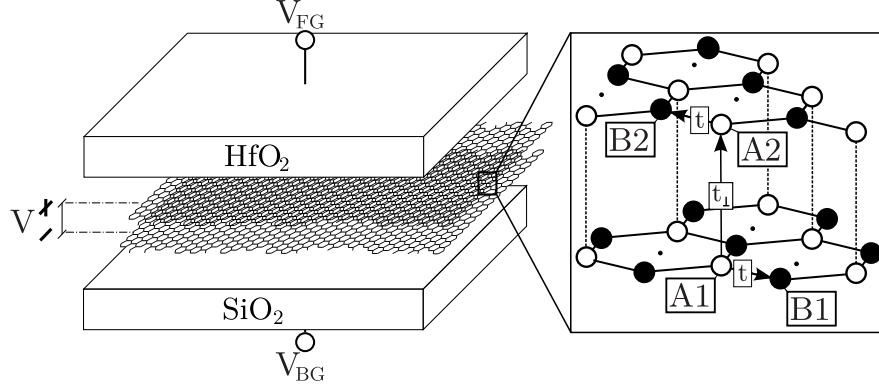


Figure 3.13: It is possible to induce a bandgap by applying an electric field to a graphene bilayer inserted in a double-gate structure (in this example an ideally flat  $\text{SiO}_2$  substrate and  $\text{HfO}_2$  top dielectric). The inset illustrates the GBL four-atoms unit cell and the alignment between atoms A1 and A2 (Bernal stacking); the hopping energies  $t$  and  $t_{\perp}$  are also shown.

and improvements in the current saturation and an increase of the  $I_{on}/I_{off}$  ratio in GFETs based on GBL have been already observed in many experiments [36, 37, 38, 39, 40, 41, 42, 43].

#### 3.4.1 Atomic structure and bandstructure calculation

The graphene bilayer is modeled as two coupled hexagonal lattices with inequivalent sites A1, B1 and A2, B2 respectively in the first and in the second layer (see Fig.3.13), arranged according to a Bernal stacking, where atoms A1 are aligned with atoms A2. We consider ideally flat interfaces and the graphene bilayer band structure unaffected by the top and the bottom dielectrics. Under these assumptions and in the absence of an external electric field such a lattice results in gapless valleys located at the six  $K$  corners of the hexagonal Brillouin zone (similarly to monolayer graphene, see Sec.3.2).

#### Complete tight-binding Hamiltonian

The TB Hamiltonian close to each of the  $K$  points can be written as [1]

$$\begin{pmatrix} eV/2 & v_f \pi^+ & t_{\perp} & -\nu_4 v_f \pi^- \\ v_f \pi^- & eV/2 & -\nu_4 v_f \pi^- & \nu_3 v_f \pi^+ \\ t_{\perp} & -\nu_4 v_f \pi^+ & -eV/2 & v_f \pi^- \\ -\nu_4 v_f \pi^+ & \nu_3 v_f \pi^- & v_f \pi^+ & -eV/2 \end{pmatrix} \Psi_{\mathbf{k}} = E(\mathbf{k}) \Psi_{\mathbf{k}} \quad (3.44)$$

where  $\mathbf{k}=(k_x, k_y)$  is the wave-vector referred to the  $K$  point,  $\pi^+=\hbar(k_x+ik_y)$  ( $\pi^-$  being its complex conjugate),  $t_{\perp}=0.35\text{eV}$ ,  $\nu_3=0.1$ ,  $\nu_4=0.05$  [1], and  $V$  is the voltage difference between the two graphene layers. This Hamiltonian is complete in the sense that it accounts for the interactions between all the four atoms of the unit cell; indeed,  $t_{\perp}$  is associated to the hopping from the site A1 to the site A2 (and vice versa), while  $\nu_3 v_f \pi$  and  $\nu_4 v_f \pi$  are related to the hoppings from B1 to B2 (and vice versa) and from B1 to A2 (and vice versa), respectively.

Finally, the hopping between atoms belonging to the same sheet are taken into account by the term  $v_f\pi$ .

This  $4 \times 4$  TB Hamiltonian operates in the space of the column vectors  $\Psi_{\mathbf{k}} = [\Psi_{A1}(\mathbf{k}), \Psi_{B1}(\mathbf{k}), \Psi_{A2}(\mathbf{k}), \Psi_{B2}(\mathbf{k})]^T$ , which are the normalized coefficients of the tight-binding expansion inside the reference unit cell [1]. The Hamiltonian provides four branches of the energy dispersion and the two branches in the valence band are simply a mirroring of the ones of the conduction band; hence all the transport properties are symmetric in the two bands. Eq.3.44 leads to an energy relation that is anisotropic, as illustrated in Fig.3.14, reporting the lowest branch of the conduction band in the  $\mathbf{k}$  space. It is very important to note that the linearity of the energy dispersion relation, that is one of the peculiar characteristics of monolayer graphene, is not present in bilayer graphene.

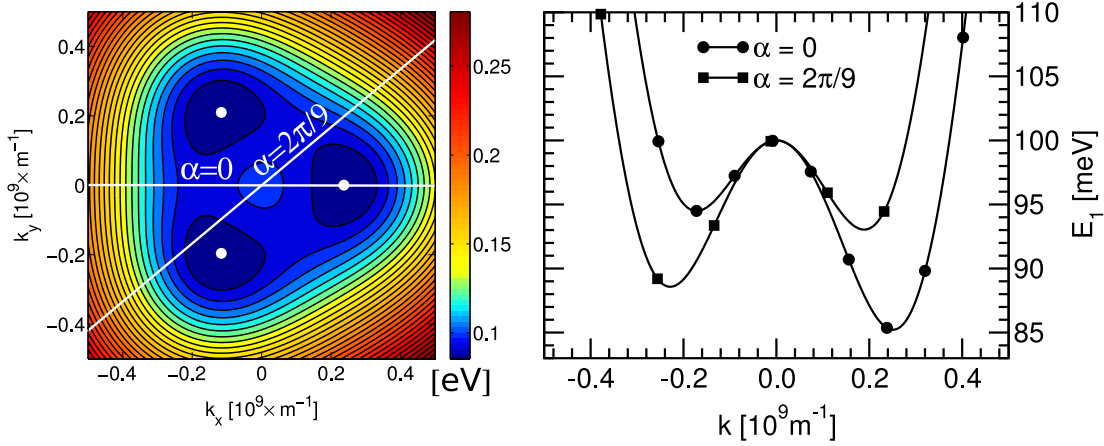


Figure 3.14: (Left) Contour of the bottom of the conduction band calculated using the TB Hamiltonian in Eq.3.44 and for  $V=0.2V$ . The three minima of the conduction band near the K point (placed at  $(k_x, k_y)=(0,0)m^{-1}$ ) are labeled by the small, white circles. (Right) Plot of the lowest branch of the conduction band along the directions  $\alpha=0$  (continuous line with filled circles) and  $\alpha=2\pi/9$  (continuous line with filled squares).

### Simplified Hamiltonian

In the literature a simplified tight binding Hamiltonian is widely used, where the only interactions accounted for between the atoms of the different layers are those between atoms which are aligned according to the Bernal stacking (A1 and A2 in Fig.3.13). The tight binding Hamiltonian close to the  $K$  points in this case can be written as [35, 1, 44]

$$\begin{pmatrix} eV/2 & v_f\pi^+ & t_{\perp} & 0 \\ v_f\pi^- & eV/2 & 0 & 0 \\ t_{\perp} & 0 & -eV/2 & v_f\pi^- \\ 0 & 0 & v_f\pi^+ & -eV/2 \end{pmatrix} \Psi_{\mathbf{k}} = E(\mathbf{k})\Psi_{\mathbf{k}} \quad (3.45)$$

where, similarly to Eq.3.44,  $\mathbf{k}=(k_x, k_y)$  is still the wave-vector referred to the  $K$  point. The Hamiltonian in Eq.3.45 provides four branches of the energy dispersion and operates in the same space of the column vectors as the Hamiltonian reported in Eq.3.44; moreover, also in this case the conduction and the valence bands are symmetric with respect to the midgap energy. The two branches  $E_1$  and  $E_2$  in the conduction band are expressed by the following analytic expression:

$$E_{1,2}(k) = \pm \sqrt{\hbar^2 v_f^2 k^2 + \frac{e^2 V^2}{4} + \frac{t_{\perp}^2}{2} \mp \frac{1}{2} \sqrt{L}}, \quad (3.46)$$

with

$$L = 4 [e^2 V^2 + t_{\perp}^2] \hbar^2 v_f^2 k^2 + t_{\perp}^4,$$

where  $k^2 = (k_x^2 + k_y^2)$ . The two branches in the conduction and in the valence bands can be obtained just by considering respectively the plus or the minus in front of Eq.3.46. As it can be seen, thanks to the simplifications used in the formulation of the TB Hamiltonian, the energy dispersion relation depends only on the modulus of the wave vector  $\mathbf{k}$ , thus the energy dispersion relation is isotropic. From Eq.3.46 it is possible to calculate the value of the energy gap  $E_G$  as a function of the applied voltage  $V$ , i.e.:

$$E_G = \frac{t_{\perp}}{\sqrt{1 + \frac{t_{\perp}^2}{e^2 V^2}}}. \quad (3.47)$$

As can be seen (see also Fig.3.15), the maximum  $E_G$  that can be induced is limited to  $t_{\perp} = 0.35\text{eV}$ . Hence, it is not possible to induce a bandgap large as the one of silicon in bilayer

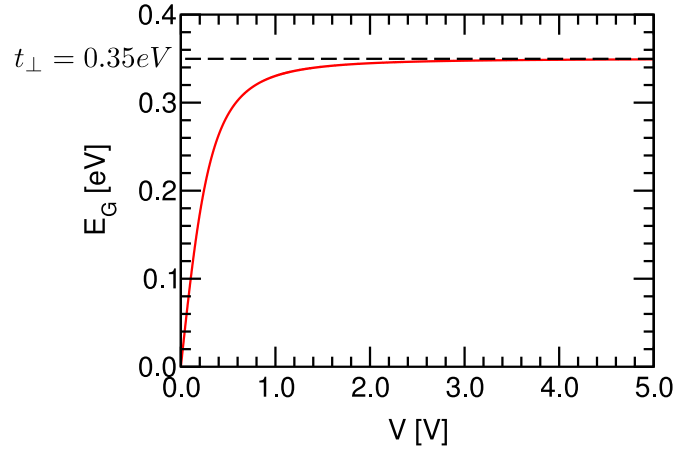


Figure 3.15: Energy gap  $E_G$  induce in bilayer graphene versus the applied voltage  $V$  calculated using Eq.3.47, derived from the simplified Hamiltonian reported in Eq.3.45.

graphene using an external electric field. Moreover, it should be noted that energy gaps larger than  $E_G \sim 0.25\text{eV}$  may not be achievable in a real device because they demand too high electric fields both between the layers (see Fig.3.16) and in the dielectrics, probably above what oxides can reliably withstand. However, according to recent theoretical studies [33] this energy gap value is sufficient for GFETs in order to outperform silicon MOSFETs in RF applications.

Fig.3.17-(a) shows  $E_1(k)$  and  $E_2(k)$  as a function of the modulus of the wave-vector  $\mathbf{k}$ , for different values of  $E_G$ , which is in turn set by the voltage  $V$  (see Eq.3.47) [35]. Fig.3.17-(b) reports a comparison between the bottom of the conduction band calculated by the Hamiltonian of Eq.3.44 and the isotropic one given by Eq.3.46: as can be seen, the simplified approach estimates with a sufficient accuracy the value of the bandgap but, since it is isotropic, is not able to describe the so-called trigonal distortion (that is the particular shape of the bilayer graphene bands clearly shown in Fig.3.14).

According to both the complete (Eq.3.44) and to the simplified (Eq.3.45) Hamiltonians, the edge of the conduction band of bilayer graphene is non-monotonic close to one of the  $K$  points of the FBZ (see Figs.3.17-(b)). For example, starting from Eq.3.46, it is possible to calculate the value of the wave-vector  $k_{min}$  where the minimum of the conduction band occurs:

$$k_{min} = \frac{e V}{2\hbar v_f} \sqrt{\frac{1 + 2\frac{t_{\perp}^2}{e^2 V^2}}{1 + \frac{t_{\perp}^2}{e^2 V^2}}} \quad (3.48)$$

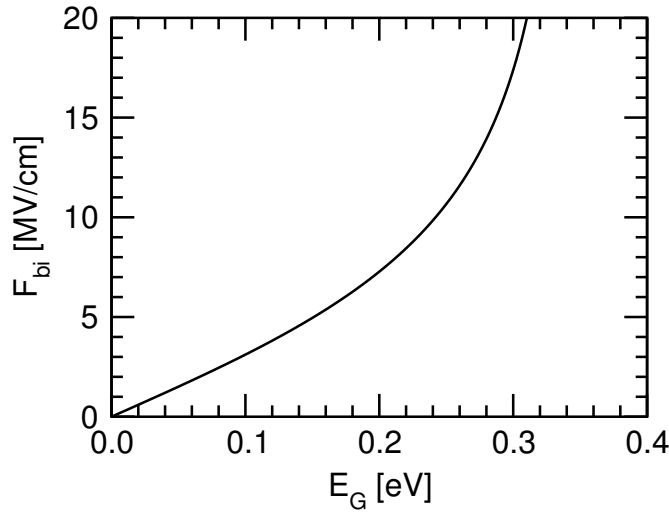


Figure 3.16: Electric field  $F_{bi}$  between the two layers of a GBL as a function of the induced energy gap  $E_G$  calculated using Eq.3.47.

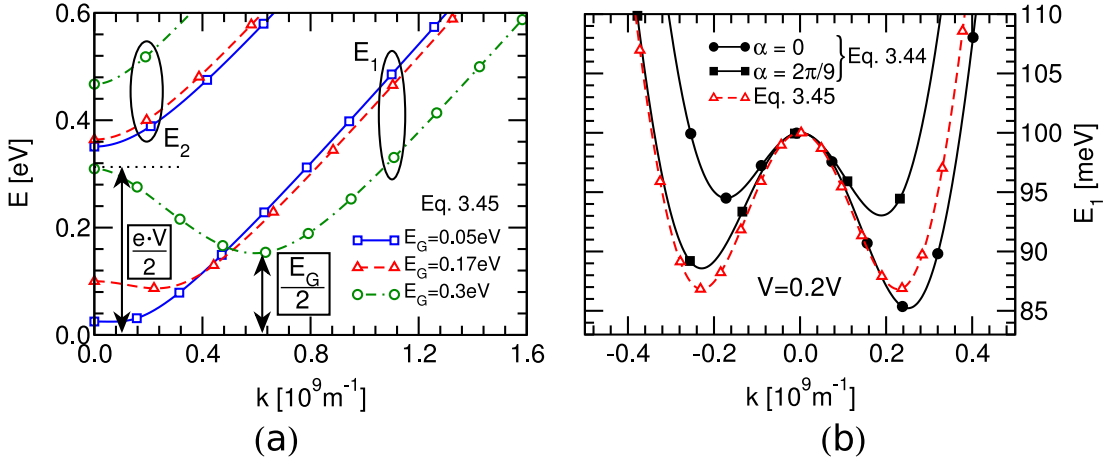


Figure 3.17: (a) Profiles of the energy dispersion relations  $E_1$  and  $E_2$  of the graphene bilayer according to the simplified Hamiltonian of Eq.3.45 for different energy gaps  $E_G$  controlled by the applied voltage  $V$ . The mid-gap is taken as the reference for the energy. (b) Comparison between the bottom of the conduction bands calculated by the Hamiltonian reported in Eq.3.44 and the simplified Hamiltonian of Eq.3.45.

As can be seen,  $k_{min}$  differs from zero, thus leading to a non monotonic conduction band. This peculiar conformation of the bandstructure, called *Mexican hat* shape, is not common in the materials studied in electronics and results in a group velocity  $v_g = \frac{1}{\hbar} \frac{\partial E}{\partial k}$  that can assume negative values for positive  $k$ , as can be easily seen in Fig.3.18. Moreover, as sketched in Fig.3.19, all the energies  $E_i$  between  $E_{cr}$  and  $E_{min}$  correspond to two different wave-vectors,  $k_{i,l}$  and  $k_{i,r}$ . Hence, it is impossible to define the inverse function of the energy dispersion relation of bilayer graphene; this limitation has a strong impact on the calculation of the DOS (see Sec.3.4.2) and of the scattering rates (see Sec.3.4.3). In Chap.5 we will give a hint on how this non-monotonic energy relation has been handled into a Monte Carlo solver of the Boltzmann Transport Equation in bilayer graphene.

Finally, the eigenvectors close to the bottom of the conduction band obtained by the solution

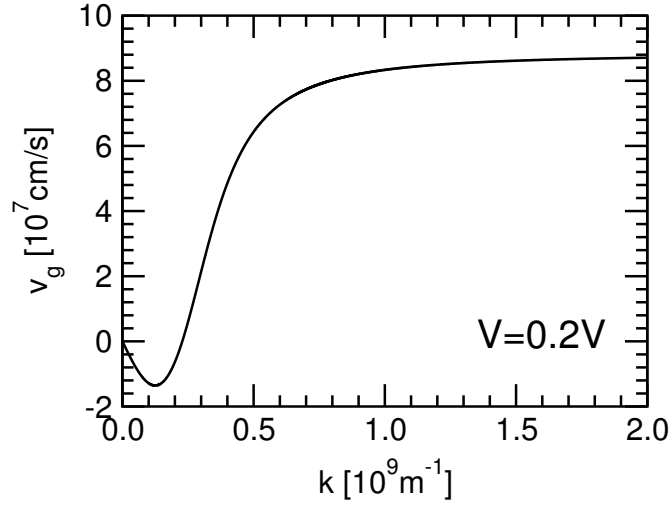


Figure 3.18: GBL group velocity  $v_g$  calculated using the isotropic energy dispersion relation of Eq.3.46 as a function of the modulus of the wave-vector  $k$  for  $V = 0.2V$ .

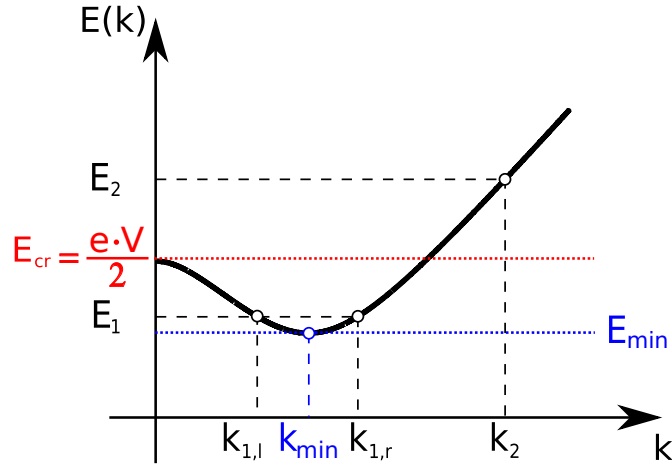


Figure 3.19: Sketch of the isotropic non monotonic energy dispersion given by Eq.3.45: all the energies  $E_i$  below  $E_{cr}$  correspond to two wave-vectors, here indicated with  $k_{i,l}$  and  $k_{i,r}$ .

of Eq.3.45 are expressed by [44]:

$$\Psi_{\mathbf{k}} = \frac{1}{C} \begin{pmatrix} [e\frac{V}{2} - E_1(k)] [(E_1(k) + e\frac{V}{2})^2 - (\hbar v_f k)^2] \\ -\hbar v_f k \exp(-i\theta) [(E_1(k) + e\frac{V}{2})^2 - (\hbar v_f k)^2]^2 \\ t_{\perp} [(e\frac{V}{2})^2 - (E_1(k))^2] \\ t_{\perp} \hbar v_f k \exp(i\theta) [e\frac{V}{2} - E_1(k)] \end{pmatrix} \quad (3.49)$$

with  $\mathbf{k} = (k, \theta)$  and

$$C^2 = \left[ \left( E_1(k) + e\frac{V}{2} \right)^2 - (\hbar v_f k)^2 \right]^2 \left[ \left( E_1(k) - e\frac{V}{2} \right)^2 + (\hbar v_f k)^2 \right] + t_{\perp}^2 \left( E_1(k) - e\frac{V}{2} \right)^2 \left[ \left( E_1(k) + e\frac{V}{2} \right)^2 + (\hbar v_f k)^2 \right] \quad (3.50)$$

### 3.4.2 Density of states

Let us consider the anisotropic energy dispersion relation obtained from the complete Hamiltonian reported in Eq.3.44. It is possible to write [6]:

$$DOS(E') = \frac{n_v n_s}{(2\pi)^2} \int_{\mathbf{k}} d\mathbf{k} \delta(E' - E(\mathbf{k})) \quad (3.51)$$

where, similarly to monolayer graphene,  $n_v = 2$ . By using polar coordinates  $(k, \theta)$  and a change of variable, we obtain:

$$DOS(E') = \frac{n_v n_s}{(2\pi)^2} \int_0^{2\pi} d\theta \left[ \int_{E_{cr}}^{E_{min}} k(E, \theta) \frac{1}{\frac{dE}{dk}} \delta(E' - E(\theta)) dE + \int_{E_{min}}^{\infty} k(E, \theta) \frac{1}{\frac{dE}{dk}} \delta(E' - E(\theta)) dE \right], \quad (3.52)$$

where  $E_{cr}$  and  $E_{min}$  are defined in Fig.3.19. Thanks to the Dirac function  $\delta$  we can write

$$DOS(E') = \frac{n_v n_s}{(2\pi)^2} \int_0^{2\pi} \sum_{k': E(k', \theta) = E'} k' \frac{1}{\left| \frac{dE}{dk} \right|_{(k', \theta)}} d\theta. \quad (3.53)$$

If we consider the simplified isotropic energy relation reported in Eq.3.46, we obtain:

$$DOS(E') = \frac{n_v n_s}{2\pi} \sum_{k': E(k') = E'} k' \frac{1}{\left| \frac{dE}{dk} \right|_{k'}}. \quad (3.54)$$

As a direct consequence of the Mexican hat shape of the energy relation, there are two different wave-vectors that contribute to the total DOS for all the energies between  $E_{cr}$  and  $E_{min}$  (see Fig.3.19). Fig.3.20 shows the GBL DOS calculated with Eq.3.54 for different energy gaps: as it can be seen, the DOS tends to infinite at  $E_{min}$  (indeed, at the bottom of the band the derivative of the energy dispersion is equal to zero) and has a discontinuity at  $E_{cr}$ .

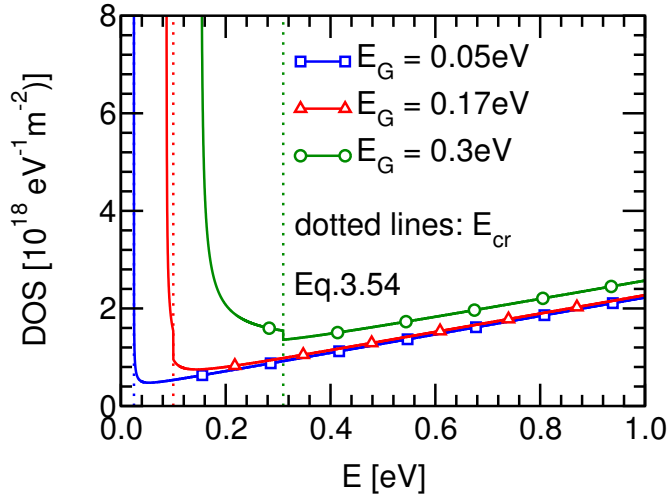


Figure 3.20: GBL DOS as a function of the energy for different energy gaps calculated using Eq.3.54, that has been obtained by employing the isotropic energy dispersion relation of Eq.3.46. Each dotted line represents the  $E_{cr} = e(V/2)$  associated to the considered  $E_G$ .

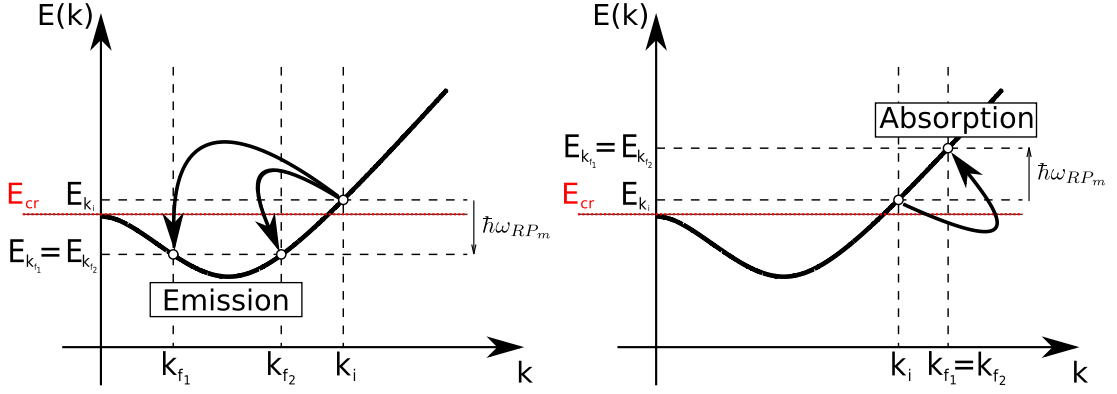


Figure 3.21: The non-monotonic behavior of the energy dispersion relation implies that all the energies smaller than  $E_{cr} = eV/2$  correspond to two possible values of the wave vector  $k$ . In the figure on the left, a phonon emission brings an electron from an initial state with the wave vector  $k_i$  to two different possible final states characterized by the wave vectors  $k_{f1}$  and  $k_{f2}$ . In contrary, a phonon absorption brings the electron to a final energy that corresponds only to a single wave-vector (see the figure on the right).

### 3.4.3 Scattering mechanisms

We have adapted the expressions obtained for the monolayer graphene scattering rates presented in Sec.3.2.4 to bilayer graphene, i.e.:

$$S_{AP}(\mathbf{k}_i, \mathbf{k}_f) = \frac{2\pi K_B T D_{ac}^2}{\rho_{GBL} A \hbar v_s^2} |F_{\mathbf{k}_i, \mathbf{k}_f}|^2 \delta[E(\mathbf{k}_i) - E(\mathbf{k}_f)], \quad (3.55)$$

$$S_{OP}(\mathbf{k}_i, \mathbf{k}_f) = \frac{\pi D_{op}^2}{\omega_{OP} \rho_{GBL} A} |F_{\mathbf{k}_i, \mathbf{k}_f}|^2 \left( n_{op} + \frac{1}{2} \mp \frac{1}{2} \right) \delta[E(\mathbf{k}_i) - E(\mathbf{k}_f) \pm \hbar\omega_{OP}], \quad (3.56)$$

and

$$S_{RP_m}(\mathbf{k}_i, \mathbf{k}_f) = \frac{2\pi}{\hbar A} |F_{\mathbf{k}_i, \mathbf{k}_f}|^2 e^2 \left( n_{RP_m} + \frac{1}{2} \mp \frac{1}{2} \right) \frac{\hbar\omega_{RP_m}}{2q\hat{\epsilon}_m} \exp(-2qd) \delta[E(\mathbf{k}_i) - E(\mathbf{k}_f) \pm \hbar\omega_{RP_m}]. \quad (3.57)$$

Note that in Eqs.3.55 and 3.56 we have used the density of bilayer graphene  $\rho_{GBL}$ , that is twice the density of monolayer graphene  $\rho$  used in Eqs.3.20 and 3.21. Moreover, in all the expressions the spinor-overlaps have been calculated by employing the eigenvectors stemming from the considered GBL Hamiltonian (reported in Eqs.3.44 and 3.45). All the other parameters are the same as defined in Sec.3.2.4.

The non-monotonic behavior of the GBL energy dispersion relation has an impact on the calculation of the total scattering rates. Let us consider for example the expression of the total scattering rate related to remote phonons, that can be obtained from Eq.3.57 just by summing together the scattering rates related to all the possible final states  $\mathbf{k}_f$ . If we consider for simplicity the isotropic energy dispersion relation reported in Eq.3.46, the total scattering rate is expressed by

$$S_{RP_m}(\mathbf{k}_i) = \frac{1}{\pi\hbar} \sum_{k_f: E(k_f)=E(k_i)+\hbar\omega_{RP_m}} k_f \left| \frac{1}{dE} \right|_{k_f} \int_0^\pi |F_{\mathbf{k}_i, \mathbf{k}_f}|^2 S_{\phi_S \phi_S}(q) d\theta \quad (3.58)$$

where

$$S_{\phi_S \phi_S}(q) = e^2 \left( n_{RP_m} + \frac{1}{2} \mp \frac{1}{2} \right) \frac{\hbar\omega_{RP_m}}{2q} \frac{1}{\hat{\epsilon}_m} e^{-2qd}, \quad (3.59)$$

$q$  is the magnitude of the exchanged wave-vector (see Sec.3.2.4) and the upper and lower signs stand for absorption and emission, respectively. It should be noted that in Eq.3.58 we have a sum over the possible values of  $k_f$ , namely over the  $k_f$  values identified by the energy after the scattering  $E_f = E(k_i) \pm \hbar\omega_{RP_m}$ . In fact, as illustrated in Fig.3.21, depending on  $E_f$  we can have either one or two corresponding  $k_f$  values, both of which contribute to the scattering rate of the initial state.

### 3.5 Conclusions

In this chapter we have reviewed the band structure, the density of states, and the scattering mechanisms considered in the PhD work for both monolayer and bilayer graphene. Moreover, we have presented two models for the simulation of the main generation/recombination mechanisms in monolayer graphene, the band to band tunneling generation/recombination and the recombination assisted by phonons. The inclusion of these phenomena in the simulation of graphene based transistors is crucial because they are the responsible of the ambipolar behavior and the consequent very poor  $I_{on}/I_{off}$  ratio and current saturation of these devices.

# Bibliography

- [1] J. Nilsson, A. H. Castro Neto, F. Guinea, and N. M. R. Peres, “Electronic properties of bilayer and multilayer graphene,” *Phys. Rev. B*, vol. 78, p. 045405, Jul 2008.
- [2] M. Bresciani, P. Palestri, D. Esseni, and L. Selmi, “Simple and efficient modeling of the e-k relationship and low-field mobility in graphene nano-ribbons,” *Solid-State Electronics*, vol. 54, no. 9, pp. 1015 – 1021, 2010.
- [3] A. Geim, “Graphene update,” *Bulletin of the American Physical Society*, vol. 55, 2010.
- [4] A. H. Castro Neto, F. Guinea, N. M. R. Peres, K. S. Novoselov, and A. K. Geim, “The electronic properties of graphene,” *Rev. Mod. Phys.*, vol. 81, pp. 109–162, Jan 2009.
- [5] T. Fang, A. Konar, H. Xing, and D. Jena, “Carrier statistics and quantum capacitance of graphene sheets and ribbons,” *Applied Physics Letters*, vol. 91, no. 9, p. 092109, 2007.
- [6] D. Esseni, P. Palestri, and L. Selmi, *Nanoscale MOS Transistors*. Cambridge University Press, 2011.
- [7] S. Vaziri, A. Smith, C. Henkel, M. Ostling, M. Lemme, G. Lupina, G. Lippert, J. Dabrowski, and W. Mehr, “An integration approach for graphene double-gate transistors,” in *Solid-State Device Research Conference (ESSDERC), 2012 Proceedings of the European*, sept. 2012, pp. 250 –253.
- [8] J.-H. Chen, C. Jang, S. Adam, M. S. Fuhrer, E. D. Williams, and M. Ishigami, “Charged-impurity scattering in graphene,” *Nat Phys*, vol. 4, no. 5, pp. 377–381, May 2008.
- [9] P. Neugebauer, M. Orlita, C. Faugeras, A.-L. Barra, and M. Potemski, “How Perfect Can Graphene Be?” *Phys. Rev. Lett.*, vol. 103, no. 13, p. 136403, Sep 2009.
- [10] M. Bresciani, A. Paussa, P. Palestri, D. Esseni, and L. Selmi, “Low-Field Mobility and High-Field Drift Velocity in Graphene Nanoribbons and Graphene Bilayers,” in *Electron Devices Meeting (IEDM), 2010 IEEE International*, dec. 2010, pp. 724 –727.
- [11] J. L. Mañes, “Symmetry-based approach to electron-phonon interactions in graphene,” *Phys. Rev. B*, vol. 76, no. 4, p. 045430, Jul 2007.
- [12] E. Mariani and F. von Oppen, “Temperature-dependent resistivity of suspended graphene,” *Phys. Rev. B*, vol. 82, no. 19, p. 195403, Nov 2010.
- [13] H. Ochoa, E. V. Castro, M. I. Katsnelson, and F. Guinea, “Temperature-dependent resistivity in bilayer graphene due to flexural phonons,” *Phys. Rev. B*, vol. 83, p. 235416, Jun 2011.
- [14] R. Shishir, F. Chen, J. Xia, N. Tao, and D. Ferry, “Room temperature carrier transport in graphene,” *Journal of Computational Electronics*, vol. 8, no. 2, pp. 43–50, June 2009.

- [15] D. Finkenstadt, G. Pennington, and M. J. Mehl, "From graphene to graphite: A general tight-binding approach for nanoribbon carrier transport," *Phys. Rev. B*, vol. 76, p. 121405, Sep 2007.
- [16] G. Pennington and N. Goldsman, "Low-field semiclassical carrier transport in semiconducting carbon nanotubes," *Phys. Rev. B*, vol. 71, p. 205318, May 2005.
- [17] Y. Ouyang, Y. Yoon, and J. Guo, "Scaling Behaviors of Graphene Nanoribbon FETs: A Three-Dimensional Quantum Simulation Study," *Electron Devices, IEEE Transactions on*, vol. 54, no. 9, pp. 2223–2231, sept. 2007.
- [18] S. Fratini and F. Guinea, "Substrate-limited electron dynamics in graphene," *Physical Review B (Condensed Matter and Materials Physics)*, vol. 77, no. 19, p. 195415, 2008.
- [19] M. Fischetti, D. Neumayer, and E. Cartier, "Effective electron mobility in Si inversion layers in metal-oxide-semiconductor systems with a high-k insulator: The role of remote phonon scattering," *Journal of applied physics*, vol. 90, no. 9, pp. 4587–4608, 2001.
- [20] F. Rana, J. H. Strait, H. Wang, and C. Manolatos, "Ultrafast carrier recombination and generation rates for plasmon emission and absorption in graphene," *Phys. Rev. B*, vol. 84, p. 045437, Jul 2011.
- [21] E. H. Hwang and S. Das Sarma, "Dielectric function, screening, and plasmons in two-dimensional graphene," *Phys. Rev. B*, vol. 75, p. 205418, May 2007.
- [22] P. Toniutti, P. Palestri, D. Esseni, F. Driussi, M. D. Michielis, and L. Selmi, "On the origin of the mobility reduction in n- and p-metal-oxide-semiconductor field effect transistors with hafnium-based/metal gate stacks," *Journal of Applied Physics*, vol. 112, no. 3, p. 034502, 2012.
- [23] A. Betti, G. Fiori, and G. Iannaccone, "Strong mobility degradation in ideal graphene nanoribbons due to phonon scattering," *Applied Physics Letters*, vol. 98, no. 21, p. 212111, 2011.
- [24] A. Konar, T. Fang, and D. Jena, "Effect of high- $\kappa$  gate dielectrics on charge transport in graphene-based field effect transistors," *Phys. Rev. B*, vol. 82, p. 115452, Sep 2010.
- [25] A. Paussa, M. Geromel, P. Palestri, M. Bresciani, D. Esseni, and L. Selmi, "Simulation of Graphene Nanoscale RF Transistors Including Scattering and Generation/Recombination Mechanisms," in *Electron Devices Meeting (IEDM), 2011 IEEE International*, dec. 2011, pp. 271–274.
- [26] L. M. Zhang and M. M. Fogler, "Nonlinear Screening and Ballistic Transport in a Graphene  $p$ - $n$  Junction," *Phys. Rev. Lett.*, vol. 100, p. 116804, Mar 2008.
- [27] V. V. Cheianov and V. I. Fal'ko, "Selective Transmission of Dirac Electrons and Ballistic Magnetoresistance of  $n$ - $p$  Junctions in Graphene," *Phys. Rev. B*, vol. 74, p. 041403, Jul 2006.
- [28] G. Fiori; G. Iannaccone (2009), "NanoTCAD ViDES," <http://nanohub.org/resources/vides>. (doi:10254/nanohub-r5116.5).
- [29] M. I. Katsnelson, K. S. Novoselov, and A. K. Geim, "Chiral tunnelling and the Klein paradox in graphene," *Nature Physics*, vol. 2, no. 9, pp. 620–625, Sep. 2006.
- [30] T. Low, S. Hong, J. Appenzeller, S. Datta, and M. Lundstrom, "Conductance Asymmetry of Graphene  $p$ - $n$  Junction," *Electron Devices, IEEE Transactions on*, vol. 56, no. 6, pp. 1292–1299, june 2009.

- [31] J. David, L. Register, and S. Banerjee, “Semiclassical Monte Carlo Analysis of Graphene FETs,” *Electron Devices, IEEE Transactions on*, vol. 59, no. 4, pp. 976–982, april 2012.
- [32] F. Rana, P. A. George, J. H. Strait, J. Dawlaty, S. Shivaraman, M. Chandrashekar, and M. G. Spencer, “Carrier recombination and generation rates for intravalley and intervalley phonon scattering in graphene,” *Phys. Rev. B*, vol. 79, p. 115447, Mar 2009.
- [33] S. Das and J. Appenzeller, “On the Importance of Bandgap Formation in Graphene for Analog Device Applications,” *Nanotechnology, IEEE Transactions on*, vol. 10, no. 5, pp. 1093–1098, sept. 2011.
- [34] P. Gava, M. Lazzeri, A. M. Saitta, and F. Mauri, “Ab initio study of gap opening and screening effects in gated bilayer graphene,” *Phys. Rev. B*, vol. 79, no. 16, p. 165431, Apr 2009.
- [35] E. McCann, “Asymmetry gap in the electronic band structure of bilayer graphene,” *Phys. Rev. B*, vol. 74, no. 16, p. 161403, Oct 2006.
- [36] J. B. Oostinga, H. B. Heersche, X. Liu, A. F. Morpurgo, and L. M. K. Vandersypen, “Gate-induced insulating state in bilayer graphene devices,” *Nature Materials*, vol. 7, no. 2, pp. 151–157, 2007.
- [37] Y. Zhang, T.-T. Tang, C. Girit, Z. Hao, M. C. Martin, A. Zettl, M. F. Crommie, Y. R. Shen, and F. Wang, “Direct observation of a widely tunable bandgap in bilayer graphene,” *Nature*, vol. 459, no. 7248, pp. 820–823, 2009.
- [38] F. Xia, D. B. Farmer, Y.-m. Lin, and P. Avouris, “Graphene Field-Effect Transistors with High On/Off Current Ratio and Large Transport Band Gap at Room Temperature,” *Nano Letters*, vol. 10, no. 2, pp. 715–718, 2010, pMID: 20092332.
- [39] L. Jing, J. Velasco Jr., P. Kratz, G. Liu, W. Bao, M. Bockrath, and C. N. Lau, “Quantum Transport and Field-Induced Insulating States in Bilayer Graphene pnp Junctions,” *Nano Letters*, vol. 10, no. 10, pp. 4000–4004, 2010.
- [40] T. Taychatanapat and P. Jarillo-Herrero, “Electronic Transport in Dual-Gated Bilayer Graphene at Large Displacement Fields,” *Phys. Rev. Lett.*, vol. 105, p. 166601, Oct 2010.
- [41] B. N. Szafranek, D. Schall, M. Otto, D. Neumaier, and H. Kurz, “Electrical observation of a tunable band gap in bilayer graphene nanoribbons at room temperature,” *Applied Physics Letters*, vol. 96, no. 11, p. 112103, 2010.
- [42] —, “High On/Off Ratios in Bilayer Graphene Field Effect Transistors Realized by Surface Dopants,” *Nano Letters*, vol. 11, no. 7, pp. 2640–2643, 2011.
- [43] B. N. Szafranek, G. Fiori, D. Schall, D. Neumaier, and H. Kurz, “Current Saturation and Voltage Gain in Bilayer Graphene Field Effect Transistors,” *Nano Letters*, vol. 12, no. 3, pp. 1324–1328, 2012.
- [44] L. A. Falkovsky, “Screening in gated bilayer graphene,” *Phys. Rev. B*, vol. 80, no. 11, p. 113413, Sep 2009.



## Chapter 4

# Linearization of the Boltzmann Transport Equation for the Calculation of the Low Field Mobility

## 4.1 Introduction

**T**HE low field mobility is a very important transport property for a large number of physical systems and electron devices with different carrier dimensionality. In particular, for MOS transistors mobility has been studied starting from the first fabricated samples [1] to the most advanced and recent nanoscale CMOS technologies [2]. This is justified by the fact that a correlation exists between the low field mobility of long devices and the  $I_{DS}$  of nanoscale MOSFETs, as predicted by simple flux-theory arguments [3], observed in numerical simulations [4, 5, 6, 7], and confirmed by experimental data [8, 9, 10, 11].

The low field mobility is an equilibrium property for the carrier gas, in fact it is defined for a vanishing small electron field. Hence, even if a general purpose approach to solve the Boltzmann transport equation (BTE) (e.g. the Monte Carlo method) can be used to calculate the mobility, a linearized BTE (LBTE) is also adequate to calculate the mobility exactly, provided that both the formulation and the solution of the LBTE involves no simplifying assumptions. Although the linearization of the BTE and its formulation in terms of momentum relaxation time (MRT) is a topic studied since a very long time [12, 13, 14], new approaches to tackle the problem have been proposed and discussed until very recently [15, 16], and, furthermore, the LBTE is still today practically employed by introducing quite drastic simplifications [17], whose impact on the final results is difficult to estimate *a priori*.

As a matter of fact not so many efforts have been devoted to develop a general method for the solution of the LBTE, while several contributions tackled special cases of practical interest dealing with circular or elliptic parabolic bands (possibly featuring non parabolic corrections) [18, 19, 20, 15]. For complex, anisotropic band-structures, as those occurring, for example, in hole inversion layers, the LBTE has been always solved by using simplifying assumptions [21, 22, 23, 24, 25, 26].

This chapter revisits the problem of the LBTE and we argue that since the scattering rates in the *kernel* of the integral equation include Dirac functions enforcing the energy conservation, then for the numerical solution of the LBTE it is convenient to use an energy driven discretization of the wave-vector. By using such a discretization approach the LBTE can be cast in the form of a linear algebraic problem, that allows for a robust and numerically efficient solution of the equation with no *a priori* simplifying assumptions. The exact solution of the LBTE is applied to the case of a bilayer graphene sheet and then used to critically analyze the possible errors stemming from the simplifications most often embraced in the mobility calculations, such as the Matthiessen's rule typically used to calculate the total momentum relaxation time in terms of the relaxation time of the single scattering mechanism. Our numerical results also show that, for a non monotonic energy relation, the momentum relaxation time can legitimately take negative values, and that this seemingly puzzling result has no unphysical implications.

The chapter is organized as follows. In Sec.4.2 we present a concise derivation of the LBTE and of its formulation in terms of the momentum relaxation time. Sec.4.3 introduces the energy driven discretization scheme for the solution of the LBTE and discusses some relevant simplifications for the case of isotropic bands and isotropic scattering rates. In Sec.4.4 we present the results for the numerical solution of the LBTE and the corresponding mobility calculations for a graphene bilayer and in Sec.4.5 we draw the conclusions of the chapter.

## 4.2 Linearization of the BTE

We hereafter discuss the linearization of the BTE for a 2D carrier gas, which is representative of the inversion layer in an MOS transistor and also of the carrier gas in a relatively wide mono-layer or bilayer graphene sheet. An electronic state is thus identified by  $(i, \mathbf{k})$  (except for spin), where  $i$  is the subband index and  $\mathbf{k}=(k_x, k_y)$  is the wave-vector. The application of the treatment discussed in this section to a 3D or a 1D carrier gas is conceptually straightforward.

Let us denote with  $x$  the transport direction and with  $F_x$  an arbitrarily small component of the electric field along  $x$ . Without any loss of generality we can write the out of equilibrium occupation function  $f_i(\mathbf{k})$  for the subband  $i$  as

$$f_i(\mathbf{k}) = f_0(E_i(\mathbf{k})) \mp eF_x g_i(\mathbf{k}) \quad (4.1)$$

where  $E_i(\mathbf{k})$  is the energy for state  $(i, \mathbf{k})$ ,  $f_0(E)$  is the equilibrium Fermi-Dirac occupation function and  $e$  is the positive electron charge. The minus sign applies to electrons and the plus sign to holes. Eq.4.1 is an implicit definition of the function  $g_i(\mathbf{k})$ , which is the *unknown* function of the LBTE problem.

For a constant electric field  $F_x$  along the  $x$  direction the steady state BTE can be written as [27, 28]

$$\mp eF_x \frac{\partial}{\hbar \partial k_x} f_i(\mathbf{k}) = S_{in,i} - S_{out,i} \quad (4.2)$$

where  $S_{in,i}$  and  $S_{out,i}$  are respectively the in and out scattering integrals for the subband  $i$ , whose form will be discussed below.

From Eq.4.1 we have

$$\frac{\partial}{\partial k_x} f_i(\mathbf{k}) = \hbar v_{x,i}(\mathbf{k}) \frac{\partial f_0(E_i(\mathbf{k}))}{\partial E} \mp eF_x \frac{\partial}{\partial k_x} g_i(\mathbf{k}) \quad (4.3)$$

where  $v_{x,i}$  is the  $x$  component of the group velocity in the subband  $i$ . We now observe that we are here interested to the occupation function of the states  $(i, \mathbf{k})$  having a non null velocity component  $v_{x,i}(\mathbf{k})$ , in fact the states with a null  $v_{x,i}(\mathbf{k})$  do not contribute to the current (see also Sec.4.2.2). For a non null  $v_{x,i}(\mathbf{k})$  the second term in Eq.4.3 is negligible with respect to the first one for a small enough  $F_x$ , hence from Eqs.4.2 and 4.3 we have

$$\mp eF_x v_{x,i}(\mathbf{k}) \frac{\partial f_0(E_i(\mathbf{k}))}{\partial E} = S_{in,i} - S_{out,i} . \quad (4.4)$$

The scattering integral in the r.h.s. of Eq.4.4 has the well known form [27, 28]

$$S_{in,i} - S_{out,i} = \sum_{j, \mathbf{k}'} f_j(\mathbf{k}') S_{j,i}(\mathbf{k}', \mathbf{k}) [1 - f_i(\mathbf{k})] - f_i(\mathbf{k}) \sum_{j, \mathbf{k}'} S_{i,j}(\mathbf{k}, \mathbf{k}') [1 - f_j(\mathbf{k}')] \quad (4.5)$$

where  $S_{i,j}(\mathbf{k}, \mathbf{k}')$  is the total scattering rate from state  $(i, \mathbf{k})$  to state  $(j, \mathbf{k}')$  and  $[S_{in,i} - S_{out,i}]$  evaluates to zero when the occupation is given by the equilibrium Fermi-Dirac function. At the equilibrium, moreover, not only the sum over  $(j, \mathbf{k}')$  in the r.h.s. of Eq.4.5 is null, but every single term in this sum is null, which represents the so called detailed balance

$$f_0(E_j(\mathbf{k}')) S_{j,i}(\mathbf{k}', \mathbf{k}) [1 - f_0(E_i(\mathbf{k}))] = f_0(E_i(\mathbf{k})) S_{i,j}(\mathbf{k}, \mathbf{k}') [1 - f_0(E_j(\mathbf{k}'))] . \quad (4.6)$$

If we now introduce Eq.4.1 in Eq.4.5, keep only the first order terms with respect to  $F_x$ , cancel out the terms containing only the equilibrium occupation function and then use Eq.4.6 to express  $S_{j,i}(\mathbf{k}', \mathbf{k})$  in terms of  $S_{i,j}(\mathbf{k}, \mathbf{k}')$ , the scattering integral can be finally rewritten in the form [28]

$$S_{in,i} - S_{out,i} = (\mp eF_x) \sum_{j, \mathbf{k}'} S_{i,j}(\mathbf{k}, \mathbf{k}') \left[ g_j(\mathbf{k}') \frac{f_0(E_i(\mathbf{k}))}{f_0(E_j(\mathbf{k}'))} - g_i(\mathbf{k}) \frac{1 - f_0(E_j(\mathbf{k}'))}{1 - f_0(E_i(\mathbf{k}))} \right] \quad (4.7)$$

We now substitute Eq.4.7 in Eq.4.4 and exploit the well know identity

$$\frac{\partial f_0(E)}{\partial E} = - \frac{f_0(E) [1 - f_0(E)]}{K_B T} \quad (4.8)$$

where  $K_B$  is the Boltzmann constant and  $T$  is the absolute temperature, so that the LBTE can be finally written as

$$v_{x,i}(\mathbf{k})f_0(E_i(\mathbf{k})) [1 - f_0(E_i(\mathbf{k}))] = K_B T \sum_{j,\mathbf{k}'} S_{i,j}(\mathbf{k}, \mathbf{k}') \left[ g_i(\mathbf{k}) \frac{1 - f_0(E_j(\mathbf{k}'))}{1 - f_0(E_i(\mathbf{k}))} - g_j(\mathbf{k}') \frac{f_0(E_i(\mathbf{k}))}{f_0(E_j(\mathbf{k}'))} \right]. \quad (4.9)$$

When the appropriate expressions for the scattering rates are inserted in Eq.4.9 and the sum over  $\mathbf{k}'$  is converted to an integral over  $\mathbf{k}'$  according to the standard prescriptions [28] Eq.4.9 takes the form of a linear integral equation for the unknown functions  $g_i(\mathbf{k})$ .

#### 4.2.1 Formulation based on the momentum relaxation time

The LBTE is very frequently cast in a form where the unknown function is a MRT. Such a formulation is readily obtained by introducing the MRT  $\tau_i(\mathbf{k})$  as

$$g_i(\mathbf{k}) = -\tau_i(\mathbf{k}) v_{x,i}(\mathbf{k}) \frac{\partial f_0(E_i(\mathbf{k}))}{\partial E} = \frac{\tau_i(\mathbf{k}) v_{x,i}(\mathbf{k})}{K_B T} f_0(E_i(\mathbf{k})) [1 - f_0(E_i(\mathbf{k}))]. \quad (4.10)$$

When Eq.4.10 is introduced in Eq.4.9 we obtain

$$v_{x,i}(\mathbf{k}) = \sum_{j,\mathbf{k}'} S_{i,j}(\mathbf{k}, \mathbf{k}') \left[ \frac{1 - f_0(E_j(\mathbf{k}'))}{1 - f_0(E_i(\mathbf{k}))} \right] [\tau_i(\mathbf{k}) v_{x,i}(\mathbf{k}) - \tau_j(\mathbf{k}') v_{x,j}(\mathbf{k}')] \quad (4.11)$$

which is equivalent to Eq.4.9 and corresponds to the LBTE written in terms of the momentum relaxation time  $\tau_i(\mathbf{k})$ .

In the r.h.s. of Eq.4.11 the term  $[\tau_i(\mathbf{k}) v_{x,i}(\mathbf{k})]$  is independent of  $(j, \mathbf{k}')$ , hence both sides of Eq.4.11 may be divided by  $[\tau_i(\mathbf{k}) v_{x,i}(\mathbf{k})]$ , to reach the most frequently quoted form of the MRT problem [29, 21, 30, 28]

$$\frac{1}{\tau_i(\mathbf{k})} = \sum_{j,\mathbf{k}'} S_{i,j}(\mathbf{k}, \mathbf{k}') \left[ \frac{1 - f_0(E_j(\mathbf{k}'))}{1 - f_0(E_i(\mathbf{k}))} \right] \left[ 1 - \frac{\tau_j(\mathbf{k}') v_{x,j}(\mathbf{k}')}{\tau_i(\mathbf{k}) v_{x,i}(\mathbf{k})} \right]. \quad (4.12)$$

#### 4.2.2 Mobility calculation

The calculation of the mobility is quite straightforward after the unknown functions of the LBTE, namely  $g_i(\mathbf{k})$  or  $\tau_i(\mathbf{k})$ , have been determined. In fact the current per unit device width can be written

$$J_{x,i} = \mp \frac{e}{A} \sum_{\mathbf{k}} v_{x,i}(\mathbf{k}) f_i(\mathbf{k}) = \mp \frac{e}{A} \sum_{\mathbf{k}} v_{x,i}(\mathbf{k}) [\mp e F_x g_i(\mathbf{k})] = \frac{e^2 F_x}{A} \sum_{\mathbf{k}} v_{x,i}(\mathbf{k}) g_i(\mathbf{k}) \quad (4.13)$$

where  $A$  is the normalization area,  $f_i(\mathbf{k})$  has been expressed as in Eq.4.1 and, furthermore, we have exploited the fact that the sum over  $\mathbf{k}$  vanishes for the term including the equilibrium Fermi-Dirac occupation function. Then the mobility can be calculated by definition as

$$\mu_{x,i} = \frac{J_{x,i}}{e N_i F_x} = \frac{e}{A N_i} \sum_{\mathbf{k}} v_{x,i}(\mathbf{k}) g_i(\mathbf{k}) = \frac{e}{A N_i} \sum_{\mathbf{k}} v_{x,i}^2(\mathbf{k}) \tau_i(\mathbf{k}) \left| \frac{df_0(E)}{dE} \right|. \quad (4.14)$$

Eq.4.14 gives  $\mu_{x,i}$  in terms of either  $g_i(\mathbf{k})$  or  $\tau_i(\mathbf{k})$  to reiterate that it is conceptually equivalent to solve the LBTE using any of the two unknown functions.

### 4.3 Numerically efficient solution of the linearized BTE

This broad section deals with the numerical solution of the LBTE. Sec.4.3.1 presents a methodology valid in the most general case, whereas Secs.4.3.2 and 4.3.3 address simplified cases of practical relevance. Sec.4.3.4 discusses the calculation of the relaxation time in the presence of multiple scattering mechanisms and Sec.4.3.5 reports a few summarizing remarks.

#### 4.3.1 Anisotropic bands and scattering rates

In order to tackle the solution of Eq.4.9 or, equivalently, Eq.4.11, we start by writing  $S_{i,j}(\mathbf{k}, \mathbf{k}')$  as the rate of a generic, inelastic scattering mechanism according to the Fermi's golden rule

$$S_{i,j}(\mathbf{k}, \mathbf{k}') = \frac{2\pi}{\hbar} |M_{i,j}(\mathbf{k}, \mathbf{k}')|^2 \delta[E_j(\mathbf{k}') - E_i(\mathbf{k}) \mp E_{ph}(\mathbf{q})] \quad (4.15)$$

where  $E_{ph}(\mathbf{q}) = \hbar\omega(\mathbf{q})$  is the phonon energy, possibly dependent on the phonon wave-vector  $\mathbf{q} = \pm(\mathbf{k}' - \mathbf{k})$ . The upper and lower sign correspond respectively to phonon absorption and phonon emission. Eq.4.15 is written in terms of a single scattering mechanism; we will return to the calculation of the MRT in the presence of multiple scattering mechanisms in Sec.4.3.4.

If we now convert the sum over  $\mathbf{k}'$  in Eq.4.11 to an integral and express  $S_{i,j}(\mathbf{k}, \mathbf{k}')$  with Eq.4.15, then Eq.4.11 can be re-written as

$$v_{i,x}(\mathbf{k}) \tau_i(\mathbf{k}) \left\{ \frac{1}{2\pi\hbar} \sum_j \int_{\mathbf{k}'} \Lambda_{i,j}(\mathbf{k}, \mathbf{k}') \delta[E_j(\mathbf{k}') - E_i(\mathbf{k}) \mp E_{ph}(\mathbf{q})] d\mathbf{k}' \right\} - \frac{1}{2\pi\hbar} \sum_j \int_{\mathbf{k}'} \Lambda_{i,j}(\mathbf{k}, \mathbf{k}') v_{j,x}(\mathbf{k}') \tau_j(\mathbf{k}') \delta[E_j(\mathbf{k}') - E_i(\mathbf{k}) \mp E_{ph}(\mathbf{q})] d\mathbf{k}' = v_{i,x}(\mathbf{k}) \quad (4.16)$$

where, for convenience of notation, we have introduced the quantity

$$\Lambda_{i,j}(\mathbf{k}, \mathbf{k}') = |M_{i,j}(\mathbf{k}, \mathbf{k}')|^2 \left[ \frac{1 - f_0(E_j(\mathbf{k}'))}{1 - f_0(E_i(\mathbf{k}))} \right]. \quad (4.17)$$

We first make a merely mathematical passage and change the integration variables first by writing the wave-vector in polar coordinates  $\mathbf{k} = (k, \theta)$ , and then by further changing, for any given subband  $i$  and direction  $\theta$ , the integration variable from the magnitude  $k$  of the wave-vector to the energy  $E_i(k, \theta)$  along the  $\theta$  direction. By doing so and if the energy dispersion relation is strictly monotonic, Eq.4.16 becomes

$$v_{i,x}(\mathbf{k}) \tau_i(\mathbf{k}) \left\{ \frac{1}{2\pi\hbar} \sum_j \int_{-\pi}^{\pi} d\theta' \int_{-\infty}^{+\infty} dE_j \Theta_{i,j}(\mathbf{k}, \mathbf{k}') \delta[E_j - E_i(\mathbf{k}) \mp E_{ph}(\mathbf{q})] \right\} - \frac{1}{2\pi\hbar} \sum_j \int_{-\pi}^{\pi} d\theta' \int_{-\infty}^{+\infty} dE_j \Theta_{i,j}(\mathbf{k}, \mathbf{k}') v_{j,x}(\mathbf{k}') \tau_j(\mathbf{k}') \delta[E_j - E_i(\mathbf{k}) \mp E_{ph}(\mathbf{q})] = v_{i,x}(\mathbf{k}) \quad (4.18)$$

where the new auxiliary quantity  $\Theta_{i,j}(\mathbf{k}, \mathbf{k}')$  is defined as

$$\Theta_{i,j}(\mathbf{k}, \mathbf{k}') = k'(E_j, \theta') \left[ \frac{dE_j(k', \theta')}{dk} \right]^{-1} |M_{i,j}(\mathbf{k}, \mathbf{k}')|^2 \left[ \frac{1 - f_0(E_j(\mathbf{k}'))}{1 - f_0(E_i(\mathbf{k}))} \right]. \quad (4.19)$$

Eq.4.18 can be generalized to non-monotonic energy dispersion relations by splitting the integral in  $\mathbf{k}'$  of Eq.4.16 in sub-integrals defined on domains in which the dispersion relation is monotonic, and then by applying the same approach shown above to each sub-domain. Eqs.4.16 and 4.18

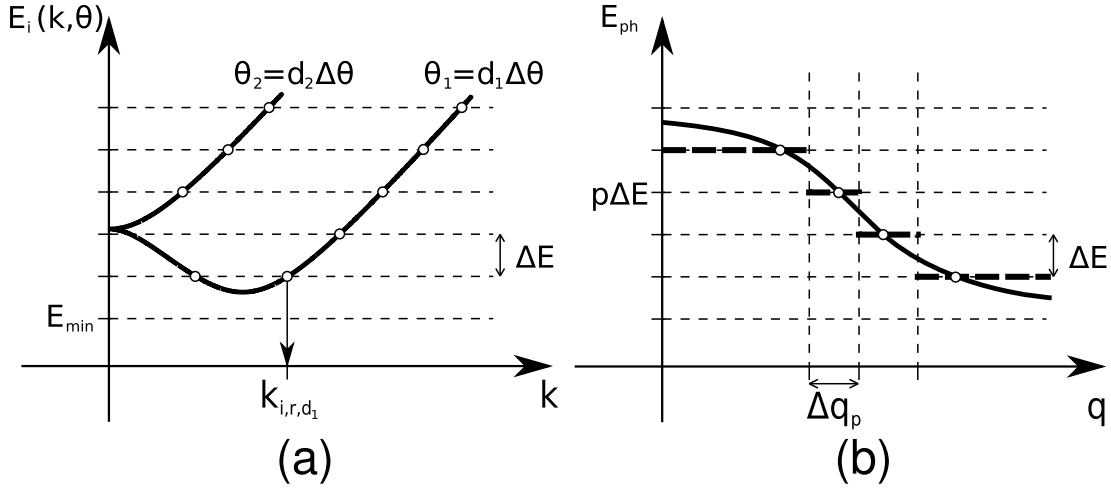


Figure 4.1: (a) Sketch of the energy driven discretization of the wave-vector for an anisotropic band-structure model.  $\Delta E$  is the energy step,  $\Delta\theta$  is the angular step and  $E_{min}$  denotes the smallest discrete energy value. The figure illustrates the discretization for a given subband  $i$  along two angular directions  $d_1\Delta\theta$  and  $d_2\Delta\theta$ . The discrete value of the wave-vector magnitude along a generic direction  $d\Delta\theta$  is denoted by the symbol  $k_{i,r,d}$ . The energy to  $k$  relation may be non monotonic, as illustrated by the direction  $\theta_1=d_1\Delta\theta$ , in which case more values of  $k_{i,r,d}$  correspond to a single energy value. (b) Energy driven discretization of the phonon wave-vector; energy  $E_{ph}(q)$  is here assumed to depend only on the magnitude  $q$  of the phonon wave-vector.  $\Delta E$  is the same energy step used also for the electron band-structure. The uniform energy discretization  $p\Delta E$  results in corresponding, non uniform intervals  $\Delta q_p$  for the magnitude  $q$  of the phonon wave-vector.

show that the linear integral equation providing  $\tau_i(\mathbf{k})$  has a kernel that consists of Dirac functions restricting the integrals over  $\mathbf{k}'$  to curves fulfilling the condition  $E_j(\mathbf{k}')=[E_i(\mathbf{k})\pm E_{ph}(\mathbf{q})]$ . In particular, in Eq.4.18 the Dirac function reduces the integral over  $E_j$  (for any given  $\theta'$ ).

In order to tackle the numerical solution of Eq.4.18, a discussion about the discretization scheme is necessary. In fact, if we use the most natural  $\mathbf{k}$  discretization consisting in taking, for instance, a uniform step in the angle  $\theta$  and a possibly non uniform step for  $k$ , then *it is impossible to satisfy exactly the constraint  $E_j(\mathbf{k}')=[E_i(\mathbf{k})\pm E_{ph}(\mathbf{q})]$  when  $\mathbf{k}$  takes only the discrete values*. It is now important to notice that if, instead, an *energy driven  $\mathbf{k}$  discretization* is employed, then Eq.4.18 can be cast in a discretized form suitable for a computationally efficient solution, and without introducing any simplifying assumption.

The basic idea is illustrated by Fig.4.1(a) showing the *energy driven discretization* of the wave-vector for an anisotropic electron energy relation. The sketch exemplifies the  $\mathbf{k}$  discretization for a generic subband  $i$ , along two angular directions  $d_1\Delta\theta$ ,  $d_2\Delta\theta$ , and for a uniform energy step  $\Delta E$  (with  $\Delta\theta$  being the step of the angular discretization). The crucial point here is that, for each subband  $i$  and discretized angular direction  $d\Delta\theta$ , the discrete values  $k_{i,r,d}$  of the wave-vector magnitude are in general different, but they correspond to one of the discrete energy values reported on the  $y$  axis of Fig.4.1(a), which are the same for all subbands and all angular directions.

The energy driven discretization of the electron wave-vector guaranties that all the discrete wave-vectors correspond to energies that differ simply by a multiple of the energy step  $\Delta E$ . The procedure is completed by the discretization of the phonon energy  $E_{ph}$ , that is illustrated in Fig.4.1(b). The discrete  $E_{ph}$  values are taken as multiple of  $\Delta E$ , and each energy bin  $p\Delta E$

identifies one interval  $\Delta q_p$  of the phonon wave-vector magnitude  $q^1$ .

By considering Figs.4.1(a) and (b) it can be understood that, if the electron and phonon energy dispersion are discretized as prescribed by these figures, then for both elastic and inelastic phonon assisted transitions the discrete  $\mathbf{k}$  values *satisfy exactly* the energy conservation constraint. This is more clearly explained by noting that for a generic discrete wave-vector  $\mathbf{k}_{i,r,d}=(k_{i,r,d},d\Delta\theta)$  identified by its magnitude  $k_{i,r,d}$  and its angle  $d\Delta\theta$ , a positive integer number  $n_{i,r,d}$  exists such that

$$E_i(\mathbf{k}_{i,r,d}) = E_{min} + n_{i,r,d} \Delta E . \quad (4.20)$$

The initial  $\mathbf{k}_{i,r,d}$  and final  $\mathbf{k}_{j,r',d'}$  wave-vectors also set  $q=|\mathbf{k}_{j,r',d'}-\mathbf{k}_{i,r,d}|$ , and the condition  $q\in\Delta q_p$  identifies in turn the interval  $\Delta q_p$  to which  $q$  belongs (see Fig.4.1(b)), that finally sets the discrete value  $p\Delta E$  of the phonon energy.

The above discussion allows us to state that, according to the energy driven discretization illustrated in Figs.4.1(a) and (b), the energy conservation for a phonon assisted transition between an initial state  $(i,\mathbf{k}_{i,r,d})$  and a final state  $(j,\mathbf{k}_{j,r',d'})$  is simply expressed as

$$[n_{j,r',d'} - n_{i,r,d} \mp p] = 0 \quad (4.21)$$

where  $p\Delta E$  is the discrete phonon energy value corresponding to the interval  $\Delta q_p$  identified by the condition  $q=|\mathbf{k}_{j,r',d'}-\mathbf{k}_{i,r,d}|\in\Delta q_p$ .

The above discussion demonstrates that, when the energy driven discretization scheme is employed, then the discrete version of Eq.4.18 takes the form

$$\begin{aligned} v_{i,x}(\mathbf{k}_{i,r,d}) & \left[ \frac{\Delta\theta}{2\pi\hbar} \sum_{j,r',d'} A_{i,r,d}^{j,r',d'} \delta_{i,r,d}^{j,r',d'} \right] \tau_{i,r,d} - \\ & - \frac{\Delta\theta}{2\pi\hbar} \sum_{j,r',d'} A_{i,r,d}^{j,r',d'} v_{j,x}(\mathbf{k}_{j,r',d'}) \delta_{i,r,d}^{j,r',d'} \tau_{j,r',d'} = v_{i,x}(\mathbf{k}_{i,r,d}) \end{aligned} \quad (4.22)$$

where the integral over  $\theta'$  in Eq.4.18 has been approximated by the sum over the index  $d'$  and with an angular step  $\Delta\theta$ , and, furthermore, we have introduced the coefficients  $A_{i,r,d}^{j,r',d'}$  defined as

$$A_{i,r,d}^{j,r',d'} = k_{j,r',d'} \left[ \frac{dE_j(\mathbf{k}_{j,r',d'})}{dk} \right]^{-1} |M_{i,j}(\mathbf{k}_{i,r,d}, \mathbf{k}_{j,r',d'})|^2 \left[ \frac{1 - f_0(E_j(\mathbf{k}_{j,r',d'}))}{1 - f_0(E_i(\mathbf{k}_{i,r,d}))} \right] . \quad (4.23)$$

Eq.4.22 is a linear algebraic system for the unknowns  $\tau_{i,r,d}$ , where the non null entries of the matrix representing the system are governed by the Kronecker symbols  $\delta_{i,r,d}^{j,r',d'}$ . The discussion leading to Eq.4.21 allows us to define  $\delta_{i,r,d}^{j,r',d'}$  as

$$\delta_{i,r,d}^{j,r',d'} \begin{cases} 1 & \text{for } [n_{j,r',d'} - n_{i,r,d} \mp p] = 0 \\ 0 & \text{otherwise} \end{cases} \quad (4.24)$$

where  $p\Delta E$  is the discrete phonon energy value corresponding to the interval  $\Delta q_p$ , with  $\Delta q_p$  such that  $q=|\mathbf{k}_{j,r',d'}-\mathbf{k}_{i,r,d}|\in\Delta q_p$ .

Eq.4.22 is a discrete version of Eq.4.18 obtained by introducing no simplifying approximations except for the discretization itself, namely the finite values of  $\Delta E$  and  $\Delta\theta$ . Thus the solution of the LBTE has been cast in the form of a linear algebraic problem.

<sup>1</sup>Fig.4.1(b) assumes for simplicity that  $E_{ph}$  depends only on the magnitude  $q$  of the phonon wave-vector and not on the  $\mathbf{q}$  direction. This is a reasonable approximation in very many practical cases and the extension to an energy  $E_{ph}$  that depends on the  $\mathbf{q}$  direction is also possible.

### 4.3.2 Isotropic scattering mechanisms

For isotropic scattering mechanisms a drastic simplification of the problem is possible and Appx.B.1 shows that  $\tau_i(\mathbf{k})$  depends on  $\mathbf{k}$  only through the energy, namely we have  $\tau_i(\mathbf{k}) = \tau_i(E_i(\mathbf{k}))$ . An explicit expression for  $\tau_i(E_i(\mathbf{k}))$  is obtained by converting the sum over  $\mathbf{k}'$  in Eq.B.4 to an integral, which leads to

$$\frac{1}{\tau_i[E_i(\mathbf{k})]} = \frac{1}{2\pi\hbar} \sum_j |M_{i,j}^{(0)}|^2 \int_{\mathbf{k}'} \left[ \frac{1 - f_0(E_j(\mathbf{k}'))}{1 - f_0(E_i(\mathbf{k}))} \right] \delta[E_j(\mathbf{k}') - E_i(\mathbf{k}) \mp \hbar\omega_0] d\mathbf{k}' \quad (4.25)$$

where  $M_{i,j}^{(0)}$  is the isotropic scattering matrix element introduced in Eq.B.1. Eq.4.25 shows that, as it is well known, for isotropic scattering mechanisms it is *not* necessary to solve any problem to determine the MRT, in fact Eq.4.25 provides an explicit expression for  $\tau_i(E_i(\mathbf{k}))$ .

### 4.3.3 Isotropic bands

Let us now consider a band-structure where the energy depends only on the magnitude  $k$  of the wave-vector, namely  $E_i(\mathbf{k}) = E_i(k)$ . We also assume that the scattering rate has a moderate anisotropy, such that it can be written as

$$S_{i,j}(\mathbf{k}, \mathbf{k}') = \frac{2\pi}{\hbar} |M_{i,j}(q)|^2 \delta[E_j(\mathbf{k}') - E_i(\mathbf{k}) \mp \hbar\omega_0] \quad (4.26)$$

where  $q = |\mathbf{k}' - \mathbf{k}|$  is the magnitude of the phonon wave-vector and the phonon energy  $\hbar\omega_0$  is independent of  $\mathbf{q}$ .

Circular parabolic bands are isotropic, for example, and some of the most often used Hamiltonians for monolayer and bilayer graphene also lead to isotropic bands (see Sec.4.4). As for the form of the scattering rate, Eq.4.26 is an acceptable approximation for most phonon scattering mechanisms and, by setting  $\hbar\omega_0 = 0$ , also for surface roughness or Coulomb scattering<sup>2</sup>. Consequently the case discussed in this section is of remarkable practical interest.

Appx.B.2 shows that, for isotropic bands and a scattering rate expressed by Eq.4.26, the momentum relaxation time  $\tau(k)$  depends only on the magnitude of the wave-vector, and it is obtained by solving Eq.B.11, that we rewrite here for convenience

$$\begin{aligned} & \frac{dE_i(k)}{dk} \tau_i(k) \left\{ \frac{1}{2\pi\hbar} \sum_j \int_{-\infty}^{+\infty} dE_j \Gamma_{i,j}(k, k') \left[ \int_{-\pi}^{\pi} |M_{i,j}(q)|^2 d\beta \right] \delta[E_j - E_i(k) \mp \hbar\omega_0] \right\} \\ & - \frac{1}{2\pi\hbar} \sum_j \int_{-\infty}^{+\infty} dE_j \Gamma_{i,j}(k, k') \frac{dE_j(k')}{dk} \left[ \int_{-\pi}^{\pi} |M_{i,j}(q)|^2 \cos(\beta) d\beta \right] \tau_j(k') \delta[E_j - E_i(k) \mp \hbar\omega_0] \\ & = \frac{dE_i(k)}{dk} \end{aligned} \quad (4.27)$$

where  $\beta$  is the angle between  $\mathbf{k}'$  and  $\mathbf{k}$  and  $\Gamma_{i,j}(k, k')$  is defined in Eq.B.9.

Before we describe the discretization of Eq.4.27 we notice that  $\tau_i(k)$  depends on the magnitude  $k$  of the wave-vector *a not on the energy*. This is a relevant distinction because when the energy relation is non monotonic (see Fig.4.1(a)), then different momentum relaxation times may be associated to the same energy, as the numerical results of Sec.4.4 will clearly show.

Eq.4.27 is an integral equation where the Dirac functions reduce the integral over  $E_j$  and, as discussed in Appx.B.2, impose that the integrals over  $\beta$  are taken along circles with a fixed  $k'$ . If we embrace the energy driven discretization discussed for the derivation of Eq.4.18, we see that the angular discretization is not necessary for the case considered in this section, so

---

<sup>2</sup>In an inversion layer Eq.4.26 neglects the possible  $\mathbf{k}$  dependence of the envelope wave-functions, which exists, for example, in a hole inversion layer described with a quantized  $\mathbf{k} \cdot \mathbf{p}$  Hamiltonian [21, 28].

that the discrete  $\mathbf{k}$  values can be denoted  $k_{i,r}$  and are in fact identified only by the subband index  $i$  and the index  $r$  for the wave-vector magnitude; the corresponding unknown values of the MRT problem can be also denoted  $\tau_{i,r}$ .

By using the energy driven discretization, Eq.4.27 can be discretized in the form

$$\frac{dE_i(k_{i,r})}{dk} \left[ \frac{1}{2\pi\hbar} \sum_{j,r'} B_{i,r}^{j,r'} \delta_{i,r}^{j,r'} \right] \tau_{i,r} - \frac{1}{2\pi\hbar} \sum_{j,r'} C_{i,r}^{j,r'} \delta_{i,r}^{j,r'} \tau_{j,r'} = \frac{dE_i(k_{i,r})}{dk} \quad (4.28)$$

where we have introduced the coefficients  $B_{i,r}^{j,r'}$  and  $C_{i,r}^{j,r'}$  defined as

$$B_{i,r}^{j,r'} = k_{j,r'} \left[ \frac{dE_j(k_{j,r'})}{dk} \right]^{-1} \left[ \frac{1 - f_0(E_j(k_{j,r'}))}{1 - f_0(E_i(k_{i,r}))} \right] \int_{-\pi}^{\pi} |M_{i,j}(q_{i,r}^{j,r'})|^2 d\beta \quad (4.29)$$

$$C_{i,r}^{j,r'} = k_{j,r'} \left[ \frac{1 - f_0(E_j(k_{j,r'}))}{1 - f_0(E_i(k_{i,r}))} \right] \int_{-\pi}^{\pi} |M_{i,j}(q_{i,r}^{j,r'})|^2 \cos(\beta) d\beta \quad (4.30)$$

with  $q_{i,r}^{j,r'} = |\mathbf{k}_{j,r'} - \mathbf{k}_{i,r}|$  being the magnitude of the wave-vector variation

$$(q_{i,r}^{j,r'})^2 = k_{i,r}^2 + (k_{j,r'})^2 - 2k_{i,r}k_{j,r'} \cos(\beta) \quad (4.31)$$

A discussion similar to the one leading to Eq.4.24 allows us to define the new Kronecker symbol  $\delta_{i,r}^{j,r'}$  as

$$\delta_{i,r}^{j,r'} \begin{cases} 1 & \text{for } [n_{j,r'} - n_{i,r} \mp p] = 0 \\ 0 & \text{otherwise} \end{cases} \quad (4.32)$$

where we have set  $\hbar_0\omega_0 \simeq p \Delta E$ , with  $p$  being a positive integer number.

The analysis in Secs.4.3.2 and 4.3.3 show that the introduction of the MRT  $\tau_i(\mathbf{k})$  as the unknown of the LBTE is practically useful for either isotropic scattering mechanisms or isotropic bands. In fact, while  $\tau_i(\mathbf{k})$  depends only on the energy  $E_i(\mathbf{k})$  for an isotropic scattering and only on the wave-vector magnitude  $k$  under the assumptions of Sec.4.3.3, this is not the case for the original unknown function  $g_i(\mathbf{k})$ , because the  $g_i(\mathbf{k})$  maintains an angular dependence through the group velocity  $v_{i,x}(\mathbf{k})$  (see Eq.4.10). In the most general case of anisotropic bands and scattering rates, however, there is no particular point in changing the unknown from  $g_i(\mathbf{k})$  to  $\tau_i(\mathbf{k})$ .

#### 4.3.4 Multiple scattering mechanisms and Matthiessen's rule

Eqs.4.22 and 4.28 have been derived by considering a single scattering mechanism, but the extension to multiple scattering mechanisms is quite straightforward. To this purpose, we first rewrite Eqs.4.22 and 4.28 for the single scattering mechanism  $s$  in the concise matrix notation  $\mathbf{M}^{(s)} \boldsymbol{\tau}^{(s)} = \mathbf{v}$ , where  $\boldsymbol{\tau}^{(s)}$  is the vector of the unknown MRT values,  $\mathbf{v}$  is the vector of the group velocities and  $\mathbf{M}^{(s)}$  is the matrix representative of the linear problem (whose elements are given by Eqs.4.23, 4.24 or 4.29, 4.30, 4.32). For a case where several scattering mechanisms are present, we see that the total momentum relaxation time  $\boldsymbol{\tau}$  is obtained by solving

$$\left[ \sum_{s=1}^{N_{sc}} \mathbf{M}^{(s)} \right] \boldsymbol{\tau} = \mathbf{v} \quad (4.33)$$

with  $N_{sc}$  being the number of mechanisms. Eq.4.33 clarifies that adding a scattering mechanism to the LBTE implies to add the corresponding matrix  $\mathbf{M}^{(s)}$  to the linear algebraic problem;

this point was already recognized many years ago in [18]. *As can be seen it is in general impossible to establish any relation between the relaxation  $\tau^{(s)}$  of the single mechanisms and the overall relaxation time  $\tau$ .* An exception occurs for isotropic scattering mechanisms, in fact Eq.4.25 shows that the relaxation times of more isotropic mechanisms simply follow the so called Matthiessen's rule, and no equation has to be solved to calculate the MRT. Consequently, strictly speaking the Matthiessen's rule is not even valid for the relaxation times if at least one of the scattering mechanisms is anisotropic. Despite its shaky theoretical foundation, the Matthiessen's rule is still routinely used to interpret both experimental and simulated mobility data and to separate the contribution of the different scattering mechanisms; a quantitative analysis of the errors produced by the use of the Matthiessen's rule has been recently presented in [31], that also refers to a number of previous contributions dealing with similar topics.

### 4.3.5 Some remarks about the numerical solution

Before we move to some results about relaxation time and mobility calculations, a few remarks about the energy driven discretization proposed in Figs.4.1(a) and (b) may be useful.

The  $\mathbf{k}$  discretization of Fig.4.1(a) implies to calculate the wave-vector magnitude along each direction and for fixed values of the energy. This is easy if we are using a parabolic effective mass energy model (possibly with non parabolic corrections), because in this case the relation between the wave-vector magnitude and the energy can be expressed analytically [28]. Furthermore, if at least the energy versus  $\mathbf{k}$  relation is known analytically, then it is still quite easy to obtain a numerical inversion of such a relation, as it is shown in Sec.4.4 for a bilayer graphene sheet. Finally, when the band structure is determined numerically, as in the case, for example, of an inversion layer described by a  $\mathbf{k}\cdot\mathbf{p}$  Hamiltonian [21, 28], the energy driven discretization can be implemented by solving the so called inverse problem, that is the eigenvalue problem that, for a given energy and in plane direction  $\theta$ , solves for the values of the wave-vector magnitude [21, 28]. As can be seen, the energy driven discretization is a feasible discretization scheme in very many cases of practical interest.

A second remark is that Eq.4.22 has been derived for an inelastic phonon scattering with a  $\mathbf{q}$  dependent phonon energy, as shown by Eq.4.15. When the phonon energy can be approximately taken as a constant (i.e.  $E_{ph}(\mathbf{q}) \simeq \hbar_0\omega_0$ ), then the energy driven discretization simply prescribes that  $\hbar_0\omega_0$  is rounded to a multiple of  $\Delta E$ , namely we have to set  $\hbar_0\omega_0 \simeq p \Delta E$  (with  $p$  being a positive integer number). Also an elastic scattering mechanism can be considered as a simplified case of Eq.4.15.

We also note, in passing, that the energy driven  $\mathbf{k}$  discretization makes it easy to obtain a set of discrete  $\mathbf{k}$  points such that the corresponding energies belong to a prescribed range, that for low field mobility calculations can be up to a few  $K_B T$  above the Fermi level. In the presence of a significant energy anisotropy, using a fixed energy range for all  $\mathbf{k}$  directions is more physically meaningful and computationally efficient than enforcing the same  $k$  range along all  $\mathbf{k}$  directions, this latter option possibly resulting in vastly different energy values along different directions.

Another point to be briefly discussed is given by the closing conditions. In fact, if we suppose to restrict the energy range to  $E_{max} = E_{min} + n_{max} \Delta E$ , then the unknown relaxation times  $\tau$  corresponding to  $E_{max}$  are linked to the  $\tau$  values at larger energies by phonon absorption transitions, so that we need closing conditions to solve the linear problem in Eq.4.22 or Eq.4.28. In this work we simply set the relaxation time constant for energies larger than  $E_{max}$ . This condition has no physical meaning and in fact it is only a computational choice. In order to verify that the closing conditions do not affect the results, we verified that mobility calculations are independent of the exact value of the maximum energy  $E_{max}$ , as long as  $E_{max}$  is larger than the Fermi level by about  $6K_B T$ ; this is because the  $\tau$  values are sensitive to  $E_{max}$  in only a small energy range below  $E_{max}$ .

As a final remark, we notice that, since the matrix representative of the linear problems

in Eq.4.22 and Eq.4.28 are sparse with many non null entries, then the CPU time for the solution of the linear problem is typically negligible with respect to the time for the calculation of the entries of the matrix. The calculation of the matrix entries, however, can be easily and effectively parallelized, which leads to acceptable CPU times even for relatively fine energy and angle discretizations <sup>3</sup>.

## 4.4 Numerical Results for mobility in graphene bilayers

We have applied our approach to solve the LBTE to the calculation of low-field mobility in a graphene bilayer (GBL). As already mentioned in Secs.1.4.2 and 3.4, the GBL consists of two interacting sheets of graphene arranged according to the Bernal stacking [32, 33, 34] (see Fig.4.2(a)), and it is a very interesting material because the potential difference  $V$  between the two layers controls the energy bandgap [32, 33, 34].

### 4.4.1 An isotropic energy relation

Most of the results of this section were obtained by using the bandstructure for bilayer graphene stemming from the simplified Tight-Binding (TB) approach reported in Eq.3.45 (see Sec.3.4.1), where the only interactions accounted for between the atoms of the different layers are those between atoms which are aligned according to the Bernal stacking [33, 34] (see Fig.4.2(a)). Here we want just to remind that this simplified  $4 \times 4$  Hamiltonian leads to a conduction band that is isotropic near the 6 K-points of the first Brillouin zone; its two branches are expressed by Eq.3.46 and depends on the voltage  $V$  between the two layers. It is important to note that a bandgap is induced when  $V$  is not equal to zero; moreover, the edges of the bands are non-monotonic (“Mexican-hat” shape, see Fig.4.2(b)). The two branches of the conduction band  $E_1$  and  $E_2$  calculated for different values of the energy gap  $E_G$  are shown in Fig.4.2(b).

Since we are interested in studying uniform transport in graphene bilayer transistors, we consider both  $V$  and the electron density  $N_s$  as independent inputs of the model, namely we have not solved the self-consistent loop coupling the bandstructure with the electrostatic problem that allows to calculate the dependence of  $V$  and the carrier density  $N_s$  on the gate voltages  $V_{TG}$  and  $V_{BG}$ .

### 4.4.2 Relaxation time and mobility for the isotropic energy relation

In the mobility calculations for the graphene bilayer we have considered only the lowest branch of the conduction band (i.e.  $E_1$  in Fig.4.2(b)), since  $E_2$  is very high in energy with respect to the Fermi level for all the considered inversion densities. Hence in this section the subband index will be dropped in the notation of scattering rates and relaxation times.

We have considered the intrinsic graphene phonons and the remote phonons stemming from the gate dielectrics (see Fig.4.2(a)) and we have used the expressions for the scattering rates reported in Eqs.3.55, 3.56, and 3.57 (see Sec.3.4.3). Hence, we are analyzing the transport for an isotropic and non-monotonic energy dispersion relation (see Fig.4.2(b)) and we account for several anisotropic scattering mechanisms. The momentum relaxation time was calculated either by solving directly Eq.4.33 (with the matrix  $\mathbf{M}^{(s)}$  for each scattering mechanism given by Eq.4.28), or by using a simplified, approximated formulation that can be explained as follows. The approximated determination of the MRT corresponds to an approach very frequently employed in the literature, that is obtained by simplifying the term  $(\tau_j(\mathbf{k}') v_{x,j}(\mathbf{k}')) / (v_{x,j}(\mathbf{k}') \tau_i(\mathbf{k}))$  in Eq.4.12 and substituting it with  $\cos(\beta)$ , where  $\beta$  is the angle between  $\mathbf{k}'$  and  $\mathbf{k}$  [29, 21, 30, 28]. As discussed in details in [28], this simplification is only justified for elastic, intra-subband transitions and for isotropic bands. However, since it allows one to circumvent the solution of the

<sup>3</sup>In our simulations, thanks to the parallelization, the CPU time goes roughly as  $\frac{1}{N}$ , where  $N$  is the number of CPUs used.

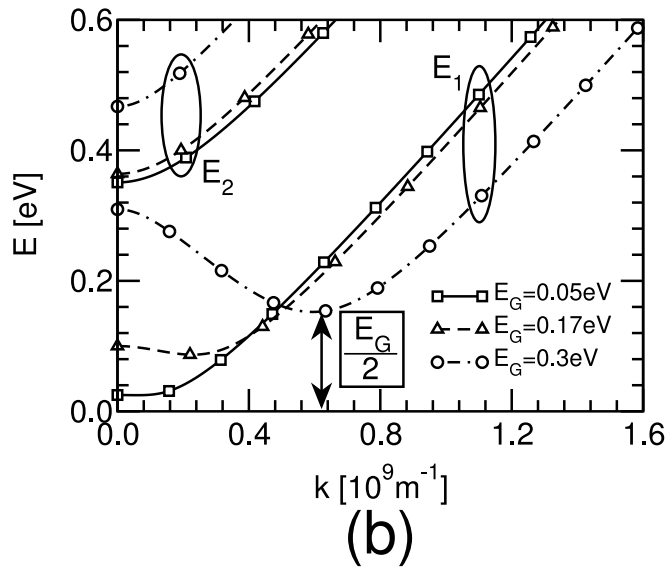
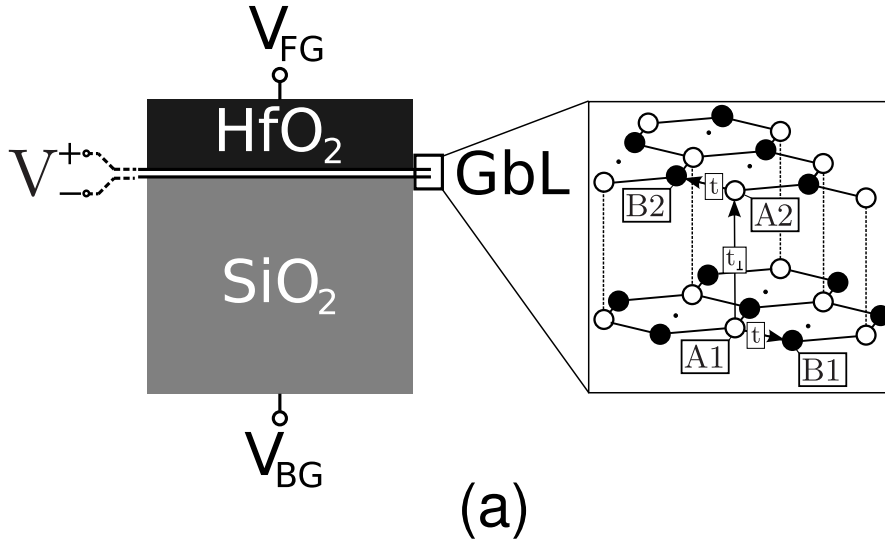


Figure 4.2: (a) Sketch of the simulated graphene bilayer physical system: the graphene bilayer is inserted in a double-gate structure, with ideally flat  $\text{SiO}_2$  substrate and  $\text{HfO}_2$  top dielectric. The inset illustrates the four-atoms unit cell and the alignment between atoms A1 and A2 (Bernal stacking); the hopping energies  $t$  and  $t_{\perp}$  are also shown. (b) Profiles of the two branches of the conduction band  $E_1$  and  $E_2$  of the graphene bilayer for different energy gap  $E_G$  controlled by the applied voltage  $V$ . The mid-gap is taken as the reference for the energy.

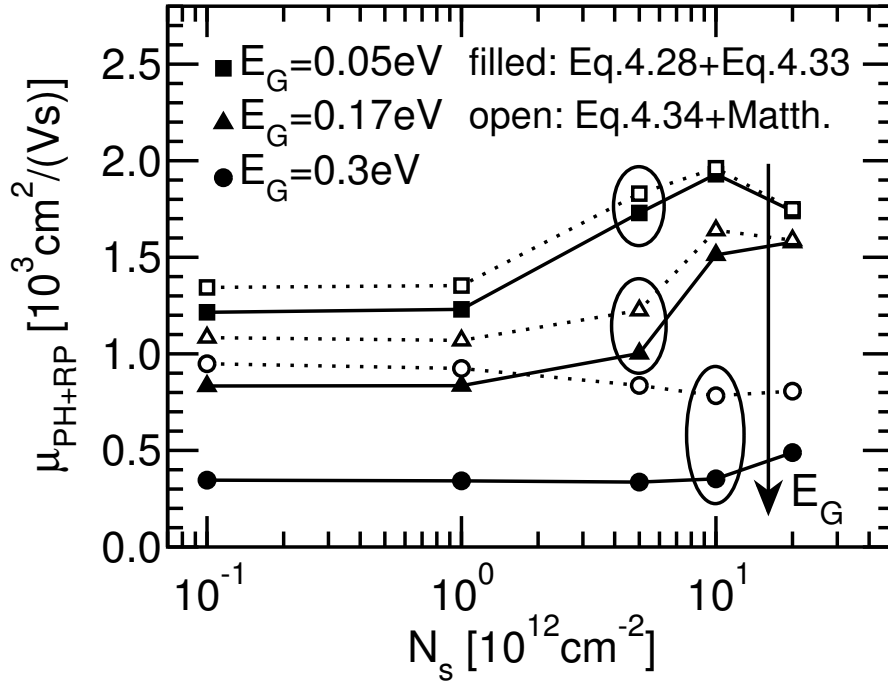


Figure 4.3: Graphene bilayer mobility versus the inversion density  $N_s$  for various values of the energy gap  $E_G$  calculated using the exact formulation (filled symbols), and the approximation given by the use of Eq.4.34 plus the Matthiessen's rule (open symbols). The error of the approximated solution is large at high energy gaps.

LBTE and obtain an explicit expression for the relaxation time, this approach has been almost universally used in the literature in a countless number of papers up to very recent contributions [17]. With such a simplification of Eq.4.12, the relaxation time  $\tau^{(s)}(k)$  for the scattering mechanism  $s$  and for an isotropic energy relation can be written as [29, 21, 30, 28]

$$\frac{1}{\tau_i^{(s)}(k)} = \frac{1}{2\pi\hbar} \sum_j \int_{\mathbf{k}'} \left[ \frac{1 - f_0(E_j(k'))}{1 - f_0(E_i(k))} \right] |M_{i,j}(q)|^2 [1 - \cos(\beta)] \delta[E_j(k') - E_i(k) \mp \hbar\omega_0] d\mathbf{k}' . \quad (4.34)$$

In this simplified approach, furthermore, the total relaxation time  $\tau_i(k)$  is finally obtained by summing the inverse of the  $\tau_i^{(s)}(k)$ , that is by using the Matthiessen's rule.

Fig.4.3 shows the mobility versus inversion density for a graphene bilayer and for different energy gaps. A physical explanation for the non monotonic behavior of calculated mobility observed especially for small band gaps is discussed in Chap.5 and in [35]. The simulated mobilities in Fig.4.3 are in fairly good agreement with the experimental values between 1000 and 2000[cm<sup>2</sup>/(Vs)] reported in previous publications [36, 37, 38, 39, 40, 41], and measured on test structure similar to the system sketched in Fig.4.2(a). Moreover, our calculated mobility increases remarkably if we switch off remote phonons (see also the results reported in Chap.5), and is quite consistent with the value of about 60000[cm<sup>2</sup>/(Vs)] recently measured for ultra-clean suspended bilayer graphene [42].

Fig.4.3 illustrates simulated mobility for either the exact MRT calculations (filled symbols) or for the simplified approach consisting in the use of Eq.4.34 and the Matthiessen's rule (open symbols). As can be seen the discrepancy between the approximated and exact mobility calculation is significant for relatively large band gaps, that is when the energy relation is markedly non monotonic (see Fig.4.2(b)). The percentage error of these simplified calculations is reported in Fig.4.4 (filled symbols), where it can be seen that the approximated MRT determination

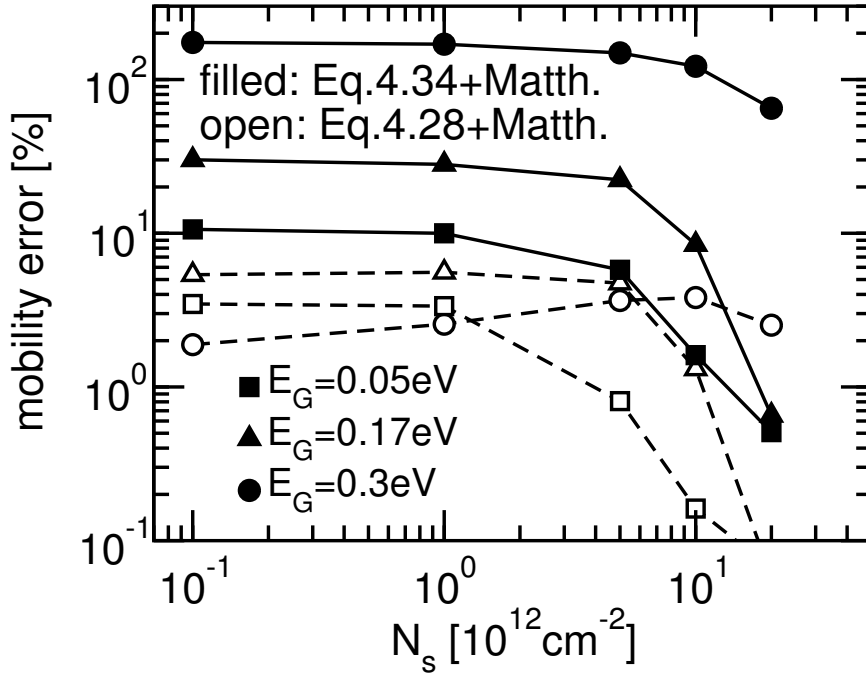


Figure 4.4: Error in the mobility calculations obtained by employing simplifying assumptions in the solution of the LBTE. The continuous lines show that the absolute error can be large when using Eq.4.34 and the Matthiessen's rule. The dotted lines show a much smaller error when the only approximation is the Matthiessen's rule. The error is calculated with respect to the results obtained using Eqs.4.28 and 4.33.

becomes inaccurate with increasing energy band gaps.

Fig.4.4 also shows the error with respect to the exact MRT calculation of a second set of approximated results (open symbols), which were obtained by first calculating the momentum relaxation time  $\tau_i^{(s)}$  of each scattering mechanism by solving exactly Eq.4.28, and then determining the total relaxation time  $\tau_i(k)$  by using the Matthiessen's rule rather than Eq.4.33; we thus consider the error of these calculations as representative as the inaccuracy introduced by the Matthiessen's rule only. As can be seen the error related to the Matthiessen's rule only is quite limited for the mobility calculations of Fig.4.3. This is because for graphene bilayer the scattering due to the remote phonons of the  $\text{HfO}_2$  oxide is largely dominant, as illustrated by the momentum relaxation time of the different scattering mechanisms reported in Fig.4.5. By increasing artificially the scattering rates of acoustic and optical phonons we also verified that the errors related to Matthiessen's rule may become significantly larger than observed in Fig.4.4 when several scattering mechanisms have comparable relaxation times (not shown).

Fig.4.6 shows the total momentum relaxation time corresponding to the mobility calculations of Fig.4.3 and for an energy gap  $E_G=0.17\text{eV}$  and an inversion density  $10^{13}\text{cm}^{-2}$ , that is for a case where the approximated mobility calculation is quite inaccurate. Consistently with the errors in the mobility shown in Fig.4.4, the discrepancy between the exact and approximated MRT is remarkably larger for the case when both Eq.4.34 and the Matthiessen's rule are used (left plot), compared to case where the Matthiessen's rule is the only approximation (right plot).

Fig.4.6 also shows that the exact momentum relaxation is negative for  $k$  values smaller than about  $0.25\text{nm}^{-1}$ . This seemingly puzzling result can be explained by recalling that  $\tau(k)$  is not the relaxation time of a real physical process, but rather an auxiliary unknown function for the LBTE problem, which is linked by Eq.4.10 to the original unknown function  $g(\mathbf{k})$  defined in

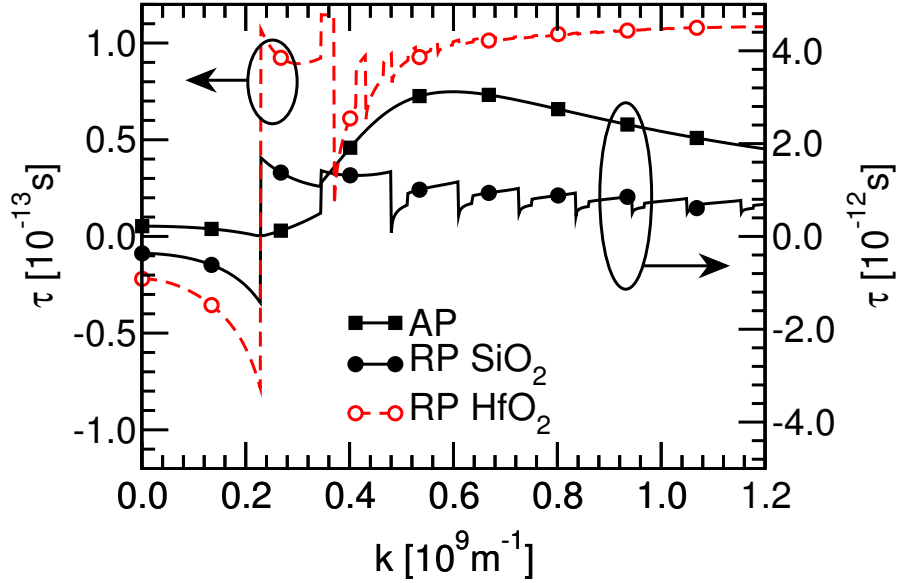


Figure 4.5: Exact relaxation times for acoustic phonon (AC, right  $y$ -axis) and for remote phonons (RP) originating in either the  $\text{SiO}_2$  (right  $y$ -axis) or the  $\text{HfO}_2$  (left  $y$ -axis) for  $E_G=0.17\text{eV}$  and  $N_s=10 \times 10^{12}\text{cm}^{-2}$  versus the magnitude  $k$  of the wave-vector; the Fermi wave-vector  $k_f$  is  $0.56 \times 10^9\text{m}^{-1}$ . The relaxation time related to the remote phonons stemming from the top gate dielectric is dominant with respect to the others. The relaxation time related to the optical phonons has been omitted because it is orders of magnitude larger.

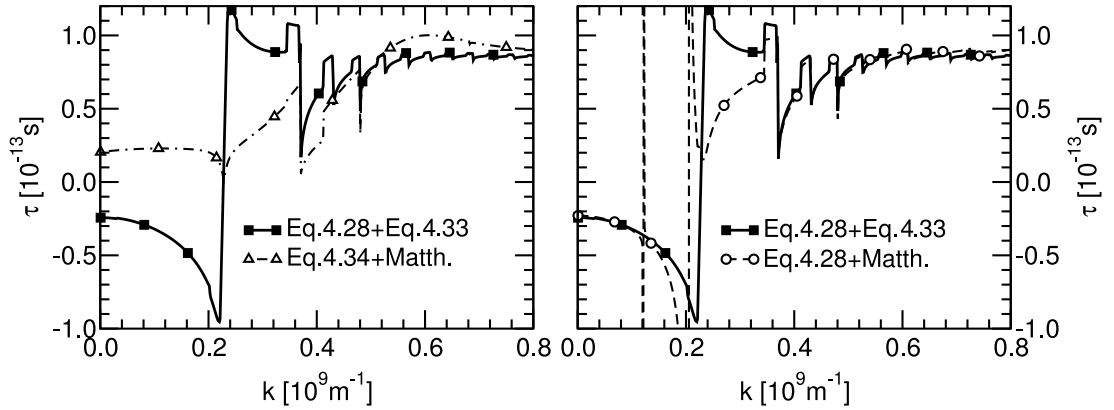


Figure 4.6: Total relaxation times calculated for  $E_G=0.17\text{eV}$  and  $N_s=10 \times 10^{12}\text{cm}^{-2}$  ( $k_f=0.56 \times 10^9\text{m}^{-1}$ ) using Eqs. 4.28 and 4.33 (continuous lines), employing Eq. 4.34 plus the Matthiessen's rule (dash-dotted line in the left plot), and considering only the effect of the Matthiessen's rule (dashed line in the right plot).

Eq.4.1. In this respect, Fig.4.7 reports the relaxation time  $\tau$ , the  $x$  component  $v_x$  of the group velocity and the  $g$  function versus the  $x$  component  $k_x$  of the wave-vector and for the energy gap and inversion density considered in Fig.4.6. As can be seen  $g(k_x)$  is a continuous function and it is positive for  $k_x > 0$  and negative for  $k_x < 0$ . In fact the discontinuities of  $\tau(k_x)$  occur at the  $k_x$  values where  $v_x$  changes its sign as a consequence of the non monotonic energy to  $k$  relation (see Fig.4.2(b) for  $E_G=0.17\text{eV}$ ). The behavior of  $\tau(k_x)$ ,  $v_x(k_x)$  and  $g(k_x)$  in Fig.4.7 is thus fully consistent with Eq.4.10.

The physical significance of the results in Fig.4.7 can be further understood if we consider, for example, a negative electric field  $F_x < 0$  and an electron gas. In this case Eq.4.1 (with the upper sign) states that the deviation of the electron occupation function from the equilibrium value is given by  $[f(\mathbf{k}) - f_0(E(k))] = e|F_x|g(\mathbf{k})$ , that is it has the same sign as  $g(\mathbf{k})$ . Hence the results in Fig.4.7 are consistent with the intuitive fact that, for a negative  $F_x$ , the states with positive  $k_x$  are repopulated and those with negative  $k_x$  are depopulated with respect to the equilibrium condition. *We thus conclude this discussion by reiterating that the momentum relaxation time  $\tau$  defined in Eq.4.10 can legitimately take negative values and that this has no unphysical implications.* Quite interestingly, however, the simplified solution for  $\tau_i(\mathbf{k})$  in Eq.4.34 implies that the corresponding approximated  $\tau_i(\mathbf{k})$  takes only positive values (see also the dash-dotted line in Fig.4.6 left).

### 4.4.3 Results for an anisotropic energy relation

In order to validate the feasibility of the method proposed in this work for the solution of the LBTE also for an anisotropic energy dispersion, we considered the energy relation of graphene bilayer obtained from the "complete" tight binding Hamiltonian already presented in Sec.3.4.1 (see Eq.3.44) [33]. This tight binding Hamiltonian is "complete" in the sense that it accounts for the interactions between all the four atoms of the unit cell [33] and leads to an energy relation that is anisotropic (differently from the one in Eq.3.45), as it is illustrated in Fig.3.14 reporting the lowest conduction band in the  $\mathbf{k}$  space (see also Sec.3.4.1).

Relaxation times and mobility were calculated by solving Eq.4.33 (with the matrix  $\mathbf{M}^{(s)}$  for each scattering mechanism given by Eq.4.28), and by using the scattering rates formulation presented in Sec.3.4.3, with energy and spinor-overlaps calculated consistently with the Hamiltonian in Eq.3.44. Note that, as already mentioned in Sec.3.4.2, due to the symmetries of the energy relation and similarly to monolayer graphene (see Fig.3.6), the six minima can be grouped in two inequivalent valleys: as it can be seen in Fig.4.8, a valley is obtained just by mirroring the other valley with respect to the axes  $k'_x = 0\text{m}^{-1}$ . Thanks to this particular feature of the GBL energy relation, when the electric field is applied along the  $x$  direction (see Fig.4.8), the mobility calculated for the two inequivalent valleys is the same.

Figs.4.9(a) and (b) show respectively the momentum relaxation time along different directions in the  $\mathbf{k}$  plane and the contour of the function  $g(\mathbf{k})$  calculated for  $V=0.2\text{V}$  and  $N_s=10 \times 10^{12}\text{cm}^{-2}$ . As expected the  $\tau$  is anisotropic, which reflects the anisotropic energy relation in Fig.3.14. Moreover, the calculated  $g(\mathbf{k})$  function is not null only for  $\mathbf{k}$  values close to the Fermi wave-vectors (indicated by the white line in Fig.4.9(b)), and it is even with respect to the angle  $\alpha$  defined in Fig.3.14, as prescribed by the symmetries of the energy relation and by the fact that the electric field is along the  $x$  direction. Moreover  $g(\mathbf{k})$  is vanishing along the  $k_y$  direction, that is for wave-vectors normal to the electric field.

Fig.4.10 finally shows a comparison between the mobility calculated employing the isotropic (filled symbols) and the complete Hamiltonian (open symbols). As can be seen, all the qualitative mobility trends are the same for the two Hamiltonians, however discrepancies as large as 30% are observed in the absolute values of the calculated mobility. As a final remark, we have also verified that the dependence of the mobility on the direction of the external electric field is negligible (see Fig.4.11).

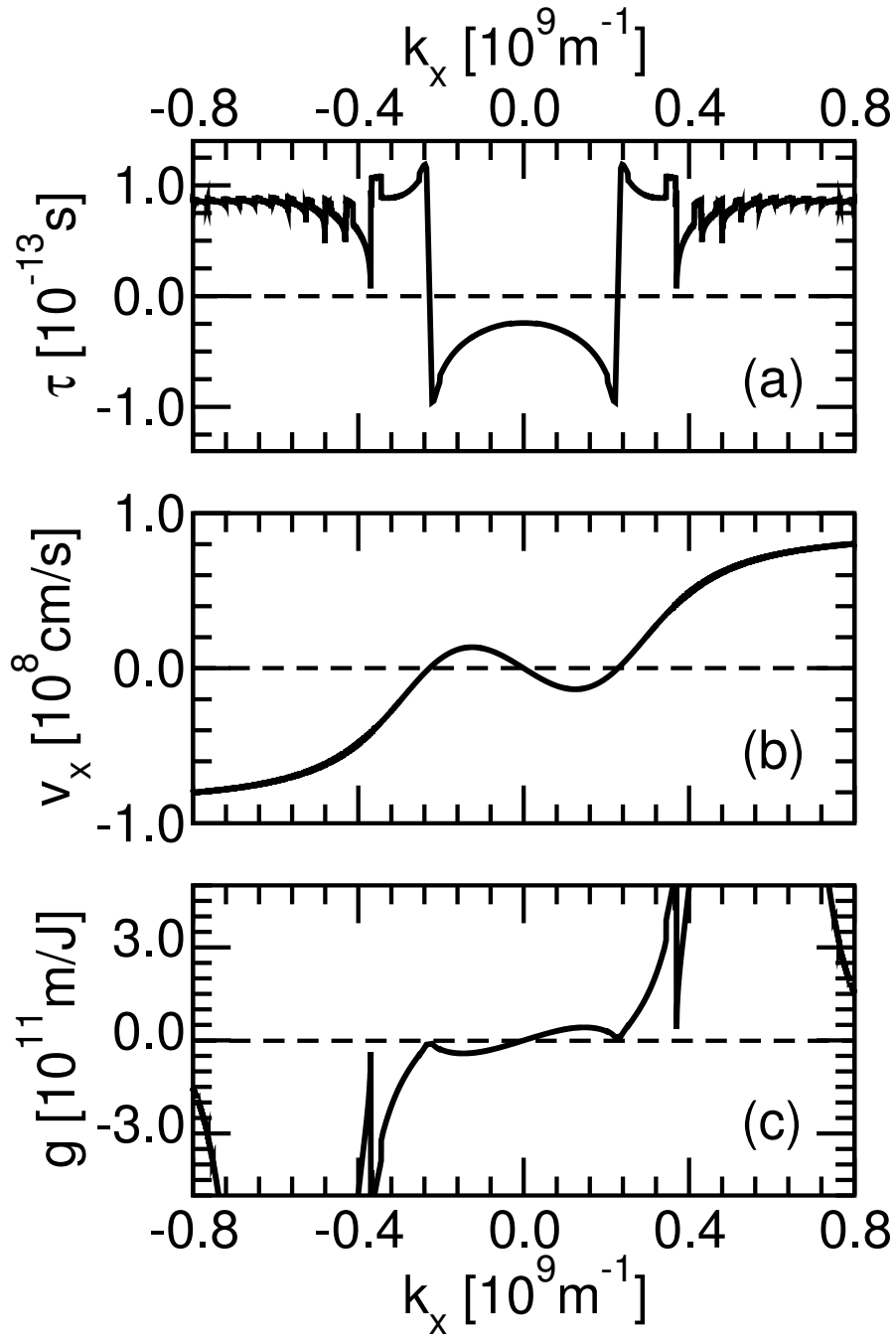


Figure 4.7: (a) Total relaxation time, (b)  $x$  component  $v_x$  of the group velocity and (c) function  $g$  versus  $k_x$  calculated with the approach proposed in this work for  $E_G=0.17\text{eV}$  and  $N_s=10 \times 10^{12}\text{cm}^{-2}$ .

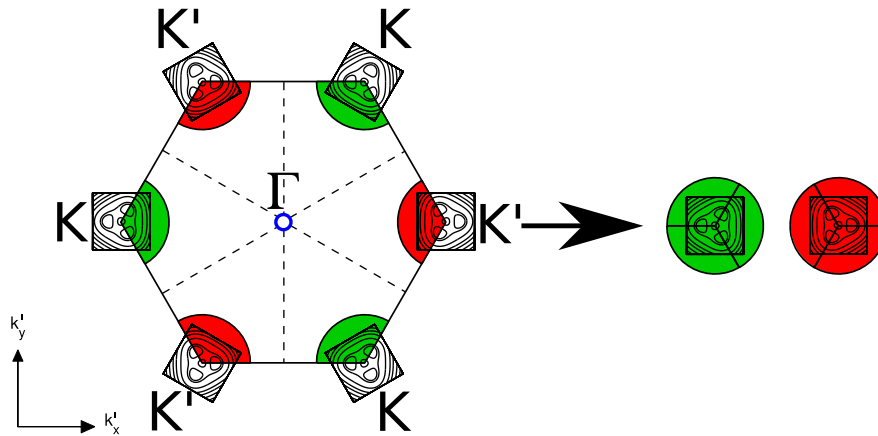


Figure 4.8: Similarly to monolayer graphene, the 6 minimum of the FBZ of GBL can be grouped in two degenerate valleys, highlighted in the figure by the green and red circles.

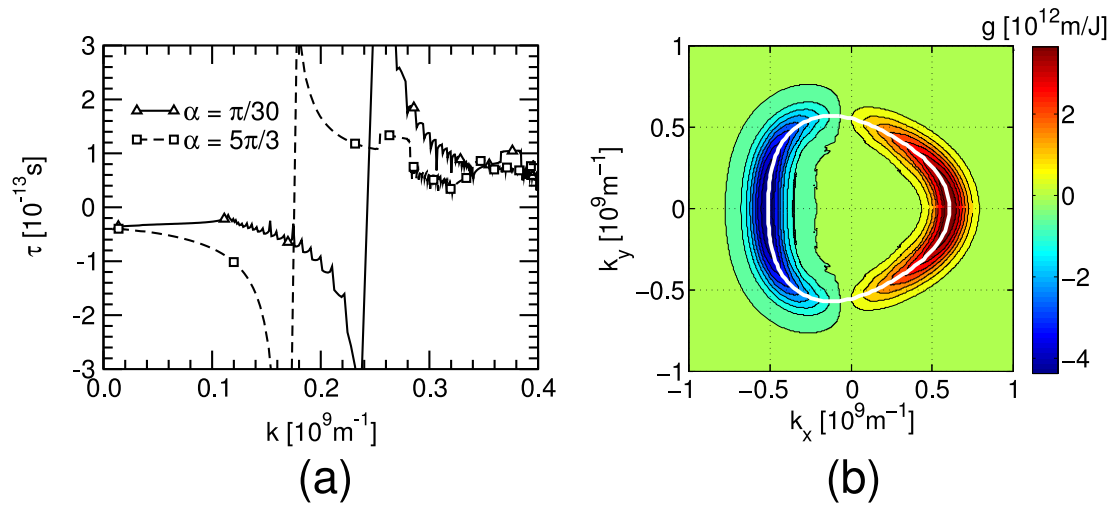


Figure 4.9: (a) Total relaxation time  $\tau$  plotted along different directions ( $\alpha=\pi/30$  and  $5\pi/3$ , see Fig.3.14 left) and (b) contour of the function  $g(\mathbf{k})$  calculated using the TB Hamiltonian in Eq.3.44 for  $V=0.2\text{V}$  and  $N_s=10 \times 10^{12}\text{cm}^{-2}$ . The white line in (b) indicates the Fermi wave-vectors. As expected, the function  $\tau$  is anisotropic and the function  $g$  reflects the symmetries of the problem.

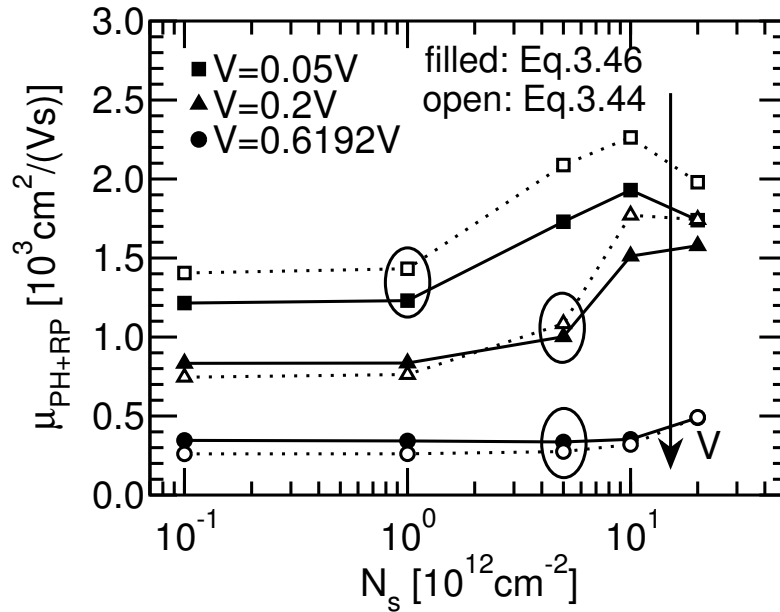


Figure 4.10: Comparison between the mobilities calculated either with the anisotropic energy relation given by Eq.3.44 (dotted curves) or with the isotropic energy relation in Eq.3.46 (continuous lines) versus the total electron density  $N_s$  and the voltage  $V$  between the layers.

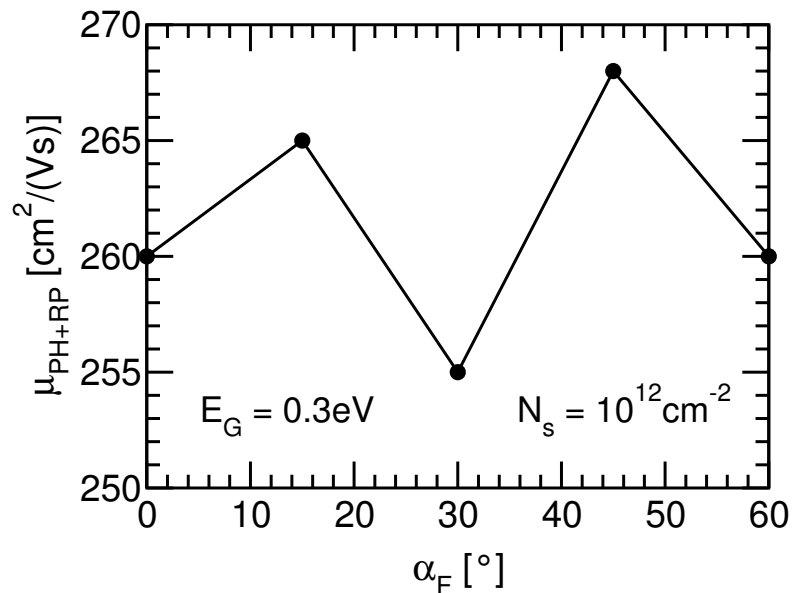


Figure 4.11: Dependence of the GBL low-field mobility calculated by applying the LBTE approach on the anisotropic energy relation stemming from the “complete” Hamiltonian of Eq.3.44 for  $E_G = 0.3\text{eV}$  and  $N_s = 10\text{cm}^{-2}$  on the direction of the external electric field  $\alpha_F$ . Note that  $\alpha_F = 0^\circ$  corresponds to the  $x$  direction.

## 4.5 Conclusions

This chapter revisited the solution of the linearized Boltzmann transport equation, which is probably the most popular approach to calculate mobility in semiconductor materials and devices. We proposed an energy driven discretization of the LBTE that allows one to write the discretized BTE in the form of a linear, algebraic problem, and we provided detailed expressions in terms of scattering matrix elements for the entries of the matrix governing the linear problem. In our approach multiple scattering mechanisms are naturally included by adding the corresponding scattering rates *before* the calculation of the MRT. Hence it is not necessary to resort to the Matthiessen's rule to compose the inverse of the relaxation times, which is a procedure theoretically legitimate for isotropic scattering rates, but essentially semi-empirical for anisotropic mechanisms.

We implemented the proposed methodology to solve the LBTE and calculate the mobility in a graphene bilayer system, and compared our exact calculations for relaxation time and mobility with the results obtained with some of the simplifying assumptions almost universally employed in the previous works; the error of the approximated solutions was quantified and discussed.

Quite interestingly, our results showed that for the non monotonic energy dispersion of graphene bilayer the momentum relaxation time can take negative values, which we explained by the fact that the MRT is an auxiliary unknown function for the LBTE problem, so that it is not always possible to interpret it as the relaxation time of a real physical process.

# Bibliography

- [1] S. Hofstein and G. Warfield, "Carrier mobility and current saturation in the MOS transistor," *Electron Devices, IEEE Transactions on*, vol. 12, no. 3, pp. 129 – 138, mar 1965.
- [2] M. Jamil, J. Oh, M. Ramon, S. Kaur, P. Majhi, E. Tutuc, and S. Banerjee, "High-Mobility TaN/Al<sub>2</sub>O<sub>3</sub>/Ge(111) n-MOSFETs With RTO-Grown Passivation Layer," *Electron Device Letters, IEEE*, vol. 31, no. 11, pp. 1208 –1210, nov. 2010.
- [3] M. S. Lundstrom, "On the mobility versus drain current relation for a nanoscale MOS-FET," *IEEE Electron Device Lett.*, vol. 22, no. 6, pp. 293–295, 2001.
- [4] G. Comparone, P. Palestri, D. Esseni, L. Lucci, and L. Selmi, "A Better Understanding of the Requirements for Predictive Modeling of Strain Engineering in nMOS Transistors," *Jour. of Computational and Theoretical Nanoscience*, vol. 5, no. 6, pp. 1106–1114, 2008.
- [5] F. Conzatti, M. De Michielis, D. Esseni, and P. Palestri, "Drain current improvements in uniaxially strained p-MOSFETs: A Multi-Subband Monte Carlo study," in *Solid-State Device Research Conference, 2008. ESSDERC 2008. 38th European*, sept. 2008, pp. 250 –253.
- [6] C. Jungemann, N. Subba, J. Goo, C. Riccobene, Q. Xiang, and B. Meinerzhagen, "Investigation of strained Si/SiGe devices by MC simulation," *Solid State Electronics*, vol. 48, p. 1417, 2004.
- [7] V. Aubry-Fortuna, P. Dollfus, and S. Galdin-Retailleau, "Electron effective mobility in strained-Si/Si<sub>1-x</sub>Ge<sub>x</sub> MOS devices using Monte Carlo simulation," *Solid State Electronics*, vol. 49, p. 1320, 2005.
- [8] Q. Xiang, J.-S. Goo, J. Pan, B. Yu, S. Ahmed, J. Zhang, and M.-R. Lin, "Strained silicon NMOS with nickel-silicide metal gate," in *VLSI Symp. Tech. Dig.*, 2003, pp. 101–102.
- [9] F. Boeuf, F. Arnaud, M. T. Basso, D. Sotta, F. Wacquant, J. Rosa, N. Bicaïs-Lepinay, H. Bernard, J. Bustos, S. Manakli, M. Gaillardin, J. Grant, T. Skotnicki, B. Tavel, B. Duriez, M. Bidaud, P. Gouraud, C. Chaton, P. Morin, J. Todeschini, M. Jurdit, L. Pain, V. De-Jonghe, R. El-Farhane, and S. Jullian, "A conventional 45 nm CMOS node lowcost platform for general purpose and low power applications," in *IEEE IEDM Technical Digest*, 2004, pp. 425–428.
- [10] A. Thean, D. Zhang, V. Vartanian, V. Adams, J. Conner, M. Canonico, H. Desjardin, P. Grudowski, B. Gu, Z.-H. Shi, S. Murphy, G. Spencer, S. Filipiak, D. Goedeke, X.-D. Wang, B. Goolsby, V. Dhandapani, L. Prabhu, S. Backer, L.-B. La, and D. Burnett, "Strain-enhanced CMOS through novel process-substrate stress hybridization of super-critically thick strained silicon directly on insulator (SC-SSOI)," in *VLSI Symp. Tech. Dig.*, 2006, pp. 130–131.

- [11] T.Ghani, M.Armstrong, C.Auth, M.Bost, P.Charvat, G.Glass, T.Hoffmann, K.Johnson, C.Kenyon, J.Klaus, B.McIntyre, K.Mistry, A.Murthy, J.Sandford, M.Silberstein, S.Sivakumar, P.Smith, K.Zawadzki, S.Thompson, and M.Bohr, "A 90 nm high volume manufacturing logic technology featuring novel 45 nm gate length strained silicon CMOS transistors," in *IEEE IEDM Technical Digest*, 2003, pp. 978–980.
- [12] R. T. Delves, "Theoretical Transport Coefficients for Polar Semiconductors," *Proceedings of the Physical Society*, vol. 73, no. 4, p. 572, 1959.
- [13] K. Fletcher and P. N. Butcher, "Solution of the Boltzmann equation in ellipsoidal valleys with application to the valleys of GaAs and GaP," *Journal of Physics C: Solid State Physics*, vol. 6, no. 6, p. 976, 1973.
- [14] —, "An exact solution of the linearized Boltzmann equation with applications to the Hall mobility and Hall factor of n-GaAs," *Journal of Physics C: Solid State Physics*, vol. 5, no. 2, p. 212, 1972.
- [15] M. P. Vaughan and B. K. Ridley, "Solution of the Boltzmann equation for calculating the Hall mobility in bulk  $\text{GaN}_x\text{As}_{1-x}$ ," *Phys. Rev. B*, vol. 72, p. 075211, Aug 2005.
- [16] C. Jungemann, A.-T. Pham, and B. Meinerzhagen, "A linear response Monte Carlo algorithm for inversion layers and magnetotransport," *Journal of Computational Electronics*, vol. 5, pp. 411–414, 2006.
- [17] J. Dura, F. Triozon, S. Barraud, D. Munteanu, S. Martinie, and J. L. Autran, "Kubo-Greenwood approach for the calculation of mobility in gate-all-around nanowire metal-oxide-semiconductor field-effect transistors including screened remote Coulomb scattering—Comparison with experiment," *Journal of Applied Physics*, vol. 111, no. 10, p. 103710, 2012.
- [18] D. L. Rode, "Electron Mobility in Direct-Gap Polar Semiconductors," *Phys. Rev. B*, vol. 2, pp. 1012–1024, Aug 1970.
- [19] D. R. Anderson, N. A. Zakhleniuk, M. Babiker, B. K. Ridley, and C. R. Bennett, "Polar-optical phonon-limited transport in degenerate GaN-based quantum wells," *Phys. Rev. B*, vol. 63, p. 245313, Jun 2001.
- [20] D. A. Broido and T. L. Reinecke, "Theory of thermoelectric power factor in quantum well and quantum wire superlattices," *Phys. Rev. B*, vol. 64, p. 045324, Jul 2001.
- [21] M. V. Fischetti, Z. Ren, P. M. Solomon, M. Yang, and K. Rim, "Six-band  $\mathbf{k} \cdot \mathbf{p}$  Calculation of the Hole Mobility in Silicon Inversion Layers: Dependence on Surface Orientation, Strain, and Silicon Thickness," *Journal of Applied Physics*, vol. 94, no. 2, pp. 1079–1095, 2003.
- [22] A.-T. Pham, C. Jungemann, and B. Meinerzhagen, "Physics-Based Modeling of Hole Inversion-Layer Mobility in Strained-SiGe-on-Insulator," *Electron Devices, IEEE Transactions on*, vol. 54, no. 9, pp. 2174–2182, sept. 2007.
- [23] M. D. Michielis, D. Esseni, P. P. Y.L. Tsang, L. Selmi, A. O'Neill, and S. Chattopadhyay, "A Semianalytical Description of the Hole Band Structure in Inversion Layers for the Physically Based Modeling of pMOS Transistors," *IEEE Transactions on Electron Devices*, vol. 54, no. 9, pp. 2164–2173, September 2007.
- [24] Y. Zhang, M. V. Fischetti, B. Sorée, and T. O'Regan, "Theory of hole mobility in strained Ge and III-V p-channel inversion layers with high-kappa insulators," *Journal of Applied Physics*, vol. 108, no. 12, p. 123713, 2010.

- [25] F. Conzatti, N. Serra, D. Esseni, M. De Michielis, A. Paussa, P. Palestri, L. Selmi, S. Thomas, T. Whall, D. Leadley, E. Parker, L. Witters, M. Hytch, E. Snoeck, T. Wang, W. Lee, G. Doornbos, G. Vellianitis, M. van Dal, and R. Lander, "Investigation of Strain Engineering in FinFETs Comprising Experimental Analysis and Numerical Simulations," *Electron Devices, IEEE Transactions on*, vol. 58, no. 6, pp. 1583–1593, June 2011.
- [26] M. De Michielis, F. Conzatti, D. Esseni, and L. Selmi, "On the Surface-Roughness Scattering in Biaxially Strained n- and p-MOS Transistors," *Electron Devices, IEEE Transactions on*, vol. 58, no. 9, pp. 3219–3223, Sept. 2011.
- [27] M. Lundstrom, *Fundamentals of carrier transport*, 2nd ed. Cambridge University Press, 2002.
- [28] D. Esseni, P. Palestri, and L. Selmi, *Nanoscale MOS Transistors*. Cambridge University Press, 2011.
- [29] M. V. Fischetti, "Effect of the electron-plasmon interaction on the electron mobility in silicon," *Phys. Rev. B*, vol. 44, pp. 5527–5534, Sep 1991.
- [30] D. Esseni and A. Abramo, "Mobility Degradation by Remote Coulomb Scattering in Ultra-thin Oxide MOSFETs," *IEEE Transaction on Electron Devices*, vol. 50, p. 1665, 2004.
- [31] D. Esseni and F. Driussi, "A Quantitative Error Analysis of the Mobility Extraction According to the Matthiessen Rule in Advanced MOS Transistors," *Electron Devices, IEEE Transactions on*, vol. 58, no. 8, pp. 2415–2422, Aug. 2011.
- [32] E. McCann, "Asymmetry gap in the electronic band structure of bilayer graphene," *Phys. Rev. B*, vol. 74, p. 161403, Oct 2006.
- [33] J. Nilsson, A. H. Castro Neto, F. Guinea, and N. M. R. Peres, "Electronic properties of bilayer and multilayer graphene," *Phys. Rev. B*, vol. 78, p. 045405, Jul 2008.
- [34] L. A. Falkovsky, "Screening in gated bilayer graphene," *Phys. Rev. B*, vol. 80, p. 113413, Sep 2009.
- [35] A. Paussa, M. Bresciani, D. Esseni, P. Palestri, and L. Selmi, "Phonon limited uniform transport in bilayer graphene transistors," in *Solid-State Device Research Conference (ESSDERC), 2011 Proceedings of the European*, Sept. 2011, pp. 307–310.
- [36] Y. Zhang, T.-T. Tang, C. Girit, Z. Hao, M. C. Martin, A. Zettl, M. F. Crommie, Y. R. Shen, and F. Wang, "Direct observation of a widely tunable bandgap in bilayer graphene," *Nature*, vol. 459, pp. 820–823, Jun 2009.
- [37] W. Zhu, V. Perebeinos, M. Freitag, and P. Avouris, "Carrier scattering, mobilities, and electrostatic potential in monolayer, bilayer, and trilayer graphene," *Phys. Rev. B*, vol. 80, p. 235402, Dec 2009.
- [38] B. N. Szafranek, G. Fiori, D. Schall, D. Neumaier, and H. Kurz, "Current Saturation and Voltage Gain in Bilayer Graphene Field Effect Transistors," *Nano Letters*, vol. 12, no. 3, pp. 1324–1328, 2012.
- [39] B. N. Szafranek, D. Schall, M. Otto, D. Neumaier, and H. Kurz, "Electrical observation of a tunable band gap in bilayer graphene nanoribbons at room temperature," *Applied Physics Letters*, vol. 96, no. 11, p. 112103, 2010.
- [40] T. Taychatanapat and P. Jarillo-Herrero, "Electronic Transport in Dual-Gated Bilayer Graphene at Large Displacement Fields," *Phys. Rev. Lett.*, vol. 105, p. 166601, Oct 2010.

- [41] B. Fallahazad, S. Kim, L. Colombo, and E. Tutuc, "Dielectric thickness dependence of carrier mobility in graphene with HfO<sub>2</sub> top dielectric," *Applied Physics Letters*, vol. 97, no. 12, p. 123105, 2010.
- [42] Velasco Jr., J., Jing, L., Lee, Y., Kratz, P., Bao, W., Smirnov, D., Bockrath, M., and Lau, C. N., "Transport measurements on ultra-clean dual-gated suspended bilayer graphene," *EPJ Web of Conferences*, vol. 23, p. 00018, 2012.

## Chapter 5

# Monte Carlo Approach for the Simulation of Uniform Transport in Bilayer Graphene

## 5.1 Introduction

As already mentioned in Chap.1, the discovery of the outstanding charge transport properties in suspended graphene [1, 2] has triggered worldwide efforts aimed at exploiting graphene sheets as the channel material for a new generation of transistors. However, the excellent mobility in monolayer graphene comes together with a zero energy bandgap  $E_G$ , which degrades the  $[I_{on}/I_{off}]$  ratio of graphene transistors and seriously hampers their use for digital circuit applications (see Sec.1.4.2). As aforementioned in Chap.3, a method to induce an energy gap is to insert a graphene bilayer (GBL) in a double-gate structure, and apply an electric field across it [3, 4] (see Sec.3.4).

The purpose of this chapter is to study the low-field mobility and the velocity saturation in GBL transistors by using a semiclassical Monte Carlo transport simulator. The model includes the scattering rates with the local graphene phonons and with the remote phonons (RP) originating in the dielectrics described in Sec.3.4.3.

## 5.2 Model description

We have simulated a GBL inserted in the idealized double gate structure depicted in Fig.5.1: as can be seen, similar to many experimental devices, the GBL is sandwiched between two oxides, the thick back  $\text{SiO}_2$  layer and the thinner high- $\kappa$  dielectric at the front gate.

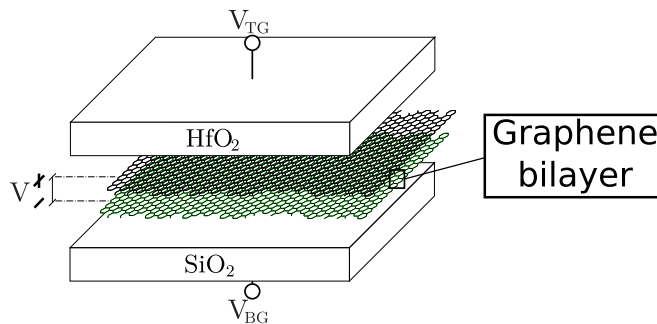


Figure 5.1: Sketch of the simulated structure: the graphene bilayer is inserted in a double-gate structure, with ideally flat  $\text{SiO}_2$  substrate and  $\text{HfO}_2$  top dielectric.

### 5.2.1 Structure of the simulator

We have solved with a Monte Carlo (MC) approach the Boltzmann Transport Equation in graphene bilayer under a uniform electric field in the transport direction. The structure of the simulator is reported in Fig.5.2: given the analytical expression of the bandstructure, the expressions of the scattering rates, the applied electric field in the direction of the transport  $F_x$ , the voltage difference between the two layers  $V$  and the carrier density  $N_s$  as inputs, the MC calculates the drift velocity  $v_d$  (thus the low-field mobility  $\mu$  when  $F_x$  is very low). As previously mentioned in Sec.3.4, the energy gap  $E_G$  in the GBL is controlled by the voltage difference  $V$  between the two layers. In a GBL transistor the bandgap  $E_G$  and the carrier density  $N_s$  can in principle be set separately by choosing appropriately the gate biases [5, 6]. However relating  $V$  and  $N_s$  to the external gate voltages  $V_{TG}$  and  $V_{BG}$  (see Fig.5.1) would require the solution of the self-consistent bandstructure and electrostatic problem. Indeed, the voltage drop  $V$  across the two layers of the GBL, for given values of the gate biases in Fig.5.1, is set by the solution of the Poisson equation, where the charge density in the two layers depends in turn on the energy dispersion relation and also on the wave-vectors of the employed Hamiltonian, that allow to calculate the local density of states in the two layers. However, since

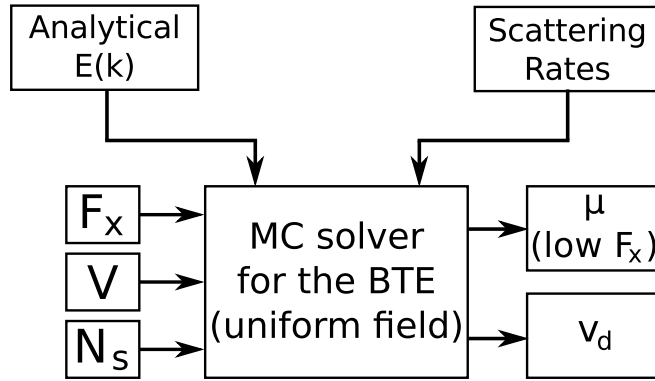


Figure 5.2: Flow chart of the simulator of the uniform transport in bilayer graphene.

we were interested to study uniform transport in a GBL transistor, we assumed an idealized test structure as in Fig.5.1 where different  $(V_{TG}, V_{BG})$  pairs allow to obtain different combinations of energy bandgap  $E_G$  and carrier density  $N_s$  [4, 7, 8]; hence, we considered  $V$  and  $N_s$  as independent inputs of the model.

In the next subsections we will present the different components of the simulator.

### 5.2.2 Model for the bandstructure

We have employed the analytical energy dispersion relation stemming from the simplified Hamiltonian reported in Eq.3.45 of Sec.3.4.1. Here we want just to remind that this Hamiltonian, which is obtained using an expansion of the full-band Hamiltonian close to one of the six K points of the FBZ of GBL, is simplified because, between the two layers, it considers only the interactions related to the atoms aligned according to the Bernal stacking [4, 9, 7] (see Sec.3.4.1 for a deeper explanation). Moreover, the interfaces are assumed ideally flat and the graphene bilayer band structure unaffected by the top and the bottom dielectrics.

As already mentioned in Sec.3.4.1, the energy dispersion reported in Eq.3.46 is isotropic and non-monotonic. Fig.5.3 shows the two branches of the conduction band  $E_1(k)$  and  $E_2(k)$  for different values of  $E_G$ , which is in turn set by the voltage  $V$  (see Eq.3.47 of Sec.3.4.1) [4].

### 5.2.3 Scattering rates

In our transport model we considered only the lowest branch of the conduction band, namely  $E_1(k)$  in Eq.3.46. In the close to equilibrium regime corresponding to the definition of mobility the second conduction band  $E_2(k)$  is well above the Fermi level for all the  $N_s$  of practical interest (see Fig.5.4), thus it can be safely neglected. We will further comment this point in Sec.5.3.2.

A discussion on the relevant scattering mechanisms in GBL can be found in Sec.3.4.3. Here we only recall that in GBL intrinsic as well as remote phonons play an important role at room temperature [10]. Hence, in this chapter we consider both the phonons intrinsic to graphene and the RP stemming from the  $\text{SiO}_2$  and  $\text{HfO}_2$  gate dielectrics (see Fig.5.1). In contrary, we neglect edge roughness scattering because we assume a wide GBL sheet and flexural phonon modes because GBL is sandwiched between two oxide layers [11, 12].

In this chapter we have employed a simplified version of the expressions of the scattering rates related to intrinsic phonons presented in Sec.3.4.3. Indeed, we have applied an approximation that results in isotropic total scattering rates. In particular, we have replaced the scattering rates with the momentum relaxation rates, following [13]. This means that we multiplied the expressions of the transition rate given by Eqs.3.55 and 3.56 by  $(1 - \cos\theta)$  and took an average

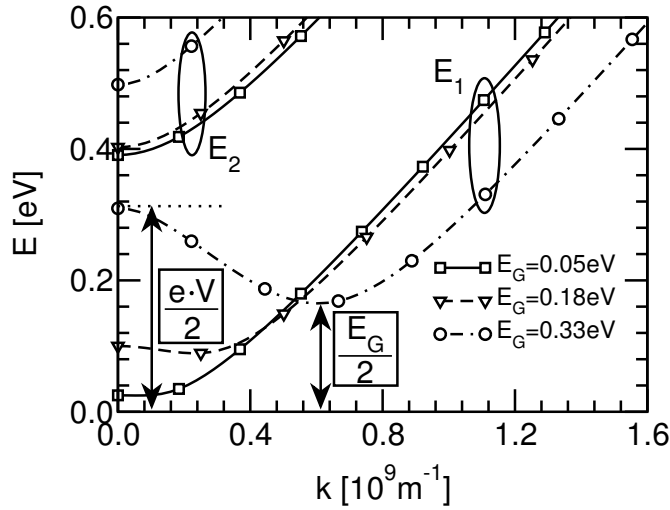


Figure 5.3: Profiles of the energy dispersion relations  $E_1$  and  $E_2$  of the graphene bilayer for different energy gap  $E_G$  controlled by the applied voltage  $V$ . The mid-gap is taken as the reference for the energy.

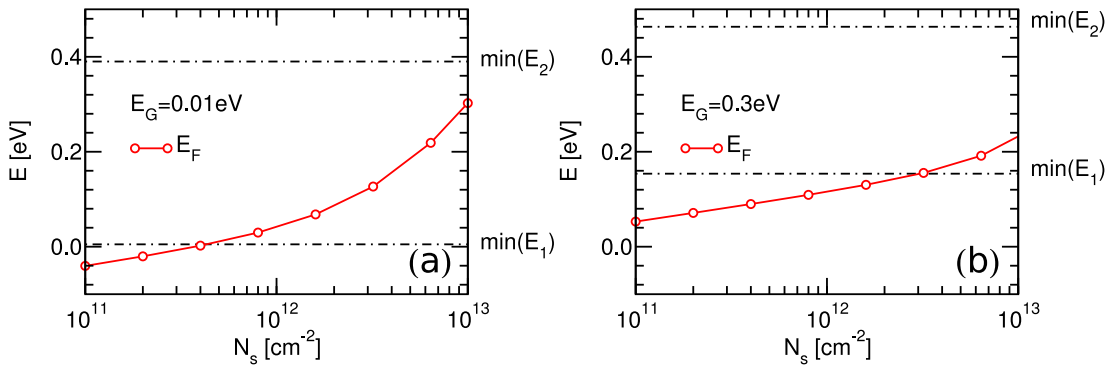


Figure 5.4: Dependence of the Fermi level versus the charge density  $N_s$  for  $E_G = 0.01 \text{ eV}$  (a) and  $0.3 \text{ eV}$  (b) calculated by solving the integral equation that links the Fermi level  $E_F$  to the carrier density  $N_s$  compared with the minimum of the two branches of the GBL conduction band calculated using Eq.3.46.

over  $\theta$ , where  $\theta$  is the angle between the initial and the final states<sup>1</sup>. We have finally obtained the following isotropic expressions for the total scattering rates related to intra-valley acoustic phonons and optical inelastic phonons:

$$S_{AP}(E(k_i)) = \frac{1}{2} \frac{2\pi K_B T D_{ac}^2}{\rho_{GBL} \hbar v_s^2} \frac{DOS[E(k_i)]}{n_s n_v} \quad (5.1)$$

$$S_{OP}(E(k_i)) = \frac{\pi D_{op}^2}{\omega_{OP} \rho_{GBL}} \left( n_{op} + \frac{1}{2} \mp \frac{1}{2} \right) \frac{DOS[E(k_i) \pm \hbar \omega_{OP}]}{n_s n_v} \quad (5.2)$$

The values of the parameters can be found in Sec.3.4.3. The density of states present in Eq.5.1 and 5.2 is divided by  $(n_s n_v)$  since acoustic and optical phonons are intra-valley and conserve the spin.

In contrary, the scattering rate with the phonons originated in the dielectrics is calculated using the same expression reported in Sec.3.4.3 [14, 10, 15]. Hence the employed expression of the total scattering rate becomes

$$S_{RP_m}(k_i) = \frac{1}{\pi \hbar} \sum_{f=f_1, f_2} \left| k_f \frac{dE}{dk} \Big|_{k_f} \right| \int_0^\pi |M_m(q, \theta)|^2 d\theta \quad (5.3)$$

where  $\theta$  is the angle between the initial  $\mathbf{k}_i$  and the final wave-vector  $\mathbf{k}_f$ ,  $q^2 = (k_i^2 + k_f^2 - 2k_i k_f \cos \theta)$  is the magnitude of the exchanged wave-vector  $\mathbf{q} = (\mathbf{k}_f - \mathbf{k}_i)$  and  $m$  indicates the material originating the phonon (i.e.  $m = \text{SiO}_2$  or  $\text{HfO}_2$ ). The matrix element is:

$$|M_m(q, \theta)|^2 = e^2 |F_{\mathbf{k}_i, \mathbf{k}_f}|^2 \left[ n_{RP_m} + \frac{1}{2} \mp \frac{1}{2} \right] \frac{\hbar \omega_{SO_m}}{2q \hat{\epsilon}_m} \quad (5.4)$$

where upper and lower sign stands for absorption and emission, respectively. As already discussed in Sec.3.4.3, due to the non-monotonic GBL energy relation it is possible that more than one wave-vector  $k_f$  contributes to the total scattering rate. The spinor-overlaps  $F_{\mathbf{k}_i, \mathbf{k}_f}$  were calculated directly by using the wave-vectors of the simplified Hamiltonian reported in Eq.3.45, that are analytically known [7]. Moreover, with respect to Eq.3.57, we set  $d=0$  because we verified that the  $d$  value does not affect the results as long as it is smaller than a few Å.

Finally, we want to remark that in our model all the remote phonon scattering rates were left unscreened; we discuss the possible effects of the screening produced by the free carriers in Sec.5.3.3.

## 5.2.4 Monte Carlo implementation

An introduction to the Monte Carlo approach to the solution of the BTE can be found in Appx.C. We have extended to GBL the Monte Carlo for monolayer Graphene NanoRibbons (GNRs) presented in [13]. This is not just a change in the energy dispersion relation, since from Eq.3.46 we cannot obtain an analytical formulation of its inverse  $k(E)$  due to its non-monotonic behavior (see Sec.3.4). The Mexican-hat shape of the  $E(k)$  implies that for a given energy  $E$  the modulus of the wave-vector  $k$  is in some cases undefined (two  $k$  values have the same energy) and this demands for a treatment of scattering as a function of  $k$  and not of as a function of  $E$ , as for an isotropic material.

Even for a simple elastic scattering mechanisms, when determining the state after scattering for ranges of energy smaller than a critical value  $E_{cr} = eV/2$  (see Fig.5.5), we should consider both the two equi-energy circles corresponding to the final energy the carrier will scatter to (see Fig.5.5). We thus compute the relative contribution of each circle to the DOS at the energy corresponding to the final state. For example, let us consider an optical phonon emission, whose

<sup>1</sup>This is the same approximation explained by Eq.4.34 in Chap.4.

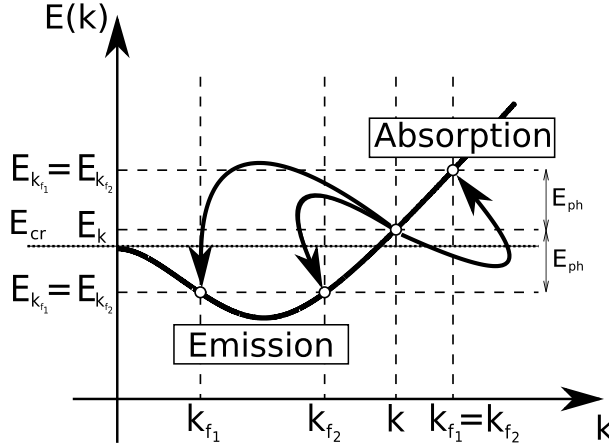


Figure 5.5: Sketch of the energy relation showing that two values of  $k_f = |\mathbf{k}'|$  are possible for any energy  $E$  below  $E_{cr} = eV/2$ . Thus the phonon emission event illustrated in the figure has two possible wave-vectors  $k_{f_1}$  and  $k_{f_2}$ .

total scattering rate depends on the DOS corresponding to the final energy  $E_f$  (see Eq.5.2). When the final energy is below  $E_{cr}$  (as depicted in Fig.5.5), the DOS can be calculated as (see Eq.3.54)

$$DOS(E_f) = \frac{n_v n_s}{2\pi} \left[ k_{f_1} \frac{1}{\left| \frac{dE}{dk} \right|_{k_{f_1}}} + k_{f_2} \frac{1}{\left| \frac{dE}{dk} \right|_{k_{f_2}}} \right] \quad (5.5)$$

where  $k_{f_1}$  and  $k_{f_2}$  are defined in Fig.5.5. In this condition, the probability for the final state to be associated to the wave-vector  $k_{f_i}$  has been calculated as:

$$p[k_f == k_{f_i}] = \frac{k_{f_i} \frac{1}{\left| \frac{dE}{dk} \right|_{k_{f_i}}}}{k_{f_1} \frac{1}{\left| \frac{dE}{dk} \right|_{k_{f_1}}} + k_{f_2} \frac{1}{\left| \frac{dE}{dk} \right|_{k_{f_2}}}} \quad (5.6)$$

with  $i = 1, 2$ .

The situation is much more complicated in anisotropic and inelastic scattering mechanisms such as remote phonons. In this case the scattering rates are calculated as a function of the initial  $k$  rather than the initial energy. Similarly to simple elastic scattering, when the final energy is smaller than  $E_{cr}$  the selection of  $k_f$  is done by calculating the contribution of each possible final  $k$  value to the total scattering rate, i.e.:

$$p[k_f == k_{f_i}] = \frac{k_{f_i} \frac{1}{\left| \frac{dE}{dk} \right|_{k_{f_i}}} \int_0^\pi |M_m(q_{f_i}, \theta)|^2 d\theta}{\sum_{f=f_1, f_2} k_f \frac{1}{\left| \frac{dE}{dk} \right|_{k_f}} \int_0^\pi |M_m(q_f, \theta)|^2 d\theta}. \quad (5.7)$$

Moreover, the contribution of all the possible final angles for both  $k_f$  values has to be known to select the direction of the particle after the scattering.

Regarding the treatment of carrier degeneracy, i.e. accounting for the Pauli's exclusion principle [16] (see Appx.C for further details), the choice of the parameters for the mesh in  $k$ -space used to sample the occupation function  $f(k_x, k_y)$  is not trivial and has been carefully optimized. If the mesh is too dense, the statistical weight of every simulated electron is high and a huge number of particles has to be used for the simulation of highly degenerate cases. At the same time, a too coarse discretization is not able to sample correctly the carrier distribution function. A trade-off between these two different requirements has been identified, by discretizing the  $\mathbf{k}$

space (described by polar coordinates) using a uniform mesh defined by constant steps equal to  $\sim 5 \times 10^6 \text{m}^{-1}$  and  $4^\circ$  in the radial and in the angular direction, respectively; with this choice, as it can be seen in Fig.5.6, we were able to obtain accurate results using 500000 particles in the simulations.

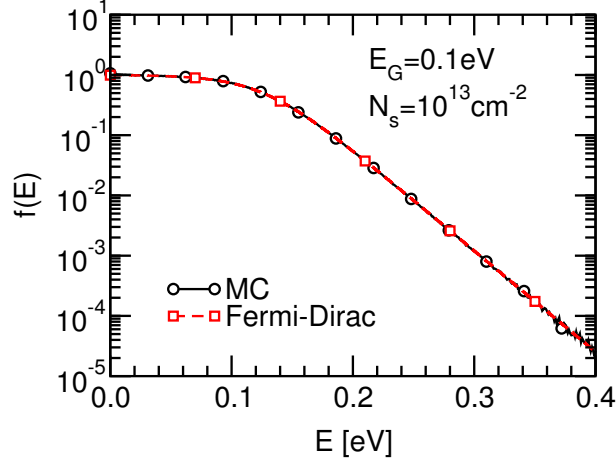


Figure 5.6: The occupation function  $f(E)$  calculated by the MC is in very good agreement with an the ideal Fermi-Dirac distribution thus validating the treatment of the Pauli's exclusion principle employed in our simulator and taken from [16].

## 5.3 Simulation results

### 5.3.1 Low-field mobility

Fig.5.7 shows the Monte Carlo simulations for the low-field mobility as a function of the total inversion density  $N_s$  for a GBL, calculated for different  $E_G$  values and either considering or not the Remote Phonons (RPs) originating in the dielectrics. As it can be seen, the mobility is largely dominated by the RPs, since it increases dramatically when switching off the RP scattering. Hence, the uncertainties in the value of the deformation potentials discussed in Sec.3.2.4 for intrinsic phonons are not expected to affect critically the main results of our analysis.

Fig.5.8 is focused on the low-field mobility calculated considering the remote phonons. As can be seen, similar to GNRs [17, 18], the mobility decreases as the bandgap increases. Moreover it should be noted that the case with the largest gap may not be achievable in a real device because it would require a too high electric field between the two layers (see Sec.3.4.1). In Fig.5.8 we also notice that the mobility slightly increases for  $N_s \geq 10^{12} \text{cm}^{-2}$ . This is an unusual behavior compared to silicon MOSFETs and it is not due to the screening effect because the screening is not included in these calculations. In order to clarify this behavior, in Fig.5.9 we analyzed the Fermi level  $E_F$  corresponding for different  $N_s$  and  $E_G$  values. Due to a lower density of states close to the band minimum, the graphene bilayers with small gaps are heavily degenerate for  $N_s \geq 10^{12} \text{cm}^{-2}$ . Most importantly,  $E_F$  increases remarkably with  $N_s$  thus populating states with progressively larger wave-vectors and carrier velocities. The higher velocities improve directly the mobility, but also the larger wave-vectors are beneficial. In fact since the RP scattering rate is inversely proportional to  $q = |\mathbf{k}_f - \mathbf{k}_i|$ , then it produces preferably small  $\mathbf{k}$  changes and it becomes progressively less effective in the randomization of  $\mathbf{k}$  when  $N_s$  is increased. The modulation of  $E_F$  with  $N_s$  is much less pronounced in bilayers with large  $E_G$  because of the larger density of states with respect to small gaps and consequently the group

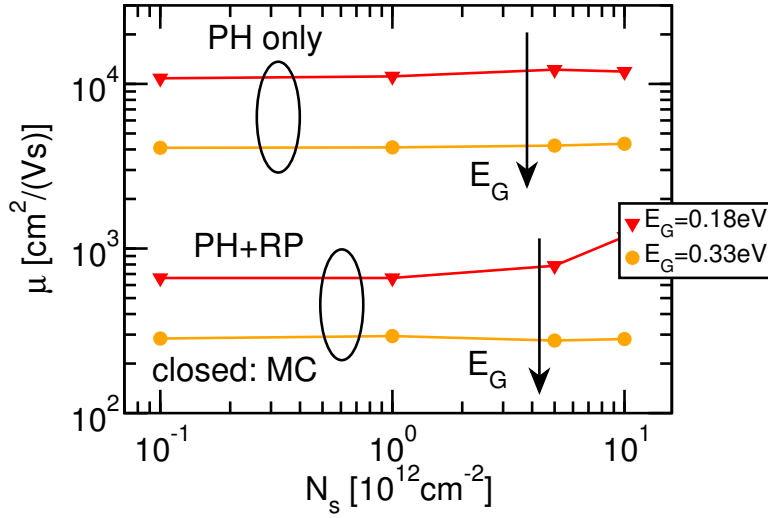


Figure 5.7: Graphene bilayer mobility versus the inversion density  $N_s$  for various values of the energy gap  $E_G$  calculated using the Monte Carlo approach considering (PH+RP curves) and not considering (PH curves) the remote phonons originating in the gate dielectrics.

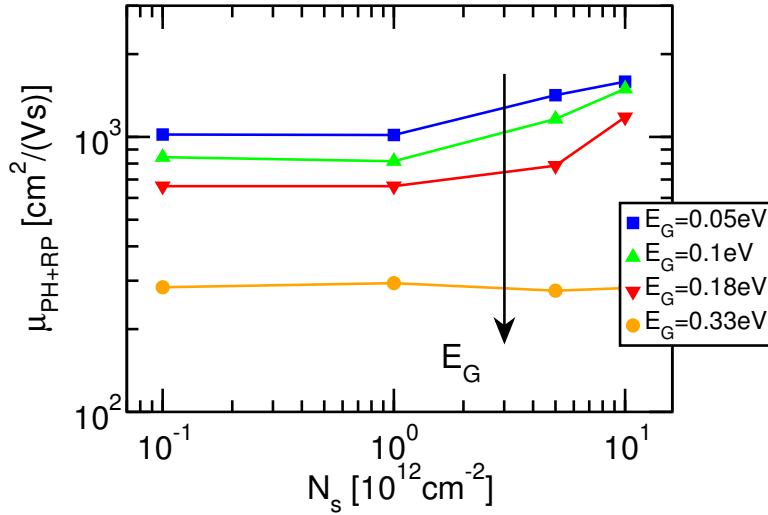


Figure 5.8: Graphene bilayer mobility versus the inversion density  $N_s$  for various values of the energy gap  $E_G$  calculated using the Monte Carlo approach.

velocity is also less sensitive to  $N_s$ . To make our argument more quantitative we calculated the effective values  $v_{mob}$  and  $k_{mob}$  for the magnitude of respectively the velocity and wave-vector. By recalling the calculation of mobility according to the MRT [19], we defined  $k_{mob}$  as

$$k_{mob} = \frac{\sum_{\mathbf{k}} k f_0(E(k)) [1 - f_0(E(k))]}{\sum_{\mathbf{k}} f_0(E(k)) [1 - f_0(E(k))]} \quad (5.8)$$

where  $f_0(E)$  is the Fermi Dirac occupation function. For each  $E_G$ , hence each energy relation, the  $N_s$  univocally determines the Fermi level, which in turn allows us to calculate  $k_{mob}$  by converting the sums in Eq.5.8 to integrals over  $\mathbf{k}$  according to the standard prescriptions [19]. The  $v_{mob}$  is obtained by substituting  $k$  with  $|v_x|$  in Eq.5.8. Fig.5.10 shows that both  $k_{mob}$  and  $v_{mob}$  increase appreciably with  $N_s$  for  $E_G=0.05\text{eV}$  and such an effect is much less pronounced at large energy gaps, thus confirming our explanation of the mobility increase with  $N_s$ .

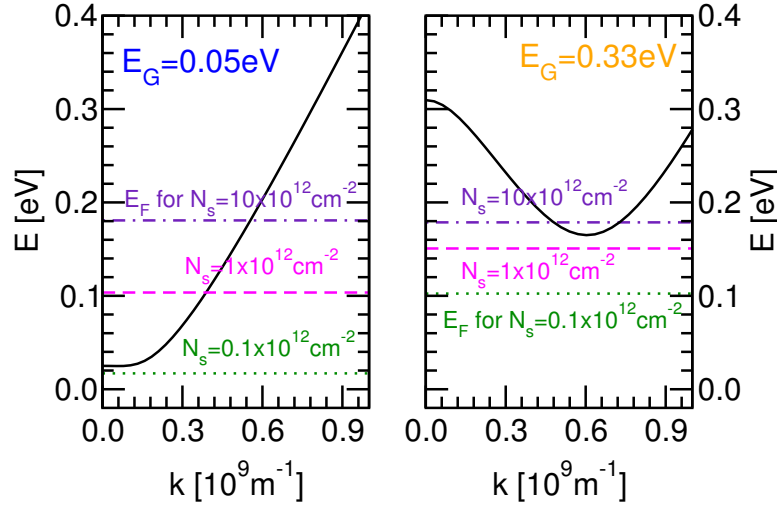


Figure 5.9: Value of the Fermi level for different inversion densities  $N_s$  and corresponding energy relation for  $E_G=0.05\text{eV}$  (left) and  $E_G=0.33\text{eV}$  (right).

Fig.5.11 compares the results calculated by the MC simulator (continuous curves) with the ones obtained by solving the linearized Boltzmann Transport Equation applied to the GBL sketched in Fig.5.1 by using the novel approach proposed in Chap.4 (dotted curves). We note that, as it should be, the LBTE solver and MC results are in close agreement. The simulations are also in good agreement with experiments in [20] for a device structure similar to the one in Fig.5.1, where an average field-effect mobility of about  $1400\text{cm}^2/(\text{Vs})$  was found (presumably with biases inducing only a small  $E_G$ ).

Fig.5.12 compares the low-field mobility calculated in this chapter with the MC and reported in Fig.5.8 with the one calculated by the LBTE solver presented in Chap.4 (see Fig.4.3): as it can be seen, the approximations employed in this chapter on the calculation of the scattering rates related to acoustic and optical phonons have a small but not negligible impact on the results at low  $E_G$  and high  $N_s$ .

Finally, Fig.5.13 shows the low-field mobility limited by intrinsic (dashed curves) and remote phonons (continuous curves) for a GBL (blue curves) and a GNR (red curves) as a function of the energy gap  $E_G$ . For the GNR, the low-field mobility has been estimated using the Monte Carlo solver presented in [10], and considering also the effect of the Edge Roughness (ER); moreover, the energy gap has been estimated as [21]

$$E_{G_{GNR}} = \frac{1.57}{W^{1.19}} \quad [\text{eV}] \quad (5.9)$$

where  $W$  is the width of the GNR expressed in nm. As can be seen, for  $E_G$  larger than the  $0.08\text{eV}$ , the mobility of the bilayer is higher than for GNRs.

### 5.3.2 Saturation velocity

The simulated drift velocity  $v_d$  versus the in-plane driving electric field  $F_x$  for a graphene bilayer with various  $E_G$  and  $N_s$  is shown in Fig.5.14. For small  $E_G$  values the velocity saturates at  $F_x \approx 5 \times 10^4 \text{V/cm}$  to the slightly  $N_s$ -dependent value of about  $3 \times 10^7 \text{cm/s}$ , which is much higher than in silicon but smaller than the saturation velocity of monolayer graphene [10, 22] (see Fig.5.15). Moreover, the entire velocity versus  $F_x$  curve decreases when the bandgap increases. We verified that at the largest  $F_x$  values the average carrier energy is comparable to the minimum of the second conduction band  $E_2$  (see Fig.5.16); in such cases the second

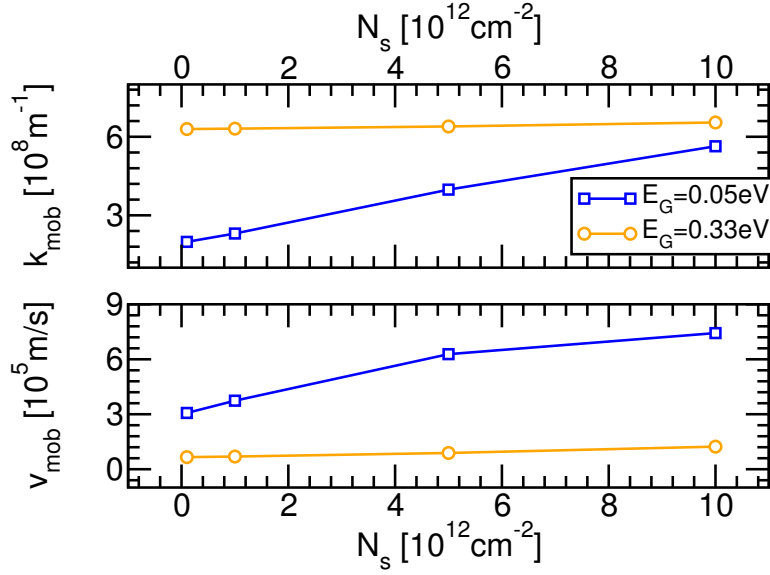


Figure 5.10: Values of  $k_{mod}$ , defined in Eq.5.8 (top), and  $v_{mod}$  (bottom) versus the inversion density  $N_s$  for different values of the energy gap  $E_G$ . For  $E_G=0.33\text{eV}$ ,  $k_{mod}$  and  $v_{mod}$  are independent of the inversion density, thus leading to a constant  $\mu_{PH+RP}$  mobility. Instead, for smaller energy gap both  $k_{mod}$  and  $v_{mod}$  increase with  $N_s$ , thus leading to an increase of the mobility (the increase of  $k_{mod}$  results in an increase of the average exchange vector  $q$  that reduces the remote phonons scattering rates).

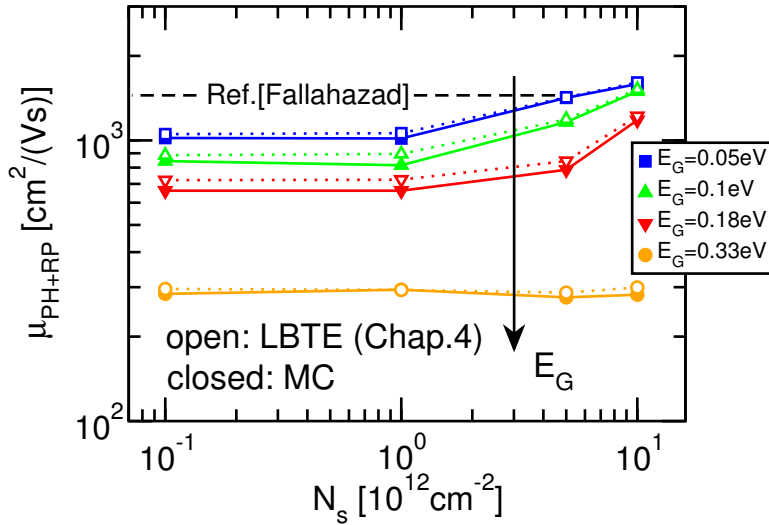


Figure 5.11: Comparison between the GBL low-field mobility versus the inversion density  $N_s$  for various values of the energy gap  $E_G$  calculated using the Monte Carlo (continuous lines with closed symbols) and the novel approach for the solution of the LBTE proposed in Chap.4 (dotted lines with open symbols). Experimental data from [20] are also reported for comparison.

conduction band should be included in the calculations, so that the accuracy of the simulations for small  $E_G$  is expected to be quite modest for  $F_x \gtrsim 5 \times 10^4 \text{V/cm}$ .

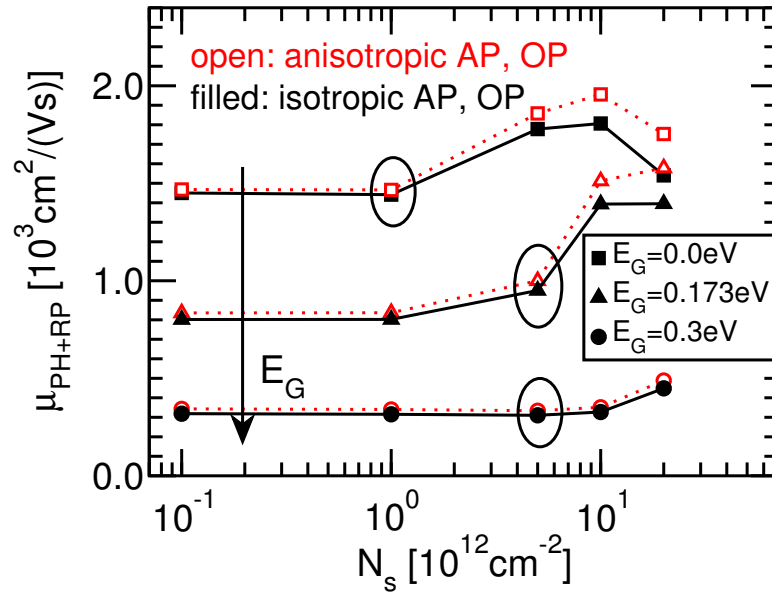


Figure 5.12: Comparison between the GBL low-field mobility calculated for different energy gaps considering (filled symbols, curves taken from Fig.5.8) and not considering (open symbols, curves taken from Fig.4.3) the approximation of isotropic scattering rate applied in this chapter to acoustic and optical phonons.

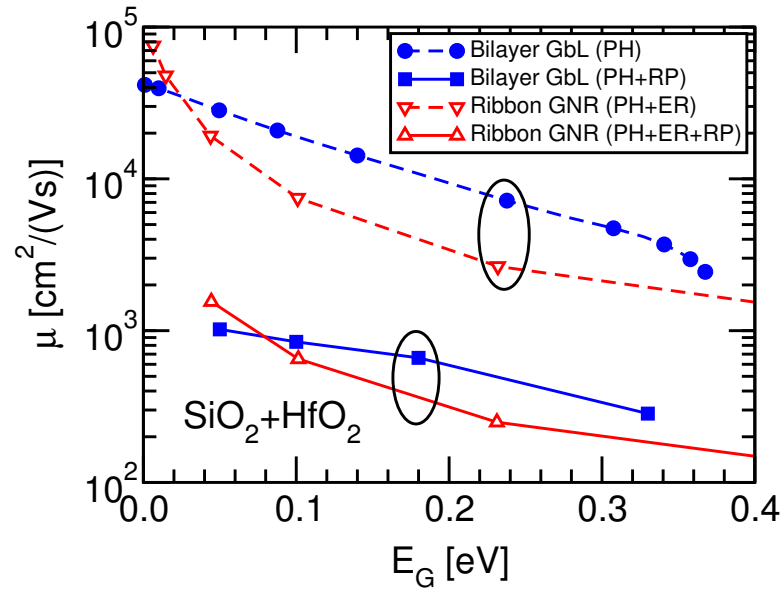


Figure 5.13: Comparison between the low-field mobilities calculated for GBL (blue curves) and GNR (red curves) versus the induced energy gap  $E_G$  considering (continuous curves) and not considering (dashed curves) the remote phonons. The width of the considered GNRs ranges between 3nm and 65nm.

### 5.3.3 Screening of remote phonons

In the simulations reported in this chapter the matrix elements for the remote phonons were left unscreened, thus implicitly assuming that the phonon energy is large enough for a complete dynamic de-screening of the scattering potential [19]. In order to test the impact of the screening

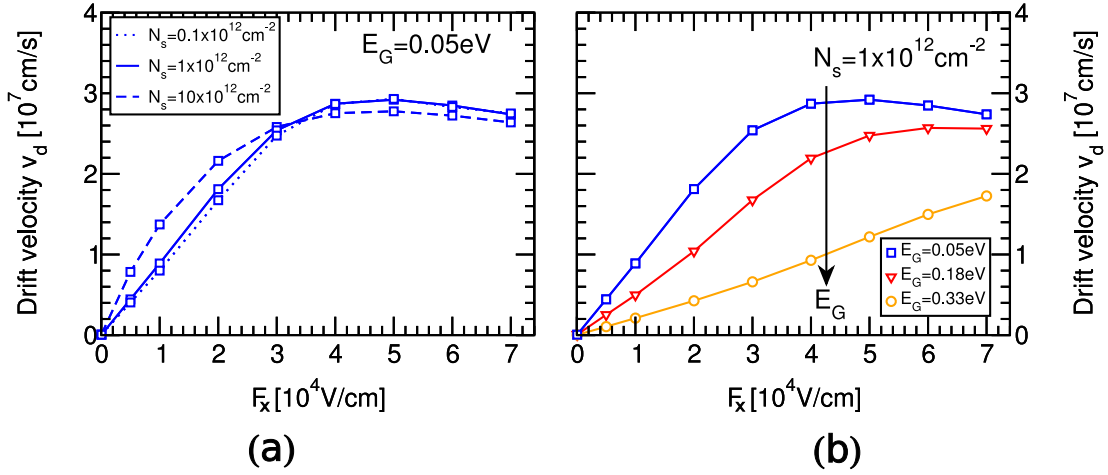


Figure 5.14: Simulated drift velocity  $v_d$  versus the driving electrical field  $F_x$  for the graphene bilayer (a) for different energy gaps at  $N_s=1 \times 10^{12}\text{cm}^{-2}$  (b) for various inversion densities  $N_s$  at  $E_G=0.05\text{eV}$ : the dependence of  $v_d$  on  $N_s$  is weak.

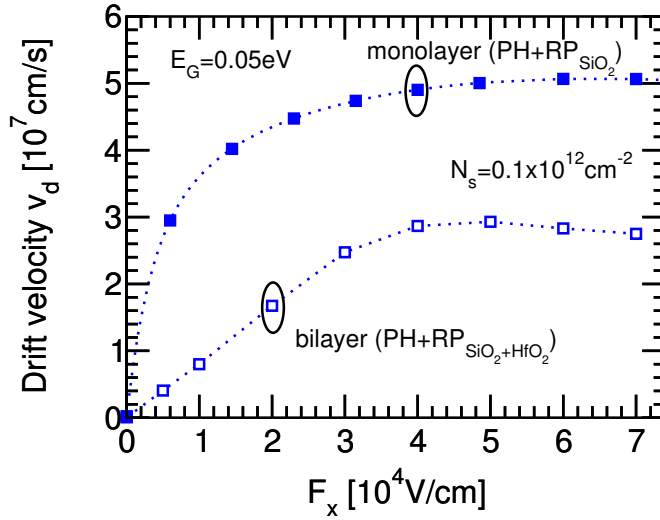


Figure 5.15: Comparison between the GBL and GNR drift velocities calculated for  $E_G=0.05\text{eV}$ , that is obtained by applying a voltage  $V = 0.05\text{V}$  on the bilayer and by considering a 26nm width GNR. The GNR simulations have been performed using the MC solver for GNR presented in [10].

on our results, in Fig.5.17 we repeated some of the mobility calculations based on the solution of the LBTE by overestimating the effect of screening, that is we used a static dielectric function  $\epsilon_{GBL}(\mathbf{q})$  to screen the remote phonons. The  $\epsilon_{GBL}(\mathbf{q})$  was calculated by extending to the bilayer graphene sheets the formulation of [23], by considering only the lowest branch of the conduction band ( $E_1$  in Fig.5.3), and by using the spinor overlaps  $F_{\mathbf{k},\mathbf{k}+\mathbf{q}}$  defined in Sec.5.2.3:

$$\epsilon_{GBL}(\mathbf{q}) = 1 + \frac{e^2}{(\epsilon_{\text{SiO}_2} + \epsilon_{\text{HfO}_2})q} \Pi(\mathbf{q}) \quad (5.10)$$

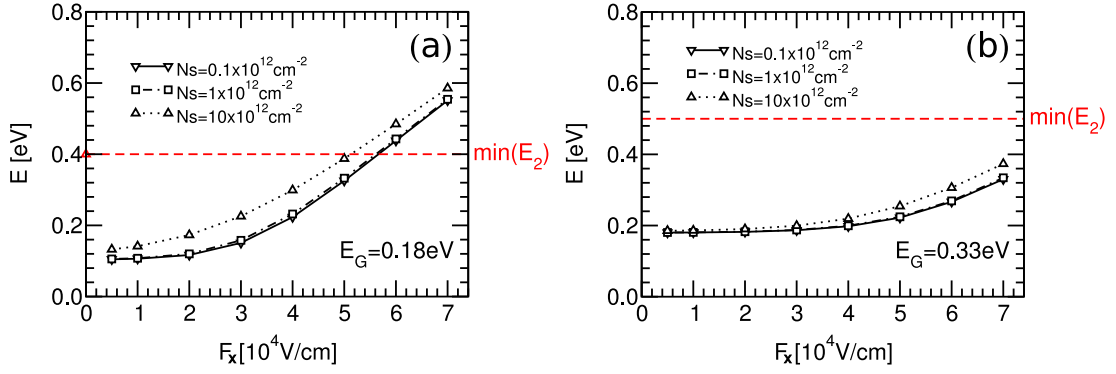


Figure 5.16: Average carrier energy as a function of the applied electric field  $F_x$  for (a)  $E_G = 0.18\text{eV}$  and (b)  $E_G = 0.33\text{eV}$  calculated for different carrier densities  $N_s$ . The dashed lines represent the bottom of the second branch of the conduction band calculated using Eq.3.46.

where

$$\Pi(\mathbf{q}) = -\frac{n_v n_s}{(2\pi)^2} \int_{\mathbf{k}} \frac{|F_{\mathbf{k}, \mathbf{k}+\mathbf{q}}|^2 [f_0(E_1(\mathbf{k})) - f_0(E_1(\mathbf{k}+\mathbf{q}))]}{E_1(\mathbf{k}) - E_1(\mathbf{k}+\mathbf{q})} d\mathbf{k}. \quad (5.11)$$

As expected, the effect of the screening emphasizes remarkably the mobility increase at large inversion density, whereas its impact is only modest at small  $N_s$ . An estimate of the energies for the plasma oscillations in the graphene bilayer shows that they are comparable to the remote phonon energies, hence screening the remote phonons with the dynamic dielectric function appears to be more appropriate and can be considered as a further development of the work presented in this chapter (see also Sec.3.2.4).

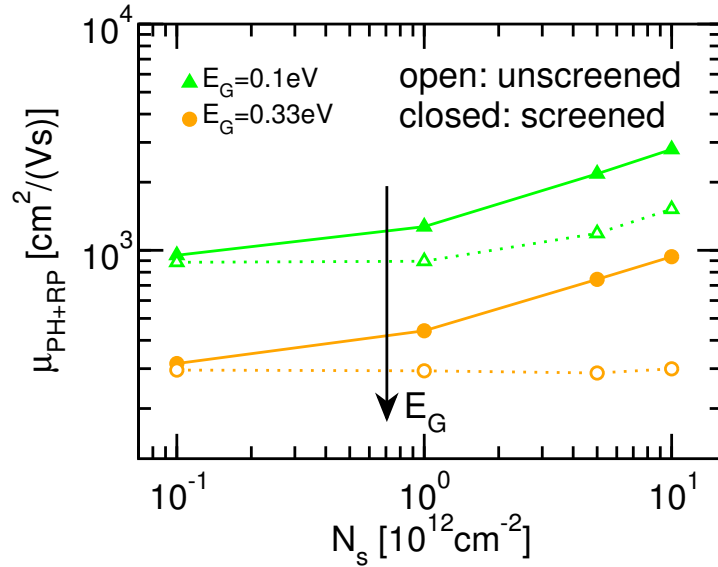


Figure 5.17: Graphene bilayer mobility versus inversion density  $N_s$  considering (lines with closed symbols) and not considering (dotted lines with open symbols) the static screening of the carriers, simulated using the LBTE approach for different values of the energy gap  $E_G$ . As expected, the behavior of increasing mobility with  $N_s$  is enhanced when screening is introduced.

## 5.4 Conclusions

We have studied the mobility and the saturation velocity of graphene bilayer using a Monte Carlo simulator, considering the local graphene phonons and the remote phonons originated in the dielectrics of an idealized double-gate stack. The simulations suggest that the low-field phonon limited mobility is strongly-dependent on the energy-gap and in some cases, due to the particular shape of the dispersion relation, increases with the inversion density. Our results are in fairly good agreement with the data reported in [20].

According to our models the mobility in these idealized GBL double-gate transistors is ultimately limited by the RP scattering. The velocity saturation is expected to reach a value of about  $3 \times 10^7$  cm/s, which is much higher than in silicon; with respect to monolayer graphene, the saturation velocity is higher in bilayer graphene only at high  $N_s$ . The model limitations and some possible refinements are also critically discussed in Sec.5.3.3.

# Bibliography

- [1] K. Bolotin, K. Sikes, Z. Jiang, M. Klima, G. Fudenberg, J. Hone, P. Kim, and H. Stormer, “Ultrahigh electron mobility in suspended graphene,” *Solid State Communications*, vol. 146, no. 9-10, pp. 351–355, June 2008.
- [2] A. Geim, “Graphene update,” *Bulletin of the American Physical Society*, vol. 55, 2010.
- [3] P. Gava, M. Lazzeri, A. M. Saitta, and F. Mauri, “Ab initio study of gap opening and screening effects in gated bilayer graphene,” *Phys. Rev. B*, vol. 79, no. 16, p. 165431, Apr 2009.
- [4] E. McCann, “Asymmetry gap in the electronic band structure of bilayer graphene,” *Phys. Rev. B*, vol. 74, no. 16, p. 161403, Oct 2006.
- [5] G. Fiori and G. Iannaccone, “On the Possibility of Tunable-Gap Bilayer Graphene FET,” *Electron Device Letters, IEEE*, vol. 30, no. 3, pp. 261 –264, 2009.
- [6] B. N. Szafranek, D. Schall, M. Otto, D. Neumaier, and H. Kurz, “Electrical observation of a tunable band gap in bilayer graphene nanoribbons at room temperature,” *Applied Physics Letters*, vol. 96, no. 11, p. 112103, 2010.
- [7] L. A. Falkovsky, “Screening in gated bilayer graphene,” *Phys. Rev. B*, vol. 80, no. 11, p. 113413, Sep 2009.
- [8] M. Cheli, G. Fiori, and G. Iannaccone, “A Semianalytical Model of Bilayer-Graphene Field-Effect Transistor,” *Electron Devices, IEEE Transactions on*, vol. 56, no. 12, pp. 2979–2986, dec. 2009.
- [9] J. Nilsson, A. H. Castro Neto, F. Guinea, and N. M. R. Peres, “Electronic properties of bilayer and multilayer graphene,” *Phys. Rev. B*, vol. 78, no. 4, p. 045405, Jul 2008.
- [10] M. Bresciani, A. Paussa, P. Palestri, D. Esseni, and L. Selmi, “Low-field mobility and high-field drift velocity in graphene nanoribbons and graphene bilayers,” in *Electron Devices Meeting (IEDM), 2010 IEEE International*, 2010, pp. 32.1.1 –32.1.4.
- [11] E. Mariani and F. von Oppen, “Temperature-dependent resistivity of suspended graphene,” *Phys. Rev. B*, vol. 82, no. 19, p. 195403, Nov 2010.
- [12] H. Ochoa, E. V. Castro, M. I. Katsnelson, and F. Guinea, “Temperature-dependent resistivity in bilayer graphene due to flexural phonons,” *Phys. Rev. B*, vol. 83, p. 235416, Jun 2011.
- [13] M. Bresciani, P. Palestri, D. Esseni, and L. Selmi, “Simple and efficient modeling of the e-k relationship and low-field mobility in graphene nano-ribbons,” *Solid-State Electronics*, vol. 54, no. 9, pp. 1015 – 1021, 2010.

- 
- [14] S. Fratini and F. Guinea, "Substrate-limited electron dynamics in graphene," *Physical Review B (Condensed Matter and Materials Physics)*, vol. 77, no. 19, p. 195415, 2008.
- [15] X. Li, E. A. Barry, J. M. Zavada, M. B. Nardelli, and K. W. Kim, "Surface polar phonon dominated electron transport in graphene," *Applied Physics Letters*, vol. 97, no. 23, p. 232105, 2010.
- [16] P. Lugli and D. K. Ferry, "Degeneracy in the ensemble Monte Carlo method for high field transport in semiconductors," *Electron Devices, IEEE Transactions on*, vol. 32, no. 11, pp. 2431–2437, 1985.
- [17] X. Li, X. Wang, L. Zhang, S. Lee, and H. Dai, "Chemically Derived, Ultrasoft Graphene Nanoribbon Semiconductors," *Science*, vol. 319, no. 5867, pp. 1229–1232, 2008.
- [18] X. Wang, Y. Ouyang, X. Li, H. Wang, J. Guo, and H. Dai, "Room-Temperature All-Semiconducting Sub-10-nm Graphene Nanoribbon Field-Effect Transistors," *Phys. Rev. Lett.*, vol. 100, p. 206803, May 2008.
- [19] D. Esseni, P. Palestri, and L. Selmi, *Nanoscale MOS Transistors: Semi-Classical Transport and Applications*. Cambridge University Press, 2011.
- [20] B. Fallahazad, S. Kim, L. Colombo, and E. Tutuc, "Dielectric thickness dependence of carrier mobility in graphene with HfO<sub>2</sub> top dielectric," *Applied Physics Letters*, vol. 97, no. 12, p. 123105, 2010.
- [21] J. Lyding and K. Ritter, "SPM Studies of Edge States in Graphene Quantum Dots and Nanoribbons," in *2009 IEEE Nanotechnology Conference*, July 2009, pp. 33–34.
- [22] I. Meric, M. Y. Han, A. F. Young, B. Ozyilmaz, P. Kim, and K. L. Shepard, "Current saturation in zero-bandgap, top-gated graphene field-effect transistors," *Nat Nano*, vol. 3, no. 11, pp. 654–659, Nov. 2008.
- [23] E. H. Hwang and S. Das Sarma, "Dielectric function, screening, and plasmons in two-dimensional graphene," *Phys. Rev. B*, vol. 75, no. 20, p. 205418, May 2007.

## Chapter 6

# Monte Carlo Approach for the Simulation of Graphene Transistors

## 6.1 Introduction

As already mentioned in Chap.1, because of its high carrier mobility graphene is being widely investigated as alternative channel material for future MOSFETs. The lack of an energy gap, the consequent high Band-To-Band Tunneling (BTBT) rate which eventually leads to large off-currents strongly limit the use of Graphene FETs (GFETs) in digital applications (see Secs.1.4.2 and 3.2.3). Patterning graphene into nanoribbons [1] or using graphene bilayers [2, 3, 4] can open a gap, but this is associated to a much lower mobility compared to large area monolayer flakes [1, 5, 6, 7, 8]. For these reasons, much of the attention has recently shifted to the use of graphene in RF transistors, where the off-current is less critical and the high carrier velocity allows to achieve large cut-off frequencies ( $f_T$ ) [9, 10, 11, 12, 13]. Indeed, as can be seen in Fig.6.1, in a few years the record performance of GFETs RF transistors have already reached the best  $f_t$  obtained by more well-established technologies.

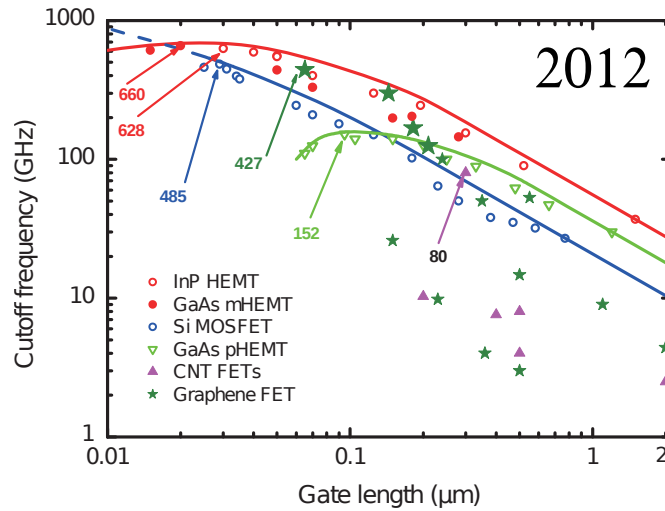


Figure 6.1: Best unity current gain cut-off frequencies  $f_t$  reached by GFETs transistors in 2012 versus the best performance obtained by using other technologies (adapted from [14]).

Numerical models for accurate simulation of realistic, large area graphene devices are necessary to understand experimental results and optimize device performance, in particular in view of analog/RF applications [7, 15]. Semi-classical transport models are well justified to this purpose, since they naturally incorporate the scattering mechanisms responsible for mobility degradation [16, 5]. However, BTBT is a purely quantum mechanical effect and, as discussed in Chap.3, it causes large output conductance, excess off current and ambipolar behavior [15, 17]. Quantum transport models based on the Non-Equilibrium Green's Functions (NEGF) with a tight-binding (TB) Hamiltonian [18] provide a rigorous treatment for BTBT and ballistic transport in graphene devices; some scattering mechanisms (for instance, inelastic phonons) have been added as well [19]. Compared to the NEGF, the semi-classical approach is computationally more efficient in the simulation of long channel devices and allows for an easier and less computationally demanding implementation of a large variety of scattering mechanisms [5, 20, 21]. Models based on the gradual channel approximation or on the drift-diffusion equations have also been proposed [22, 23, 24, 25, 26] but they suffer severe limitations when it comes to describe far from equilibrium transport conditions in short channel GFETs as those expected to yield the largest  $f_T$  [12, 27].

In this chapter we firstly present (Sec.6.2) a Monte Carlo (MC) model to solve the semi-classical transport in GFETs with large width and arbitrary gate length including the main

Generation/Recombination (G/R) mechanisms. Secondly, in Sec.6.3 we validate our model by comparison with the results of a state-of-the-art NEGF simulator based on a TB description of the graphene layer. Finally, in Sec.6.4 we use the MC model to estimate the effect of the BTBT and scattering mechanisms on the output characteristics and RF figures of merit of GFETs with different channel lengths and source/drain (S/D) to channel underlaps.

## 6.2 Semi-classical Monte Carlo model

Fig.6.2 reports the flow chart of the developed simulator.

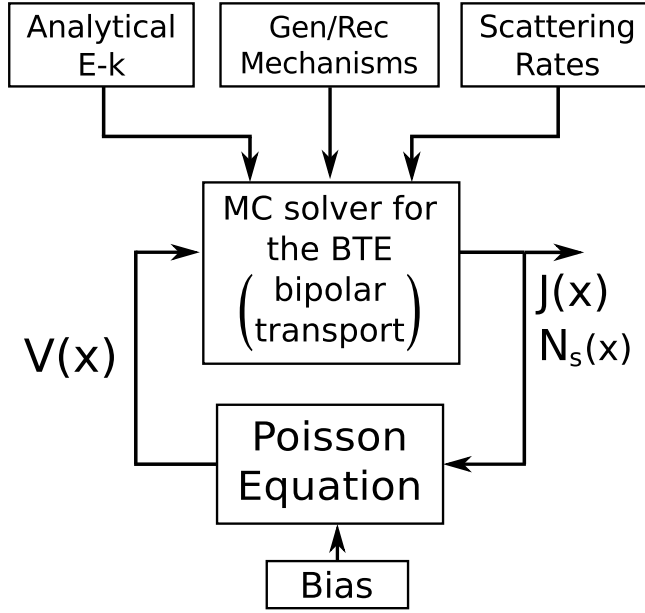


Figure 6.2: Flow chart of the developed simulator: the Boltzmann Transport Equation, solved using a Monte Carlo technique for bipolar transport, has been coupled in a self-consistent loop to the non-linear Poisson's equation that describes the electrostatics of the GFET device.

The gapless energy dispersion relation  $E = \hbar v_f |\mathbf{k}|$  is assumed (see Sec.3.2.2), which is adequate for wide devices as those considered for analog/RF applications. Translational invariance is assumed along the width direction.

An introduction to the Monte Carlo approach to the solution of the BTE can be found in Appx.C. We have extended to short channel GFETs the MC simulator for uniform transport presented in [5]. In particular, we have coupled in a self consistent loop the Boltzmann Transport Equations for electrons and holes to the non-linear Poisson equation, i.e.:

$$\nabla \cdot \left[ \frac{\epsilon(\mathbf{r})}{e} \nabla \Phi(\mathbf{r})^{(k+1)} \right] = n(\mathbf{r})^{(k)} \exp \left( \frac{\Phi(\mathbf{r})^{(k+1)} - \Phi(\mathbf{r})^{(k)}}{K_B T} \right) - p(\mathbf{r})^{(k)} \exp \left( \frac{\Phi(\mathbf{r})^{(k+1)} - \Phi(\mathbf{r})^{(k)}}{K_B T} \right) - N_D(\mathbf{r}) + N_A(\mathbf{r}). \quad (6.1)$$

where  $\Phi(\mathbf{r})^{(k+1)}$  and  $\Phi(\mathbf{r})^{(k)}$  are respectively the potential calculated at the current and at the preceding iteration,  $n(\mathbf{r})^{(k)}$  and  $p(\mathbf{r})^{(k)}$  are the electrons and holes densities at the preceding iteration,  $N_D(\mathbf{r})$  and  $N_A(\mathbf{r})$  are respectively the donor and acceptor densities, and  $\epsilon(\mathbf{r})$  is the

electric permittivity. The non-linear Poisson scheme has been employed in order to achieve a robust coupling between transport and the electrostatics [28]. The boundary conditions for the Poisson equation consist in fixing the potential at top and bottom gates to the gate biases  $V_{TG}$  and  $V_{BG}$  (*Dirichlet conditions*) and setting to zero the derivative of the potential at the S/D contacts (*Neumann conditions*), similarly to what is done in NEGF solvers [29]. Following [30], carriers exiting at the contacts are removed from the simulation, while electron and hole fluxes are steadily injected into the simulation domain according to:

$$I_{e,i} = e W \int_0^{+\infty} \frac{2v_f}{\pi} \frac{DOS(E)}{2} \frac{1}{1 + \exp\left(\frac{E - eV_i - E_{F,i}}{K_B T}\right)} dE \quad (6.2)$$

$$I_{h,i} = e W \int_0^{+\infty} \frac{2v_f}{\pi} \frac{DOS(E)}{2} \frac{1}{1 + \exp\left(\frac{E + eV_i + E_{F,i}}{K_B T}\right)} dE \quad (6.3)$$

where  $v_f \approx 8.8 \times 10^7$  cm/s is the Fermi velocity (defined in Eq.3.10),  $i$  is  $S$  or  $D$ ,  $DOS(E)$  is the density of states of a wide monolayer graphene (see Eq.3.14),  $W$  is the width of the monolayer graphene,  $V_i$  is the electrostatic potential at the source and drain contacts, and  $E_{F,i}$  the corresponding Fermi levels. Fig.6.3 shows a sketch resuming how the contacts are treated in the MC simulator.

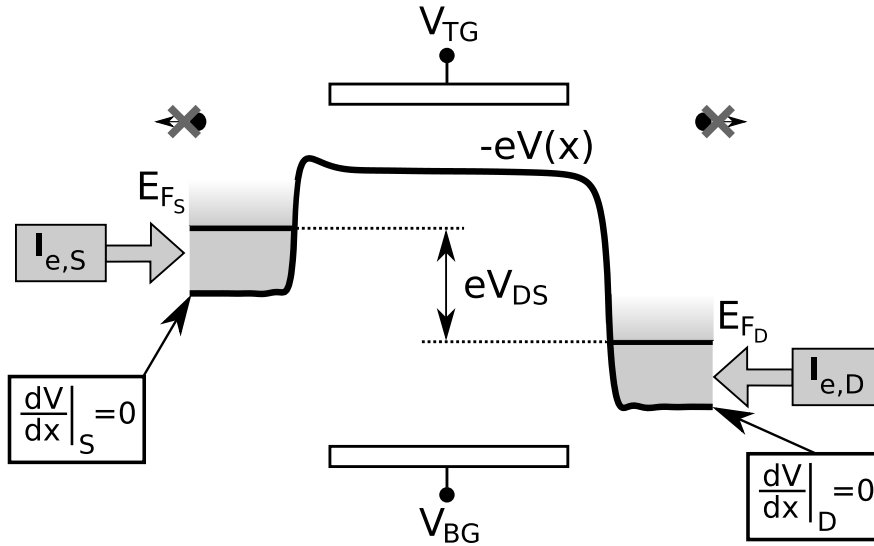


Figure 6.3: Sketch explaining the treatment of the contacts in the MC simulator: electron (or hole) fluxes are steadily injected into the simulation domain at the drain and the source contacts according to Eqs.6.2 and 6.3. The carriers exiting at the contacts are removed from the simulation. Similarly to NEGF simulators, the derivative of the potential at the edges of the domain is set to zero. Moreover, a difference equal to  $eV_{DS}$  has been set between the Fermi levels in the source and in the drain contacts.  $E_{F,S}$  is set to zero.

We have modeled the acoustic and optical phonons of the graphene as in [31], i.e., we have replaced the scattering rates with the momentum relaxation rates, averaged over the angle  $\theta$  between the initial and the final state, similarly to what we have done in Chap.5 for bilayer graphene. The resulting isotropic expressions of the total scattering rates are:

$$S_{AP}(E(k_i)) = \frac{1}{2} \frac{2\pi K_B T D_{ac}^2}{\rho \hbar v_s^2} \frac{DOS[E(k_i)]}{n_s n_v} \quad (6.4)$$

$$S_{OP}(E(k_i)) = \frac{\pi D_{op}^2}{\rho \omega_{OP}} \left( n_{op} + \frac{1}{2} \mp \frac{1}{2} \right) \frac{DOS[E(k_i) \pm \hbar \omega_{OP}]}{n_s n_v} \quad (6.5)$$

where we have used the same parameters reported in Sec.3.2.4. The remote phonons originating in surrounding dielectrics have been modeled using the remote phonon model presented in Sec.3.2.4 [5].

The degeneracy of the carriers has been taken into account with a careful and non trivial numerical implementation of the rejection technique originally proposed in [32], whose effectiveness is demonstrated in Fig.6.4 by comparison with a simple 1D model that couples the 1D electrostatics with the calculation of the charge in the graphene layer according to the Fermi-Dirac statistics. The agreement between the two models indicates that the degeneracy effects (finite DOS) are well reproduced by the self-consistent Monte Carlo model.

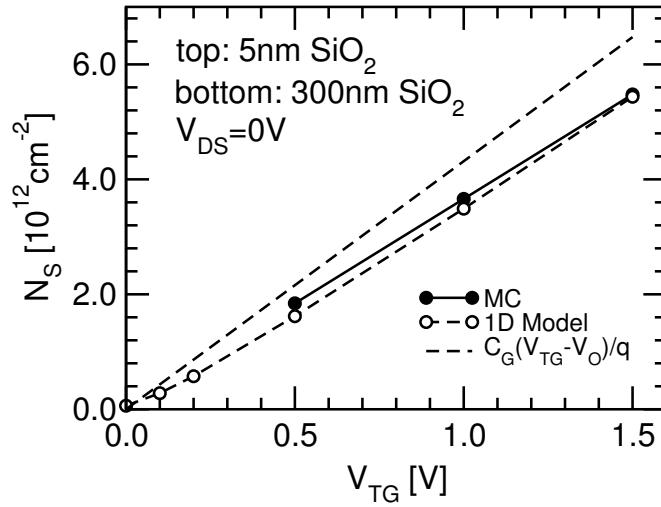


Figure 6.4: Inversion density  $N_s$  versus the top-gate voltage  $V_{TG}$  for a device with a large  $W$  biased with a  $V_{DS} = 0V$  and a back-gate voltage  $V_{BG} = 0V$ .  $V_0$  is the  $V_{TG}$  yielding zero sheet charge density.

Coming now to the G/R mechanisms, we have considered both the BTBT (see Sec.3.3.1) and the recombination assisted by optical phonons (see Sec.3.3.2). Concerning the BTBT, since wide graphene sheets have zero bandgap, we have employed the local model described in Sec.3.3.1 in terms of generation-recombination [20], i.e.:

$$\begin{aligned} G_{BTBT}(x) - R_{BTBT}(x) &\approx \frac{2qF_x(x)(f_v(x) - f_c(x))}{(2\pi)^2 \hbar} \int_{-\infty}^{+\infty} dk_y \exp\left(-\frac{k_y^2 \hbar v_f \pi}{qF_x(x)}\right) \\ &= \frac{f_v(x) - f_c(x)}{\pi^2 \sqrt{v_f}} \left(\frac{qF_x(x)}{\hbar}\right)^{3/2} \end{aligned} \quad (6.6)$$

where  $F_x(x)$  is the magnitude of the local electric field in the transport direction  $x$ ,  $k_y$  the wave-vector in the direction normal to the transport, and  $f_v(x)$  and  $f_c(x)$  are, respectively, the local occupation probabilities of the particles impinging on the classical turning points in the valence and in the conduction bands. Here we want to remind that this net generation rate, derived following the WKB approximation, is consistent with previous works found in the literature [33, 34]; moreover, the maximum net generation rate, obtained by setting  $(f_v - f_c) = 1$  in Eq.6.6<sup>1</sup>, is close to the results obtained with the state of the art NEGF simulator NanoTCAD

<sup>1</sup>I.e. the occupations of the initial and the final states are not limiting the BTBT phenomena.

ViDES<sup>2</sup> over a wide range of electric fields (see Sec.3.3.1, in particular Fig.3.11).

Fig.6.5 depicts the particle fluxes which are relevant in determining  $f_v$  and  $f_c$  in a GFET device. At the drain side, due to the large and negative electric field, only holes with positive

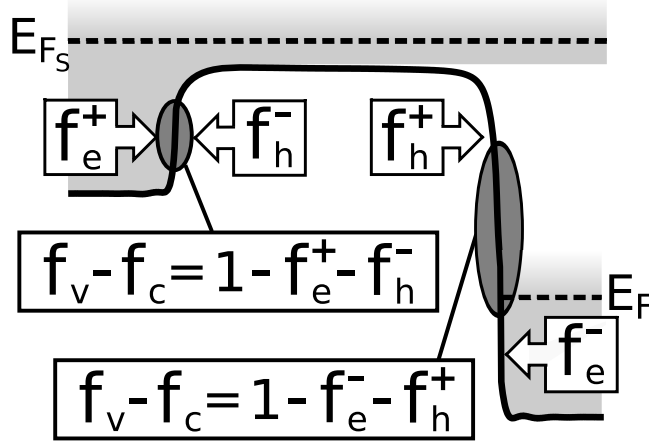


Figure 6.5: Sketch of the potential energy profile along the channel in a ballistic GFET:  $E_{F,S}$  ( $E_{F,D}$ ) denotes the Fermi level at the source (drain) contact, while the gray areas represent the regions populated by conduction band electrons injected by the contacts. The fluxes of particles contributing to  $(f_v - f_c)$  at the source and at the drain are also indicated. The sketch refers to a situation where the channel is  $n$ -type.

group velocity (with occupation  $f_h^+$ ) contribute to  $f_v$  and only electrons with negative group velocity (occupation probability  $f_e^-$ ) contribute to  $f_c$ , since the other fluxes are not impinging the classical turning points. In regions with large and positive electric field instead (as at the source side of the channel) only the flux  $f_h^-$  contributes to  $f_v$  and flux  $f_e^+$  contributes to  $f_c$ . Note that this formulation of the net BTBT rate naturally includes the generation as well as the recombination, that are both important in GFETs. Fig.6.6 shows qualitatively how the BTBT influences a ballistic GFET device. At the drain side there is a large and negative electric field and a region in which there are no electrons coming from the drain; hence in this region the occupation term is  $(f_v - f_c) = (1 - f_e^- - f_h^+)$  (see Fig.6.5) and it is almost equal to 1, thus we observe a strong generation of electrons and holes. These holes move toward the source and some of them experience BTBT recombination with electrons coming from the source. Part of them instead are injected directly into the source contact. The presence of holes in the channel influences the electrostatics of the system with respect to the case without BTBT (as we will see in Sec.6.3).

In order to limit the number of the simulated particles and the discretization points, in the calculation of the occupation probabilities  $f_h^i$  and  $f_e^i$  (with  $i$  being  $+$  and  $-$ ) we have not considered only the particles with zero kinetic energy, i.e. the ones impinging the classical turning point. Indeed, we have also taken into account the electrons and the holes with a kinetic energy up to  $E_{max} = 350\text{meV}$ , by weighting their contribution to the occupation probability with the value of the DOS at the energy of each considered particle, i.e. for example:

$$f_e^+ = \sum_{\substack{e_p: v_x(e_p) > 0 \\ E(e_p) < E_{max}}} \frac{2SW_{e_p}}{Wd_x E_{max} DOS[E(e_p)]} \quad (6.7)$$

<sup>2</sup>The simulations were run on a uniform device characterized by a constant electric field, with the appropriate boundary conditions such that  $(f_v - f_c) = 1$  is verified. For a short introduction on the NanoTCAD ViDES simulator see Appx.A.

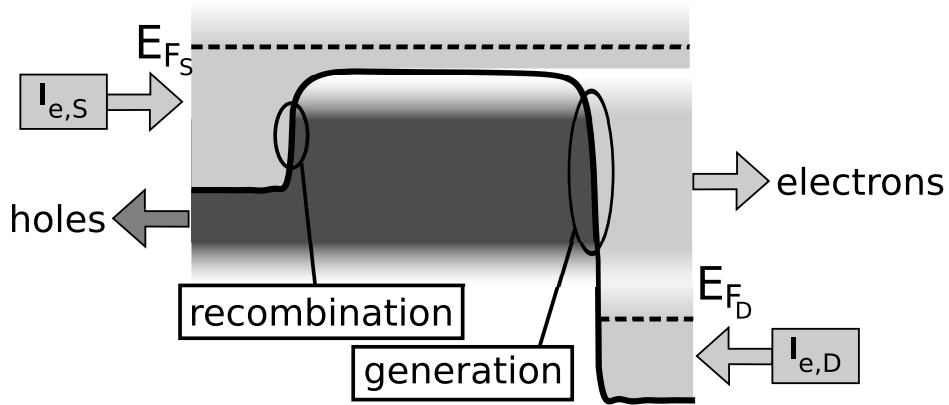


Figure 6.6: Sketch depicting the effect of the BTBT on a GFET device: electron-hole pairs are generated at the drain contact. The generated holes, indicated by the dark gray area, move toward the source: some of them reach the source contact while others recombine with electrons coming from the source due to BTBT. The sketch refers to a situation where the channel is  $n$ -type and reports also the electron fluxes injected by the contacts.

where  $e_p$  indicates the considered electron,  $v_x(e_p)$ ,  $E(e_p)$  and  $SW_{e_p}$  are respectively the velocity of the electron in the direction of the transport  $x$ , its kinetic energy and its statistical weight,  $W$  is the width of the graphene sheet, and  $d_x$  is the length of the considered spatial bin in the direction  $x$ . Similar expressions have been used for  $f_e^-$ ,  $f_h^+$  and  $f_h^-$ . We have verified by comparison with NEGF simulations that the 350meV energetic limit gives the best agreement between the MC and the full-quantum results. Moreover, in order to limit the effect of the statistical noise on the calculations, the simulator averages the obtained occupation probabilities over a huge number of MC iterations and periodically resets them<sup>3</sup>. The particles are generated at each time-step of the Monte Carlo procedure and their  $k_y$  value is assigned according to the distribution set by the total generation rate (see the integral over  $k_y$  in Eq.6.6). As already mentioned in Sec.3.3.1, compared to more accurate models for chiral tunneling in graphene [35, 36] the tunneling model described in this section does not account for wave-functions mismatch [35], considers  $k_y$  ranging from  $-\infty$  to  $+\infty$  and averages the dependence on the carriers angle. However, the good agreement with the NEGF simulations reported in Sec.3.3.1 (see Fig.3.11) and in the following section suggests that these effects are of small relevance in practical, wide channel GFETs.

Our approach for the BTBT is similar to that of a recent paper [21], although the expression of the net generation rate appears to differ by a factor of 1/4 in the argument of the exponential in Eq.6.6. Moreover, in our model  $f_v$  and  $f_c$  are estimated and employed in a different way compared to what is done in [21]. However, the consistency with [33, 34] and the good agreement with NEGF results shown in the following section support the validity of Eq.6.6.

Finally, in our model we have also considered the interband recombination assisted by phonons. The recombination rate has been modeled by employing the simplified expression presented in [37] (see Sec.3.3.2)

$$R_{IR}(x) = \frac{\min(n(x), p(x))}{\tau} \quad (6.8)$$

where  $n(x)$  and  $p(x)$  are respectively the electron and hole densities and  $\tau$  is the recombination time; we fixed  $\tau=1$ ps in all the calculations (consistently with [37] for  $n = p \approx 10^{12}$ cm<sup>-2</sup> (see

<sup>3</sup>In the simulations we reset the occupation probabilities every 10000 iterations of the MC simulator, that correspond to a 0.1ps time step.

Fig.3.12)), hence we neglect the dependence of  $\tau$  on  $n(x)$  and  $p(x)$ .

### 6.3 Model validation

First, we compared the simulation with the experimental mobility of a graphene foil as a function of the carrier density extracted from published data [5, 20, 38, 39, 40]: as can be seen in Fig.6.7, our model reproduces fairly well the experiments, thus validating the transport model at low electric field.

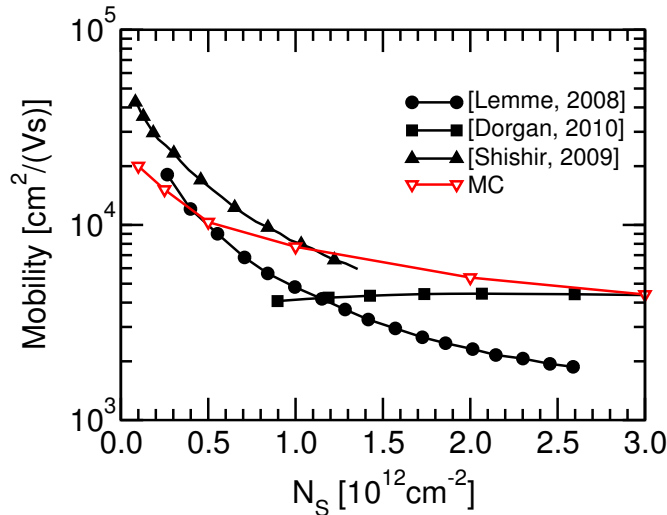


Figure 6.7: Experimental (black curves) and simulated (red curve) low-field mobility for a large sheet of graphene as a function of the electron density  $N_s$ . The experimental data are taken respectively from [38], [39] and [40].

In contrary, we do not obtain a good agreement with the experiments when we consider the saturation velocity; in fact, as it can be seen in Fig.6.8, where we compare the simulated drift velocity at the maximum field for which measurements are available ( $F_x \approx 2.5 \times 10^4 \text{V/cm}$ ) with the experiments reported in [41] and [39], a good agreement is observed only at low  $N_s$ ; the rapid decrease at high  $N_s$  is not observed in our simulations. Thus, in contrast to [41] and [39], our numerical model suggests that the degradation of  $v_{sat}$  with  $N_s$  is not due to remote phonons scattering but deserves further investigation and it is due to additional mechanisms activated at high  $N_s$  values.

We have then compared our model with the full quantum simulator NanoTCAD ViDES [42] (see Appx.A for a brief introduction to this simulator) considering the double gate GFET sketched in Fig.6.9, with a channel length of 30nm, two 1nm thick  $\text{SiO}_2$  layers as top and bottom gate dielectrics, uniformly doped source and drain extensions ( $N_D = 5 \times 10^{13} \text{cm}^{-2}$ ) with an abrupt doping profile. Furthermore, we have considered either a perfect alignment between the gate and the S/D extensions or a 10nm underlap at the source and the drain sides. The scattering mechanisms (acoustical, optical, and remote phonons) and the interband recombination assisted by phonons have been switched off in the MC model for a fair comparison with the ballistic NEGF results. Fig.6.10-(a) shows that the current calculated by the MC (closed symbols) is in quite good agreement with the NEGF simulations (open symbols) over a wide range of  $V_{DS}$  and  $V_{TG} = V_{BG}$  values for the device without underlap. A similar agreement and, as expected, essentially the same current values have been achieved for shorter gate lengths (down to 15nm), different  $t_{ox}$  (up to 3nm) and for various temperatures (up to  $100^\circ\text{C}$ ). The

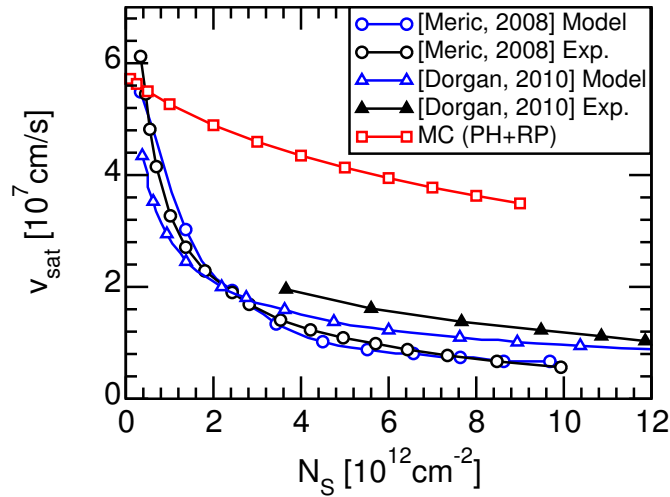


Figure 6.8: Simulated saturation velocity  $v_{sat}$  versus the electron density  $N_s$  in a graphene sheet on  $\text{SiO}_2$  considering the effect of remote phonons (adapted from [5]).  $v_{sat}$  is extracted at  $F_x = 2.5 \times 10^4 \text{V/cm}$ . Experimental data and modeling results from [41] and [39] are reported as well.

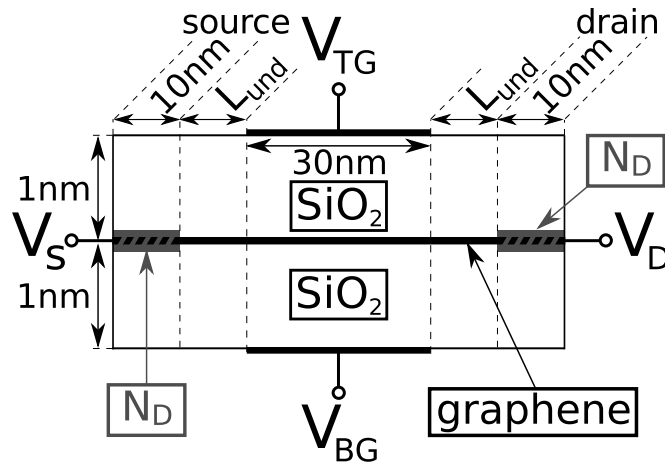


Figure 6.9: Sketch of the simulated device for the comparison between the MC and the NEGF simulators. The figure is not to scale.

output conductance is large, especially at low gate voltages, where also the transconductance is low, thus leading to very low intrinsic gains as previously reported in [17]. The output characteristics instead saturate to an almost constant value when the BTBT is switched off in the MC simulator (dotted line in Fig.6.10-(a)). The currents reported in Fig.6.10-(a) are much higher than the published experimental data, mainly because the simulations do not account for scattering, self-heating and series resistance [16]. Regarding this latter effect, both the semi-classical and the full quantum simulators are characterized by a simplified treatment of the contacts. In fact it is assumed that graphene can be doped with high concentration of ions such that the lateral electric field is essentially null in the S/D regions; also ideal ohmic contacts are assumed, so that the applied  $V_{DS}$  directly translates into a difference of the source and drain

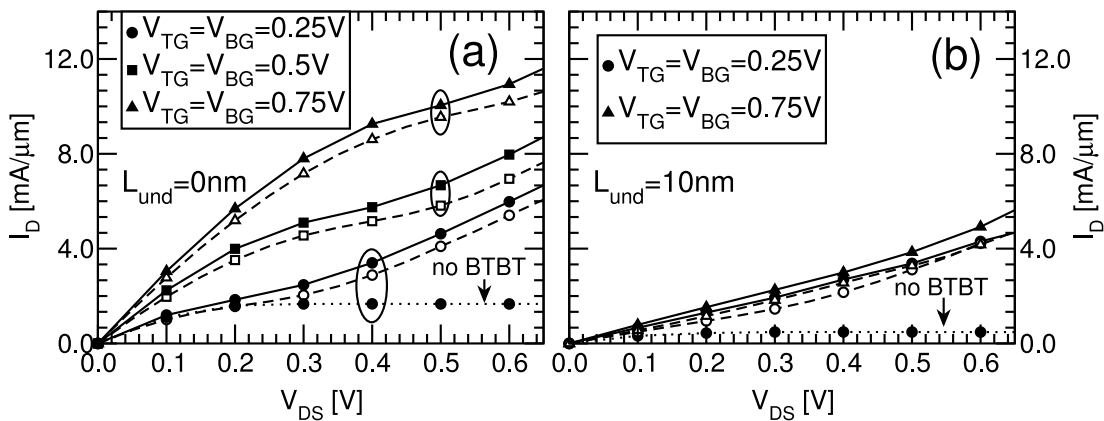


Figure 6.10: Output characteristics calculated by the MC (closed symbols) and the NEGF (open symbols) models for the double gate GFET sketched in Fig.6.9 with no underlap (Fig.6.10-(a)) and with a 10nm underlap between the gates and the S/D extensions (Fig.6.10-(b)). The dotted lines represent the MC current obtained by neglecting BTBT at  $V_{TG} = V_{BG} = 0.25\text{V}$ .

Fermi levels (see Fig.6.3). Realistic models of metal contacting graphene as in [43, 44, 45] are at present mainly aimed to estimate the resistance at low  $V_{DS}$  and are not straightforward to implement in the MC simulator. Because of the simple contact model used the results should be considered as an upper limit of the drain current in the intrinsic device with ideal contacts and null series resistance.

Fig.6.10-(b) shows that a good agreement between the two different transport models has been obtained also for a device with underlap. As expected the introduction of a 10nm underlap strongly reduces the control of the gates over the channel and strongly degrades the transconductance, while the output conductance remains high due to strong BTBT.

Fig.6.11 shows the electron and hole currents calculated by the two simulators at  $V_{TG} = V_{BG} = 0.5\text{V}$  for the device without underlap: the semi-classical and the full quantum models provide consistent predictions of both current components. The electron current is slightly overestimated by the MC (possibly due to the neglect of quantum reflections for carriers above the injection barrier) over the whole  $V_{DS}$  range, which explains the larger MC current in Fig.6.10.

Figs.6.12-(a) and (b) show that the potential energy profile and the net carrier density ( $n-p$ ) calculated with the MC and NEGF models are in quite good mutual agreement. Increasing  $V_{DS}$  leads to an increase of the hole current (Fig.6.11) and of the hole density in the channel due to the BTBT; this in turn lowers the potential barrier height at the source side (see Fig.6.12-(c)), thus leading to an increase of the electron concentration [15]. This is responsible for the rapid increase of the current with  $V_{DS}$  shown in Fig.6.10. It is also interesting to note that, as can be seen in Fig.6.12-(a), the channel potential is almost flat in the ballistic case, thus validating the assumption embraced in the semi-classical ballistic calculations of [46]. However, this simplified approach overestimates the holes injection and thus the effect of the BTBT on the output characteristics with respect to the full quantum simulator, as it can be seen in Fig.6.13.

Fig.6.14-(a) compares the transfer characteristics calculated by the two models for the GFET with no underlap shown in Fig.6.9 for various  $V_{DS}$ . A good agreement is observed for positive  $V_{TG} = V_{BG}$ ; moreover, for both the simulators the Dirac voltage, that is the voltage at which the minimum of the current occurs, tends to be equal to  $V_{DS}/2$ , as it is expected since we do not have considered any fixed charge in the simulations [13]. However, for negative gate biases the current of the MC is lower than the one provided by the NEGF, although the inversion charges are similar (see Fig.6.14-(b)). The discrepancy shows up when the type of carriers in

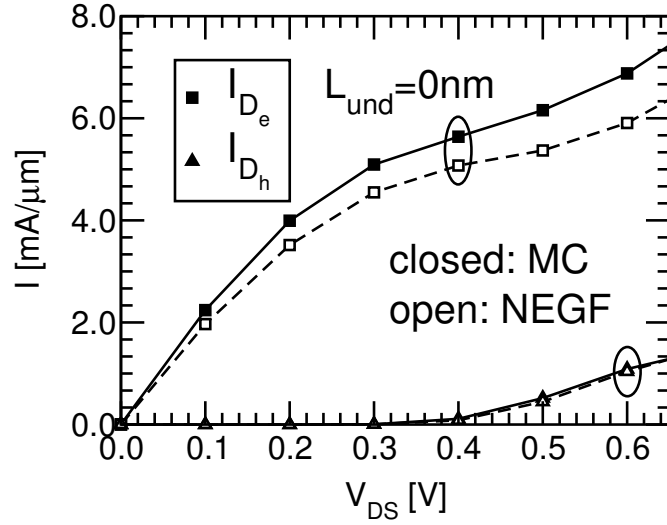


Figure 6.11: Electron and hole current per unit width calculated by semi-classical (closed symbols) and full quantum (open symbols) models at  $V_{TG} = V_{BG} = 0.5V$  versus  $V_{DS}$  for the device of Fig.6.9 without underlap.

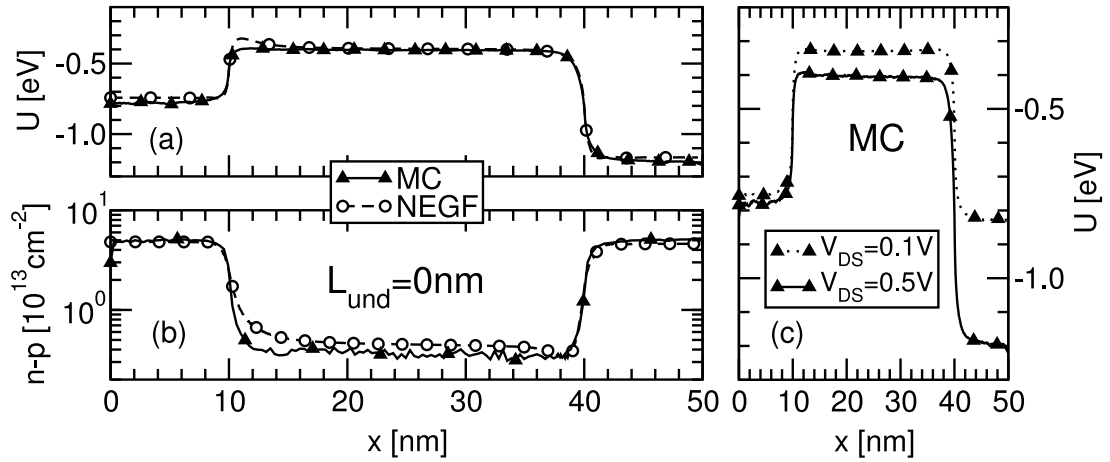


Figure 6.12: Simulations for the device in Fig.6.9 without underlap at  $V_{TG} = V_{BG} = 0.5V$ : potential energy (a) and net carrier density ( $n - p$ ) (b) along the channel calculated by the MC (closed symbols) and NEGF (open symbols) models at  $V_{DS} = 0.5V$ . (c) Potential energy calculated by the MC at  $V_{DS} = 0.1V$  (dashed) and  $0.5V$  (solid).

the channel is not the same as in the S/D extensions. In fact, we have verified that for a  $p+$  S/D doping and  $V_{TG} < 0$ , the MC model provides as expected the same results calculated with  $n+$  S/D and  $V_{TG} > 0$ , but with hole and electron densities essentially exchanged. The origin of the discrepancy in Fig.6.14-(a) for  $V_{TG} < 0$  stems from the approximations made in deriving Eq.6.6, where an average, effective  $f_v$  and  $f_c$  is taken out of the integral over  $k_y$  (see Sec.3.3.1). As a result, the hole distribution in  $k$ -space is not accurately calculated. This simplification is adequate to compute the correct hole concentration (Fig.6.14-(b)), but it influences the  $k_y$  distribution of the generated holes yielding a current which deviates from

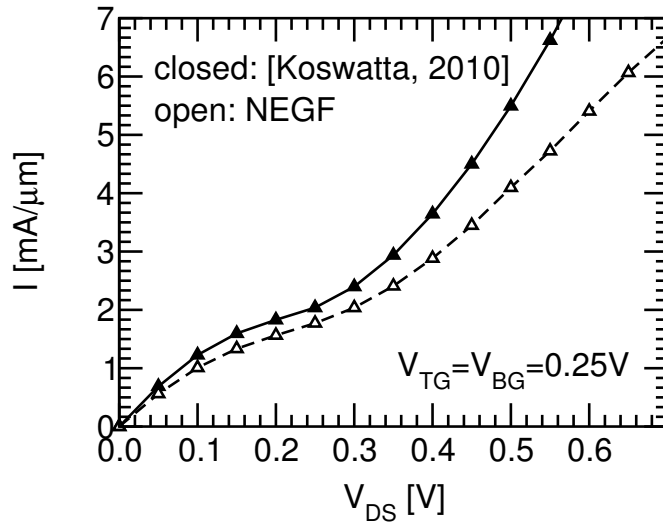


Figure 6.13: Output characteristics of the device sketched in Fig.6.9 calculated for  $V_{TG} = V_{BG} = 0.25\text{V}$  by the semi-classical model of [46] (closed symbols) and the NEGF simulator NanoTCAD ViDES [42] (open symbols): the former overestimates the effect of the BTBT.

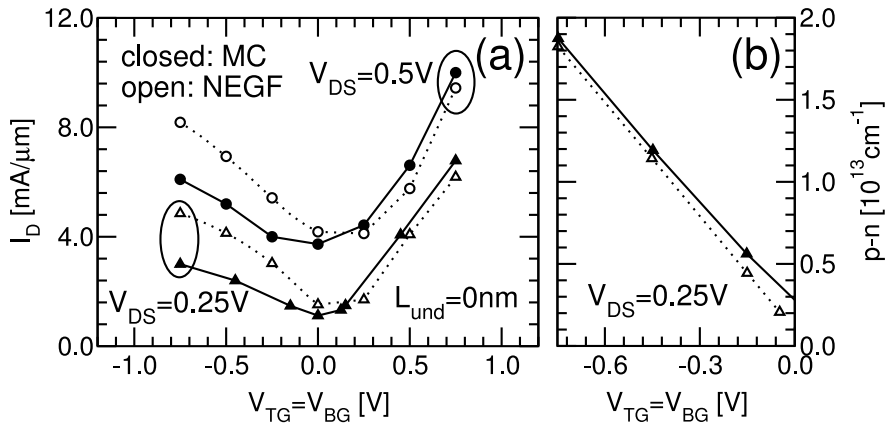


Figure 6.14: (a) Comparison between the transcharacteristics calculated by the MC (closed symbols) and the NEGF (open symbols) models for the device of Fig.6.9 without underlap, for  $V_{DS}=0.25\text{V}$  and  $0.5\text{V}$ . (b) Comparison between the average net carrier density  $p - n$  in the channel calculated by the two models for negative gate voltages at  $V_{DS}=0.25\text{V}$ .

the NEGF results (Fig.6.14-(a)). However, we see in Fig.6.14-(a) that the ambipolar behavior of GFETs is qualitatively captured by the MC model and the  $I_{on}/I_{off}$  ratio (the relevant performance metric from a device engineer perspective) is in fairly good agreement with NEGF calculations. For these reasons, in all the following analysis we will consider only devices in which the charge in the channel is dominated by the same type of carriers that are present also in the S/D extensions (i.e. in devices with  $n+$  S/D we consider only  $V_{TG}>0$ ).

## 6.4 Results

### 6.4.1 Effect of scattering

In this section the MC simulator, that has been previously validated against NEGF results, is employed to analyze the effect of carrier scattering in GFETs with various gate lengths  $L_G$ .

First we study the effect of the scattering mechanisms (i.e. the graphene intrinsic phonons and the remote phonons stemming from the gates dielectrics, see Sec.6.2) on the output characteristics of GFETs. We have simulated a single gate device with a 100nm channel length, a 5nm thick  $\text{Al}_2\text{O}_3$  top gate dielectric and a 300nm  $\text{SiO}_2$  substrate, without any underlap between the gate and the S/D extensions, inspired by the devices fabricated in [47]. A sketch of the simulated device is shown in Fig.6.15. For the remote phonons originating in the  $\text{Al}_2\text{O}_3$  top

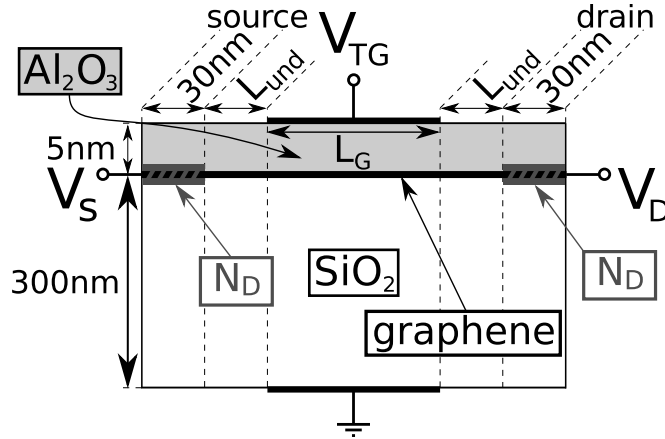


Figure 6.15: Sketch of the simulated device for the study of the effects of the scattering and of the scaling on the main RF figures of merit. The figure is not to scale.

gate dielectric we have used the parameters reported in Tab.6.1.

Table 6.1: Values of the parameters used for the calculation of the scattering rates due to remote phonons originating in the  $\text{Al}_2\text{O}_3$  top gate dielectric.

Parameter	Value [48]
$\hbar\omega_{TO_{\text{Al}_2\text{O}_3}}$	48.18meV
$\epsilon_{\text{Al}_2\text{O}_3}^0$	12.53
$\epsilon_{\text{Al}_2\text{O}_3}^i$	7.27

Fig.6.16 reports the output characteristics calculated for  $V_{TG}=0.5\text{V}$  and  $1\text{V}$  with (closed symbols) or without (open symbols) scattering. The effect of the scattering is twofold: it decreases the current and it broadens the regions of the output characteristics with low output conductance. Although the former effect is obvious, the latter needs an explanation. The scattering has an influence on the term  $(f_v - f_c)$  of the net tunneling generation rate (see Eq.6.6); as explained in Sec.6.2 this term accounts for the occupation of the states impinging the classical turning point (see also Fig.6.5). Generation takes place at the drain side and  $f_c = f_e^-$  is null above  $E_{FD}$  in the ballistic case (see Fig.6.6), whereas it is increased (thus decreasing the BTBT generation rate at the drain) when scattering is activated, since part of the electrons

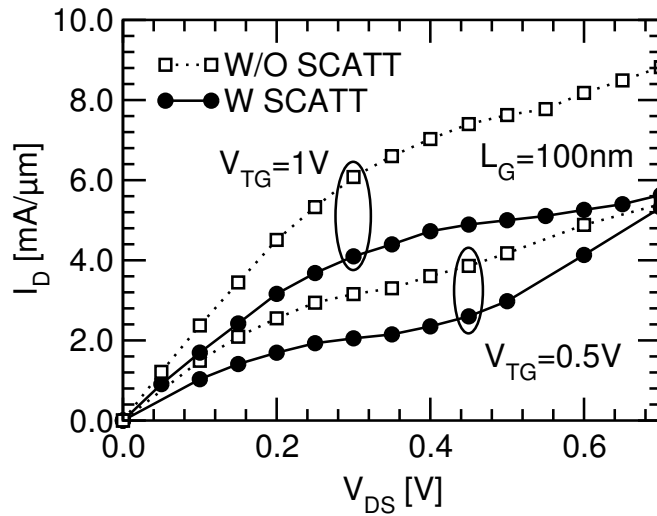


Figure 6.16: Simulated output characteristics for the single-gate device with  $L_G=100\text{nm}$  (Fig.6.15), considering and not considering the scattering mechanisms, for  $V_{TG}=0.5\text{V}$  and  $1\text{V}$ .

entering the drain is back-scattered and hits the classical turning point. Scattering also increases the  $f_v=f_h^-$  term at the source, thus increasing the BTBT recombination. The above reasoning helps explain why the output characteristics of GFETs are flatter in long devices, since in this case the effect of the scattering is stronger [47], as confirmed by Fig.6.17, that shows the output characteristics of the device sketched in Fig.6.15 with a  $400\text{nm}$  channel length. Indeed, the

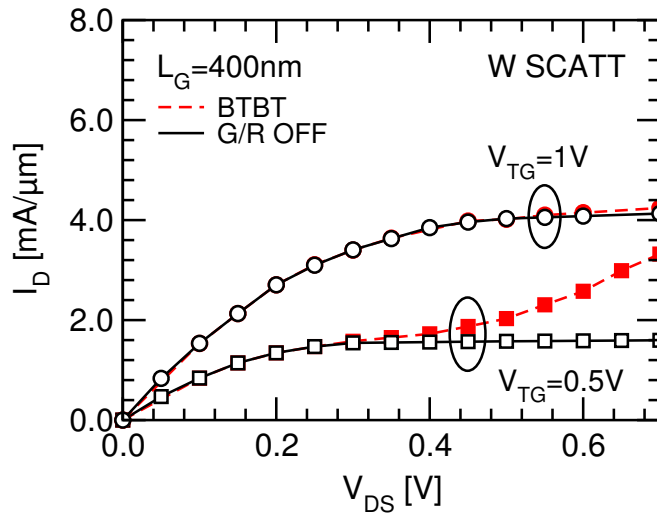


Figure 6.17: Simulated output characteristics for the single-gate device depicted in Fig.6.15 with  $L_G=400\text{nm}$ , considering and not considering the effect of the G/R mechanisms, for  $V_{TG}=0.5\text{V}$  and  $1\text{V}$ .

effect of the BTBT is weak in this longer device, especially at high  $V_{TG}$ .

Another phenomenon that could explain why the saturation behavior is better in long devices is the interband recombination assisted by phonon: the longer is the device, the stronger

is the effect of the recombination. However, we have to remark here that in our simulator the model for this phenomenon is very simplified and the value of the recombination time is critical, as it can be seen in Fig.6.18, that shows the output characteristic calculated for the 400nm device for different values of  $\tau$ . Hence, the inclusion of the interband recombination

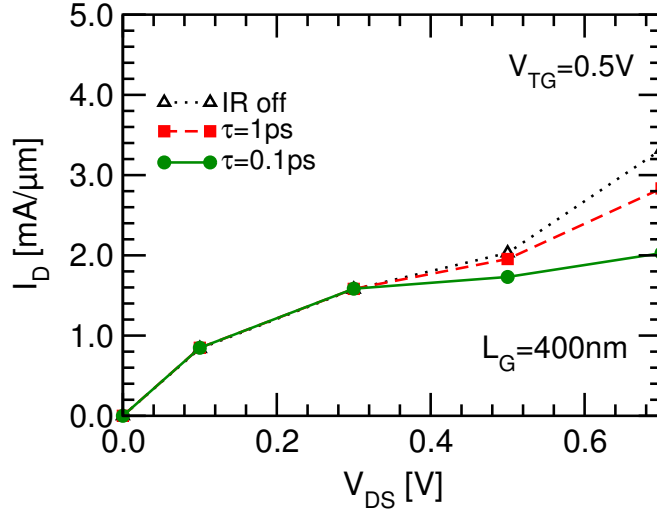


Figure 6.18: Effect of the interband recombination on the simulated output characteristics for the single-gate device depicted in Fig.6.15 with  $L_G=400\text{nm}$ , for  $V_{TG}=0.5\text{V}$  and considering different values of the recombination time  $\tau$ .

with the right value for  $\tau$  is critical: first of all, neglecting this phenomenon only slightly increases the output conductance, on the other hand, small  $\tau$  values effectively counterbalance the BTBT and reduce the output conductance. The exact determination of  $\tau$  is not straightforward both experimentally [49] and from the modeling point of view, also due to the high carrier concentrations and to other possible recombination mechanisms beside phonon assisted interband transitions. Hence, further studies are needed in order to model more accurately this phenomenon and understand its actual impact on the GFETs performance.

#### 6.4.2 Effect of the scaling

We now move to the study of the dependence of the GFET performance on the channel length  $L_G$ . To this purpose, we compute the main RF figures of merit for different gate lengths. We selected the bias by looking at the 100nm device of Fig.6.16, considering the point characterized by the minimum output conductance in the case with the scattering, which is approximately the point with the maximum intrinsic voltage gain:  $V_{DS}=0.3\text{V}$  and  $V_{TG}=0.5\text{V}$  (see Fig.6.16). Fig.6.19 shows the dependence of the drain current  $I_D$  on the channel length  $L_G$  with (closed symbols) or without (open symbols) scattering. The case without scattering provides a larger current essentially independent of the gate length. In the case with scattering, instead, the current is appreciably lower and decreases with the increase of the channel length. It is important to note that, in spite of the large low-field mobility ( $\mu \approx 4500[\text{cm}^2/(\text{Vs})]$  for  $N_s \approx 3 \times 10^{12}\text{cm}^{-2}$  as in Fig.6.19; see Fig.6.7), scattering plays a significant role even at  $L_G=50\text{nm}$ .

Fig.6.20 shows the simulated unity current gain cut-off frequency  $f_T$ , calculated using the quasi-static approach, i.e.

$$f_T = \frac{\Delta I_D}{2\pi \Delta Q} \Big|_{V_{DS}=0.3V} \quad (6.9)$$

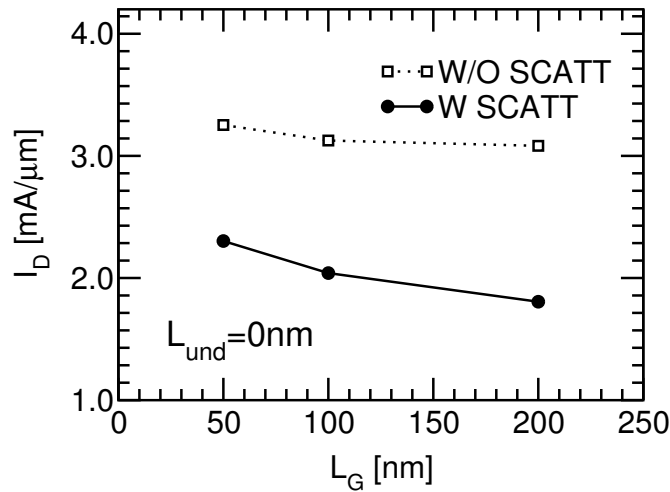


Figure 6.19: Dependence of the current  $I_D$  on the channel length  $L_G$  in devices with a perfect alignment between the gate and the S/D extensions, considering and not considering the scattering mechanisms, for  $V_{TG}=0.5\text{V}$  and  $V_{DS}=0.3\text{V}$ . Device of Fig.6.15.

where  $\Delta I_D$  and  $\Delta Q$  are, respectively, the variations of the current and of the total charge in the entire device between two DC simulations calculated considering two different gate voltages. We found that for  $L_G < 100\text{nm}$  the variation of the charge in the S/D extensions plays a non-

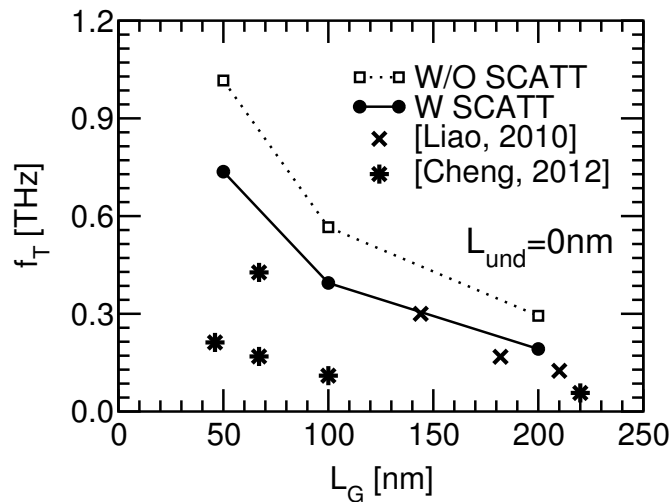


Figure 6.20: Dependence the cut-off frequency  $f_T$  on the channel length  $L_G$  for the same devices and voltages as in Fig.6.19. The crosses and the stars are experimental results respectively taken from [11] and [50].

negligible role, so that models based on 1D descriptions [13] may overestimate  $f_T$  (see Fig.6.21). This statement is confirmed by Fig.6.22, where a non-negligible variation of the electron density is observed in the S/D extensions when passing from  $V_{TG} = 0.5\text{V}$  to  $V_{TG} = 1\text{V}$  in the 50nm device.

As can be seen in Fig.6.20, in the ballistic simulations the  $f_T$  is overestimated with respect

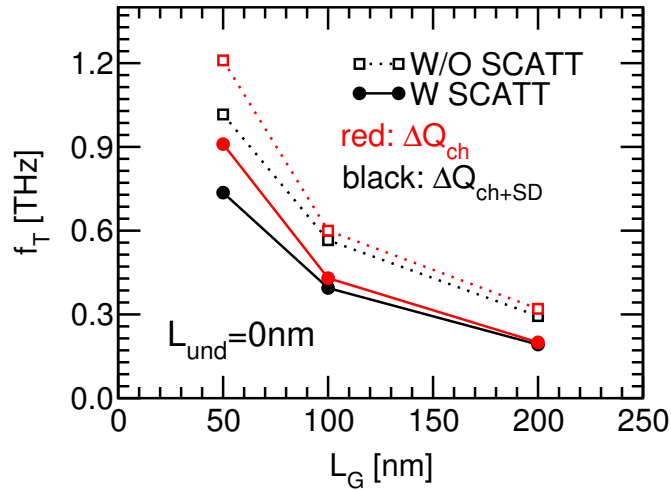


Figure 6.21: Comparison between the cut-off frequencies calculated by considering the variation of the total charge in the entire device (black curves) or only the variation of the charge in the channel (red curves, similarly to models based on 1D descriptions [13]): the latter approach overestimates  $f_t$  both considering and not considering the scatterings.

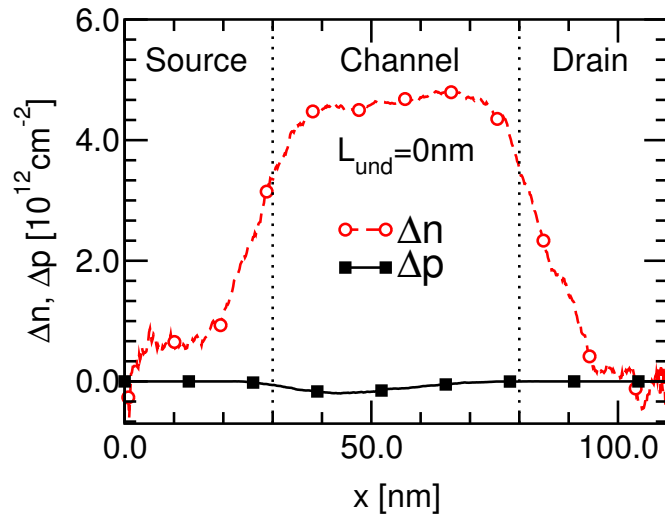


Figure 6.22: Variation of the carrier densities  $\Delta n$  and  $\Delta p$  in the 50nm device of Fig.6.15 passing from  $V_{TG} = 0.5V$  to  $V_{TG} = 1V$ , calculated by the MC considering the scatterings. As it can be seen, the variation of  $n$  in the S/D extensions is not negligible.

to the case with scattering. In this latter case, the calculated  $f_T$  is consistent to the best data reported in [11, 50]. The authors of [11, 50] claimed that they were able to reach a very high cut-off frequency thanks to the perfect alignment between the gate and the S/D extensions obtained with their fabrication process. This statement is confirmed by our simulations, as can be seen in Figs.6.23-(a) and (b), reporting the dependence of  $I_D$  and  $f_T$  on the underlap length  $L_{und}$  for the 100nm device: a very strong degradation of both figures of merit with the underlap length is observed.

We then study the effect of  $L_G$  on the transconductance  $g_m$ , output conductance  $g_{ds}$  and

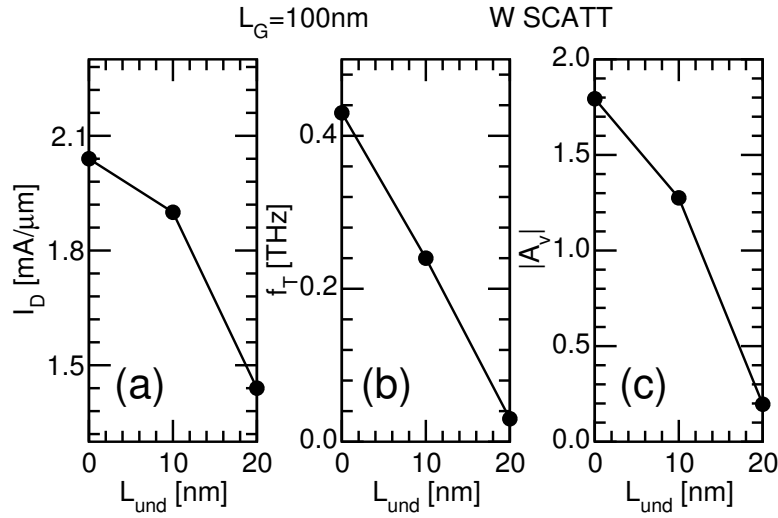


Figure 6.23: Drain current  $I_D$  (a), cut-off frequency  $f_T$  (b) and intrinsic voltage gain  $|A_v|$  (c) as a function of the length of the underlap between the gate and the S/D extensions  $L_{und}$  for the device with  $L_G=100\text{nm}$  (Fig.6.15) considering the scattering mechanisms.  $V_{TG}=0.5\text{V}$ ,  $V_{DS}=0.3\text{V}$ .

intrinsic voltage gain calculated as  $|A_v| = g_m/g_{ds}$ . As expected, the transconductance is larger without scattering (see Fig.6.24-(a)) because the carrier velocity is higher; however, also the output conductance is higher since the BTBT is stronger (see Figs.6.16 and 6.24-(b)), thus resulting in a lower intrinsic gain with respect to the case with scattering (see Fig.6.25). The intrinsic voltage gain is substantially larger in the case with scattering but not much larger than one; hence the adoption of alternative device architectures may be necessary to achieve adequate performance, for example using nanoribbons [15] or bilayer graphene [51].

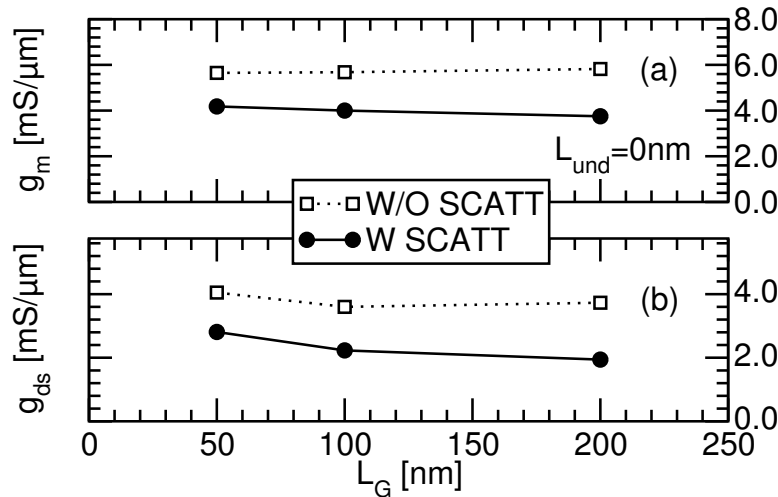


Figure 6.24: Trans-conductance  $g_m$  (a) and output conductance  $g_{ds}$  (b) as a function of the channel length  $L_G$  for the same devices of Fig.6.19.  $V_{TG}=0.5\text{V}$ ,  $V_{DS}=0.3\text{V}$ .

The underlap has a strong influence also on  $g_m$ ,  $g_{ds}$  and consequently on  $A_v$ , which, as

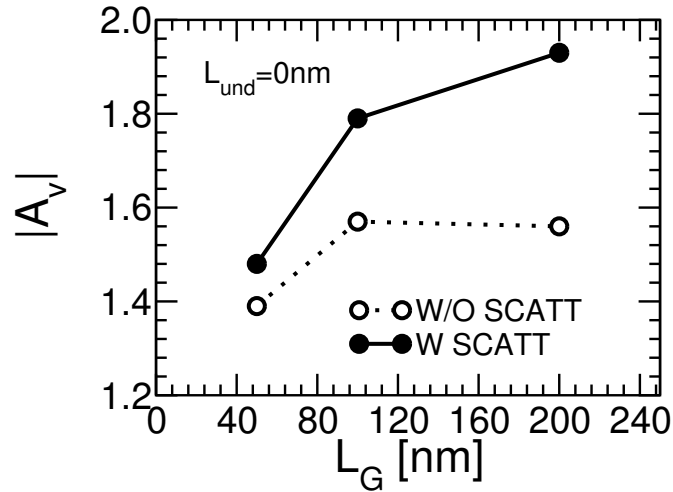


Figure 6.25: Intrinsic voltage gain versus  $L_G$  calculated for the same devices of Fig.6.19, considering and not considering the scattering mechanisms.  $V_{TG}=0.5V$ ,  $V_{DS}=0.3V$ .

can be seen in Fig.6.23-(c), is degraded as the underlap length  $L_{und}$  increases thus confirming the importance of an excellent alignment and small gap between the gate edge and the S/D contacts.

## 6.5 Conclusions

We have presented a semi-classical model for graphene FETs including a simple local model for band-to-band tunneling. The model is based on an appropriate expression of the occupancy terms in the conduction and valence bands and has been carefully validated by comparison with ballistic NEGF calculations. The simulator improves the range of applications of semi-classical MC models for GFETs, and makes them more accurate and generally applicable to graphene devices where scattering still plays a relevant role in determining the performance [19, 20]. We found that scattering has a non negligible influence on  $f_T$ ,  $g_m$ ,  $g_{ds}$  and  $|A_v|$  even in 50nm long devices. In particular, the  $g_{ds}$  is lower when including scattering partly explaining why experimental data [47] show output characteristics flatter than the predictions of ballistic simulations. Simulated  $f_T$  are in fairly good agreement with the best reported experimental data.



# Bibliography

- [1] X. Wang, Y. Ouyang, X. Li, H. Wang, J. Guo, and H. Dai, “Room-Temperature All-Semiconducting Sub-10-nm Graphene Nanoribbon Field-Effect Transistors,” *Phys. Rev. Lett.*, vol. 100, p. 206803, May 2008.
- [2] E. McCann, “Asymmetry gap in the electronic band structure of bilayer graphene,” *Phys. Rev. B*, vol. 74, p. 161403, Oct 2006.
- [3] G. Fiori and G. Iannaccone, “On the Possibility of Tunable-Gap Bilayer Graphene FET,” *Electron Device Letters, IEEE*, vol. 30, no. 3, pp. 261–264, march 2009.
- [4] —, “Ultralow-Voltage Bilayer Graphene Tunnel FET,” *Electron Device Letters, IEEE*, vol. 30, no. 10, pp. 1096–1098, oct. 2009.
- [5] M. Bresciani, A. Paussa, P. Palestri, D. Esseni, and L. Selmi, “Low-Field Mobility and High-Field Drift Velocity in Graphene Nanoribbons and Graphene Bilayers,” in *Electron Devices Meeting (IEDM), 2010 IEEE International*, dec. 2010, pp. 724–727.
- [6] A. Paussa, M. Bresciani, D. Esseni, P. Palestri, and L. Selmi, “Phonon Limited Uniform Transport in Bilayer Graphene Transistors,” in *Solid-State Device Research Conference (ESSDERC), 2011 Proceedings of the European*, sept. 2011, pp. 307–310.
- [7] A. Betti, G. Fiori, and G. Iannaccone, “Atomistic Investigation of Low-Field Mobility in Graphene Nanoribbons,” *Electron Devices, IEEE Transactions on*, vol. 58, no. 9, pp. 2824–2830, sept. 2011.
- [8] —, “Drift Velocity Peak and Negative Differential Mobility in High Field Transport in Graphene Nanoribbons Explained by Numerical Simulations,” *Applied Physics Letters*, vol. 99, no. 24, p. 242108, 2011.
- [9] F. Schwierz, “Graphene Transistors,” *Nat. Nano.*, vol. 5, no. 7, pp. 487–496, 2010.
- [10] Y. Wu, Y.-m. Lin, A. A. Bol, K. A. Jenkins, F. Xia, D. B. Farmer, Y. Zhu, and P. Avouris, “High-Frequency, Scaled Graphene Transistors on Diamond-Like Carbon,” *Nature*, vol. 472, pp. 74–78, 2011.
- [11] L. Liao, Y.-C. Lin, M. Bao, R. Cheng, J. Bai, Y. Liu, Y. Qu, K. L. Wang, Y. Huang, and X. Duan, “High-Speed Graphene Transistors With a Self-Aligned Nanowire Gate,” *Nature*, vol. 467, pp. 305–308, 2010.
- [12] Y.-M. Lin, C. Dimitrakopoulos, K. A. Jenkins, D. B. Farmer, H.-Y. Chiu, A. Grill, and P. Avouris, “100-GHz Transistors from Wafer-Scale Epitaxial Graphene,” *Science*, vol. 327, no. 5966, p. 662, 2010.
- [13] S. Koswatta, A. Valdes-Garcia, M. Steiner, Y.-M. Lin, and P. Avouris, “Ultimate RF Performance Potential of Carbon Electronics,” *Microwave Theory and Techniques, IEEE Transactions on*, vol. 59, no. 10, pp. 2739–2750, oct. 2011.

- [14] F. Schwierz, "Graphene transistors 2011," in *VLSI Technology, Systems and Applications (VLSI-TSA), 2011 International Symposium on*, april 2011, pp. 1–2.
- [15] I. Imperiale, S. Bonsignore, A. Gnudi, E. Gnani, S. Reggiani, and G. Baccarani, "Computational Study of Graphene Nanoribbon FETs for RF Applications," in *Electron Devices Meeting (IEDM), 2010 IEEE International*, dec. 2010, pp. 732–735.
- [16] V. Perebeinos and P. Avouris, "Inelastic Scattering and Current Saturation in Graphene," *Phys. Rev. B*, vol. 81, p. 195442, May 2010.
- [17] I. Meric, N. Baklitskaya, P. Kim, and K. Shepard, "RF Performance of Top-Gated, Zero-Bandgap Graphene Field-Effect Transistors," in *Electron Devices Meeting, 2008. IEDM 2008. IEEE International*, dec. 2008, pp. 513–516.
- [18] G. Fiori and G. Iannaccone, "Simulation of Graphene Nanoribbon Field-Effect Transistors," *Electron Device Letters, IEEE*, vol. 28, no. 8, pp. 760–762, aug. 2007.
- [19] Y. Lu and J. Guo, "Role of Dissipative Quantum Transport in DC, RF, and Self-Heating Characteristics of Short Channel Graphene FETs," in *Electron Devices Meeting (IEDM), 2011 IEEE International*, dec. 2011, pp. 263–266.
- [20] A. Paussa, M. Geromel, P. Palestri, M. Bresciani, D. Esseni, and L. Selmi, "Simulation of Graphene Nanoscale RF Transistors Including Scattering and Generation/Recombination Mechanisms," in *Electron Devices Meeting (IEDM), 2011 IEEE International*, dec. 2011, pp. 271–274.
- [21] J. David, L. Register, and S. Banerjee, "Semiclassical Monte Carlo Analysis of Graphene FETs," *Electron Devices, IEEE Transactions on*, vol. 59, no. 4, pp. 976–982, april 2012.
- [22] S. A. Thiele, J. A. Schaefer, and F. Schwierz, "Modeling of Graphene Metal-Oxide-Semiconductor Field-Effect Transistors with Gapless Large-Area Graphene Channels," *Journal of Applied Physics*, vol. 107, no. 9, p. 094505, 2010.
- [23] E. Pince and C. Kocabas, "Investigation of High Frequency Performance Limit of Graphene Field Effect Transistors," *Applied Physics Letters*, vol. 97, no. 17, p. 173106, 2010.
- [24] B. Scott and J. Leburton, "Modeling of the Output and Transfer Characteristics of Graphene Field-Effect Transistors," *Nanotechnology, IEEE Transactions on*, vol. 10, no. 5, pp. 1113–1119, sept. 2011.
- [25] H. Wang, A. Hsu, J. Kong, D. Antoniadis, and T. Palacios, "Compact Virtual-Source Current-Voltage Model for Top- and Back-Gated Graphene Field-Effect Transistors," *Electron Devices, IEEE Transactions on*, vol. 58, no. 5, pp. 1523–1533, may 2011.
- [26] M. Ancona, "Electron Transport in Graphene From a Diffusion-Drift Perspective," *Electron Devices, IEEE Transactions on*, vol. 57, no. 3, pp. 681–689, march 2010.
- [27] Y. Wu, D. Farmer, A. Valdes-Garcia, W. Zhu, K. Jenkins, C. Dimitrakopoulos, P. Avouris, and Y.-M. Lin, "Record High RF Performance for Epitaxial Graphene Transistors," in *Electron Devices Meeting (IEDM), 2011 IEEE International*, dec. 2011, pp. 528–530.
- [28] P. Palestri, N. Barin, D. Esseni, and C. Fiegna, "Stability of self-consistent Monte Carlo Simulations: effects of the grid size and of the coupling scheme," *Electron Devices, IEEE Transactions on*, vol. 53, no. 6, pp. 1433–1442, june 2006.
- [29] Z. Ren, R. Venugopal, S. Goasguen, S. Datta, and M. Lundstrom, "nanoMOS 2.5: A two-dimensional simulator for quantum transport in double-gate MOSFETs," *Electron Devices, IEEE Transactions on*, vol. 50, no. 9, pp. 1914–1925, sept. 2003.

- [30] P. Palestri, L. Lucci, S. Dei Tos, D. Esseni, and L. Selmi, "An Improved Empirical Approach to Introduce Quantization Effects in the Transport Direction in Multi-Subband Monte Carlo Simulations," *Semicond. Sci. Technol.*, vol. 25, no. 5, p. 055011, 2010.
- [31] M. Bresciani, P. Palestri, D. Esseni, and L. Selmi, "Simple and efficient modeling of the E-k relationship and low-field mobility in Graphene Nano-Ribbons," *Solid-State Electronics*, vol. 54, pp. 1015–1021, Sep 2010.
- [32] P. Lugli and D. K.Ferry, "Degeneracy in the Ensemble Monte Carlo Method for High-Field Transport in Semiconductors," *IEEE Trans. Electron Devices*, vol. 32, no. 11, pp. 2431–2437, 1985.
- [33] L. M. Zhang and M. M. Fogler, "Nonlinear Screening and Ballistic Transport in a Graphene  $p$ - $n$  Junction," *Phys. Rev. Lett.*, vol. 100, p. 116804, Mar 2008.
- [34] V. V. Cheianov and V. I. Fal'ko, "Selective Transmission of Dirac Electrons and Ballistic Magnetoresistance of  $n$ - $p$  Junctions in Graphene," *Phys. Rev. B*, vol. 74, p. 041403, Jul 2006.
- [35] M. I. Katsnelson, K. S. Novoselov, and A. K. Geim, "Chiral tunnelling and the Klein paradox in graphene," *Nature Physics*, vol. 2, no. 9, pp. 620–625, Sep. 2006.
- [36] T. Low, S. Hong, J. Appenzeller, S. Datta, and M. Lundstrom, "Conductance Asymmetry of Graphene  $p$ - $n$  Junction," *Electron Devices, IEEE Transactions on*, vol. 56, no. 6, pp. 1292–1299, June 2009.
- [37] F. Rana, P. A. George, J. H. Strait, J. Dawlaty, S. Shivaraman, M. Chandrashekar, and M. G. Spencer, "Carrier recombination and generation rates for intravalley and intervalley phonon scattering in graphene," *Phys. Rev. B*, vol. 79, p. 115447, Mar 2009.
- [38] M. Lemme, T. Echtermeyer, M. Baus, B. Szafrank, J. Bolten, M. Schmidt, T. Wahlbrink, and H. Kurz, "Mobility in graphene double gate field effect transistors," *Solid-State Electronics*, vol. 52, no. 4, pp. 514–518, 2008.
- [39] V. E. Dorgan, M.-H. Bae, and E. Pop, "Mobility and saturation velocity in graphene on SiO<sub>2</sub>," *Applied Physics Letters*, vol. 97, no. 8, p. 082112, 2010.
- [40] R. Shishir, D. Ferry, and S. Goodnick, "Intrinsic mobility limit in graphene at room temperature," in *Nanotechnology, 2009. IEEE-NANO 2009. 9th IEEE Conference on*, July 2009, pp. 21–24.
- [41] I. Meric, M. Y. Han, A. F. Young, B. Ozyilmaz, P. Kim, and K. L. Shepard, "Current Saturation in Zero-Bandgap, Top-Gated Graphene Field-Effect Transistors," *Nat. Nano.*, vol. 3, no. 9, pp. 654–659, 2008.
- [42] G. Fiori; G. Iannaccone (2009), "NanoTCAD ViDES," <http://nanohub.org/resources/vides>. (doi:10254/nanohub-r5116.5).
- [43] D. Berdebes, T. Low, Y. Sui, J. Appenzeller, and M. Lundstrom, "Substrate Gating of Contact Resistance in Graphene Transistors," *Electron Devices, IEEE Transactions on*, vol. 58, no. 11, pp. 3925–3932, Nov. 2011.
- [44] J. Knoch, Z. Chen, and J. Appenzeller, "Properties of Metal-Graphene Contacts," *Nanotechnology, IEEE Transactions on*, vol. 11, no. 3, pp. 513–519, May 2012.
- [45] Y. Khatami, H. Li, C. Xu, and K. Banerjee, "Metal-to-Multilayer-Graphene Contact-Part I and Part II," *Electron Devices, IEEE Transactions on*, vol. 59, no. 9, pp. 2444–2460, September 2012.

- 
- [46] S. Koswatta, S. Koester, and W. Haensch, "On the Possibility of Obtaining MOSFET-Like Performance and Sub-60-mV/dec Swing in 1-D Broken-Gap Tunnel Transistors," *IEEE Trans. Electron Devices*, vol. 57, no. 12, pp. 3222–3230, dec. 2010.
- [47] I. Meric, C. R. Dean, A. F. Young, N. Baklitskaya, N. J. Tremblay, C. Nuckolls, P. Kim, and K. L. Shepard, "Channel Length Scaling in Graphene Field-Effect Transistors Studied with Pulsed Current-Voltage Measurements," *Nano Letters*, vol. 11, no. 3, pp. 1093–1097, 2011.
- [48] M. V. Fischetti, D. A. Neumayer, and E. A. Cartier, "Effective electron mobility in Si inversion layers in metal-oxide-semiconductor systems with a high-K insulator: The role of remote phonon scattering," *Journal of Applied Physics*, vol. 90, no. 9, pp. 4587–4608, 2001.
- [49] P. A. George, J. Strait, J. Dawlaty, S. Shivaraman, M. Chandrashekar, F. Rana, and M. G. Spencer, "Ultrafast Optical-Pump Terahertz-Probe Spectroscopy of the Carrier Relaxation and Recombination Dynamics in Epitaxial Graphene," *Nano Letters*, vol. 8, no. 12, pp. 4248–4251, 2008.
- [50] R. Cheng, J. Bai, L. Liao, H. Zhou, Y. Chen, L. Liu, Y.-C. Lin, S. Jiang, Y. Huang, and X. Duan, "High-frequency self-aligned graphene transistors with transferred gate stacks," *Proceedings of the National Academy of Sciences*, 2012.
- [51] B. N. Szafranek, G. Fiori, D. Schall, D. Neumaier, and H. Kurz, "Current Saturation and Voltage Gain in Bilayer Graphene Field Effect Transistors," *Nano Letters*, vol. 12, no. 3, pp. 1324–1328, 2012.

## Chapter 7

# Concluding Remarks and Future Developments

**D**URING the course of the PhD program we have explored the potentials of two different new approaches proposed in the electron device community to reach the requirements imposed by the ITRS for the future technology nodes. To do so, we developed several TCAD simulation tools based on advanced numerical techniques to describe the electrostatics and the transport in the devices.

In Chap.2 we have demonstrated the applicability of the Pseudospectral method to the simulation of the electrostatic of the channel section of FinFETs and nanowires with realistic shapes. In all the considered cases we observed a significant speed up given by this approach with respect to more standard methods such as the finite differences. However, here it should be noted that, due to its intrinsic limits, this approach can be applied only to convex geometries; another innovative approach, the Spectral Element Method, is not affected by this limitation since it is based on an element based formulation of the problem (similarly to the finite element approach) [1, 2]. Hence, it would be very interesting trying to apply this approach that embodies the extreme computational efficiency of Pseudospectral method to the flexibility given by the element-based approach to problems relevant in nanoelectronics.

Regarding the modeling of the transport in graphene, in order to extend the applicability of the model proposed in Chap.3 to CVD graphene, two very important phenomena must be added to the actual simulator: the effect of the charged impurities and of the crystal defects. Moreover, a deeper understanding of the screening of the remote phonons modes (hence a study of the phonon to plasmon coupling) is needed.

Regarding the novel approach for the solution of the linearized Boltzmann transport equation presented in Chap.4, it would be very interesting employing such an approach to the calculation of the low-field mobility dependence on the strain in graphene sheets. Indeed, experiments show that the resistivity change with the strain is very high and can be exploited in the production of high-sensitivity pressure sensors [3, 4, 5]: hence an accurate physics-based modeling of this property would be very useful.

Regarding the simulator for the uniform transport in bilayer graphene presented in Chap.5, a very useful improvement would be the inclusion of the higher branch of the conduction band in the calculation of the saturation velocity.

Finally, in order to obtain results more close to the available experiments, the simulator for RF GFETs presented in Chap.6 needs a more physical treatment of the contacts (based for example on the model presented in [6]) and of the self-heating. Moreover, the development of a similar simulation tool for graphene bilayer based transistors would be extremely interesting since recent studies suggest that the bandgap induced in this material may improve both the digital and the analog performance of these devices with respect to the wide sheet graphene based transistors [7, 8, 9].

# Bibliography

- [1] J.-H. Lee and Q. H. Liu, “An Efficient 3-D Spectral-Element Method for Schrödinger Equation in Nanodevice Simulation,” *IEEE Trans. on Computer-Aided Design of Integrated Circuits and Systems*, vol. 24, pp. 1848–1858, 2005.
- [2] C. Cheng, J.-H. Lee, H. Z. Massoud, and Q. H. Liu, “3-D Self-Consistent Schrödinger-Poisson Solver: the Spectral Element Method,” *Journal of Computational Electronics*, vol. 7, pp. 337–341, 2008.
- [3] M. Huang, T. A. Pascal, H. Kim, W. A. Goddard, and J. R. Greer, “Electronic-Mechanical Coupling in Graphene from in situ Nanoindentation Experiments and Multiscale Atomistic Simulations,” *Nano Letters*, vol. 11, no. 3, pp. 1241–1246, 2011.
- [4] X. Chen, X. Zheng, J.-K. Kim, X. Li, and D.-W. Lee, “Investigation of graphene piezoresistors for use as strain gauge sensors,” *Journal of Vacuum Science Technology B: Microelectronics and Nanometer Structures*, vol. 29, no. 6, pp. 06FE01–06FE01–5, nov 2011.
- [5] A. Smith, S. Vaziri, A. Delin, M. Ostling, and M. Lemme, “Strain engineering in suspended graphene devices for pressure sensor applications,” in *Ultimate Integration on Silicon (ULIS), 2012 13th International Conference on*, march 2012, pp. 21–24.
- [6] D. Berdebes, T. Low, Y. Sui, J. Appenzeller, and M. Lundstrom, “Substrate Gating of Contact Resistance in Graphene Transistors,” *Electron Devices, IEEE Transactions on*, vol. 58, no. 11, pp. 3925–3932, nov. 2011.
- [7] B. N. Szafranek, D. Schall, M. Otto, D. Neumaier, and H. Kurz, “Electrical observation of a tunable band gap in bilayer graphene nanoribbons at room temperature,” *Applied Physics Letters*, vol. 96, no. 11, p. 112103, 2010.
- [8] —, “High On/Off Ratios in Bilayer Graphene Field Effect Transistors Realized by Surface Dopants,” *Nano Letters*, vol. 11, no. 7, pp. 2640–2643, 2011.
- [9] B. N. Szafranek, G. Fiori, D. Schall, D. Neumaier, and H. Kurz, “Current Saturation and Voltage Gain in Bilayer Graphene Field Effect Transistors,” *Nano Letters*, vol. 12, no. 3, pp. 1324–1328, 2012.



Appendix A

**NanoTCAD ViDES full quantum  
simulator**

In this appendix we briefly present the full-quantum transport simulator NanoTCAD ViDES [1], that has been used as the reference in Chaps.3 and 6.

The two-dimensional Poisson equation is solved self-consistently with the open-boundary Schrödinger equation and implemented in the open-source code NanoTCAD ViDES [1]. In particular, the graphene Hamiltonian is expressed by means of a real-space  $p_z$  orbitals basis set [2]. The elementary cell is repeated periodically along the longitudinal ( $x$ ) and transversal ( $y$ ) directions. Bloch periodic boundary conditions are imposed along the  $y$  direction with period equal to  $\sqrt{3}a_{cc}$ , where  $a_{cc} = 0.144$  nm is the carbon-carbon bonding distance. Semi-infinite contacts have been instead modeled along the  $x$  direction by means of self-energies. Assuming a point charge approximation and a ballistic transport regime, the electron concentration can be expressed as

$$\begin{aligned} p(\vec{r}) - n(\vec{r}) &= 1 + 2 \int_{BZ} dk_y \int_{-\infty}^{+\infty} dE \times \\ &\times [|\psi_S(E, k_y, \vec{r})|^2 f(E - E_{F_S}) \\ &+ |\psi_D(E, k_y, \vec{r})|^2 f(E - E_{F_D})] \end{aligned} \quad (\text{A.1})$$

where  $\vec{r}$  is the coordinate of the carbon site,  $f$  is the Fermi-Dirac occupation factor,  $|\psi_S|^2$  ( $|\psi_D|^2$ ) is the probability that states injected by the source (drain) reach the carbon site  $\vec{r}$ ,  $E_{F_S}$  ( $E_{F_D}$ ) is the Fermi level of the source (drain), and the +1 term accounts for C atom ionization. The  $k_y$  integral is performed over the Brillouin zone (BZ).

The ballistic current is expressed as

$$\begin{aligned} I &= \frac{2e}{h} \int_{BZ} dk_y \int_{-\infty}^{+\infty} dE \times \\ &\times \mathcal{T}(E, k_y) [f(E - E_{F_S}) - f(E - E_{F_D})], \end{aligned} \quad (\text{A.2})$$

where  $h$  is Planck's constant and  $\mathcal{T}(E, k_y)$  is the transmission coefficient.

# Bibliography

- [1] G. Fiori; G. Iannaccone (2009), "NanoTCAD ViDES," <http://nanohub.org/resources/vides>. (doi:10254/nanohub-r5116.5).
- [2] G. Fiori and G. Iannaccone, "On the Possibility of Tunable-Gap Bilayer Graphene FET," *Electron Device Letters, IEEE*, vol. 30, no. 3, pp. 261 –264, march 2009.



## Appendix B

# Simplifications of the MRT problem

## B.1 Isotropic scattering mechanisms

In this appendix we discuss the simplification of the MRT problem implied by an isotropic scattering mechanism. Let us consider a mechanism with a rate given by

$$S_{i,j}(\mathbf{k}, \mathbf{k}') = \frac{2\pi}{\hbar} |M_{i,j}^{(0)}|^2 \delta[E_j(\mathbf{k}') - E_i(\mathbf{k}) \mp \hbar\omega_0] \quad (\text{B.1})$$

where the matrix element is independent of  $\mathbf{k}, \mathbf{k}'$  and the phonon energy  $\hbar\omega_0$  is independent of  $\mathbf{q}$ . We now substitute Eq.B.1 in Eq.4.11 and, furthermore, make the following *ansatz*

$$\tau_i(\mathbf{k}) = \tau_i[E_i(\mathbf{k})] . \quad (\text{B.2})$$

By doing so the second term in the r.h.s. of Eq.4.11, that is the sum involving  $[\tau_j(\mathbf{k}') v_{x,j}(\mathbf{k}')]$ , becomes

$$\frac{2\pi}{\hbar} \sum_{j,\mathbf{k}'} |M_{i,j}^{(0)}|^2 \left[ \frac{1 - f_0(E_j(\mathbf{k}'))}{1 - f_0(E_i(\mathbf{k}))} \right] \tau_i[E_j(\mathbf{k}')] v_{x,j}(\mathbf{k}') \delta[E_j(\mathbf{k}') - E_i(\mathbf{k}) \mp \hbar\omega_0] . \quad (\text{B.3})$$

The sum over  $\mathbf{k}'$  in Eq.B.3 is restricted by the Dirac function to a curve corresponding to a fixed  $E_j(\mathbf{k}')$  equal to  $[E_i(\mathbf{k}) \mp \hbar\omega_0]$ . Since along such a curve  $E_j(\mathbf{k}')$  is constant whereas we have  $v_{x,j}(-\mathbf{k}') = -v_{x,j}(\mathbf{k}')$ , then the sum over  $\mathbf{k}'$  in Eq.B.3 is null.

We now notice that in the r.h.s. of Eq.4.11 the term  $[\tau_i(E_i(\mathbf{k})) v_{x,i}(\mathbf{k})]$  can exit the sum over  $\mathbf{k}'$ , so that we can readily obtain an explicit expression for the momentum relaxation time  $\tau_i(E_i(\mathbf{k}))$  that reads

$$\frac{1}{\tau_i[E_i(\mathbf{k})]} = \frac{2\pi}{\hbar} \sum_{j,\mathbf{k}'} |M_{i,j}^{(0)}|^2 \left[ \frac{1 - f_0(E_j(\mathbf{k}'))}{1 - f_0(E_i(\mathbf{k}))} \right] \delta[E_j(\mathbf{k}') - E_i(\mathbf{k}) \mp \hbar\omega_0] . \quad (\text{B.4})$$

Since the expression for the momentum relaxation time provided by Eq.B.4 is consistent with the *ansatz* in Eq.B.2, then it is an acceptable solution of the MRT problem.

## B.2 Isotropic bands

This appendix discusses the MRT for an isotropic electron energy dispersion and shows that, even for fairly anisotropic scattering mechanisms, the momentum relaxation time is isotropic. We thus assume an isotropic band-structure (i.e.  $E_i(\mathbf{k}) = E_i(k)$ ) and a scattering rate written as in Eq.4.26. Under such assumptions, we make the *ansatz* that the momentum relaxation time depends only on the magnitude  $k$  of the electron wave-vector, namely we write

$$\tau_i(\mathbf{k}) = \tau_i(k) . \quad (\text{B.5})$$

We now consider the MRT problem in Eq.4.18, where the wave-vector has been expressed in polar coordinates as  $\mathbf{k} = (k, \theta)$ . For isotropic bands  $E_i(\mathbf{k}) = E_i(k)$ , the  $x$  component of the group velocities can be written as

$$\begin{aligned} v_{i,x}(\mathbf{k}) &= \frac{1}{\hbar} \frac{dE_i(k)}{dk} \cos(\theta) \\ v_{j,x}(\mathbf{k}') &= \frac{1}{\hbar} \frac{dE_j(k')}{dk} \cos(\theta') = \frac{1}{\hbar} \frac{dE_j(k')}{dk} [\cos(\theta) \cos(\beta) - \sin(\theta) \sin(\beta)] \end{aligned} \quad (\text{B.6})$$

where we have introduced the angle  $\beta = (\theta' - \theta)$  between  $\mathbf{k}'$  and  $\mathbf{k}$ , which also allows us to write

$$q^2 = |\mathbf{k}' - \mathbf{k}|^2 = k^2 + (k')^2 - 2kk' \cos(\beta) . \quad (\text{B.7})$$

Furthermore, since  $\hbar\omega_0$  is independent of  $\mathbf{q}$ , then the Dirac function in Eq.4.18 restricts the integrals over  $\theta'$  along curves with a fixed energy  $E_j(k')=E_i(k) \pm \hbar\omega_0$ , which for isotropic bands are circles with fixed  $k'$  values. Along one of such circles all the terms of the  $\Theta_{i,j}(\mathbf{k}, \mathbf{k}')$  defined in Eq.4.19 are constant, except for the matrix element which, according to Eq.4.26, depends on  $\theta'$  (or on  $\beta$ ) through  $q$ . Furthermore, according to the *ansatz* in Eq.B.5,  $\tau_j(k')$  is also constant along a circle in  $\mathbf{k}$  space.

If we now rewrite the integral over  $\theta'$  in Eq.4.18 by changing the integration variable from  $\theta'$  to  $\beta=(\theta'-\theta)$ , then Eq.4.18 becomes

$$\begin{aligned} v_{i,x}(\mathbf{k}) \tau_i(k) & \left\{ \frac{1}{2\pi\hbar} \sum_j \int_{-\infty}^{+\infty} dE_j \Gamma_{i,j}(k, k') \left[ \int_{-\pi}^{\pi} |M_{i,j}(q)|^2 d\beta \right] \delta[E_j - E_i(k) \mp \hbar\omega_0] \right\} \\ & - \frac{1}{2\pi\hbar} \sum_j \int_{-\infty}^{+\infty} dE_j \Gamma_{i,j}(k, k') \tau_j(k') \left[ \int_{-\pi}^{\pi} v_{j,x}(\mathbf{k}') |M_{i,j}(q)|^2 d\beta \right] \delta[E_j - E_i(k) \mp \hbar\omega_0] \\ & = v_{i,x}(\mathbf{k}) \end{aligned} \quad (\text{B.8})$$

where we have introduced the auxiliary quantity

$$\Gamma_{i,j}(k, k') = k'(E_j) \left[ \frac{dE_j(k')}{dk} \right]^{-1} \left[ \frac{1 - f_0(E_j(k'))}{1 - f_0(E_i(k))} \right]. \quad (\text{B.9})$$

We now consider in Eq.B.8 the integral over  $\beta$  involving  $v_{j,x}(\mathbf{k}')$  and rewrite it according to Eq.B.6 as

$$\begin{aligned} \frac{1}{\hbar} \frac{dE_j(k')}{dk} \int_{-\pi}^{\pi} [ |M_{i,j}(q)|^2 \cos(\theta) \cos(\beta) - |M_{i,j}(q)|^2 \sin(\theta) \sin(\beta) ] d\beta = \\ = \frac{1}{\hbar} \frac{dE_j(k')}{dk} \cos(\theta) \int_{-\pi}^{\pi} |M_{i,j}(q)|^2 \cos(\beta) d\beta \end{aligned} \quad (\text{B.10})$$

where the integral involving  $\sin(\beta)$  evaluates to zero because  $\sin(\beta)$  is odd while  $q$  is even with respect to  $\beta$  (see Eq.B.7).

It is now important to notice that according to Eq.B.10 and the expression of  $v_{i,x}(\mathbf{k})$  in Eq.B.6, the term  $\cos(\theta)$  simplifies in Eq.B.8, which can be thus rewritten

$$\begin{aligned} \frac{1}{\hbar} \frac{dE_i(k)}{dk} \tau_i(k) & \left\{ \frac{1}{2\pi\hbar} \sum_j \int_{-\infty}^{+\infty} dE_j \Gamma_{i,j}(k, k') \left[ \int_{-\pi}^{\pi} |M_{i,j}(q)|^2 d\beta \right] \delta[E_j - E_i(k) \mp \hbar\omega_0] \right\} \\ & - \frac{1}{2\pi\hbar} \sum_j \int_{-\infty}^{+\infty} dE_j \Gamma_{i,j}(k, k') \frac{1}{\hbar} \frac{dE_j(k')}{dk} \left[ \int_{-\pi}^{\pi} |M_{i,j}(q)|^2 \cos(\beta) d\beta \right] \tau_j(k') \delta[E_j - E_i(k) \mp \hbar\omega_0] \\ & = \frac{1}{\hbar} \frac{dE_i(k)}{dk}. \end{aligned} \quad (\text{B.11})$$

Eq.B.11 reveals an important point, namely the fact that the angle  $\theta$  identifying the direction of  $\mathbf{k}$  is no longer present in the equation determining the momentum relaxation time. This is consistent with the *ansatz*  $\tau_i(\mathbf{k})=\tau_i(k)$  made in Eq.B.5, and thus validates our derivation.

It is probably useful to reiterate that, for any  $k$ , the integrals over  $\beta$  in Eq.B.11 are actually integrals along circles with a fixed  $k'$  value set by the condition  $E_j(k')=E_i(k) \pm \hbar\omega_0$ . Such integrals do not involve the unknowns of the equation (i.e. the relaxation times  $\tau_i(k)$ ), but are instead just part of the kernel of the integral equation, as it is more explicitly shown in Sec.4.3.3 where we discuss the numerical solution of Eq.B.11.



## Appendix C

# Monte Carlo approach for the solution of the Boltzmann Transport Equation

The Monte Carlo approach is a direct statistical method for the exact solution of an integral-differential equation such as the BTE [1]. Since we want to simulate transport in large graphene sheets (see Chaps.5 and 6) we have considered the particles moving in a two-dimensional space described by the position vector  $\mathbf{r} = (x, y)$ . The motion of each simulated particle can be

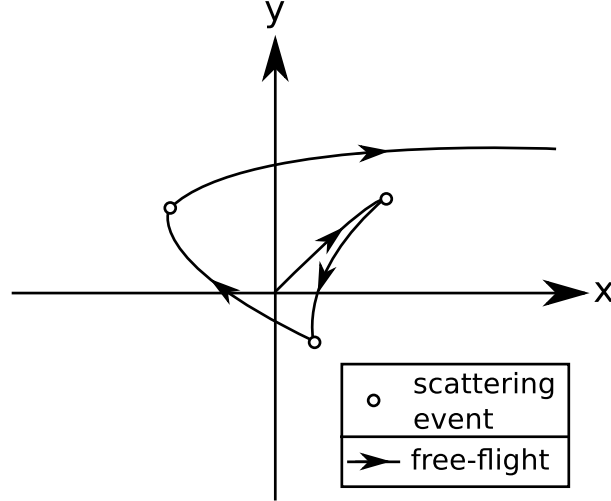


Figure C.1: Sketch of the motion of a particle in the MC simulator: free-flights governed by the classical mechanics are interspersed by scattering events calculated using the quantum mechanics.

divided in two phases (see Fig.C.1): in the first phase, the so-called *free-flight*, the particle is free to move according to the Newton law, i.e.:

$$\Delta k_x = \pm \frac{eF_x t}{\hbar} \quad (\text{C.1})$$

where  $\Delta k_x$  is the variation of the component of the particle wave-vector in the direction of the transport  $x$  during the free-flight,  $F_x$  is the value of the external electric field (we suppose a null  $F_y$ ),  $t$  is the time-length of the free-flight and the upper and lower signs are associated respectively to holes and electrons. The velocity of the particles can be calculated from the energy dispersion relation  $E(\mathbf{k})$  according to

$$\mathbf{v} = \frac{1}{\hbar} \left( \frac{\partial E(\mathbf{k})}{\partial k_x} \hat{x} + \frac{\partial E(\mathbf{k})}{\partial k_y} \hat{y} \right). \quad (\text{C.2})$$

In contrast, in the second phase, that happens at the end of each free-flight, the motion of the particle can be modified by a scattering event. The scattering events are described by the scattering rates  $S_i(\mathbf{r}, \mathbf{k}, \mathbf{k}')$ , that are defined as the probability that a carrier in the position  $\mathbf{r}$  and with wave-vector  $\mathbf{k}$  scatters to a state with wave-vector  $\mathbf{k}'$  due to the mechanism  $i$ .

In summary, the motion of the particles in a MC simulation can be represented by free-flights governed by the classical mechanics interspersed by scattering events calculated using the quantum mechanics (see Fig.C.1): this is the reason why the MC approach is called semi-classical. Moreover, the method is statistical because the duration of the free-flights, the scattering events and the state-after-scattering are selected using random-generated numbers.

In our simulator we have employed a *synchronous ensemble* MC, in which the statistics regarding all the particles are collected at the same time (see Fig.C.2). Thanks to the collected data we are able to calculate the occupation function  $f(\mathbf{r}, \mathbf{k})$  and thus solve the BTE.

Another important aspect is the treatment of carrier degeneracy, i.e. accounting for the Pauli's exclusion principle. We have employed here the technique presented in [2] in which

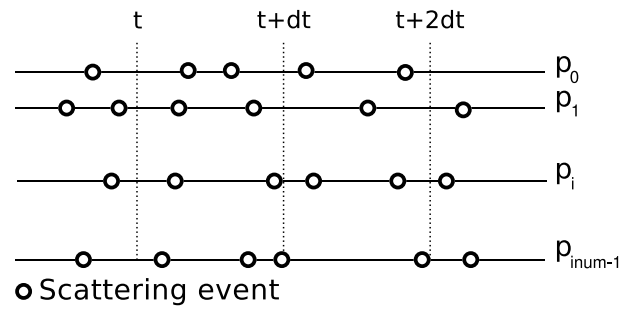


Figure C.2: Synchronous ensemble MC: the statistics of the entire set of particles  $p_i$  are collected at the same time.

the exclusion principle is taken into account by rejecting scattering events according to the occupation of the final state  $\mathbf{k}'$ .

As a final remark regarding the MC solver presented in Chap.5, since in this case we consider a uniform electric field, the occupation function  $f(\mathbf{k})$  solution of the BTE is independent of the position vector  $\mathbf{r}$ .



# Bibliography

- [1] C. Jacoboni and L. Reggiani, "The Monte Carlo method for the solution of charge transport in semiconductors with applications to covalent materials," *Rev. Mod. Phys.*, vol. 55, pp. 645–705, Jul 1983.
- [2] P. Lugli and D. K.Ferry, "Degeneracy in the Ensemble Monte Carlo Method for High-Field Transport in Semiconductors," *IEEE Trans. Electron Devices*, vol. 32, no. 11, pp. 2431–2437, 1985.



# Publications of the Author

## Articles in international journals

A. Paussa, F. Conzatti, D. Breda, R. Vermiglio, D. Esseni, and P. Palestri, “Pseudospectral Methods for the Efficient Simulation of Quantization Effects in Nanoscale MOS Transistors”, *IEEE Transactions on Electron Devices*, Vol. 57, n. 12, December 2010, pp. 3239-3249.

F. Conzatti, N. Serra, D. Esseni, M. De Michielis, A. Paussa, P. Palestri, L. Selmi, S. Thomas, T.E. Whall, D.R. Leadley, E.H.C. Parker, L. Witters, M.J. Hytch, E. Snoeck, T.J. Wang, W.C. Lee, G. Doornbos, G. Vellianitis, M.J.H. van Dal, and R.J.P. Lander, “Investigation of strain engineering in FinFETs comprising experimental analysis and numerical simulations”, *IEEE Transactions on Electron Devices*, 2011, pp. 1583-1593.

D. Breda, D. Esseni, A. Paussa, R. Specogna, F. Trevisan, and R. Vermiglio (alphabetical order), “Comparison between Pseudospectral and Discrete Geometric Methods for Modeling Quantization Effects in Nanoscale Electron Devices”, in *IEEE Transactions on Magnetism*, Vol. 48, n. 2, February 2012, pp. 203-206.

A. Paussa, and D. Esseni, “An exact and computationally efficient solution of the linearized Boltzmann Transport Equation for mobility calculations”, accepted for publication on *AIP Journal of Applied Physics*, 2013.

S. Vaziri, G. Lupina, A. Paussa, A. Smith, C. Henkel, G. Lippert, J. Dabrowski, W. Mehr, M. Östling, and M. Lemme, “A Manufacturable Process Integration Approach for Graphene Devices”, accepted for publication on *Solid State Electronics*, 2013.

A. Paussa, R. Specogna, D. Esseni, and F. Trevisan, “Pseudospectral method and Discrete Geometric Approach for Modeling Quantization Effects in Nanoscale Electron Devices”, submitted to *Journal of Computational Physics*, 2012.

A. Paussa, G. Fiori, P. Palestri, M. Geromel, D. Esseni, G. Iannaccone, and L. Selmi, “Simulation of the Performance of Graphene FETs with a Semi-Classical Model Including Band to Band Tunneling”, submitted to *IEEE Transactions on Electron Devices*, 2012.

**Presentations in international conferences**

A. Paussa, F. Conzatti, D. Breda, R. Vermiglio, and D. Esseni, “Pseudo-spectral method for the modeling of quantization effects in nanoscale MOS transistors”, in *Proc. IEEE SISPAD*, Bologna, 2010, pp. 299-302.

M. Bresciani, A. Paussa, P. Palestri, D. Esseni, and L. Selmi, “Low-Field Mobility and High-Field Drift Velocity in Graphene Nanoribbons and Graphene Bilayers”, in *IEEE IEDM Technical Digest*, San Francisco, 2010, pp. 724-727.

A. Paussa, M. Bresciani, D. Esseni, P. Palestri, and L. Selmi, “Phonon Limited Uniform Transport in Bilayer Graphene Transistors”, in *Proc. ESSDERC*, Helsinki, 2011, pp. 307-310.

A. Paussa, M. Geromel, P. Palestri, M. Bresciani, D. Esseni, and L. Selmi, “Simulation of Graphene Nanoscale RF Transistors Including Scattering and Generation/Recombination Mechanisms”, in *IEEE IEDM Technical Digest*, Washington, 2011, pp. 11.7.1-11.7.4.

**Seminars**

A. Paussa, “Graphene and Its Possible Applications to Electronics: A Theoretical Study”, A seminar by IEEE Sweden Electron Devices Chapter, Stockholm, August 2012.

**Posters in international conferences**

D. Breda, D. Esseni, A. Paussa, R. Specogna, F. Trevisan, and R. Vermiglio (alphabetical order), “Comparison between Pseudospectral and Discrete Geometric Methods for Modeling Quantization Effects in Nanoscale Electron Devices”, in *IEEE COMPUMAG Technical Digest*, Sydney, 2011.